The *Abca4*$^{-/-}$ mouse model of Stargardt disease – phenotype and therapeutic strategies

by

Peter Charbel Issa

A thesis submitted to the University of Oxford in partial fulfillment of the requirements for the degree of Doctor of Philosophy (D.Phil.)

University of Oxford & Merton College

2013

For Britta

Everything should be made as simple as possible, but not simpler.
(Albert Einstein)

Declaration

I declare that this thesis is my own original work. Where I have consulted or quoted the work of others, this is always clearly attributed. No part of this thesis has previously been submitted for a degree or any other qualification at this University or any other institution. I have acknowledged all the main sources of help. In particular, bisretinoid analyses were performed by Dr. Roxana Radu and Dr. Ilyas Washington, and electron microscopy was performed by Dr. Ulrich Schraermeyer. Parts of this work have been published as detailed in the List of Publications.

Peter Charbel Issa
University of Oxford
2013

List of Publications (see also appendix)

Original articles:

Charbel Issa P, Singh M, Lipinski DM, Chong NV, Delori FC, Barnard AR, MacLaren RE (2012) Optimization of In vivo confocal autofluorescence imaging of the ocular fundus in mice and its application to models of human retinal degeneration. Invest Ophthalmol Vis Sci 53(2):1066-1075.

Charbel Issa P, De Silva SR, Lipinski DM, Singh MS, Mouravlev A, You Q, Barnard AR, Hankins MW, During MJ, MacLaren RE (2013) Assessment of the tropism and effectiveness of new primate derived hybrid recombinant AAV serotypes in the mouse and primate retina. PLOS ONE 8(4): e60361. doi:10.1371/journal.pone.0060361

Charbel Issa P, Barnard AR, Singh MS, Carter E, Jiang Z, Radu R, Schraermeyer U, MacLaren RE (2013) Fundus Autofluorescence in the *Abca4*$^{-/-}$ Mouse – Correlation with Retinal Function, Histology and Accumulation of A2E. Invest Ophthalmol Vis Sci 54(8):5602-5612

Review

Charbel Issa P, MacLaren RE (2012) Non-viral retinal gene-therapy. Clin Exp Ophthalmol. 40(1):39-47

Acknowledgements

In particular, I would like to thank my supervisor at Oxford, Professor Robert E. MacLaren *FRCOphth FRCSEd DPhil* (Professor of Ophthalmology, Nuffield Laboratory of Ophthalmology, University of Oxford, and Consultant Ophthalmologist at the Oxford Eye Hospital) who suggested that I apply to the University in 2009. His generosity, advice, and support have been exemplary. I feel particularly fortunate to have spent time in his lab at Oxford University, a place of inspiring intellectual exchange, extraordinary teaching, and freedom to pursue own ideas.

I also thank Alun Barnard and Mandeep Singh for their support and friendship inside and outside the lab. It was a great pleasure to learn from their constant critical thinking.

Also, I would like to thank all colleagues in the lab who helped with their experimental expertise and/or by spending time together during and after lengthy experiments or analysis: Sher Aslam, Rachel Butler, Wayne Davies, Samantha De Silva, Daniel Lipinski, Steven Hughes, Michelle McClements, Georgia Perganta, Sumathi Sekaran, Haidong Shan, Athanasios Vachtsevanos, Quisheng You.

It was a great pleasure and opportunity to discuss many aspects of retinal imaging with Professor François Delori (Professor of Ophthalmology, Schepens Eye Research Institute, Harvard Medical School).

I am thankful to Matthew During and Alexandre Mouravlev who supplied the viral vectors for some of the experiments on gene therapy. Also, I thank Ilyas Washington and Roxana Radu for the fruitful and pleasant collaboration in assessing bisretinoid levels and Ilyas Washington for providing C20-deuterized vitamin A. I also thank Ulrich Schraermeyer for helping with electron microscopy.

I thank Victor Chong and Hendrik Scholl for their help in securing funding to come to Oxford. I feel privileged to have had their counsel throughout the years, which was always possible despite their busy schedules.

I am most grateful to have had the love and support of my family – Britta, Jakob and Anna. I thank Britta for her encouragement and understanding for this work. Jakob was born during our second year in Oxford. Together with Anna who was born three years later, he since fills our life with happiness.

I also want to thank my parents and my sister for their encouragement and support over many years. The path I went was only possible on this fundament.

The *Abca4*$^{-/-}$ mouse model of Stargardt disease – phenotype and therapeutic strategies

Peter Charbel Issa
Merton College, University of Oxford, Trinity 2013

Abstract

Stargardt disease is caused by mutations in the *ABCA4* gene and is probably the commonest inherited cause for retinal degeneration in youth with progressive visual deterioration. The *Abca4*$^{-/-}$ mouse is an animal model mimicking certain aspects of the human disease, including an accumulation of autofluorescent lipofuscin in the retinal pigment epithelium (RPE). The model is therefore ideally suited for preclinical investigation of novel treatment approaches for Stargardt disease.

Imaging of lipofuscin- and melanin-related fundus autofluorescence (AF) was optimized in mice, which subsequently allowed investigating the mouse ocular phenotype in vivo. The *Abca4*$^{-/-}$ mouse showed an age-related increase in lipofuscin- and melanin-related AF intensity, correlating to an increase of ex vivo assessed *bis*-retinoid-fluorophores and formation of melanolipofuscin granules, respectively. Retinal function remained largely unaffected by those changes within the RPE.

Abca4$^{-/-}$ mice were fed with C20-deuterized vitamin A (C20dVitA) which had been shown to inhibit lipofuscin-formation in the RPE. The diet markedly reduced lipofuscin- and melanin-related AF intensity to levels measured in wild type animals on a normal diet. This treatment did not affect retinal function. The possibility of performing similar fundus AF measurements in humans may allow fast translation of this therapy into clinical trials.

The only causative treatment approach for Stargardt disease will be gene replacement therapy. Investigation of various mutant adeno-associated viruses (AAVs) as vector for delivering *ABCA4* revealed that photoreceptors in *Abca4*$^{-/-}$ mice were more difficult to transduce than photoreceptors in wild type mice. This indicates an influence of the diseased retina on gene delivery. Thus, very efficient viruses might be needed to achieve relevant ABCA4 expression in the retina of patients with Stargardt disease.

In summary, application of a clinically relevant imaging method allows to assess the ocular phenotype of the mouse model for Stargardt disease and to investigate novel treatment strategies

Table of contents

Declaration II
List of Publications III
Acknowledgements IV
Abstract V
Table of contents VI
List of abbreviations IX
1 Introduction 1
1.1 Stargardt disease – the clinical phenotype 1
1.2 The function of ABCA4 4
1.2.1 Vitamin A and vision 4
1.2.2 ABCA4 function on a molecular level 6
1.2.3 The *Abca4*$^{-/-}$ mouse – an animal model for Stargardt disease 7
1.3 Towards therapy for Stargardt disease 9
1.3.1 Outcome measures in preclinical studies - ERG 10
1.3.2 Outcome measures in preclinical studies – in vivo fundus autofluorescence imaging 10
1.3.3 Pharmacotherapy for Stargardt disease 12
1.3.4 The challenge of gene therapy for Stargardt disease 13
1.4 Aims 15
2 General methods 17
2.1 Mice 17
2.1.1 Origin and maintenance 17
2.1.2 Anesthesia and pharmacological recovery of animals, pharmacological pupil dilation 18
2.2 Genotyping 18
2.3 Electroretinography 19
2.4 Preparation and embedding of mouse eye cups for light and electron microscopy 20
2.5 Statistical analysis 21
3 Optimization of fundus autofluorescence imaging in mice 22
3.1 Introduction 22
3.2 Methods 23
3.2.1 Animal preparation for imaging procedures 23
3.2.2 Fundus imaging using a confocal scanning laser ophthalmoscopy 23
3.2.3 Quantitative grey level image analysis 26
3.2.4 Recording of the pupil diameter 28
3.3 Results 29
3.3.1 Image acquisition 29
3.3.2 Recording and quantifying autofluorescence from the RPE 38
3.3.3 Bleaching experiments 40

3.4 Discussion 42
3.4.1 Image acquisition 42
3.4.2 Recording and quantifying autofluorescence from RPE 43
3.4.3 Bleaching experiments 45
3.4.4 Conclusion 46
3.5 Appendix: Standard protocol for recording fundus autofluorescence AF in mice 47
4 The *Abca4*$^{-/-}$ Mouse Model – Fundus Autofluorescence and its Correlation with Accumulation of A2E and Histology 49
4.1 Introduction 49
4.2 Methods 50
4.2.1 Fundus autofluorescence imaging and image analysis 50
4.2.2 *RPE65* Genotyping 50
4.2.3 Fluorescence microscopy 51
4.2.4 Outer nuclear layer count 51
4.2.5 Electron microscopy and pigment granule quantification 51
4.2.6 Quantification of A2E 53
4.3 Results 54
4.3.1 *RPE65* Genotyping 54
4.3.2 Longitudinal recordings of 488 nm and 790 nm fundus autofluorescence intensity 55
4.3.3 Cross sectional recordings of 488nm and 790nm fundus autofluorescence 57
4.3.4 Comparison of fundus autofluorescence recordings and A2E measurements 61
4.3.5 Bright light and fluorescence microscopy 62
4.3.6 Ultrastructural observations in the TEM 66
4.3.7 Quantification of lipofuscin granules by electron microscopy 74
4.4 Discussion 79
4.4.1 488 nm and 790 nm fundus AF: its relation to A2E accumulation and sub-cellular RPE-alterations 79
4.4.2 Conclusion 83
5 Functional Characterization of the *Abca4*$^{-/-}$ Mouse 84
5.1 Introduction 84
5.2 Methods 85
5.2.1 Electroretinography 85
5.3 Results 87
5.3.1 Electroretinography 87
5.4 Discussion 92
5.4.1 Functional relevance of increased fundus AF levels and A2E-accumulation 92
5.4.2 Dark adaptation kinetics 93
5.5 Conclusion 95

6 Fundus autofluorescence for evaluating a novel lipofuscin-lowering pharmacotherapy in the *Abca4*$^{-/-}$ mouse 97
6.1 Introduction 97
6.2 Methods 98
6.2.1 Diet 98
6.2.2 Fundus autofluorescence imaging and image analysis 98
6.2.3 Quantification of A2E 99
6.2.4 Electroretinography 99
6.3 Results 100
6.3.1 Treatment with C20dVitA reduces A2E- and autofluorescence levels 100
6.3.2 C20dVitA has no effect on retinal function 108
6.4 Discussion 113
7 Towards gene therapy for Stargardt disease 115
7.1 Introduction 115
7.2 Methods 116
7.2.1 Viral vectors 116
7.2.2 Subretinal injection 117
7.2.3 Fundus *in vivo* imaging 118
7.2.4 Immunohistology 118
7.2.5 Light microscopy 120
7.2.6 Image Analysis 120
7.2.7 Confocal microscopy 121
7.3 Results 121
7.3.1 *In vivo* measurement of fluorescence intensity 121
7.3.2 Tropism of rAAV2/Rec2 and rAAV2/Rec3 in *Abca4*$^{-/-}$ and WT mice 123
7.3.3 Histological analysis of fluorescence intensity 127
7.4 Discussion 131
8 General discussion 134
8.1 Fundus autofluorescence imaging in mice 135
8.2 The phenotype of the *Abca4*$^{-/-}$ mouse 139
8.2.1 The functional phenotype of the *Abca4*$^{-/-}$ mouse 140
8.2.2 The phenotype of the *Abca4*$^{-/-}$ mouse on fundus autofluorescence imaging 141
8.2.3 Comparison of the mouse phenotype with human disease 142
8.3 Assessment of novel therapies for Stargardt disease 144
8.3.1 Pharmacotherapy using C20-deuterized Vitamin A 144
8.3.2 Gene therapy in the *Abca4*$^{-/-}$ mouse model for Stargardt disease 146
8.4 The therapeutic window 148
8.5 Comment on masked assessment in preclinical studies 150
9 Conclusions 151
References 152
Appendix 160

List of abbreviations

A2E	N-retinylidene-N-retinylethanolamine
AAV	Adeno-associated virus
ABCA4	ATP-binding cassette A4
AF	Autofluorescence
AMD	Age-related macular degeneration
CNS	Central nervous system
cSLO	confocal scanning laser ophthalmoscope
ERG	Electroretinography
GFP	Green fluorescent protein
ITR	Inverted terminal repeats
M	Molar
min	minute
NIR	Near-infrared
NrPE	N-retinylidene-phosphatidylethanolamine
OCT	Optical coherence tomography
ORF	Open reading frame
PBS	Phosphate buffered saline
POS	Photoreceptor outer segments
RPE	Retinal pigment epithelium
WT	Wild-type

1 Introduction

1.1 Stargardt disease – the clinical phenotype

Mutations in the *ABCA4* gene cause Stargardt disease, which was first described by Karl Bruno Stargardt, a German ophthalmologist, in1909.[1] When working in Strassburg, he described seven members of two families with a relatively uniform alteration of the central retina, characterized by white-yellowish flecks at the level of the retinal pigment epithelium (RPE) which – in later disease stages – may surround an area of chorioretinal atrophy (Figure 1.1).

Stargardt disease is probably the most common recessively inherited retinal degeneration in Europe and North America. The disease usually becomes symptomatic during late childhood and leads to progressive visual deterioration. Patients lose the ability to read, recognize faces and perform daily tasks - they therefore lose their independence. Mutations in *ABCA4* may also cause similar disease manifestations later in life ("late-onset Stargardt disease"),[2, 3] as well as cone-rod dystrophy or retinitis pigmentosa,[4-8] and might also influence disease severity in AMD [9] which is the most common cause of blindness in western societies.

A hallmark of the disease is an increased fundus autofluorescence (AF) exhibiting the fluorescence characteristics of lipofuscin in the retinal pigment epithelium (RPE).[10, 11] Later, atrophy of the central retina develops, which spreads centrifugally over time.[12] Accumulation of fluorophores can be visualized in fundus AF images using a confocal scanning laser ophthalmoscope (cSLO).[13] This technique may also facilitate the diagnosis and monitoring of disease progression

over time (Figure 1.2).[12, 14, 15] Currently, there is no therapy with proven benefit for patients with Stargardt disease. However, there are major research efforts worldwide to find cure for this disease that is amongst the most common causes for childhood blindness.

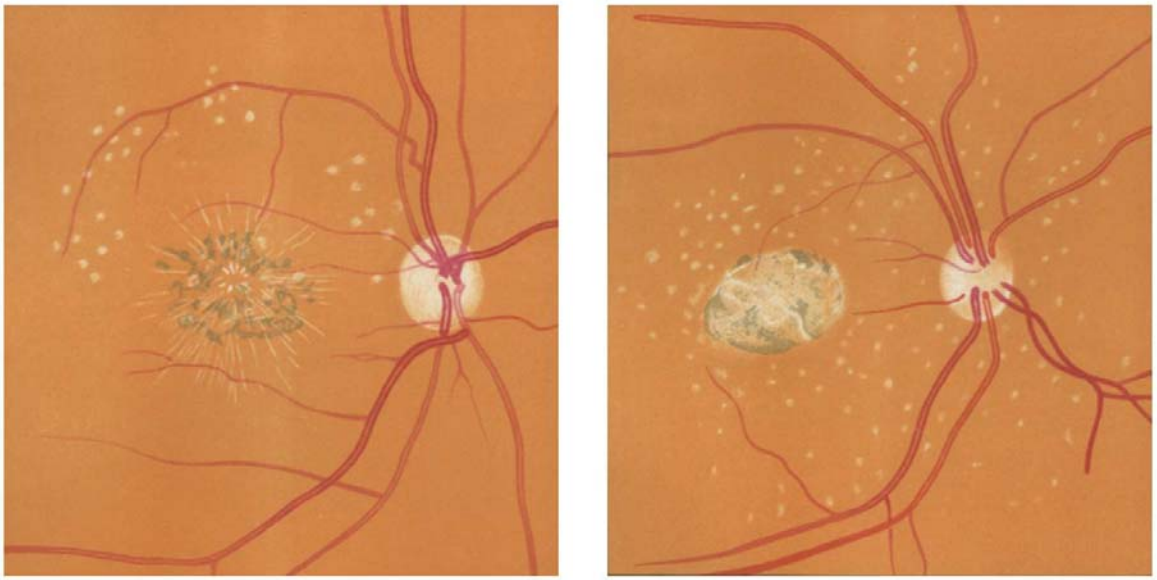

Figure 1.1: Original drawings from the first description of Stargardt disease in 1909 [reprint with permission from Springer Media].[1]

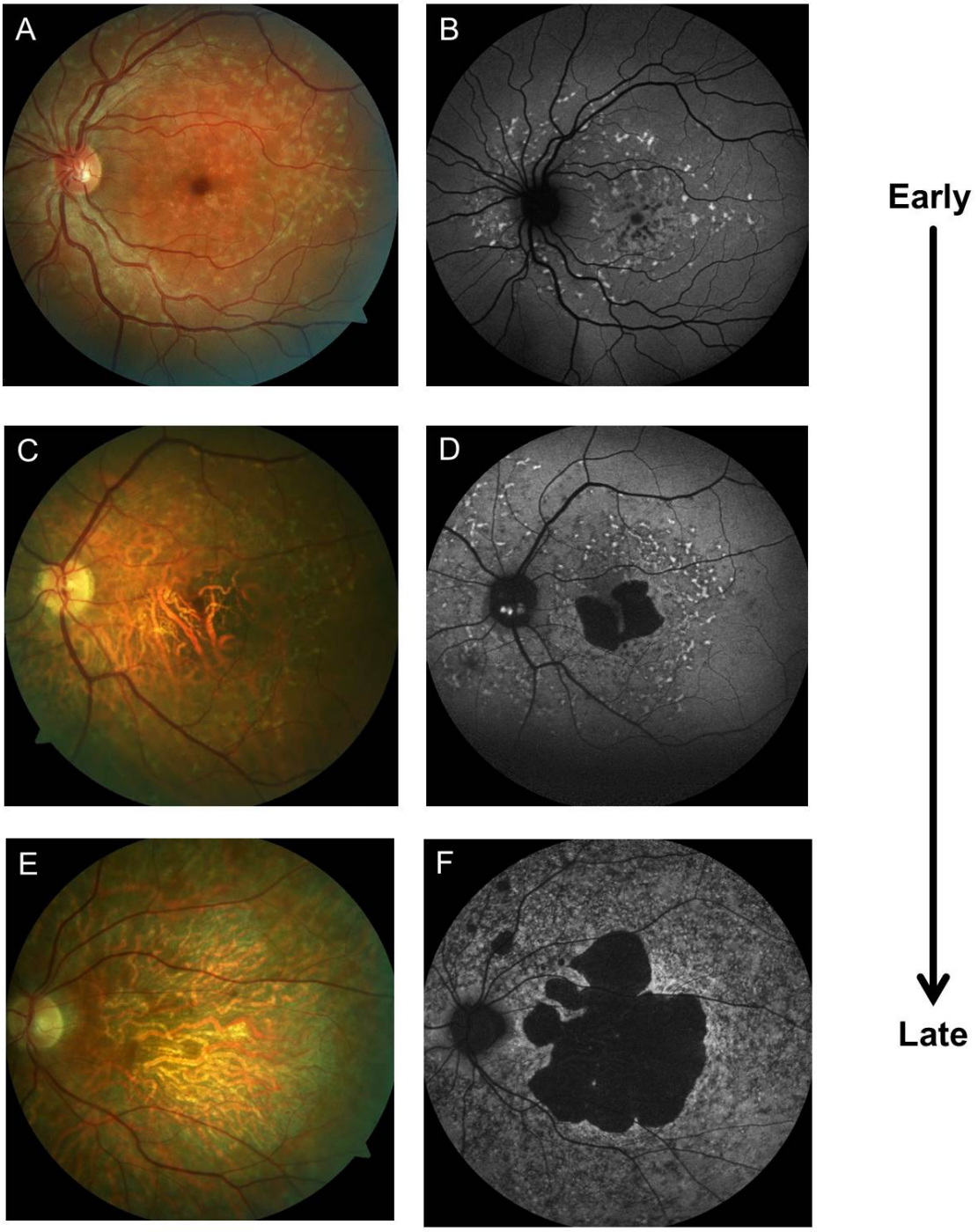

Figure 1.2: Clinical appearance of Stargardt disease captured with a colour fundus camera (A, C, E). Corresponding fundus autofluorescence (AF) images (B, D, F) reveal flecks of increased and decreased autofluorescence. The figure also illustrates the natural history of the disease with increasing atrophy (black area in the AF images D and F) in later disease stages.

1.2 The function of ABCA4

1.2.1 Vitamin A and vision

Understanding the function of ABCA4 and the pathophysiology of Stargardt disease requires explanation of the role of vitamin A and its metabolites in vision.

Visual pigments are the molecular basis for light absorption by retinal cells. There are various such pigments depending on the light absorbing cell type in the retina (e.g. rods, various cone types). However, independent from the absorption characteristics of each specific cell type, they have a common chromophore: 11-*cis* retinal, which is an aldehyde form of vitamin A.

The initiating event in vision is the photoisomerization of 11-*cis* retinal into all-*trans* retinal by light, followed by release of the covalently bound opsin from all-*trans*-retinal in the photoreceptor outer segment discs. While the actual activation of the signal cascade is mediated via the activated opsin, 11-*cis* retinal is regenerated from all-*trans* retinal via the visual cycle. All-*trans* retinal is converted into all-*trans* retinol which subsequently is moved from the photoreceptor cell to the RPE where it is recycled to 11-*cis* retinal via various enzymatic reactions.[16] The essential steps of the visual cycle are outlined in Figure 1.3.

All-*trans* retinal is a highly reactive molecule and therefore, recycling of all-*trans* retinal is not only necessary to restore 11-*cis* retinal but also to remove this potentially cytotoxic compound from photoreceptors.[17] All-*trans*-retinal may for instance form reactive oxygen species or react with phosphatidyl-ethanolamine (PE), a major lipid component in the cell membrane of photoreceptor outer segments. The latter reaction, forming N-retinylidene-phosphatidylethanolamine

(N-ret-PE), is reversible and might be seen as a buffering mechanism or temporary sink for all-*trans* retinal (Figure 1.3). A second all-*trans* retinal molecule may react with N-ret-PE, forming *bis*-retinoids including precursors (e.g. A2-PE) of N-retinylidene-N-retinylethanolamine (A2E).[18] A2E is a major component of lipofuscin [19-21] which accumulates in the RPE of Stargardt patients after phagocytosis of photoreceptor outer segment discs loaded with bis-retinoids.[22]

Figure 1.3 (next page): Illustration of the visual cycle and the function of ABCA4. A: The visual cycle is located at the interface (marked in red) between photoreceptors and retinal pigment epithelium (RPE). It is necessary to reconstitute visual pigment and comprises several steps in the photoreceptors and the RPE. Enzymes involved in the visual cycle include several retinal dehydrogenases (RDH8 and RDH5), the isomerohydrolase RPE65, or lecithin retinol acyltransferase (LRAT). B: Magnified illustration of the photoreceptor-RPE interface. Incident light causes the photoisomerization of 11-cis retinal in the discs of the photoreceptor outer segment. The resulting all-trans-retinal is highly reactive and may form a Schiff base with phosphatidyl-ethanolamine (PE), N-retinylidene-phosphatidylethanol-amine (N-ret-PE). ABCA4 flips its substrate N-ret-PE into the cytosol where it can enter the visual cycle again. ABCA-dysfunction may lead to accumulation of N-ret-PE with subsequent addition of a second all-trans-retinal molecule or similar vitamin A derivative, hence forming bis-retinoids such as A2-PE.

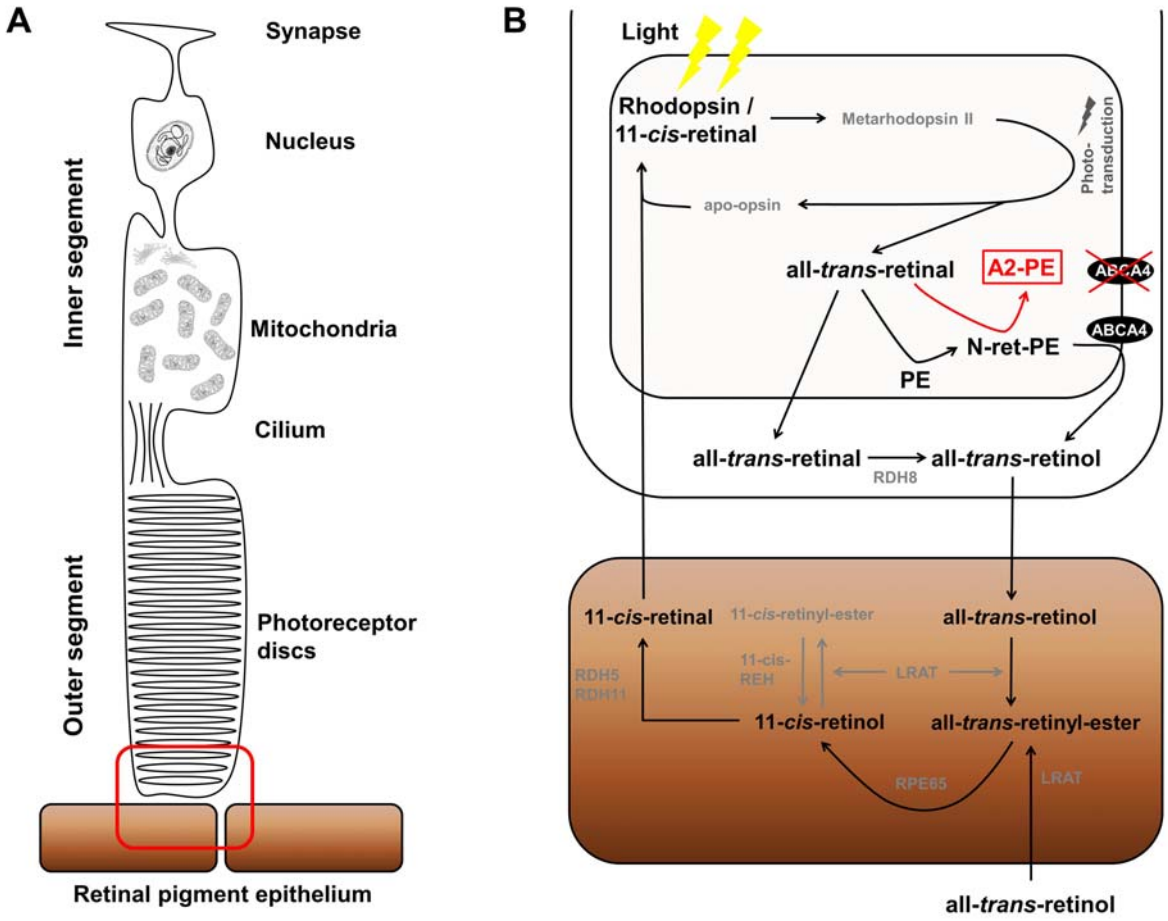

1.2.2 ABCA4 function on a molecular level

The ATP-binding cassette A4 (ABCA4) protein is a member of the superfamily of ATP-binding cassette (ABC) trans-membrane transporters.[4, 23, 24] ABCA4 is expressed in photoreceptor outer segments (POS) where it is bound to the rim of the disc membranes.[25] POS discs constantly undergo renewal. They are shed into the subretinal space at a rate of about 10% per day while new discs are produced at the base of the POS.[26] In the rhesus monkey, 80 to 90 new rod POS disc are assembled and shed daily.[27] Assuming similar rates in humans, there would be a complete replacement of the stack of disc membranes every 9 to 12 days. Similar

renewal rates (11 to 12 days) have been described for the human cone POS.[28] Similar kinetics have been described for mouse photoreceptors.[29] Shed discs are phagocytosed by RPE cells where they are metabolized.

ABCA4 is thought to accelerate the elimination of vitamin A-derived compounds (all-*trans* retinal and its *bis*-retinoids) from the POS disc lumen into the cytoplasm.[30-32] In the POS cytoplasm, all-*trans* retinal can be reduced to all-*trans* retinol by an all-*trans* retinol dehydrogenase (RDH8 and RDH12),[33] and thus move the vitamin A-derivatives back into the visual cycle.[31]

Dysfunction or loss of function of ABCA4 may result in accumulation of all-*trans* retinal and *bis*-retinoids in POS discs.[34] Such loaded POS discs cannot completely be metabolized by RPE cells after phagocytosis, resulting in lipofuscin accumulation in the lysosomal compartment of RPE cells. RPE lipofuscin is a mixture of complex molecules, including *bis*-retinoids and various lipid peroxidation products. Excessive accumulation of those compounds – particular in their oxidized form – appears to have toxic effects on RPE cells, although the exact mechanisms have not yet been completely understood.[31] Eventually, degeneration of overlying photoreceptors occurs secondary to RPE cell death.

1.2.3 The *Abca4*$^{-/-}$ mouse – an animal model for Stargardt disease

Retinal research, including the investigation of novel therapies for retinal degenerative diseases, relies heavily on the use of animal models. Small rodents comprise the majority of disease models that have been developed to date,[35] and with regard to Stargardt disease, only one mouse model has as yet been developed (*Abca4*$^{-/-}$ mouse).[34]

Knowledge of the above described biological role of ABCA4 is largely derived from studies of the *Abca4*$^{-/-}$ mouse, a disease model generated by targeted disruption of the *Abca4* locus.[34] Compared to wild type (WT) controls, the following main phenotypic differences were identified in the *Abca4*$^{-/-}$ mouse by Weng et al.[34]

- *Delayed rod dark adaptation with otherwise normal functional parameters.*

  It was discussed that Abca4 therefore would have no direct role in visual transduction (i.e. the activation of photoreceptors by light). However, persistent all-*trans* retinal in photoreceptor outer segments could interact with the opsin, resulting in a low level activation of photoreceptors. This would make them less sensitive to light until the all-*trans* retinal has been replaced by recycled11cis-*trans* retinal.
- *Transient accumulation of all-trans retinal and transient depletion of all-trans retinol and all-trans retinyl-ester following a photobleach.*

  Accumulation of all-*trans* retinal may be explained by its reduced clearance due to non-functional Abca4. All-*trans* retinol is a downstream product in the visual cycle after a photobleach and all-*trans* retinyl-ester may be seen as a storage form for retinal in the RPE. Accumulation of both would be reduced if less all-*trans* retinal is recycled in the visual cycle.
- *Increased phosphatidyl-ethanolamine in POS.*

  It was hypothesized by Weng et al. that this may be due to a decreased turnover of phosphatidyl-ethanolamine and thus increased accumulation in the inner leaflet of the disc bilayer.[34]

- *Dramatically increased A2E in RPE cells*

  This clearly was the most pronounced effect of non-functioning Abca4 in this mouse model. Weng et al. hypothesized that the accumulation of *bis*-retinoids in POS and their subsequent impaired digestion after phagocytosis of shed discs by the RPE would lead to the buildup of A2E in the lysosomal compartment of RPE cells.

Except for the delayed dark adaptation, measurements of those parameters require sacrifice of animals. In later studies by others, delayed dark adaptation was not consistently found in the *Abca4*$^{-/-}$ mouse. The most robust reported phenotypic feature throughout studies proved to be increased A2E levels in the RPE.

1.3 Towards therapy for Stargardt disease

Using the search term “Stargardt disease” in an official clinical trials database (www.clinicaltrials.gov; accessed 12.9.2013) revealed various therapeutic strategies currently under investigation. These include gene therapy (clinical trials identifiers NCT01367444, NCT01736592), pharmacotherapy to slow the visual cycle (e.g. using 4-methylpyrazole; NCT00346853), subretinal transplantation of human embryonic stem cell-derived RPE cells (NCT01345006, NCT01469832, NCT01625559), various treatments using bone marrow derived stem cells (NCT01920867), dietary supplementation with docosahexaenoic acid (NCT00060749), and microcurrent stimulation (NCT01790958). Although some of those therapeutic concepts have a more profound rational then others, none of those therapies has yet proven to be effective in positively affecting the disease course in Stargardt patients.

Independent from the chosen treatment approach, there are a number of challenges when developing such therapies. A prerequisite for translating such novel therapeutic concepts into clinical trials is to demonstrate safety and proof of principle in appropriate animal models. For Stargardt disease, this would be the *Abca4*$^{-/-}$ mouse described above.

1.3.1 Outcome measures in preclinical studies - ERG

In vivo assessments of this mouse model, especially when studying the effect of potential novel treatments for Stargardt disease, mainly relied on functional testing using electroretinography (ERG).[36-39] However, protocols, read out parameters, as well as results were markedly different when trying to detect the apparently characteristic prolonged dark adaptation of the *Abca4*$^{-/-}$ mouse. Because of this high variability of ERG assessments, the reliability of this phenotype and its reliability as an outcome measure in preclinical studies currently remain unclear. Clearly, consistent and robust differences compared to controls would be needed to reliably evaluate the potential benefit of novel therapies in preclinical studies.

1.3.2 Outcome measures in preclinical studies – in vivo fundus autofluorescence imaging

The most pronounced phenotypic difference of this mouse model for Stargardt disease compared to controls was the accumulation of *bis*-retinoid related lipofuscin in the RPE. Its assessment as yet relied on post-mortem studies using quantification of A2E as a surrogate marker for overall *bis*-retinoid accumulation.[34, 36-39] Translation of preclinical studies showing effectiveness in the reducing A2E in the

Abca4$^{-/-}$ mouse would, however, strongly benefit from an in vivo surrogate measure that could also be used in subsequent clinical trials.

Marked agreement between the spatial distribution of A2E in comparison to fluorescent measurements from the mouse ocular fundus has recently been found using an ex vivo mass spectrometry-based technique.[40] Therefore, in vivo fundus AF measurements appear to be a good surrogate marker for A2E accumulation in the RPE.

In vivo fundus AF imaging using a confocal scanning laser ophthalmoscope (cSLO) is the currently most widely used technique in clinical settings. A cSLO is an imaging device that allows recording of high resolution fundus images.[41] Depending on the usage of filters, various imaging modes may be employed, including fundus reflectance and AF images.

During cSLO imaging, the retina is illuminated by a laser beam projected through the scan pupil, which is the small area within the pupil plane through which the oscillating laser beam enters the eye. Reflected or fluorescent light from the ocular fundus is detected in the detection pupil, which is a larger area within the anatomic pupil centered concentric to the scan pupil. A pinhole is placed in front of the detector to block scattered light and light reflected from other retinal planes than the focal plane, resulting in a confocal high contrast image of the ocular fundus.

The recent advances in retinal imaging, particularly in vivo AF imaging, now provide the opportunity to visualize lipofuscin accumulation in vivo and thus to re-explore the in vivo phenotype of the *Abca4*$^{-/-}$ mouse in more detail. Application of

an outcome measure such as AF imaging in preclinical studies would certainly facilitate transition into clinical trials, since similar and comparable read outs could then be applied as an endpoint in clinical studies.

Although cSLO technology is widely used in clinical ophthalmology to diagnose and monitor retinopathies including Stargardt disease,[42] cSLO in vivo AF imaging has not yet been optimized for the use in small animal models including the mouse and to reliably reflect biochemical and/or structural alterations.

1.3.3 Pharmacotherapy for Stargardt disease

Based on the understanding that *bis*-retinoid-related lipofuscin accumulation would play a major role in the pathophysiology of Stargardt disease, various pharmacotherapies have been suggested to decrease *bis*-retinoid formation. These interventions aimed at reducing *bis*-retinoid accumulation by reducing the availability of vitamin A to the retina,[36, 37, 43] by inhibition of the visual cycle,[44] or by slowing dimerization of *bis*-retinoids using C20-deuterized Vitamin A (C20dVitA) as dietary supplement.[45, 46]

Most approaches have been shown to effectively reduce A2E and lipofuscin accumulation in the RPE of the *Abca4*$^{-/-}$ mouse, but none has so far been investigated in a clinical trial. Reduction of Vitamin A availability and inhibition of the visual cycle have in common that the reduced production and recycling of 11-*cis* retinal results in a functional impairment of rod function and thus leads to a reduced capability to adapt to dim light situations. In contrast, C20dVitA does not interfere with the availability of 11-*cis* retinal and thus is unlikely to cause reduced rod function and dark adaptation problems, although formally this has not been shown yet.

1.3.4 The challenge of gene therapy for Stargardt disease

The genetic nature of Stargardt disease makes it a logical target for gene therapy. The principal feasibility of retinal gene therapy has been proven in a large number of animal models and in several human clinical trials, most of which used adeno-associated viral (AAV) vectors.[47-54] Most importantly, the human trials have not suggested any relevant safety concerns that would impede further clinical evaluation of retinal gene therapy using AAV vectors.

The retina presents a straightforward target for gene therapy.[55] It is easily accessible, allowing treatment without the necessity of systemic gene delivery. Subretinal injection is usually the preferred route of delivery in retinal gene therapy because high concentrations and a long contact time of the gene construct can be achieved at the site of the target cells, which are usually the photoreceptors. The subretinal space is a discrete anatomical compartment which in recent retinal gene therapy clinical trials has been shown to contain vector spread. The small volume of the target tissue requires only minor amounts of therapeutics, further decreasing the likelihood of systemic adverse events. Moreover, the therapeutic effect can be monitored anatomically, due to the clear media of the eye, as well as functionally, for example, by visual field testing or retinal electrophysiology.

Challenges with regards to *Abca4* gene delivery for Stargardt disease include the large size of the gene (~6.7kB) and the necessity to deliver it to photoreceptors, where Abca4 is physiologically expressed and which are inherently more difficult to transduce than RPE cells in the previous RPE65 trials.

AAV is non-pathogenic, non-enveloped dependovirus which cannot replicate without concurrent active infection of the cell with an additional virus, such as

adenovirus or herpes simplex virus.[56] AAV has a packaging capacity for single-stranded DNA with a maximum length of 5.1kb. The AAV genome has two open reading frames (ORF), *rep* required for replication and *cap* coding for capsid proteins. The coding sequence is flanked by two inverted terminal repeats (ITRs), each 145kb long, which are required for efficient genome packaging, escape from host immune reaction against single stranded DNA and sustained transcription in the host cell. For the construction of AAV vectors useful for gene therapy, the *rep* and *cap* genes are replaced for the transgene cassette. The coding sequence of the transgene is limited to about 4.8kb because the two ITRs cannot be deleted. This 4.8kb packaging limit for genomic DNA per viral particle at least includes the promoter, the therapeutic cDNA, the poly-adenylation signal, and possibly additional genetic sequences to enhance effectiveness.

Against this background, gene therapy for Stargardt disease is hindered by the 6.8kb size of the *Abca4* cDNA. However, delivery of larger transgene cassettes exceeding the 4.8kb limitation using AAV as vector has been shown in principle, although at a reduced efficiency. Allocca et al. showed expression of ABCA4 protein in the mouse retina from a single 8.9 kb transgene cassette packaged into AAV.[38] Since then, several other virology groups have shown that the AAV packaging limit is not exceeded, but the transgene is most likely split into fragments across independent vector particles, requiring a recombination mechanism after viral transduction and limiting the efficacy of transgene delivery.[38, 57-60] Thus, high levels of transduction using AAV would be required to aid recombination of two halves of a split *Abca4* transgene.

Transduction efficiency of AAV vectors for specific cell populations can be manipulated by recombination of different AAV serotypes. The various AAV serotypes differ in their capsid proteins which confer different binding affinities to cell surface structures. The process of pseudotyping involves packaging of an expression cassette – usually including the ITRs of AAV2 – into a capsid from a different AAV serotype, resulting in a so called recombinant AAV (rAAV). Such pseudotyping and various other optimization steps may be employed in order to achieve efficient gene delivery and expression of a split *ABCA4* transgene cassette.

1.4 Aims

In summary, an enormous knowledge has been accumulated on the molecular genetic cause and the pathogenesis of Stargardt disease over the last decade. Studies in an animal model for Stargardt disease, the *Abca4*$^{-/-}$ mouse, have not only led to improved understanding of the disease, but now also allows to evaluate novel therapies for Stargardt patients in preclinical studies. However, the mouse phenotype has not yet been determined using clinically relevant imaging methods, such as fundus AF imaging, which would allow using the same outcome parameters when evaluating novel therapies in a preclinical and clinical trial. Moreover, the development of gene therapy for Stargardt disease is hampered by the size of the *Abca4*$^{-/-}$ gene and the much needed highly effective vectors for transducing photoreceptors. Against this background, the overall objectives of the studies described herein were:

- To identify a phenotype using fundus AF imaging in the *Abca4*$^{-/-}$ mouse that can be determined reliably in vivo. If it parallels the human disease phenotype, this would allow reliable preclinical evaluation of novel therapeutic concepts for Stargardt disease and would facilitate straightforward translation of therapies into clinical trials.
- To apply this novel phenotypic evaluation for investigating the effect of C20-dVitA pharmacotherapy in the *Abca4*$^{-/-}$ mouse model for Stargardt disease.
- To evaluate a novel gene therapy approach as a potential means for delivering *Abca4* to photoreceptors.

To achieve those objectives, the following work packages logically followed each other. Each of these projects will be introduced and discussed in separate chapters.

1. To optimize the fundus AF imaging of the ocular fundus in mice.
2. To characterize the *Abca4*$^{-/-}$ mouse model of Stargardt disease using AF imaging and to correlate findings with post-mortem A2E accumulation and histology.
3. To investigate a potential functional phenotype of the *Abca4*$^{-/-}$ mouse using ERG recordings.
4. To investigate the applicability of fundus AF imaging for evaluating a pharmacological therapy of inhibiting lipofuscin accumulation.
5. To explore the efficiency of novel AAV constructs for gene delivery to the retina of the *Abca4*$^{-/-}$ mouse.

2 General methods

2.1 Mice

2.1.1 Origin and maintenance

Pigmented wild type (WT) 129S2/SvHsd (referred herein as WT129) mice were purchased from Harlan Laboratories (Hillcrest, UK). WT C57Bl/6 and albino BALB/c mice were provided by the Biomedical Sciences division, University of Oxford. Pigmented *Abca4* knockout mice (129S4/SvJae-*Abca4*^{tm1Ght}, referred herein as *Abca4*$^{-/-}$) [34] were provided by Gabriel Travis, David Geffen School of Medicine, University of California, Los Angeles, USA. Rhodopsin knockout mice (B6.129S1- *Rho*^{tm1Phm}, referred to herein as *Rho*$^{-/-}$) [61] were a kind gift obtained under MTA from Jane Farrar, Trinity College Dublin, Ireland. Mice expressing the fluorescent reporter protein DsRed under a modified actin promoter (Tg(CAG-DsRed*MST)1Nagy/J) were purchased from The Jackson Laboratory (Bar Harbor, Maine, USA).

Animals were kept in a 12 hour light (<100 lux) / dark cycle, with standard mouse chow (Lab Diet 5001; PMI Nutrition Inc., LLC, Brentwood, MO) and water available *ad libitum*. Mice were housed at 23 °C in facilities managed by the Oxford University Biomedical Science Division. All animal breeding and procedures were performed under the approval of local and national ethical and legal authorities and in accordance with the Association for Research in Vision and Ophthalmology statements on the care and use of animals in ophthalmic research.

2.1.2 Anesthesia and pharmacological recovery of animals, pharmacological pupil dilation

Mice were anesthetized by intraperitoneal injection of 1 mg/kg medetomidine (Dormitor® 1 mg/ml, Pfizer, Sandwich, UK), 60mg/kg ketamine (Ketaset® 100mg/kg, Fort Dodge, Southampton, UK) and sterile water in the ratio 1:0.6:8.4. Recovery from anesthesia was initiated by intraperitoneal injection of atipamezole (Antisedan®, 5mg /kg, Pfizer, Sandwich, UK). During the first period of recovery, animals were kept in a heating chamber at 37°C.

Pupils were dilated with tropicamide (Mydriaticum® 1%, Bausch & Lomb, Kingston-Upon-Thames, UK) and phenylephrine (Phenylephrine hydrochloride 2.5%, Bausch & Lomb) eye drops

2.2 Genotyping

Tissue samples for genotyping were taken in the form of ear biopsies during tagging or as tail clips and the protocol below was followed.

- Digest ear biopsy in 1.5 ml tube by the addition of 100 µL 50 mM NaOH.
- Heat at 95°C in a heat block for 1 hour
- After 1 hour digestion vortex tissue and centrifuge at 13.000 RPM for 2 minutes
- Add 10 µL 1M tris-HCl (pH 6.0), vortex and centrifuge at 13.000 RPM for 2 minutes; not all tissue dissolves (e.g. cartilage)
- On ice dilute the DNA containing supernatant based on the amount of tissue that was digested (e.g. for a standard ear biopsy make a 1:6 dilution with sterile H_2O)

- Re-suspend primers on ice to a final concentration of 10 µM in sterile H_2O; you need 1.25 µL primer per reaction.
- Make a PCR master mix containing 12.5 µL ImmoMix Red (Bioline,London, UK), 1.25 µL forward primer, 1.25 µL reverse primer and 8 µL sterile H_2O per reaction required.
- To a PCR tube add 23 µL PCR master mix and 2 µL appropriately diluted DNA sample and spin down briefly.
- General conditions for genotyping PCR that may need to be adapted (e.g. different magnesium concentration etc):
- 10 minutes at 95°C (for hot start enzymes)
- 30 cycles of:
    - 10 seconds at 95°C (denaturing phase)
    - 30 seconds at 55°C (anealing phase)
    - 30 seconds at 72°C (elongation phase)
- Followed by
    - 10 minutes at 72°C (final elongation) and holding at 4°C

2.3 Electroretinography

Animals were dark adapted for at least 6 hours before ERG responses were recorded from one eye. The other eye remained undilated and was protected by a contact lens. A DTL-type silver-coated nylon thread active electrode (DTL Plus Electrode; Diagnosys LLC, Cambridge, UK) was modified to include a custom-made contact lens of clear Aclar film (Honeywell International, Inc., supplied by Agar Scientific, Stansted, UK).[62] This was positioned concentrically on the cornea

using hypromellose eye drops (1% methylcellulose solution) for coupling. Platinum needles in the scruff and at the base of the tail served as reference and ground electrodes, respectively. Unfiltered signals were differentially amplified and digitized at a rate of 5 kHz using an Espion E2 system (Diagnosys LLC). The amplitude and latency of major ERG components were measured with the Espion software (Diagnosys LLC) using automated and manual methods. Brief (4 ms) single flash stimuli were delivered in a Ganzfeld dome. Animals were placed on a heated platform, maintained at 38°C using a circulating pump-water bath. All recordings were made in a custom-made light-tight Faraday cage. Details on the ERG protocols are provided in the respective chapters.

2.4 Preparation and embedding of mouse eye cups for light and electron microscopy

After enucleation, the eyes were cleaned of orbital tissue. For light microscopy, including immunohistology, eyes were transferred directly into 4% paraformaldehyde (Thermo Fisher, Loughborough, UK) in PBS and the anterior segment was dissected off. After fixation for 20-25 min, the eyecups were transferred into 30% sucrose solution for cryoprotection and kept at 4°C over night. The eyecups were embedded in optimal cutting temperature (OCT) compound (Tissue-Tek, Sakura Finetek, The Netherlands), frozen on dry ice and stored at -80°C until further processing. For electron microscopy, the cornea was removed and eyes were fixed overnight at 4 °C in 2% glutaraldehyde in 0.1 M cacodylate buffer (pH 7.4) containing 100 mM sucrose. After washing with cacodylate buffer, areas of interest in flat mount preparations were excised and

post-fixed with 1% osmium tetroxide in 0.1 M cacodylate buffer at room temperature for 1 h. Dehydration was then started by a series of incubations in 30%, 50%, and 70% ethanol. The samples were stained with saturated uranyl acetate. Dehydration was continued by incubations in 70%, 80%, 95% ethanol, absolute ethanol, and propylene oxide. The samples were then embedded in Epon (SPI-Pon™812 Epoxy Embedding Kit, SPI supplies, West Chester, PA). For light and fluorescence microscopy, staining with osmium and uranylacetate was omitted.

2.5 Statistical analysis

PRISM (Version 6.02, GraphPad Software, La Jolla, USA) was used for statistical analysis. Two-way ANOVA was performed to detect significant differences between *Abca4*$^{-/-}$ mice and WT controls, using strain and age as factors. The Holm-Sidak or Bonferroni method was applied in all instances to correct for multiple testing (e.g. in pairwise comparisons). The significance level was set at 0.05.

3 Optimization of fundus autofluorescence imaging in mice

3.1 Introduction

Fundus AF imaging allows non-invasive assessment of retinal disease. In humans, fundus AF findings may inform disease diagnosis, characterization, prognostication and monitoring.[42] Most commonly, a 488 nm laser light source is currently used for AF excitation. At this excitation wavelength, the main fluorophore in the human fundus is lipofuscin.[63] Lipofuscin is a natural byproduct of the visual cycle composed of compounds that normally accumulate in the RPE with age.[63, 64] Retinal disease may be associated with abnormally increased [11] or decreased [65-67] 488 nm AF and/or specific alterations of the AF pattern.[42] Near-infrared (NIR) light using a 790 nm laser has also been used for fundus AF imaging. The AF signal at this excitation wavelength appears to originate from melanin in the RPE and choroid.[68-70] 790 nm AF may show similar, but distinct alterations in retinal diseases when compared to 488 nm AF, possibly due to changes in the melanosome compartment.[10, 71, 72]

A high-resolution, high-contrast image of fundus AF distribution in humans can be visualized with a cSLO. The use of cSLO imaging in animal models has been described.[73, 74] Despite these pioneering advances in this field, cSLO AF imaging of the ocular fundus in mice has not been investigated systematically. Hence, the aim was to explore factors influencing fundus AF imaging in mice and to optimize the technique to be able to apply fundus AF imaging in a standardized, consistent and reproducible way. The data presented here provide evidence that a

standardized approach to fundus AF imaging allows the determination of fundus AF intensity (i.e., quantitative changes) *in vivo* as an alternative to *post mortem* measurements of lipofuscin components.

3.2 Methods

3.2.1 Animal preparation for imaging procedures

Mice were anesthetized and pupils were dilated. A custom made contact lens was used for all recordings (except where stated otherwise) to prevent corneal desiccation and subsequent cataract formation, and also to improve image quality (PMMA mouse plano lens, back optic zone radius of 1.7 mm, total diameter of 3.2 mm, centre thickness of 0.4 mm, straight sides; Cantor and Nissel, Brackley, UK). Hypromellose eye drops (Hypromellose eye drops BPC 0.3%, Matindale Pharmaceuticals, Romford, UK) were used as viscous coupling fluid between the contact lens and cornea. For image acquisition, the animal was placed on a platform mounted on the chin rest of the imaging device so that the mouse's eyes were positioned approximately at the level of the marking for a human patients' eye position.

3.2.2 Fundus imaging using a confocal scanning laser ophthalmoscopy

cSLO imaging was performed with a device commercially available for human fundus imaging (Spectralis® HRA; Heidelberg Engineering, Heidelberg, Germany).[75] Fluorescence was excited using laser diodes centered at about 488 nm and 788 nm. Emission was recorded between 500 and 700 nm or above 805 nm, respectively. The beam powers were about 280 µW and 2.6 mW, respectively.

The NIR reflectance mode (820 nm laser) was used for camera alignment to obtain an evenly illuminated fundus image and to focus on the confocal plane of interest. A confocal reference plane of high reflectivity could be consistently identified in the outer retina, using the NIR reflectance mode with slight overexposure. Signals beyond the dynamic range of the detector were highlighted as red pixels by the Spectralis software. This feature assisted the user in detecting the areas of highest reflectivity and therefore also the confocal plane with the largest overexposed area. Using this technique the dioptric focus was adjusted and the camera aligned so that the highest fundus NIR reflectivity was paracentral (uniform illumination in the entire 55 degree field of the mouse fundus is usually not possible using the Spectralis HRA). If the paracentral overexposure characteristic appeared similar in consecutive planes (sometimes spanning a range of up to 6 diopters (D)), the middle focus setting was chosen. Cross sectional OCT imaging – using a similar wavelength as NIR reflectance – shows highest reflective bands at the approximate level of the RPE,[76] suggesting that the highly reflective confocal NIR reflectance reference plane corresponds to anatomical structures at or close to the RPE.

The alignment for obtaining an optimal signal also insured that the camera was aligned such that its “scan pupil” and its “detection pupil” were centered in the dilated pupil of the mouse and in focus in the plane of the mouse’s iris. The “scan pupil” is the area where the incident laser beam oscillates as it scans the fundus, and the “detection pupil” is the area through which the fundus AF is detected. Both pupils are conjugate with the scan mirrors in the camera and are concentric with each other. It is important to monitor the diameter of the dilated pupil during

measurements (see later), since it may obstruct the scan- and detection pupil and thus influence fundus AF measurements.

Images were usually recorded using the “automatic real time” (ART) mode which was able to track slight movements of the fundus (e.g. due to respiration) based on fundus landmarks with high contrast. This allowed up to 100 consecutive frames to be averaged in real time and improved the signal-to-noise ratio. Single averaged images were recorded with an intensity resolution of 8 bits/pixel, a 1536x1536 pixel resolution (“high resolution” mode) and a frame rate of 4.8 frames/second. Rapid non-averaged image sequences (“high speed” mode, 768x768 pixel resolution, 8.9 frames/second) were used only for capturing photopigment bleaching effects.

For quantitative analysis, non-normalized images were recorded in a dimmed room. Experiments on photopigment bleaching were performed in a dark room under dim red light after a minimum of 6 hours dark adaptation. Normalized images (i.e. automatic software enhancement of contrast by histogram stretching) were used if high contrast was required. No further image processing was performed unless stated otherwise. The full angle of view using the 55° lens (Heidelberg Engineering) of the Spectralis HRA was displayed.

The Spectralis HRA detector sensitivity setting can be adjusted between 31 and 107, resulting in a non-linear increase in detector gain by a factor of about 3600. Because detected AF levels in mice are low, a sensitivity of 100 was used to acquire all mouse images (except for the DsRed mouse where lower sensitivity settings are appropriate due to the expression of a fluorescent reporter protein). At this sensitivity, the zero-corrected grey level (GL; see below) linear range extends

up to about 150 GLs.[77] In normal human subjects, such sensitivity settings would usually result in non-linear effects (i.e. GLs >150) and partial saturation, which is only rarely observed in mice. Although mouse fundus AF images may appear dark at a sensitivity ≤100, higher sensitivity settings were avoided because of an increasing contribution of noise and a decreasing linear range with increasing sensitivity.[77]

3.2.3 Quantitative grey level image analysis

Quantitative GL analysis of non-normalized and unprocessed fundus AF images (recorded with the same detector sensitivity) was performed using ImageJ (Version 1.43, National Institute of Health, http://rsb.info.nih.gov/ij).[78] After applying a standard Gaussian blur with a 3-pixel radius (σ) to reduce image noise, analysis included a plot of the mean GL profile within a 30-pixel wide horizontal band through the optic nerve head, and a measurement of the mean GL within the mid-peripheral fundus (*Figure 3.1*). All measured GLs were corrected for the zero-GL, which is automatically recorded for individual images ("Grey value offset (0-level)", in the Image Information panel). This zero-signal is measured with the laser switched off but the detector on and thus is potentially affected by room light (dimmed room light was used for experiments). The resulting corrected GL (cGL) represented mean fundus AF and allowed comparisons between animals, on assumption that detector gain and laser diode power were both relatively constant and did not vary significantly in the ~12 months time period of this study.

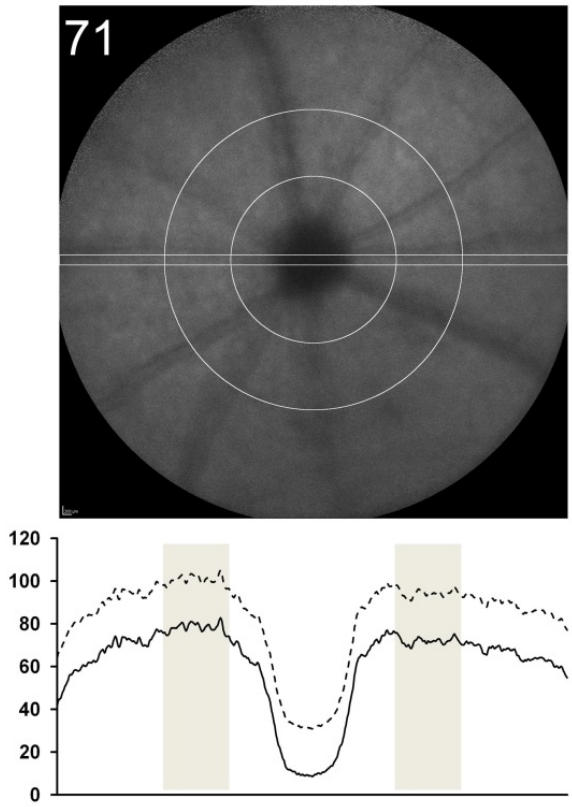

Figure 3.1: Quantitative grey level (GL) analysis of fundus autofluorescence (AF) images. The dashed line in the graph (bottom) represents the GL profile along the horizontal 30 pixels wide band (top). The continuous line in the graph represents the corrected GL (cGL), which results after subtracting the zero GL and which is used for all comparisons. The mean cGL within an annular area, concentric to the optic disc center, defined by circles with 250 and 450 pixels radius (grey background on the bottom graph), was used for all quantitative GL-measurements (indicated in the left upper corner, range from 0 to 255-zero GL). This sampling area avoids the optic disk and the more peripheral part of the image, where darkening and distortion are usually observed.

3.2.4 Recording of the pupil diameter

The dilated pupil diameter in mice was usually larger than the diameter of the scan pupil resulting in no relevant loss of the incident excitation light. However, the dilated pupil diameter was generally smaller than the diameter of the detection pupil causing a loss of AF detection. To monitor this we measured the pupil diameter from an image of the pupil captured before each fundus AF image or each sequence of images. Each time, the focus was set at +50D and the pupil was brought into focus by adjusting the z-position of the camera, with the eye in the center of the image to avoid distortions. This approach standardized the distance between camera and pupil plane, and hence the magnification factor. The pupil diameter was measured in pixels using ImageJ after fitting a circular area to the largest pupil diameter (*Figure 3.2*). A scale factor of 83 pixels per mm (based on measurements of the image of the diameter of the contact lens centered in the iris image) allowed conversion into mm. The refraction at the anterior segment of the mouse eye and especially at the interface air / contact lens results in a magnification of the image of the pupil plane, acquired with the Spectralis at a refraction setting of +50D. This magnification was estimated by Zemax simulation to be in the order of 16% (Dr. Jörg Fischer, Heidelberg Engineering, data on file) and may explain differences of our measurements compared with smaller post-mortem measurements of the pupil.[79] This magnification factor also affects the optical path. Thus, the calculated sizes of the scan pupil and the detection pupil (1.7 mm and 3.4 mm, respectively, for the 55° field lens; HRA2 55° Objective User Information, Heidelberg Engineering) are reduced to approximately 1.4 mm and 2.9 mm, respectively.

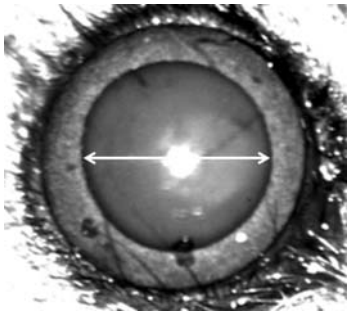

Figure 3.2: Documentation of pupil width. Images were recorded with standardized camera settings, resulting in comparable image magnification. The largest pupil diameter was measured (white arrow). The eye shown has a pupil width of 188 pixels, corresponding to 2.27 mm.

3.3 Results

3.3.1 Image acquisition

Contact lens: Anesthetized mice with dilated pupils may develop cataract within few minutes, which may be related to corneal desiccation.[80] To investigate the optimal strategy to maintain clear ocular media throughout, fundus AF images were recorded using a contact lens (with Hypromellose coupling fluid as described earlier), artificial tears (Hypromellose) alone, or with neither of these protective measures (*Figure 3.3*). The lack of corneal protection consistently resulted in cataract formation and reduced fundus AF signal intensity in minutes. Contact lens placement was found to be a reliable means to avoid this. Application of artificial tears alone also resulted in protective effect, although this was more variable than with the contact lens.

Contact lens use allowed better comparability between animals due to the consistent curvature of the contact lens. Additionally, the small eyes of very young mice could be imaged with contact lens application.

For optimal recordings of the posterior pole, the contact lens had to be placed exactly on the corneal center (*Figure 3.4*). Off-center lens position caused shadowing in the direction of lens displacement. However, when imaging the peripheral retina, deliberate displacement of the lens towards the incident light beam usually improved peripheral fundus illumination.

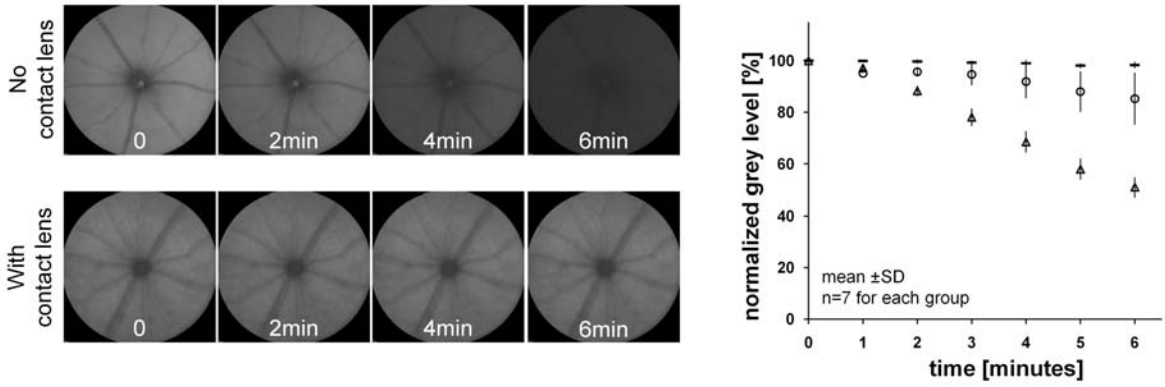

Figure 3.3: Prevention of media opacity using a contact lens. Cataract development in anesthetized mice with dilated pupils, without measures to prevent corneal desiccation, results in image deterioration within minutes (upper row). Quantification of the decreasing fundus autofluorescence (normalized to the first measurement at 0 minutes) is shown in the graph (triangles). Such media opacity can be avoided by protecting the cornea from drying using a contact lens (lower row; horizontal bars). A similar but less consistent effect can be achieved using a corneal lubricant (circles).

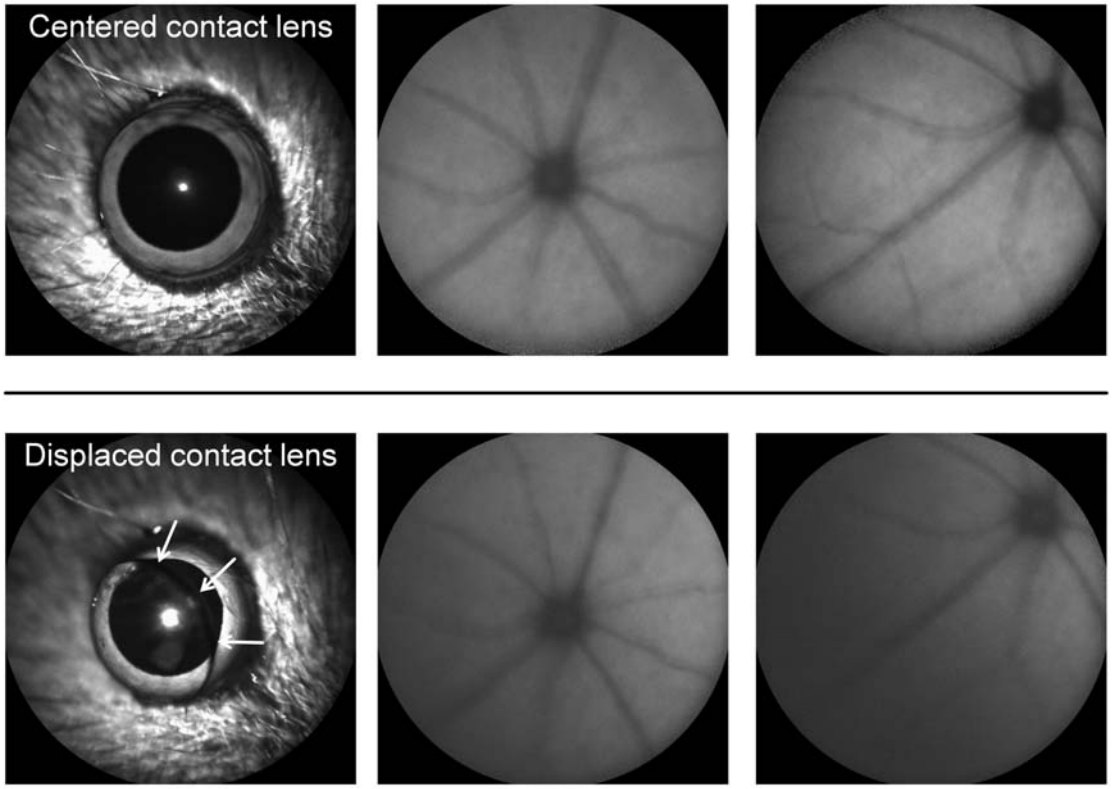

Figure 3.4: Correct placement of the contact lens is necessary for recording images with even illumination of the fundus (upper row). Displacement of the contact lens results in shadowing of the fundus image (lower row, arrows mark lens margin). Adequate lens position can be controlled using the cSLO image focused on the anterior segment (e.g. +50dptr).

Camera position: Uneven retinal illumination may be also be caused by poor camera alignment with the pupillary axis and plane and improper camera position along the *z*-axis (*Figure 3.5*, upper row). Notably, the latter factor also significantly affected image magnification. Translation of camera z-position by only 4mm resulted in an approximate doubling of the apparent optic disc diameter (*Figure 3.5*, bottom row).

Focus: After aligning the camera using the NIR reflectance mode (820 nm laser), a dioptric shift of approximately +8D to +10D (due to chromatic aberration) is needed to refocus the 488 nm fundus AF image on the same retinal plane as the NIR image (*Figure 3.6*). Focusing on other layers of the retina then necessitates additional dioptric shifts. The shorter focal length of the mouse eye results in greater confocality than in humans. Thus, a large change of approximately +30D to +40D was necessary to change the focus from the outer retinal reference plane (see methods) to the nerve fiber layer of the inner retina in adult wild type mice. With the contact lens in place and maximal pupil dilation, a focus setting of about +30D was often a good estimated initial configuration to identify the outer retinal reference plane in adult mice. However, mouse strain, age and pupil dilation may considerably affects the nature of the dioptric adjustments necessary for optimal focus.

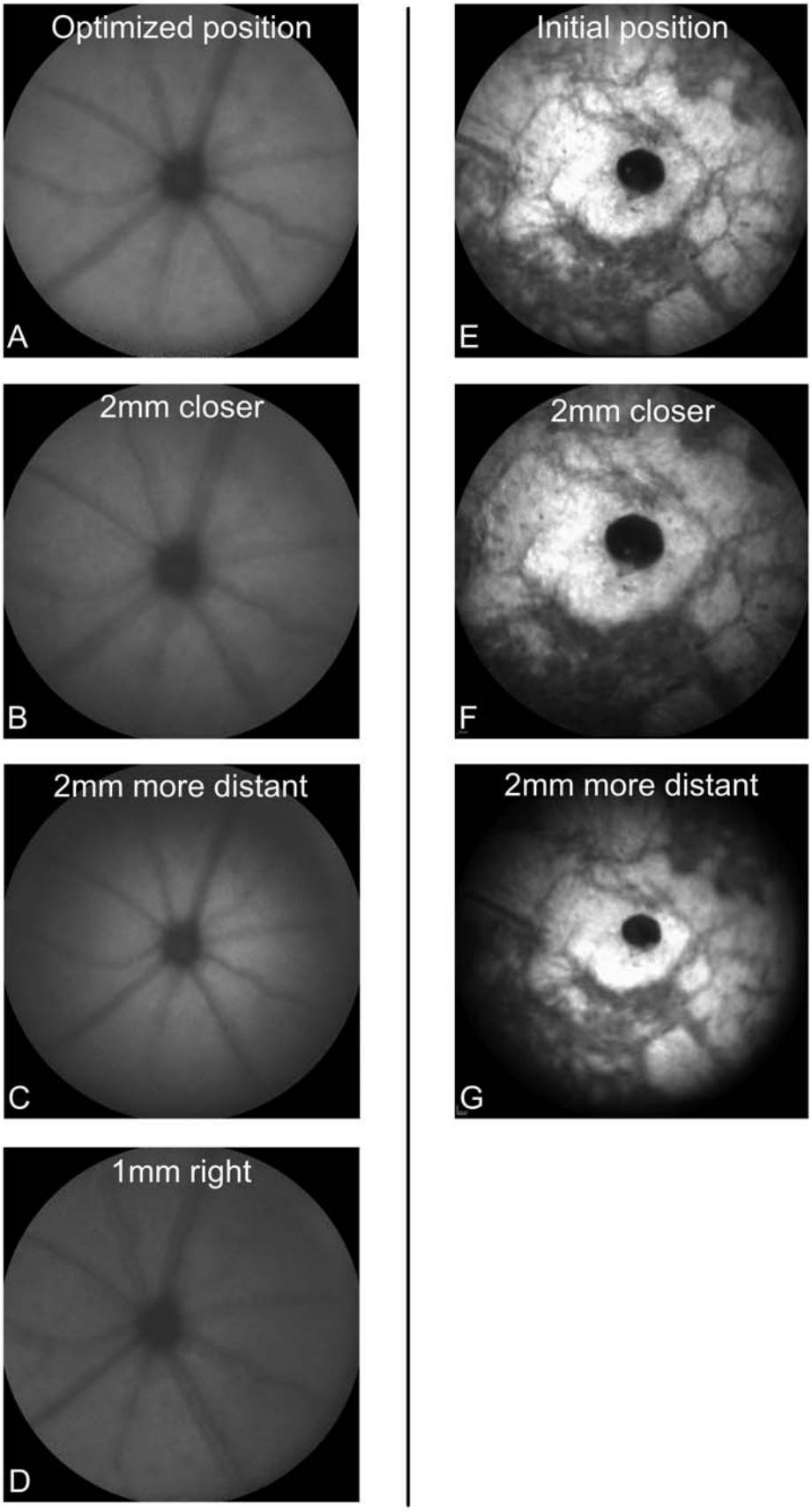
Optimized position
A
2mm closer
B
2mm more distant
C
1mm right
D
Initial position
E
2mm closer
F
2mm more distant
G

Figure 3.5 (previous page): Influence of camera position on fundus shadowing and magnification. Left: Misalignment of the camera in the z-axes (B, C) or laterally (D) from an optimized camera position (A) results in peripheral image shadowing as shown on these fundus autofluorescence images of a normal mouse eye. Right: Changes of the camera position in the z-axis moreover lead to significant changes in image magnification and thus influence the scale factor. A degenerated retina was recorded using the near-infrared reflectance mode due to the superior visibility of the disc margin as anatomic landmark. Compared to an optimal initial position (E), the optic disc appears larger (F) or smaller (G) when the camera is positioned closer to (F) or more distant (G) from the eye. The focus was re-adjusted for each camera position.

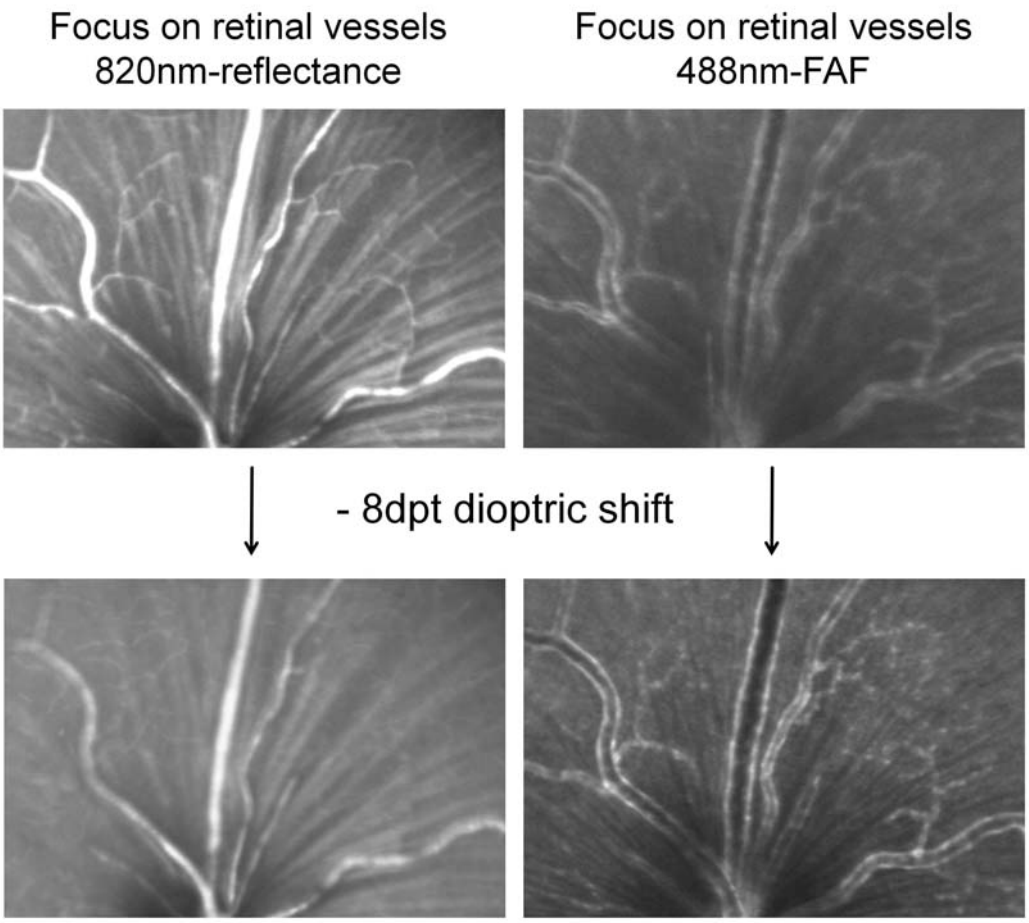

Figure 3.6: Dioptric shift with change in illumination wavelength. When using the 820 nm reflectance image for positioning of the camera and locating the confocal plane of interest (upper left), the 488 nm fundus AF image is not in focus (upper right, the vascular walls are visible due to expression of the fluorescent reporter protein DsRed under control of the actin promoter). The confocal plane needs to be corrected by about 8 diopters. Images are cropped from images recorded with the 55° field lens.

Pupil Diameter: The pupil size in mice after dilation with tropicamide and phenylephrine varies greatly with age (exemplified for C57Bl/6 mice in *Figure 3.7* A). The dilated pupil diameters measured in this study ranged from 1.9 mm to 2.3 mm (black bar in *Figure 3.7* C), and thus remained below the diameter of the detection pupil. To assess the effect of pupil size on AF measurement, repetitive combined measurements of pupil size and fundus AF intensity were obtained during successive pharmacological pupil dilation (phenylephrine in fellow eye, tropicamide in recorded eye, additional phenylephrine in recorded eye). The focus of the fundus AF image changed slightly for each pupil diameter (most likely due to spherical aberrations). *Figure 3.7* B illustrates the effect of increasing pupil size in the same eye on fundus AF. Measurements in our study were at pupil diameters between that of the scan pupil and that of the detection pupil (*Figure 3.7* C). The time needed to refocus and reposition the camera between fundus and pupil imaging, and the relatively fast pupil dilation in mice, remained sources of imprecision in our study when attempting to correlate pupil diameter with fundus AF measurements.

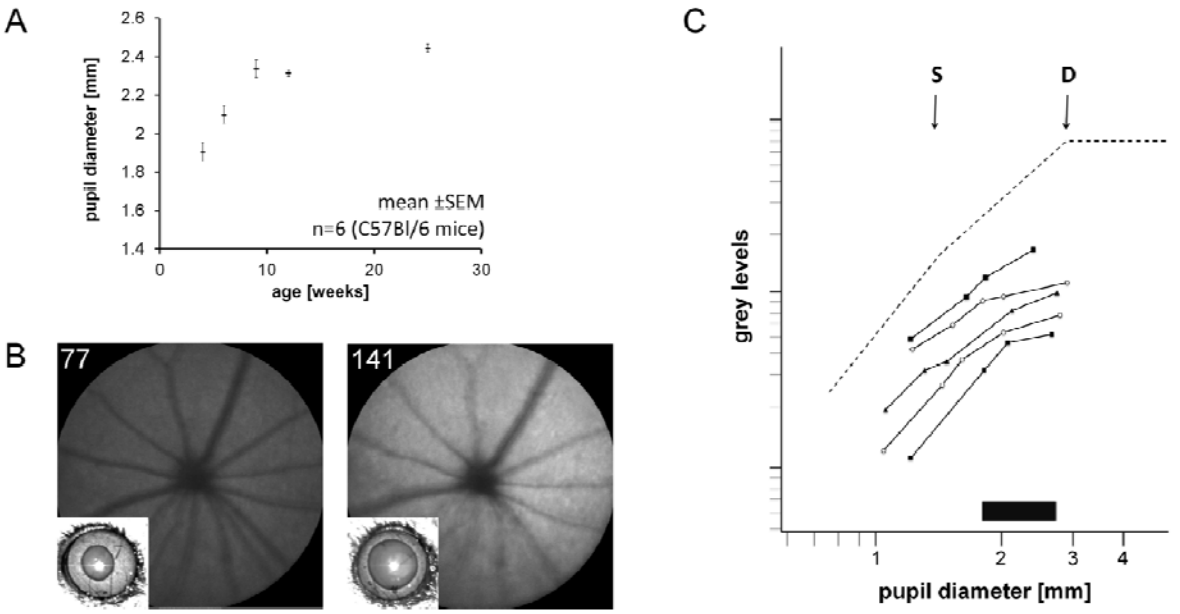

Figure 3.7: A: Pupil size increases with age, especially during the first three months of age. B: Effect of different pupil diameters on fundus autofluorescence (AF) measurement, exemplified in a five months old Abca4$^{-/-}$ mouse. The midperipheral cGL was measured (indicated in the left upper corner of each fundus image). The insets show the NIR iris images acquired before the AF image. C: Log-log plots showing the variation of fundus AF with pupil diameter for 5 eyes (different symbols, minimum of 4 measures per eye). The curves were slightly displaced vertically for clarity (no more than 5%). The interrupted line represents the theoretical prediction of how AF would change with change in pupil diameter in the assumptions those pupils are concentric with the iris, that the laser irradiance in the scan pupil is uniform, and that the pupil diameter is recorded at the same time as the fundus AF image. The arrows represent the diameters of the scan pupil (S) and the detection pupil (D), respectively. The black horizontal bar shows the range of pupil diameters for all other instances in this study.

3.3.2 Recording and quantifying autofluorescence from the RPE

cGL analysis of fundus AF images in the reference plane (see methods) and adjacent confocal planes suggested that the reference plane was a good approximate position from which to record the highest AF signal originating from the RPE (*Figure 3.8* A). The deviation of the mean cGL from the mean maximum cGL was ≤5% within ±4D defocus and ≤10% within ±8D defocus from the reference plane. The highest fundus AF signal was always measured within ±6D defocus from the reference plane. More severe defocus further reduced the AF signal detected (*Figure 3.8* A).

The test-retest variability of RPE AF measurements was assessed in 31 eyes of 31 animals (C57Bl/6 and *Abca4*$^{-/-}$). After the reference plane was identified, a 488 nm fundus AF image was recorded (test 1). The mouse was then taken off the platform and the contact lens was removed. Hypromellose eye drops were applied again, the lens was replaced and imaging was performed (test 2) as in test 1. Midperipheral cGL was measured as described earlier in the methods. Measures from test 1 and test 2 were not significantly different (p=0.93, paired t-test). The intersession coefficient of repeatability (1.96 times the standard deviations of the differences between the two measurements) was approximately ±22% (95% confidence interval; *Figure 3.8* B).

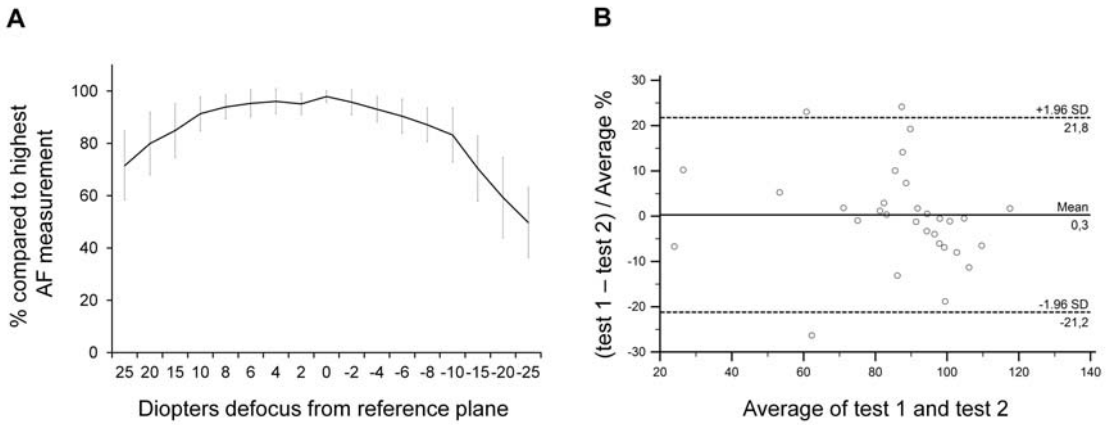

Figure 3.8: Recording autofluorescence (AF) from the retinal pigment epithelium in mice. ***A:*** *Effect of defocus from a reference plane, defined as the confocal plane with the highest reflectivity in the near-infrared reflectance mode. AF images were recorded in 2D steps in a range of ±10D from a reference plane and 5-diopters steps outside of this range up to ±25D defocus from the reference plane. n=13. Mean±SD.* ***B:*** *Bland-Altman plot of % difference against mean for quantitative fundus AF measurements (cGL). Continuous line: mean difference. Dashed lines: 95% limits of agreement.*

3.3.3 Bleaching experiments

Bleaching of rhodopsin in photoreceptors changes its absorption maximum (λ_{max}) from ~500nm to ~330nm, which leads to decreased 488 nm absorption by the photoreceptor layer. This results in higher 488 nm light exposure of the RPE layer, and thus an increased excitation of RPE autofluorescence.[77, 81]

Because of the high retinal irradiance (~30 times what is used in human with the 30° lens, see Discussion) and no possibility to reduce the excitation light through the user interface, we predicted that bleaching would occur much more rapidly than the ~30 sec is takes in humans.[77] Therefore, the "high-speed" movie mode was started and the laser activated while the optical path was manually occluded with black card. Rapid removal of the occluder allowed the retina to be imaged from the commencement of bleaching due to 488 nm laser exposure. There was an ~40% increase in fundus AF in the first 1.5 seconds of laser illumination in 2-month-old C57Bl/6 mice, leveling off thereafter (*Figure 3.9* A). In age-matched *Rho*$^{-/-}$ mice, where rhodopsin as the major photopigment in the mouse retina was absent, no change in fundus AF intensity was noted. Photopigment bleaching can be mapped topographically by subtraction of the unbleached from a bleached fundus AF image (*Figure 3.9* A).

In addition to photopigment bleaching, we observed a slow decrease of fundus AF during several minutes of blue light exposure. Continuous exposure to the excitation light over 3 minutes resulted in lower fundus AF measurements. If a 3 minutes control interval preceded the continuous light exposure, there was no change during the initial dark phase (*Figure 3.9* B).

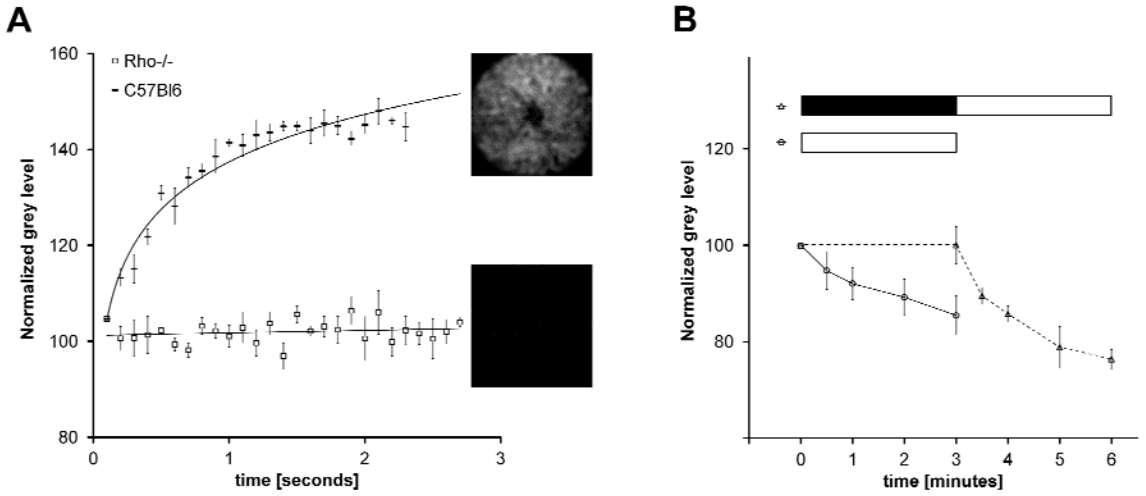

Figure 3.9: Effect of blue light exposure on the measured fundus autofluorescence (AF) signal. ***A:*** *Photopigment bleaching increases fundus AF considerably within the first 1.5 seconds of blue light exposure in wild type C57Bl/6 mice. This increase is not seen in Rho$^{-/-}$ mice that lack photopigment. The mean of 4 independent measurements ±SEM is shown. The insets show enhanced fundus differential maps (at 2 seconds – baseline) in wild type (top) and Rho$^{-/-}$ mice (bottom).* ***B:*** *During continuous light exposure over 3 minutes (lower horizontal white bar), there is a ~15% decrease in measured fundus AF (circles, solid line). A similar change was observed after a 3 minutes interval without light exposure, during which AF remained stable (upper black and white horizontal bar). The mean of 4 independent measurements ±SEM in C57Bl/6 mice is shown.*

3.4 Discussion

In this chapter, the parameters affecting fundus AF imaging in mice were studied so the procedure could be optimized and standardized to allow reproducible recordings for the qualitative and quantitative assessment of fundus autofluorescence (AF). Based on the results, a standard protocol for fundus AF imaging in mice has been designed (see appendix at the end of this chapter).

For consistent recordings across animals allowing grey level analysis, imaging was performed under anesthesia throughout this study. It should be noted that for other purposes, e.g. investigating retinal expression of green fluorescent protein (GFP), recordings with dilated pupils can also be performed with only brief physical restraint, without general anesthesia and without placing a contact lens on the cornea.

3.4.1 Image acquisition

Considerable improvement in image quality may be achieved by using a contact lens (*Figure 3.3*). Media opacities decrease the detectable signal and the signal-to-noise ratio of the already low fundus AF signal in mice. The contact lens prevents the development of cataract and ensures a consistent surface profile across different mice. It also enables recording from very small eyes in young animals, where adjustment of the confocal plane can otherwise be very difficult.

A scale factor would allow the conversion of cSLO fundus image measurements in pixels into actual size. Differences in the optical properties and sizes of the human and mouse eyes render current software algorithms unsuitable for use in mice. Assuming a full angle of view of the murine fundus with the 55° lens, a 1.1-1.2 µm/pixel scale factor may be calculated based on the number of

pixels per degree (1536 pixels per 55° fundus image = 28 pixels/1° visual angle) and estimates of the lateral measure of the visual angle on the mouse retina (1° visual angle = 31-34 µm [79, 82]). The exposed circular retinal area can thus be calculated as 3.14 × (1.1 to 1.2µm/pixel × 768 pixels × 10^{-3} mm/µm)^2 or 2.2 to 2.7 mm^2.

Small changes in camera z-position resulted in large effects on image magnification (*Figure 3.5*, bottom), a finding not usually obvious in humans. This effect increases with high positive focus settings as used in mice, which are rarely needed in patients. The dependency of magnification on the distance between retina and camera, and thus also on eye growth, implies that fixed scales for cSLO images of the mouse fundus will remain imprecise. Possible effects of image magnification on AF measurements thus were not accounted for in this study.

Both the dioptric shift necessary to correct for chromatic aberrations (*Figure 3.6*) and the high confocality of the mouse eye are in line with previous reports [73, 83], with the latter allowing for excellent discrimination between retinal planes. Retinal thickness measurements *in vivo* revealed variable results in mice, ranging from ~200 µm to ~300 µm.[84, 85] Based on the +30-40D change necessary to focus from the outer to the inner retinal border, an effect of ~5-10 µm change per diopter change in focus may be estimated. A lower dioptric range between inner and outer retina may suggest retinal atrophy.

3.4.2 Recording and quantifying autofluorescence from RPE

Fundus AF originates mainly from fluorophores in the RPE [63] and therefore from a defined plane between Bruch's membrane and the neurosensory retina. A reliable localization of this confocal plane while recording fundus AF is difficult to

achieve due to the lack of fluorescent structures or landmarks with high contrast or signal intensity, and only minor effects on measured AF with small focus changes in the outer retina of mice (*Figure 3.8* A). A reference plane of highest NIR reflectivity may instead be used to approximate the plane of highest fundus AF (*Figure 3.8* A). An origin of the high NIR reflectance from the Bruch's membrane/RPE complex is supported by human cSLO reflectance studies that suggested higher reflectivity due to melanin,[86] and by the high reflectivity from Bruch's membrane/RPE complex on OCT recordings using a similar wavelength in the NIR range. Small dioptric shifts between highest AF signal and reference plane may be due to slightly different planes of origin, chromatic aberrations and minor measurement errors. The limited changes of measured AF with defocusing from the reference plane ±4D. may be explained by the high confocality in the mouse eye, resulting in a change of only ±20-40 µm (see above) across the RPE.

Measurement of fundus AF in mice is substantially affected by the small size of the dilated pupil in mice, restricting the detection pupil and thus underestimating the fundus AF (*Figure 3.7*).The scan pupil was generally smaller than the dilated pupil. When pupil diameter was varied in the same animal, we found a near-exponential relationship between fundus zero-corrected grey level (cGL) and pupil diameter (log-log plot, *Figure 3.7* C); the slopes for the 5 animals varied between 1.4 and 2.8 (mean: 2.0±0.4) indicating that the cGL was roughly proportional to the area of the pupil aperture (the data for the largest diameter were removed because these may have been equal as or larger than the diameter of the detection pupil). This suggests that correction for loss of AF due to pupil obstruction may be feasible, but further experiments are needed to confirm these

somewhat variable data. Smaller custom made cSLO apertures may be used in future studies to reduce both the size of the scan pupil and the detection pupil, although at the expense of resolution and signal strength.

When measuring fundus AF in mice, the procedure as performed in this study has limitations. To allow comparison between mice with different pupil diameters (e.g. in longitudinal observations and when comparing fundus AF between mice of different ages), a correction for variation in pupil diameter would be needed. Alternatively, only mice with about equal pupil diameters could be compared. In order to obtain data comparable across different laboratories, it would furthermore be valuable to record and investigate the effect of the ambient light level that might affect AF grey levels. In the current analysis, images were consistently recorded in a dimmed room with standardized the ambient light level.

3.4.3 Bleaching experiments

An effect of photopigment bleaching on fundus AF in mice was observed within the first 1.5 seconds of exposure to the excitation light using the 55°-cSLO lens (*Figure 3.9* A), which is much faster than in human AF imaging using the 30°-cSLO lens (20-30 seconds [77, 81]). The difference can be explained by the fact that approximately the same beam power (~260 µW) is used to scan a smaller retinal area in mice (2.2 to 2.7 mm^2, see above) than it does for human imaging (79 mm^2, with a 30° field). As a result, the retinal irradiance occurring in mouse imaging is about 30-times higher than for human imaging (488 nm AF imaging using the Spectralis HRA: ~10 mW/cm^2 and 0.3 mW/cm^2 for mice and humans, respectively, ignoring media-related light loss).

In addition, a slight decrease of fundus AF over time was observed during continuing blue light exposure. A photochemical effect of relevant fluorophores or a masking of fluorophores by photochemical generation of additional absorbers might explain this finding. A reversible decrease in fundus AF ("fading") has been observed in monkeys after exposure to 5-210 J/cm^2 with 568 nm light over long exposure periods (15 minutes).[87, 88] The lower end of the range observed in monkeys would just approximate the 1.8 J/cm^2 retinal radiant exposure during 488 nm cSLO AF imaging in mice (retinal irradiance of 10mW/cm^2 for 3 minutes). More experimental evidence is needed here to ascertain whether or not this represents the same process.

Photoreversal of bleaching is a process where rhodopsin is photochemically regenerated within photoreceptors during intense blue light exposure. The reported kinetics appears to be in line with our experiments. The effect was observed in rats with a retinal irradiance of 300µW/cm^2 using 403 nm light[2, 89] which is ~2 log units below the irradiance during 488 nm AF imaging using the Spectralis HRA in mice. If photoreversal of bleaching underlies the observed decrease in fundus AF, the higher irradiance might compensate for a mismatch of the 488 nm excitation light with the absorption maximum of the suggested photoreversible intermediate.

3.4.4 Conclusion

After optimizing fundus AF imaging, consistent and reproducible fundus AF imaging is feasible in mice through adherence to key principles such as prevention of media opacities and standardization of camera position and confocal plane during image acquisition. Fundus AF, now increasingly accepted as a meaningful

clinical outcome measure, may allow non-invasive and longitudinal assessment in pre-clinical models, potentially reducing the number of research animals needed. The most obvious phenotype in the *Abca4*$^{-/-}$ mouse model of Stargardt disease is lipofuscin accumulation, and lipofuscin autofluorescence is detected by fundus AF imaging. Therefore, fundus AF imaging promises to be ideal for improving the phenotyping, monitoring disease progression and evaluate response to treatments in the *Abca4*$^{-/-}$ mouse.

3.5 Appendix: Standard protocol for recording fundus autofluorescence AF in mice

Recordings using a confocal scanning laser ophthalmoscope (cSLO[1])

1. Apply tropicamide and phenylephrine eye drops. Allow sufficient time for full pupil dilation.
2. Dab away dilating eye drops and apply Hypermellose eye drops 0.3% as viscous coupling between the contact lens and cornea. Don't let the cornea become dry
3. Place a contact lens to prevent corneal drying and to improve image quality
4. Place mouse on a platform in front of the cSLO camera so that the eyes are positioned approximately at the level of the marking for a patients' eye position
5. Set focus to 50dptr. and align contact lens on the corneal center under infrared reflectance (labeled "IR" on the SpectralisHRA control panel) image control
6. Record an image with the pupil in the confocal plane for documentation of the pupil dilation

7. Move cSLO camera forward to visualize the fundus
8. Adjust focus to the outer retina (high reflectivity) in the IR-reflectance mode [3]
9. Optimize camera position, moving it slightly forward, backwards and side to side. Use the position with the least shadowing at the image margins.
10. Slightly overexpose the image and adjust the focus to the confocal plane of highest reflectivity [3]
11. Switch to fundus AF mode (labeled “FA” on the SpectralisHRA control panel) [4] and darken room light
12. Expose retina to excitation light for a standardized time interval (e.g. 30 or 60sec) to ensure standardized bleaching
13. Acquire an averaged fundus AF image [5] with standardized detector settings [6]
14. If required, acquire near-infrared fundus AF (labeled “ICG” on the SpectralisHRA control panel; much lower signal!) images with standardized detector settings

1. SpectralisHRA (Heidelberg Engineering, Heidelberg, Germany)[75] used in this study.
2. PMMA mouse lens used in this study: see methods
3. This protocol is for recording AF from the retinal pigment epithelium. Confocal plane and detector setting have to be adjusted if fluorescence from other retinal planes need to be recorded, e.g. when imaging mice expressing fluorescent reporter proteins in retinal cells.
4. Default settings: high resolution (1536x1536 pixels). Normalization switched off.
5. Either by recording a movie of 9+ images and averaging all adequate images post-acquisition, or by using the ART mode of the SpectralisHRA.
6. If the SpectralisHRA is used, don’t exceed a detector setting of 100 (see methods). Contact manufacturer for details of other cSLO devices.

4 The *Abca4*$^{-/-}$ Mouse Model – Fundus Autofluorescence and its Correlation with Accumulation of A2E and Histology

4.1 Introduction

Based on previous findings in the *Abca4*$^{-/-}$ mouse, the lack of ABCA4 function results in marked accumulation of *bis*-retinoids such as A2E in the RPE.[34] A2E is a major component of RPE lipofuscin and appears to have a role in retinal disease pathophysiology. This includes its potential to increase blue light cytotoxicity,[90, 91] induce lysosomal dysfunction [92, 93] and activate complement.[94] Increased RPE lipofuscin has been shown in postmortem specimens of *Abca4*$^{-/-}$ mice.[34, 36, 40, 95] However it is not known if this increase in lipofuscin/A2E levels is indeed correlated with increased fundus AF measured *in vivo* in *Abca4*$^{-/-}$ mice.

Feasibility and reproducibility of standardized fundus AF imaging in mice has been shown in chapter 3. Being able to monitor A2E/lipofuscin accumulation using noninvasive fundus AF imaging as surrogate measure would allow longitudinal *in vivo* assessment when evaluating potential treatments for Stargardt disease and other potentially lipofuscin-related retinopathies such as AMD. Moreover, studying this clinically meaningful imaging modality in the *Abca4*$^{-/-}$ mouse along with further structural, biochemical and functional parameters may have implications for interpreting the human retinal disease phenotype and natural history.

Therefore, the next step was to investigate quantitative and qualitative fundus AF characteristics in *Abca4*$^{-/-}$ mice at various ages compared to age-matched wild-type (WT) controls. In addition to conventional fundus AF with short wavelength

excitation (here: 488 nm light), NIR excitation (790 nm light) was also used. Results were correlated with tissue A2E levels, histological findings, and retinal function using electroretinography (ERG).

4.2 Methods

4.2.1 Fundus autofluorescence imaging and image analysis

Fundus AF imaging was performed in anesthetized animals following the standard protocol developed beforehand (see chapter 3.5). Only one eye per mouse was recorded. All images were recorded using the 55° lens (Heidelberg Engineering) of the Spectralis HRA.

For quantitative analysis of fundus AF, the mean grey level on mouse fundus AF images (acquired with standardized signal detector sensitivity, unprocessed, 1536x1536 pixels) was measured within a ring shaped area between 250 and 450 pixel radii from the optic disc center using ImageJ software (Version 1.43, National Institute of Health, http://rsb.info.nih.gov/ij), as outlined in chapter 3.2.3. The "electronic zero" was subtracted from each measured grey value to obtain the corrected grey level (cGL), which was used for all calculations.

4.2.2 *RPE65* Genotyping

Rpe65 was sequenced by the PCR restriction fragment length polymorphism method according to Kim et al.[96] Genomic DNA was extracted from ear biopsies and PCR-amplified with the forward 5'-ACCAGAAATTTGGAGGGAAAC-3' and reverse 5'-CCCTTCCATTCAGAGCTTCA-3' primers. The Leu-450 variant

introduces a Mwo1 restriction site in the resulting 545-bp product, leading to 180 and 365 bp products.

4.2.3 Fluorescence microscopy

Autofluorescent lipofuscin and melanolipofuscin granules were photographed in semi thin sections using a fluorescence microscope (Zeiss Axioplan2, Carl Zeiss, Jena, Germany; excitation 370/36 nm, emission 575/15 nm, 40x objective) connected to a computer equipped with a CCD camera. Since the granules could not clearly be separated from each other and lipofuscin cannot be differentiated from melanolipofuscin, the quantification of lipofuscin granules was only performed using electron microscopy.

4.2.4 Outer nuclear layer count

Serial 16 µm thick cryosections were affixed to poly-L-lysine coated glass slides (Polysine®; Thermo Scientific, Loughborough, UK), air-dried and then stored at -20°C until further histological processing. Outer nuclear layer (ONL) count was performed after nuclear staining using Hoechst 33342 (Invitrogen Ltd, Paisley, UK) 1:5000 at three eccentricities, 500 µm and 1000 µm from the optic disc center, and 500 µm from the ora serrata. Nuclei were counted manually within a box of fixed width (20 pixels ≈ 19.6 µm) placed over the ONL. To present data as number of nuclear layers, the total ONL nuclear count was divided by the number of nuclei along the width of the box. Per eye, results from three sections and both sides of the optic nerve head were averaged.

4.2.5 Electron microscopy and pigment granule quantification

Ultrathin Epon sections (70 nm) from WT control eyes and *Abca4*$^{-/-}$ eyes were post-stained with lead citrate and investigated under a transmission electron

microscope (TEM; Model 902 A, Carl Zeiss, Oberkochen, Germany). For statistical analysis, the areas occupied by different types of pigment granules were quantified in 5-8 micrographs from each group. As lipofuscin is somewhat unusual in *Abca4*$^{-/-}$mice, the morphological definition used in this study of the RPE was as follows: lipofuscin in *Abca4*$^{-/-}$mice is a type of intracellular granule which appears in the electron microscope as a membrane bound body with heterogeneous staining and very variable shape generally darker than the cytosol. Melanin granules are easily and reliably distinguished from lipofuscin in the electron microscope, in that melanosomes are uniformly electron dense (black), are not fused with other organelles and appear spindle shaped, ovoid or round. Melanosomes that are fused with lipofuscin are considered as melanolipofuscin and were included in the combined category of lipofuscin and melanolipofuscin. For lipofuscin and melanolipofuscin quantification, image analysis software (iTEM, Olympus Soft imaging Solutions, Münster, Germany) was used. For each image, the total area of RPE cytoplasm was determined. Nuclei were not included in this measurement. Apical microvilli and extracellular space in the region of the basal infoldings were also excluded. The included area totalled from about 50-100 μm^2 per image. The area fraction of lipofuscin/melanolipofuscin is expressed as area in μm^2 occupied by lipofuscin per 1000 μm^2 RPE cytoplasm.

Electron microscopy, including the preparation of eye cups for such imaging, was performed by Ulrich Schraermeyer, University Eye Hospital, University of Tübingen, Germany.

4.2.6 Quantification of A2E

For A2E quantification, the cornea and lens were removed in phosphate buffered saline (PBS). Dissected eye cups were immediately snap frozen and stored at -80°C until further processing.

Quantification of A2E was performed by Roxana Radu, Jules Stein Eye Institute, Department of Ophthalmology, University of California at Los Angeles School of Medicine, USA. The detailed method of *bis*-retinoids extraction and analysis is described in the paper by Radu et al.[97]

4.3 Results

4.3.1 *RPE65* Genotyping

Abca4$^{-/-}$ mice and wild type controls were genotyped for a polymorphism in *RPE65* which is known to affect lipofuscin accumulation.[96] *Abca4*$^{-/-}$ and WT mice used in this study were homozygous for the (Leu450) allele of Rpe65 (*Figure 4.1*), suggesting that differences in A2E / lipofuscin accumulation would mainly be due to differences in ABCA4 function.

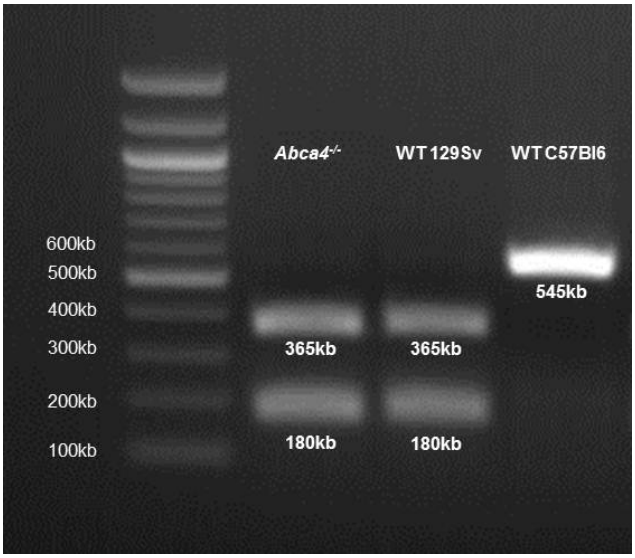

Figure 4.1: Abca4$^{-/-}$ *mice and wild type controls (129S2/SvHsd) used in this study showed presence of the Leu-450 variant which is associated with a higher A2E-accumulation compared to the Met-450 variant. The latter is present in the C57BL6 strain which is shown for comparison.*

4.3.2 Longitudinal recordings of 488 nm and 790 nm fundus autofluorescence intensity

Repeated recordings in the same animals were performed between the ages of 1 and 9 months in *Abca4*$^{-/-}$ mice and WT controls to investigate the change in fundus AF levels over time. 488 nm and 790 nm fundus AF in *Abca4*$^{-/-}$ mice was similar to WT at 1 month (*Figure 4.2* A,B). Thereafter, 488 nm fundus AF rose significantly faster in *Abca4*$^{-/-}$ mice compared to WT, leveling off at 6 months (*Figure 4.2* A). Following a different time course, 790 nm AF in *Abca4*$^{-/-}$ mice increased relative to WT only after 3 months of age (*Figure 4.2* B). 488 nm fundus AF levels in all ≥9-week-old *Abca4*$^{-/-}$ mice studied were higher than the 95% confidence interval of WT measurements. The same applied for 790 nm AF in *Abca4*$^{-/-}$ mice aged 6 and 9 months.

Fundus AF levels in *Abca4*$^{-/-}$ mice were normalized to that in age-matched WTs to control for possible age-related confounders including pupil size, and thus to allow a better estimation of the effect of *Abca4* deficiency on AF levels over time (*Figure 4.2* C). 488nm AF rose from 1.2x that of WT at 1 month, to 2x by 3 months, to a maximum of approximately of 2.2x, thereafter showing a ceiling effect. 790nm AF was 1x WT level in the first 3 months, increased to 1.7x from 3 to 6 months, and to 1.9x by 9 months.

Pupil size, which has a major impact on measured fundus AF in mice,[98] significantly increased with age in both strains to a similar degree (*Figure 4.2* D). Thus, differences in pupil size would not explain the differences between strains.

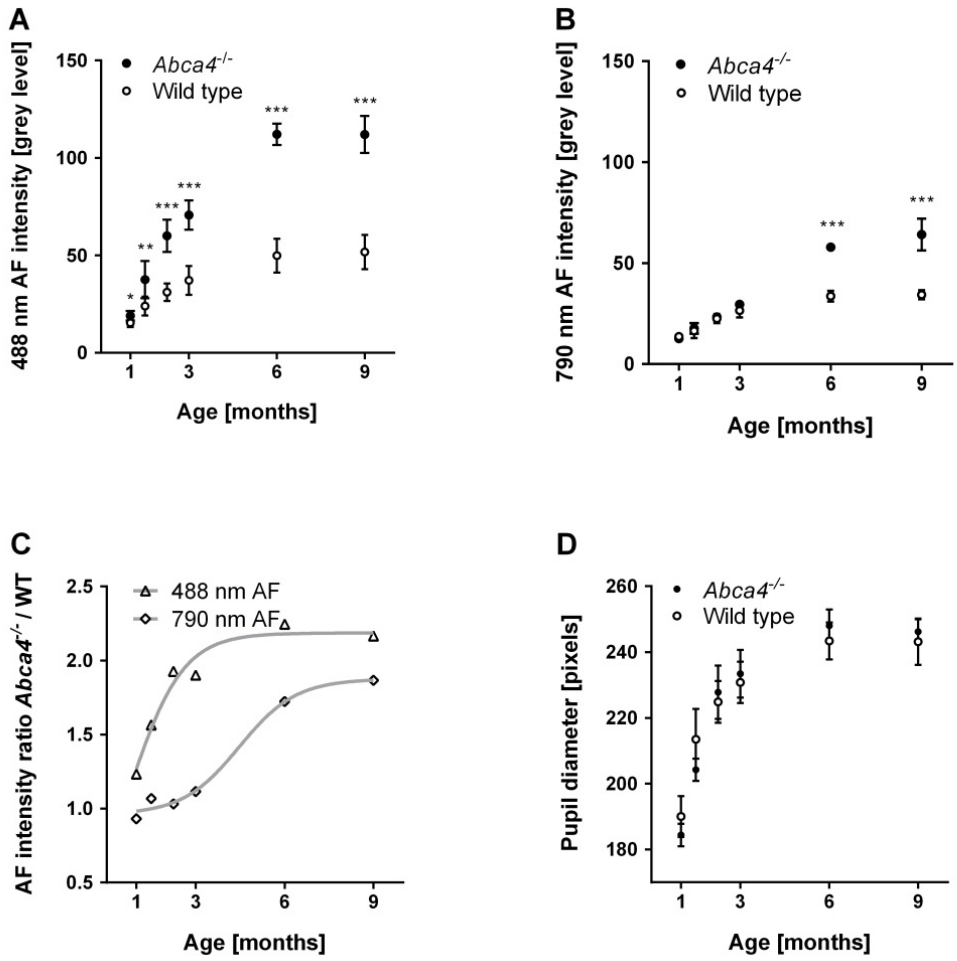

*Figure 4.2: A-C: Longitudinal measurements of fundus autofluorescence (AF) intensity in the Abca4$^{-/-}$ mouse (n=5) and wild type (WT; n=8) controls between 1-9 months of age. To distinguish lipofuscin- and melanin-related fundus AF, 488 nm (A) and 790 nm (B) wavelengths were used for excitation, respectively. Levels of fundus AF (mean±SD) were significantly different between strains and between age groups (p<0.01, two-way ANOVA) for 488 nm and 790 nm fundus AF. *p<0.05; **p<0.01; ***p<0.001. (C) Using the ratio of mean fundus AF between Abca4-/- and WT mice controlled for potential age related factors. Curves were fitted to illustrate the time course of AF increase in Abca4-/- relative to WT at the two different excitation wavelengths. (D) The pupil diameter (mean±SD), which strongly influences autofluorescence intensity measurements in mice, increased with age (p<0.001) but was not different between strains (2-way ANOVA).*

4.3.3 Cross sectional recordings of 488nm and 790nm fundus autofluorescence

To investigate AF in aged animals naïve to any imaging that may have influenced A2E levels, separate cohorts of *Abca4*$^{-/-}$ and WT control mice were assessed cross sectionally at 3, 6, 9, 12 and 18 months of age. Eyes of these animals were used to correlate fundus AF levels with postmortem A2E measurements and histology (see below). Quantitative fundus AF assessment in animals 12 months and older was hampered by suspected incident cataract in *Abca4*$^{-/-}$ and WT mice. AF levels in animals aged 3, 6 and 9 months from this independent cross sectional cohort confirmed the findings of the longitudinal assessment (*Table 4.1*), and suggested that repeated cSLO imaging in the longitudinally observed animals did not significantly modify AF levels over time. Representative recordings with an age- and strain-dependent increase of fundus AF intensity are shown in (Figure 4.3).

Qualitatively, flecks of increased or decreased 488 nm AF were obvious in 6-month-old *Abca4*$^{-/-}$ mice (*Figure 4.4* A) whereas in WT these appeared later at 9 months and were noticeably less distinct. On 790 nm AF, a fleck pattern was consistently observed in *Abca4*$^{-/-}$ mice 6 months and older. Flecks on 790 nm AF were not seen in WT controls up to the age of 18 months.

Large areas of geographic atrophy, as typically observed in patients with Stargardt disease, were not observed. However, in *Abca4*$^{-/-}$ mice 12 months and older, there were spots of decreased AF. Such loss of fluorophores may suggest focal damage and/or incident atrophy of the RPE. Overall, this was observed more frequently in 790 nm AF, sometimes in presence of near-normal 488 nm AF

pattern (*Figure 4.4* B,C). In a few eyes the opposite pattern occurred, i.e. that a reduced 488nm AF was more obvious alongside near-normal 788 nm AF (*Figure 4.4* D).

Age [months]	*Abca4*$^{-/-}$		Wild type	
	Longitudinal	Cross sectional	Longitudinal	Cross sectional
3	71 [±7.5] (n=5)	73 [±20.0] (n=7)	37 [±7.4] (n=8)	41 [±3.4] (n=7)
6	112 [±5.6] (n=5)	103 [±16.3] (n=6)	50 [±8.7] (n=8)	45 [±5.7] (n=6)
9	112 [±9.6] (n=5)	108 [±11.0] (n=5)	52 [±9.6] (n=8)	59 [±10.9] (n=6)

Table 4.1: Comparisons of data derived from longitudinally recorded animals (same data as in Figure 4.2) and from a separate cross sectional data set. Mean levels of fundus autofluorescence (AF) [±SD] are presented. The two different experiments confirm each other, providing evidence for the reliability of the method of quantitative analysis of fundus AF intensity in mice. Also, the data suggested that repeated assessments did not significantly modify AF levels over time.

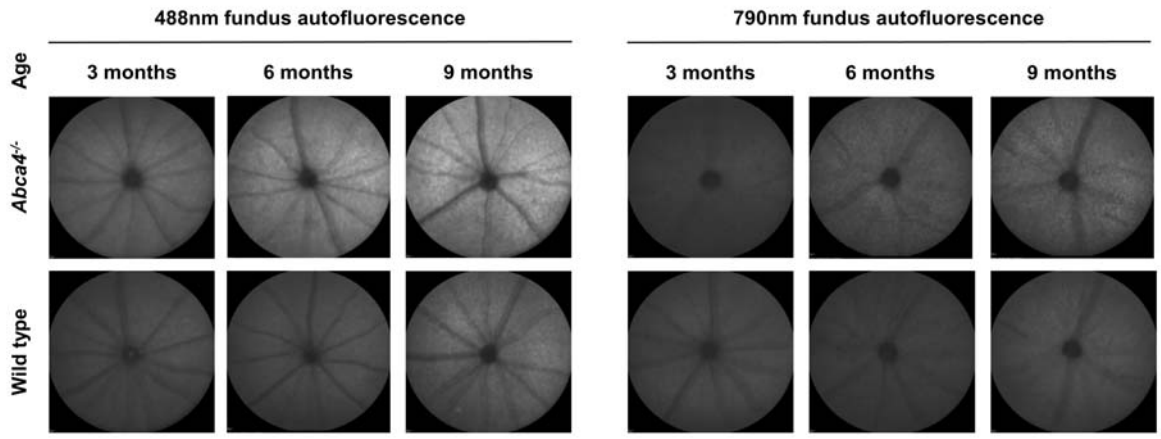

Figure 4.3: Unprocessed representative recordings of fundus AF excited at 488 nm and 790 nm in Abca4$^{-/-}$ and WT control mice (cross sectional cohort). Overall, the AF signal was higher with excitation light at 488 nm compared to 790 nm. At 3, 6 and 9 months, 488 nm AF in Abca4$^{-/-}$ mice is higher than in WT, with a larger difference in older animals. 790 nm AF was only significantly different in 6 and 9 months old animals, where Abca4$^{-/-}$ mice show a higher AF level than controls.

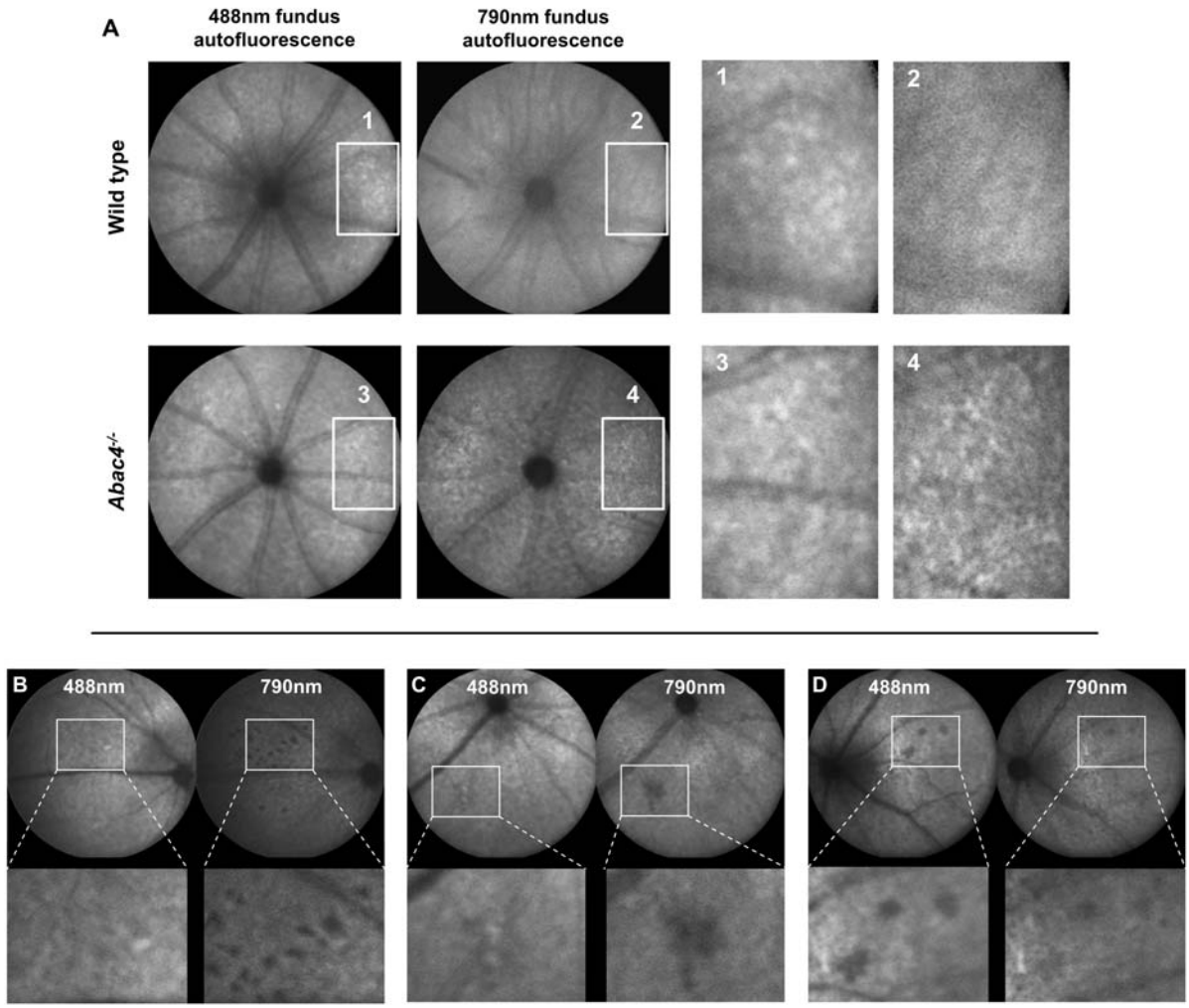

Figure 4.4: Representative autofluorescence (AF) fleck patterns in a 12 month old Abca4$^{-/-}$ mouse and an age matched control (images processed for contrast). Flecks on 488 nm AF images were visible in both mice but were more pronounced in the Abca4$^{-/-}$ mouse. On 790 nm AF, a fleck pattern was only visible in the Abca4$^{-/-}$ mouse but not in the WT control. B-D: Dark areas on fundus AF imaging suggesting focal damage of the RPE in aged Abca4$^{-/-}$ mice. B, C: 488 nm fundus AF (left) in a 12 (B) and 18 (C) months old mouse showing fleck-like increased AF and faint spots of reduced AF. The latter are also hypofluorescent on the 790 nm AF image (right). D: Rarely, spots of markedly reduced AF were more obvious on 488 nm AF images. These lesions were not seen in similarly aged wild-type mice.

4.3.4 Comparison of fundus autofluorescence recordings and A2E measurements

A2E is regarded as a major fluorophore of lipofuscin at the ocular fundus. Therefore, we assessed if A2E levels in *Abca4*$^{-/-}$ and WT control mice increased in parallel with 488 nm AF levels (cross sectional data set). AF ratios between *Abca4*$^{-/-}$ and WT mice confirmed results from the longitudinal data set. 488 nm AF levels in *Abca4*$^{-/-}$ mice were ~1.8-fold higher than controls at 3 months and ~2-fold at 6 and 9 months (*Figure 4.5* A). In contrast, A2E levels in 3-month-old *Abca4*$^{-/-}$ mice were 8 times higher than controls and increased to ~12-fold at 9 months (*Figure 4.5* B).

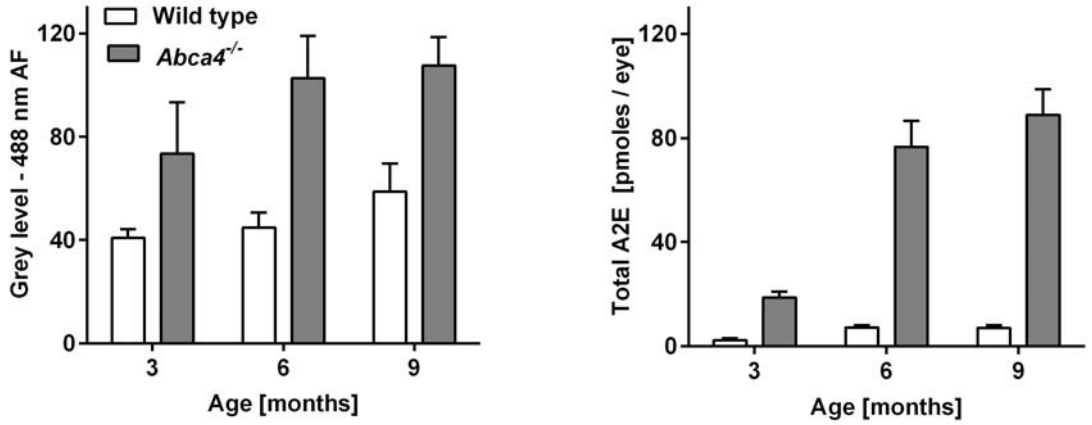

Figure 4.5: Difference of mean±SD fundus autofluorescence (AF) intensity and A2E-levels between Abca4$^{-/-}$ *and wild type control mice aged 3, 6 and 9 months. While fundus AF intensity approximately doubles in Abca4*$^{-/-}$ *mice compared to controls (A), A2E levels are 10 and 12 times higher in Abca4*$^{-/-}$ *mice aged 6 and 9 months, respectively (B).*

4.3.5 Bright field and fluorescence microscopy

In line with the functional ERG data, quantification of the photoreceptor layer thickness revealed loss of photoreceptors with age in *Abca4*$^{-/-}$ mice similar to WT controls up to 18 months (*Figure 4.6*).

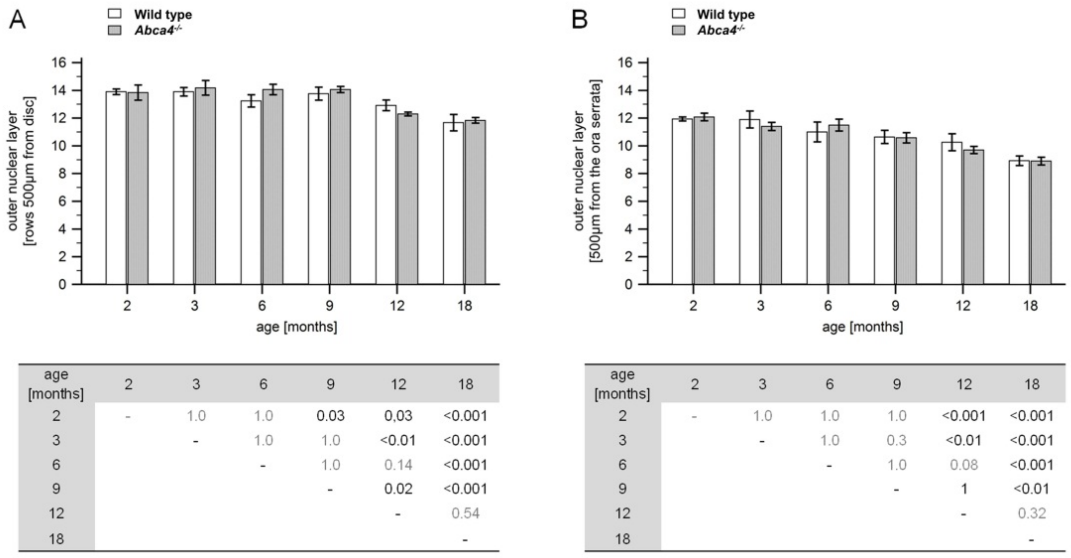

age [months]	2	3	6	9	12	18
2	-	1.0	1.0	0.03	0,03	<0.001
3		-	1.0	1.0	<0.01	<0.001
6			-	1.0	0.14	<0.001
9				-	0.02	<0.001
12					-	0.54
18						-

age [months]	2	3	6	9	12	18
2	-	1.0	1.0	1.0	<0.001	<0.001
3		-	1.0	0.3	<0.01	<0.001
6			-	1.0	0.08	<0.001
9				-	1	<0.01
12					-	0.32
18						-

Figure 4.6: Quantitative analysis of the photoreceptor layer: Age-related loss of photoreceptors in the central (A) and peripheral (B) retina of Abca4$^{-/-}$ *and wild type control mice. At all ages, there was no significant difference in photoreceptor layers (mean ± SEM) between the two strains in the central and peripheral retina. However, there was a significant change with age which was most pronounced after 9 months of age (tables, 2-way ANOVA). Similar results were found in the midperipheral retina 1000µm from the disc (data not shown). n=5 for each data point, except n=4 for 18 months old wild types.*

Semithin sections (*Figure 4.7* A) qualitatively illustrate the similarity between retinas of *Abca4*$^{-/-}$ and WT mice even in 18-month-old animals. In contrast, the RPE of *Abca4*$^{-/-}$ mice showed marked structural differences compared to WT controls, with bright dots representing extensively accumulated lipofuscin granules (arrowhead in *Figure 4.7* A). Also vacuolisation of RPE cells was observed focally in 18-month-old *Abca4*$^{-/-}$ mice (*Figure 4.8*). Under fluorescent light lipofuscin was virtually absent in 3-month-old WT mice and increased little in animals aged 12 and 18 months (*Figure 4.7* B). In contrast, fluorescent granules accumulated extensively with age in *Abca4*$^{-/-}$ mice.

Figure 4.7 (following page): A: Bright field microscopy of semithin sections of eyes from Abca4$^{-/-}$ *and wild type (WT) mice. In the RPE of 18 month old Abca4*$^{-/-}$ *mice bright dots (arrowhead) representing lipofuscin are detected but are lacking in the age matched WT control. Retinal morphology is otherwise similar. RPE = retinal pigment epithelium; OS = photoreceptor outer segments; IS = photoreceptor inner segments; NL = photoreceptor nuclear layer. B: Under fluorescent light lipofuscin AF is virtually absent in WT mice at age 3 month and increased only little at 12 and 18 month. In contrast a strong accumulation of fluorescent granules with age occurred in Abca4*$^{-/-}$ *mice. Individual lipofuscin granules are indicated by a white arrowhead. Red blood cells also are somewhat autofluorescent (black arrowheads).*

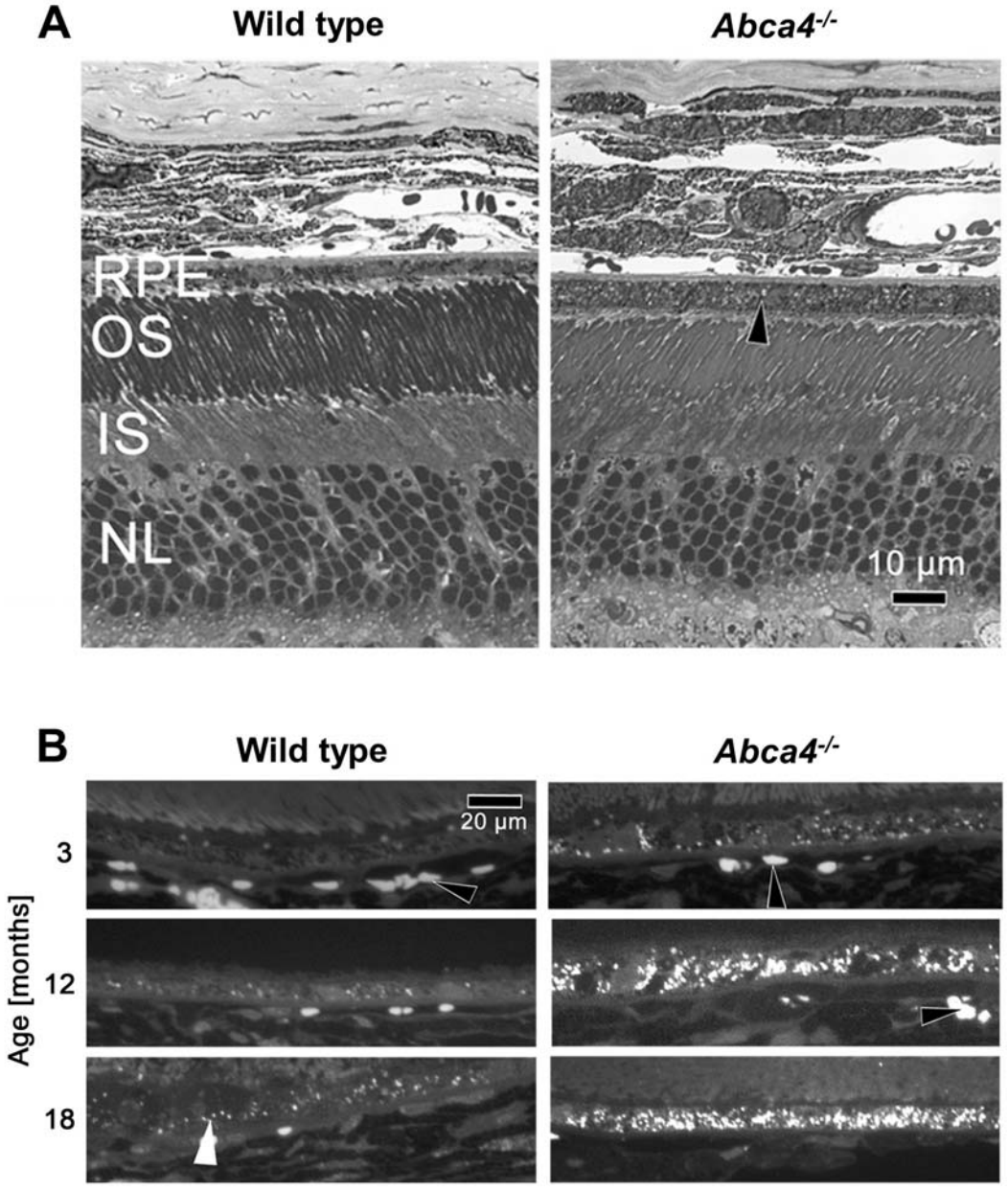
A
Wild type
Abca4-/-
RPE
OS
IS
NL
10 µm
B
Wild type
Abca4-/-
20 µm
Age [months]
3
12
18

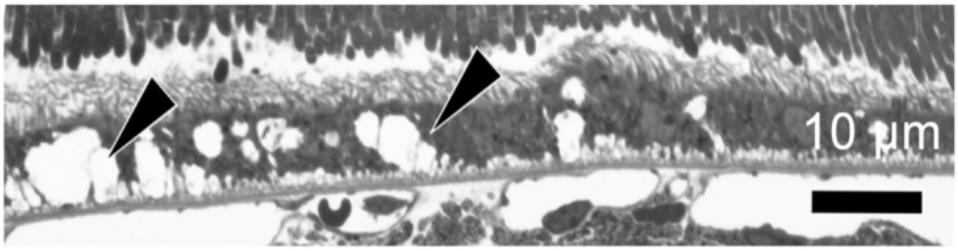

Figure 4.8: Vacuolization of RPE cells is indicated by arrowheads in the RPE of an 18 month old Abca4$^{-/-}$ mouse (bright field microscopy of a semithin section).

4.3.6 Ultrastructural observations in the TEM

Retina, RPE and choroid were examined to determine ultrastructural differences in *Abca4*$^{-/-}$ mice and WTs. Prominent differences were only detected in the RPE. In young *Abca4*$^{-/-}$ mice, electron-opaque homogeneous granules as shown in *Figure 4.9* A were frequent but significantly reduced in number in 12-month-old *Abca4*$^{-/-}$ mice. These granules had the typical appearance described in aged human or monkey RPE and were virtually absent in WT mice. With increasing age in *Abca4*$^{-/-}$ mice, irregularly shaped and electron-dense material accumulated in the RPE cytoplasm (*Figure 4.9*). This type of organelle was virtually absent from WT mice. Although it is possible that these organelles are similar to the typical membrane bound lipofuscin granule, membranes were difficult to detect. The latter organelles showed a tendency to fuse with each other and occasionally with melanosomes (*Figure 4.9* B). Eighteen-month-old mice of both groups contained electron opaque material between Bruch´s membrane and basal infoldings of the RPE cells (asterisks, *Figure 4.9* A).

4.3.7 Quantification of lipofuscin granules by electron microscopy

The total areas (in μm^2) occupied by lipofuscin and melanolipofuscin per 1000 μm^2 sectioned RPE cytoplasm was significantly higher in *Abca4*$^{-/-}$ mice at 12 and 18 months (53.4 + 39.2 μm^2 and 115.6 +18.8 μm^2) compared to age-matched WT mice (2.2 + 3.9μm^2 and 0.5 + 1.1 μm^2; *Figure 4.10*). This increase was statistically significant at 12 and 18 months of age ($p<0.001$, Dunnett's test) but not at 3 months. The classical lipofuscin granules shown in Figure 6A occupied 16.1 + 6.9 μm^2 in 3-month- and 5.7 + 6.6 μm^2 in 12-month-old *Abca4*$^{-/-}$ mice ($p<0.02$). They were virtually absent in 18-month-old *Abca4*$^{-/-}$ mice.

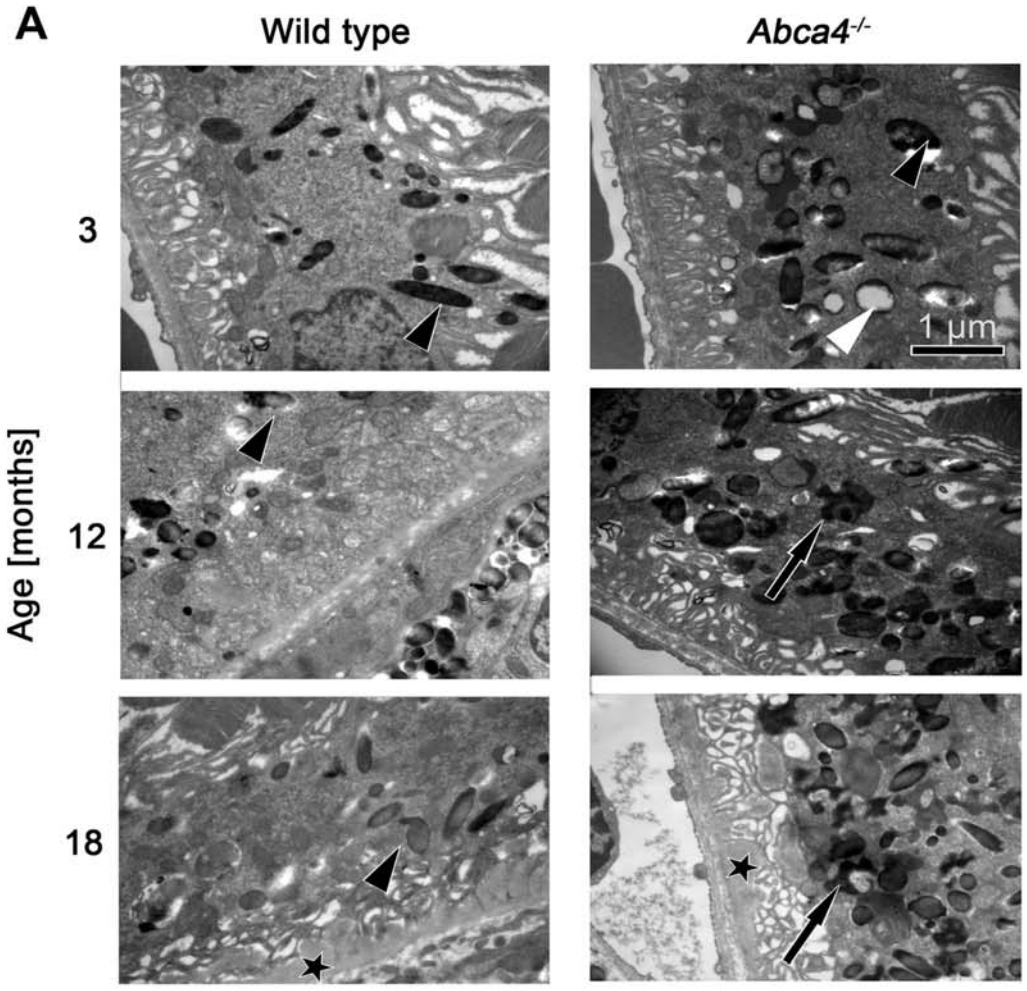
A
Wild type
Abca4-/-
3
12
18
Age [months]
1 µm

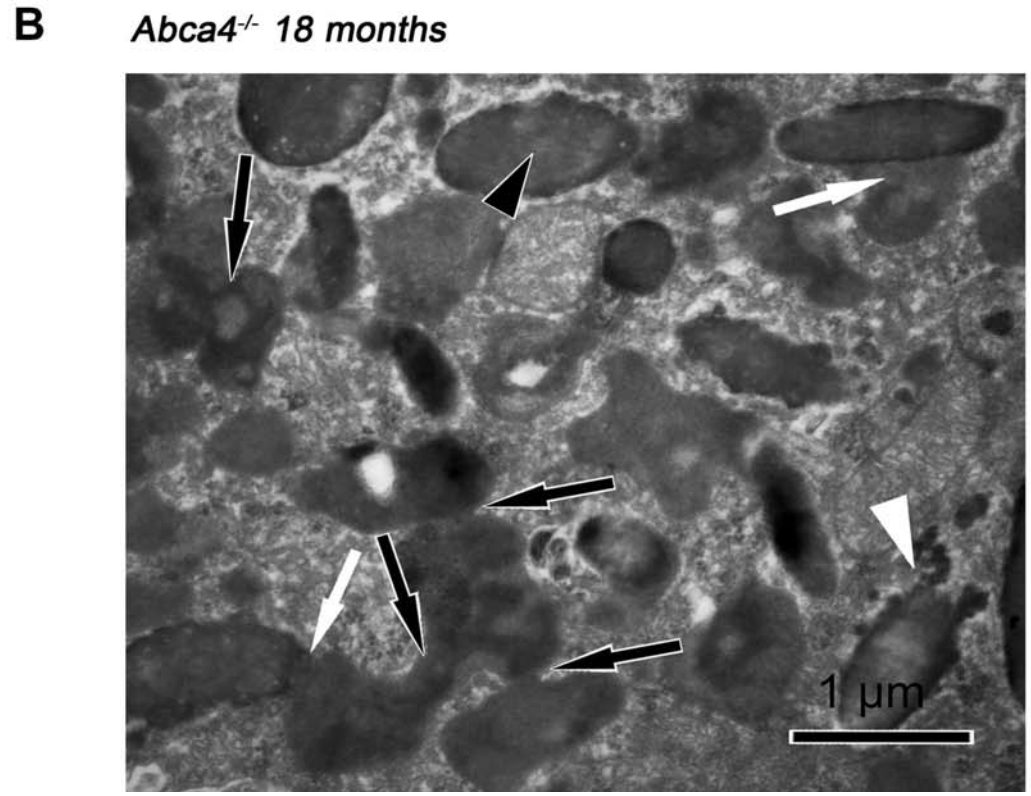
B
Abca4-/- 18 months
1 µm

Figure 4.9 (previous page): A: TEM micrographs of RPE cells of from Abca4$^{-/-}$ and WT mice at ages 3, 12 and 18 months. In 3-month-old Abca4$^{-/-}$ mice, electron-opaque homogeneous granules are labeled by a white and a melanosome by a black arrowhead. The granule labeled by the white arrowhead represents the more classical type of lipofuscin. With progression of age unusual granules of irregular shape and electron density (black arrows) accumulate in the RPE cytoplasm of 12- and 18-month-old Abca4$^{-/-}$ mice. This type of organelle is nearly absent from WT mice. Melanosomes are indicated by black arrowheads. Eighteen-month-old mice of both groups contain electron opaque material (asterisks) between Bruch´s membrane and basal infoldings of the RPE cells. B: TEM micrograph of the RPE from an 18-month-old Abca4$^{-/-}$ mouse at high magnification. With progression of age, unusual granules accumulated in the cytoplasm of RPE cells. A melanosome is marked by an arrowhead and Bruch´s membrane by an asterisk. The material accumulated in the cytoplasm is irregular in shape and electron dense (black arrows). These granules appear to fuse with each other (black arrows) and with melanosomes (white arrows). The electron density of these confluent granules is occasionally as dense as in melanosomes (black arrowhead). A melanosome in a state of disintegration is indicated by a white arrowhead. They were also present in WT mice.

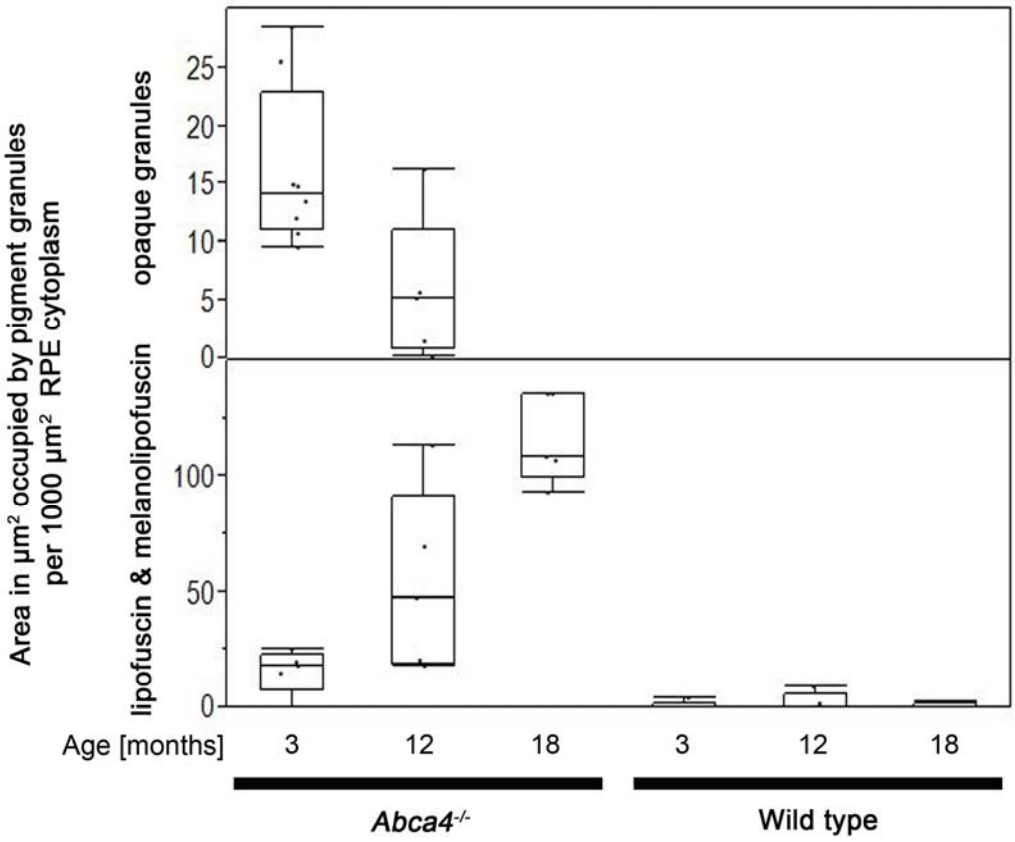

Figure 4.10: Quantification of lipofuscin and melanolipofuscin granules by electron microscopy. The total areas (in µm^2) occupied by lipofuscin and melanolipofuscin per 1000 µm^2 sectioned RPE cytoplasm increased significantly in Abca4$^{-/-}$ mice at 12 and 18 months compared to age-matched WTs. The area occupied by the classic (opaque) lipofuscin granules in Abca4$^{-/-}$ mice declined with age.

4.4 Discussion

4.4.1 488 nm and 790 nm fundus AF: its relation to A2E accumulation and sub-cellular RPE-alterations

Quantitative analysis of AF intensity was performed in animals aged up to 9 months, when *Abca4*$^{-/-}$ mice were not different from WT controls in function and photoreceptor count, and without media opacity that could influence AF measurement. Because fundus AF quantification in mice is influenced by various factors that change with age, such as pupil width, eye size and optical magnification (see chapter 3), AF measures in *Abca4*$^{-/-}$ mice were normalized to WT controls. This should control for age-related changes in knock-out and control mouse strains.

The ratio of 488 nm AF measurements between *Abca4*$^{-/-}$ and WT mice increased steeply within the first 3 months of life to about 2, followed by a ceiling effect with only a minor further increase until age 9 months. These values are similar to those previously reported in patients with Stargardt disease compared to healthy controls.[63, 99] Although the ratio of A2E levels between *Abca4*$^{-/-}$ and WT mice changed with a similar time course, its increase was considerably higher compared to the increase in lipofuscin-related 488 nm AF levels. One hypothesis to explain this discrepancy (assuming *Abca4*$^{-/-}$ mice had *bis*-retinoid and AF levels similar to WT mice at birth) would be that a substantial fraction of the 488 nm fundus AF signal in WT mice derives from fluorophores other than A2E and related *bis*-retinoids that do not vary considerably between WT and *Abca4*$^{-/-}$ mice (e.g. connective tissue flavoproteins, retinoids that do not depend on functional Abca4; *Figure 4.11*). A large increase in A2E content would then be necessary before

relevant changes of 488 nm AF may be detected. Thus, increased 488 nm fundus AF levels parallel the accumulation of A2E in the RPE of *Abca4*$^{-/-}$ mice, but may not quantitatively represent its accumulation in direct proportion. Such "incongruence" was also reported based on post mortem experiments by Boyer et al. who found a lack of correspondence in the rates of increase between lipofuscin-related AF in eyecups and quantification of A2E.[100] Similar to our data, AF and A2E-levels in eyes from aged *Abca4*$^{-/-}$ mice (background strain: 129Sv) compared to WT controls were approximately 2- and 10-fold higher, respectively.[100] Boyer et al. also challenged the current hypothesis on the function of Abca4 by providing evidence that light exposure and thus all-*trans*-retinal formation is not necessary for accumulation of A2E- and lipofuscin in the RPE. Assessment of AF intensity *in vivo* in dark reared animals was not performed in our study, but would complement those findings.

An additional explanation for the faster increase of A2E-levels compared to AF levels would be an interaction between lipofuscin-accumulation and fundus AF intensity. Lipofuscin located in the apical RPE cell compartment may absorb excitation light and thus reduce the contribution to the AF signal from more basally located lipofuscin. Yet another process that might lead to reduction of fluorescence intensity in RPE cells densely packed with lipofuscin fluorophores is quenching. Proportionality of fluorophore concentration and fluorescence is usually only seen in a given concentration range. However, at very high fluorophore concentrations, non-radiative energy transition (self-quenching) may occur and reduce the overall fluorescence intensity.

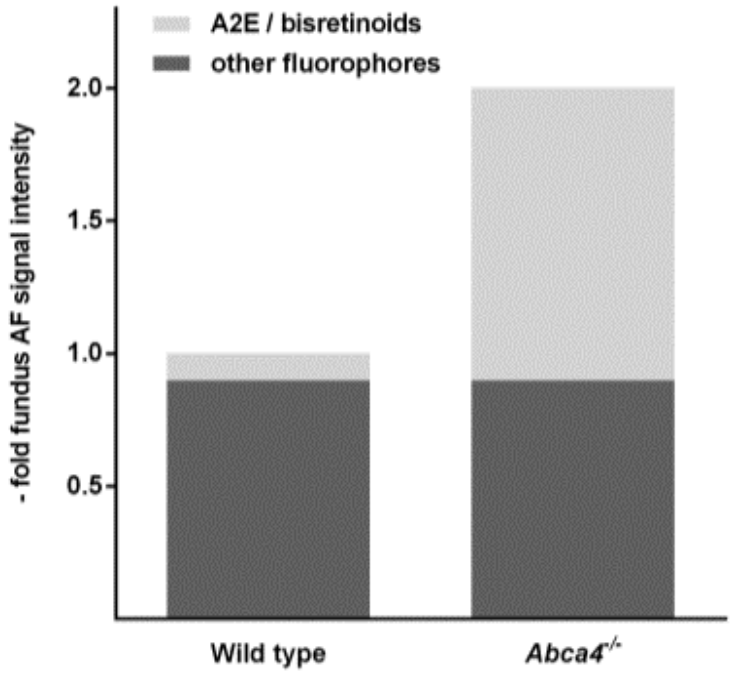

Figure 4.11 (previous page): Model to explain the discrepancy between the ~2-fold higher fundus AF levels and ~10-fold higher A2E levels in Abca4$^{-/-}$ mice compared to wild type (WT) controls. There may be an only low contribution of A2E and related bis-retinoids to fundus AF intensity in WT mice.

Melanin-related 790 nm AF levels also revealed a pronounced but considerably later increase compared to 488 nm AF. The major fluorophore for NIR excitation and thus the origin of 790 nm AF at the ocular fundus appears to be melanin.[68] Oxidative stress on the RPE has been suggested to play a pathophysiological role in a variety of retinal diseases, and oxidation of melanin has been shown to increase its autofluorescence.[101, 102] The observed time course of 790 nm AF could therefore be explained by increased oxidative stress in RPE cells after pronounced A2E accumulation. Based on electron microscopy findings,

a significant increase in melanin-related AF due to an increase in melanin granules appears unlikely. However, melanin granules revealed marked morphological alteration with a similar time course as the increase in 790 nm AF. Oxidative stress increases in RPE cells with increased lipofuscin load, possibly leading to melanin oxidation and formation of melanolipofuscin granules. Thus, altered AF properties of melanin, e.g. through oxidation or fusion with lipofuscin granules, appears to be the most likely explanation for the increased 790 nm AF. It is notable that in contrast to the results of this study, in albino *Abca4*$^{-/-}$ mice there is a progressive photoreceptor cell loss that is detectable at 8 months of age and worsens at 11 and 13 months.[103] Because melanin has an antioxidative capacity [104] the formation of melanolipofuscin as observed in the present study may reduce the formation of oxidative damage caused by lipofuscin alone.

No larger areas of RPE atrophy similar to those observed in Stargardt patients were observed in animals up to an age of 18 months. However, small patches of AF loss suggestive of RPE damage were observed in some *Abca4*$^{-/-}$ mice 9 months and older, but were never present in WT mice examined at similar stages. Besides RPE cell atrophy and/or a change in fluorophores, vacuolization within the RPE (*Figure 4.8*) might contribute to this finding. Loss of 790 nm AF often appeared to precede loss of 488 nm AF. Those findings suggest that high A2E levels may not be the direct cause of damage within the RPE, which appears to develop after an increase in melanin-related AF. If oxidation products of A2E are causing the changes in the melanin compartment and/or are cytotoxic, increased light exposure might lead to earlier development of the observed changes.

4.4.2 Conclusion

The data presented in chapter 4 show that quantitative and qualitative change in fundus AF can be assessed in the *Abca4*$^{-/-}$ mouse. Increased fundus AF intensity (488 nm excitation light) is related to an increase in lipofuscin and one of its major constituents, A2E, and may therefore be used as a surrogate marker for monitoring treatment effects of drug or gene therapy treatments aimed at lowering RPE-lipofuscin. Using similar imaging techniques in patients, results from preclinical studies may potentially be directly translated into clinical trials.

5 Functional Characterization of the *Abca4*$^{-/-}$ Mouse

5.1 Introduction

Although morphological changes can be assessed more objectively and with very high resolution using novel imaging techniques, preservation of retinal function is the ultimate endpoint for any given therapy for patients with Stargardt disease. Visual acuity and visual field testing are psychophysical measures and would be most important in patients. However, their assessment in mouse models – if feasible at all – is very difficult and unreliable.

The most commonly used objective functional assessment of the human and mouse retina is ERG testing. The full-field ERG measures the sum response of the entire retina and thus is a measure for functional compromise of the entire retina. Focal damage as it may first occur in the macula of typical Stargardt patients therefore would remain undetected. However, patients with Stargardt disease commonly develop reduced responses on full-field ERG testing either later in the disease course or, in some patients, even early on.[105-107] The functional phenotype initially described in the *Abca4*$^{-/-}$ mouse included a reduction of amplitudes on scotopic full-field ERG testing in aged mice.

Another functional parameter assessable on ERG testing is dark adaptation – or recovery of responses to a standardized light stimulus after exposure to bright light exposure that bleaches photopigment. There has been some debate if impaired dark adaptation would be a characteristic finding in Stargardt patients,[108] or if it is merely a secondary and possibly rather nonspecific consequence from the degeneration of the retina.[99, 109] Notably, dark adaptation testing in the *Abca4*$^{-/-}$

mouse model for Stargardt disease has also been inconclusive. The protocols and parameters assessed were not standardized across studies, making comparability and conclusions difficult (see discussion).

It was therefore the aim to test whether a robust functional phenotype could be identified in the *Abca4*$^{-/-}$ mouse.

5.2 Methods

5.2.1 Electroretinography

The general set up used for ERG testing is described in chapter 2.3. For dark-adapted testing, responses were elicited by brief flashes of white light on a dark background. Stimulus intensity was increased across ~5 log unit range (*Table 5.1*). For light-adapted testing, animals were pre-exposed to steady full-field white background illumination (30 cd/m^2) for 10 min. The recovery of dark-adapted function was measured after a 30 second exposure to 400 cd/m^2 white light (*Table 5.2*). For this latter experiment, *Abca4*$^{-/-}$ mice were crossed to WT mice and the heterozygote progeny intercrossed to obtain littermate homozygous *Abca4*$^{-/-}$ and WT mice.

In single flash ERGs, the b-wave amplitude (from a-wave trough to b-wave peak) was measured for all ERGs, whereas the a-wave amplitude (from baseline to a-wave trough) was measured only when recognizable as a distinct component (stimulus intensities ≥0.1 cd.s/m^2). Both amplitudes were measured in unfiltered recordings. Amplitudes of flicker ERGs were measured in recordings with 0-100 Hz bandpass and 50 Hz notch filters applied.

Flash intensity [cd.s/m^2]	Repetitions	Inter-stimulus interval [sec]	interval after intensity step [sec]	
0.0001	10	5	20	Scotopic testing
0.001	10	5	20	
0.01	10	5	20	
0.1	5	20	60	
3	5	20	60	
10	5	20	60	
25	5	20	120	
3	20 traces	20Hz flicker		
Pre-exposure: steady full-field white background illumination (30 cd/m^2) for 10 min				
3	10	0.5		Photopic testing
10	10	0.5		
3	20 traces	20Hz flicker		
10	20 traces	20Hz flicker		

Table 5.1: Details of the ERG protocol. The scotopic dose-response curve results of the three highest intensities were not averaged and only the first flash response was analyzed, because incomplete recovery between stimuli was noted.

Flash intensity [cd.s/m^2]	Repetitions	Interval between sets [sec]	interval after intensity step [sec]	
0.001	3, applied as set	120	1-2 (manual)	After ≥6 hours dark adaptation
10				
Photobleach (400 cd/m^2) for 30 sec				
0.001	1	300	1-2 (manual)	Dark re-adaptation
10				

Table 5.2: Details of ERG protocol to test recovery of dark-adapted function. The results of the three baseline measures were not averaged and only the first flash response was analyzed because incomplete recovery between sets of stimuli was noted.

5.3 Results

5.3.1 Electroretinography

In *Abca4*$^{-/-}$ and WT control mice, scotopic a-wave and b-wave amplitudes depended on age and stimulus intensity (*Figure 5.1* A,B; 2-way ANOVA, all $p<0.001$). a- and b-wave amplitudes depended on stimulus intensity in all age groups, but only in 18-month-old animals were affected by genotoype (2-way ANOVA, $p<0,05$). Scotopic and photopic flicker ERG as well as photopic flash ERG were no different in *Abca4*$^{-/-}$ compared to WT mice (*Figure 5.1* C). A full range of mean traces for the two oldest groups tested is shown in *Figure 5.2*.

The mean EC50 (as a sensitivity parameter) and mean hill slope (as a parameter for the dynamic range) on curve-fitted a-wave recordings in *Abca4*$^{-/-}$ mice were similar to WT mice, and did not vary with age (2-way ANOVA) at all intensities. Mean Vmax (the maximum amplitude) varied with age ($p<0.001$) but not genotype (2-way ANOVA). Bonferroni-corrected post-hoc analysis revealed significant differences between animals aged 18 and 2 ($p<0.001$), 3 ($p<0.001$) and 6 ($p<0.01$) months, as well as between mice aged 2 and 9 ($p<0.05$) and 12 ($p<0.001$) months.

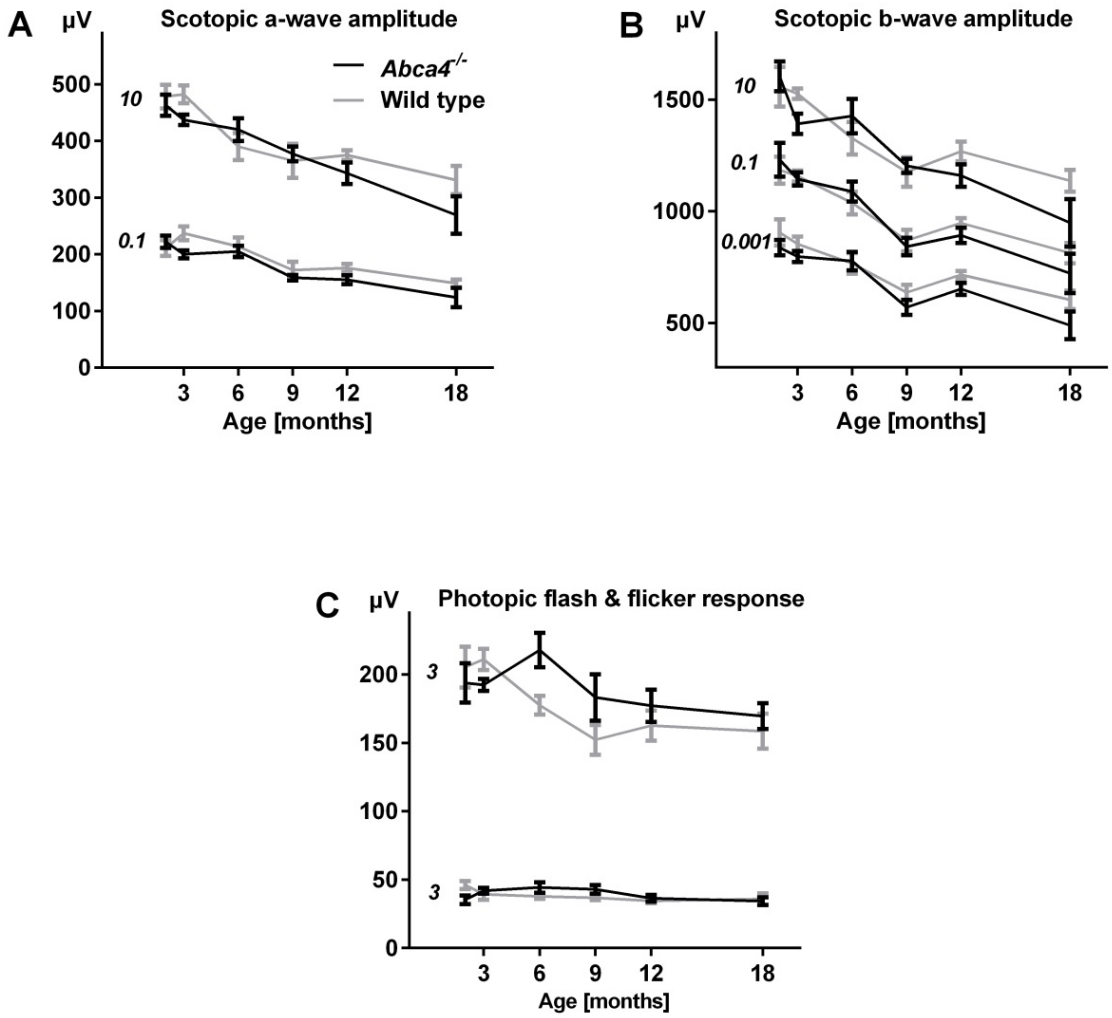

Figure 5.1: Functional testing by means of electroretinography in Abca4$^{-/-}$ and wild type (WT) control mice. ***A-C:*** *Mean scotopic and photopic amplitudes ±SEM across all tested ages for representative flash intensities (for full range of mean traces see supplementary figure 4). Numbers in italics indicate flash intensity in cd.s/m^2. The only significant difference between Abca4$^{-/-}$ mice and WT controls was observed in the scotopic testing of 18-month-old animals. n=5-8 in each group, except n=4 for 18-months old WTs.*

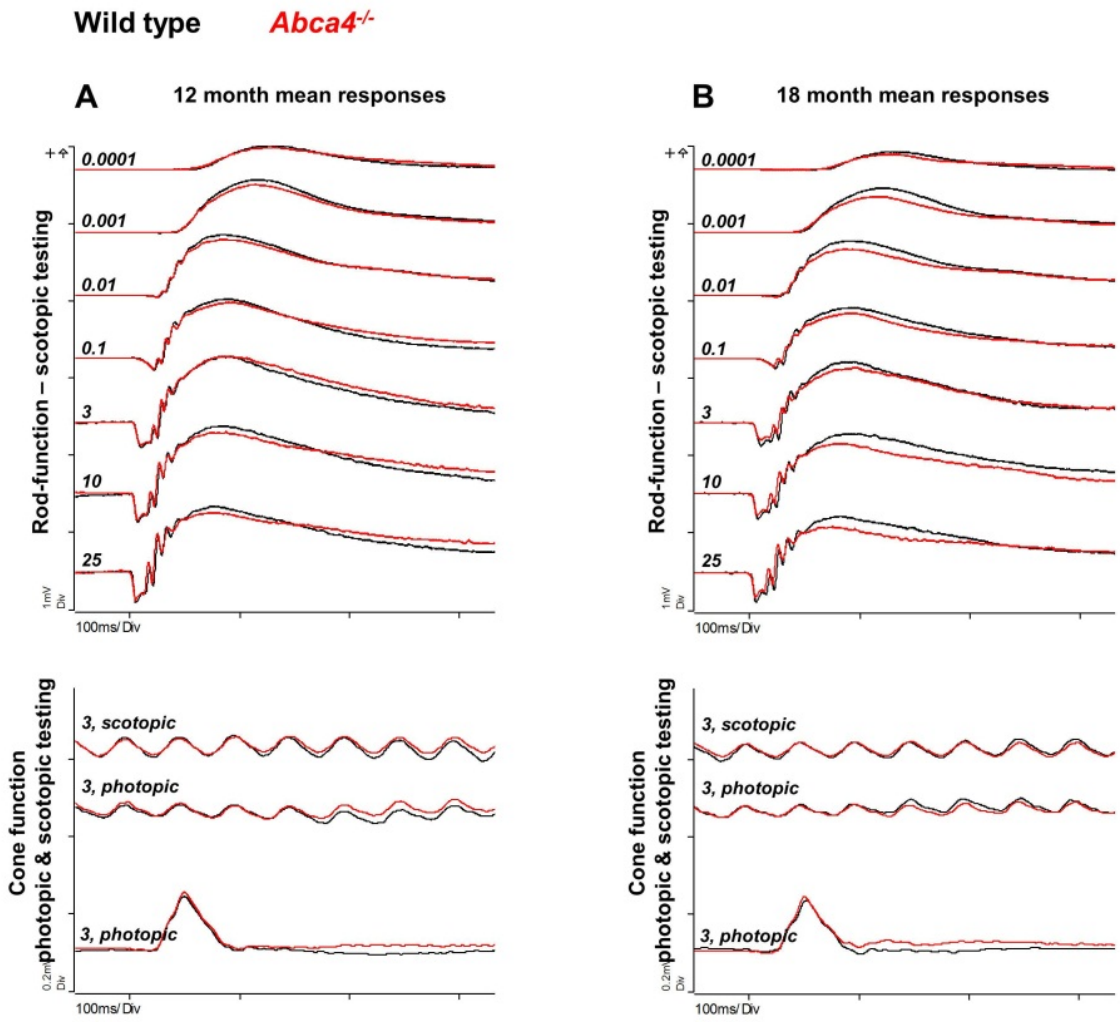

Figure 5.2: Electroretinography responses in Abca4$^{-/-}$ and wild type mice aged 12 and 18 months. Mean responses (full range of mean traces) in animals aged 12 months (A; n=8 Abca4$^{-/-}$; n=6 wild type) and 18 months (B; n=5 Abca4$^{-/-}$; n=4 wild type). Slightly lower a- and b-wave amplitudes are present in the 18 month old Abca4$^{-/-}$ mice compared to wild types. There is no difference in cone function. Numbers in italics indicate flash intensity in cd.s/m^2.

Based on previous reports of an inhibitory effect of A2E on RPE65,[110] a key enzyme in the visual cycle, we hypothesized that dark adaptation after a photobleach as a functional measure for visual cycle efficiency would be slowed down with age (and thus, significantly increased A2E-levels) in the *Abca4*$^{-/-}$ mouse compared to age-matched WT controls. Baseline a-wave amplitudes before the photobleach decreased with age but were not different between strains (*Figure 5.3* A), recapitulating the above results in a separate set of animals. Dark adaptation after a photobleach was slower in 4- and 8-months-old *Abca4*$^{-/-}$ mice than at age 1 month (*Figure 5.3* B,C). This age effect was similar in WT mice (*Figure 5.3* D-E).

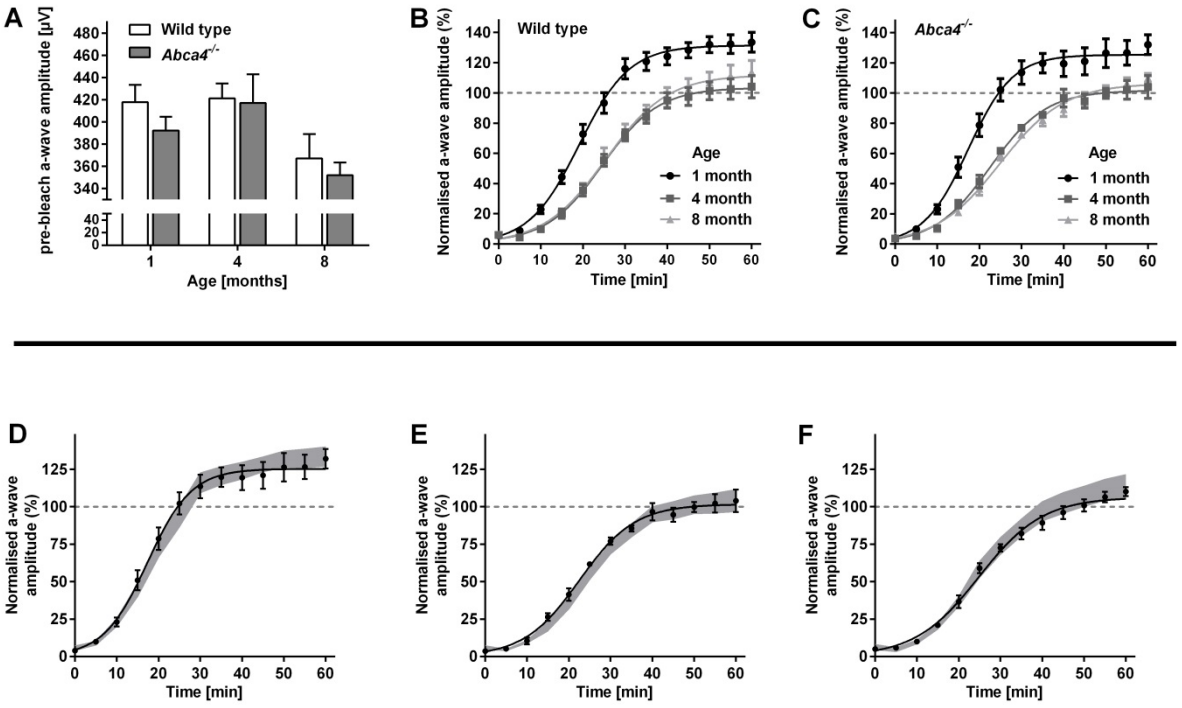

Figure 5.3: Dark adaptation kinetics. A: Before the photobleach, dark adapted a-wave amplitudes were similar between Abca4$^{-/-}$ and wild type (WT) animals at all ages tested. B,C: The mean scotopic a-wave amplitude (±SEM) relative to baseline before a photobleach is shown. Dark adaptation after the photobleach was slower in 4- and 8-months-old animals compared to 1-month-old mice. This age-effect was observed in both, WT (B) and Abca4$^{-/-}$ (C) mice. n=5-7 in each group. D-F: Kinetics of dark adaptation in Abca4$^{-/-}$ compared to WT control mice (n=5-7 in each group) aged 1 (D), 4 (E) and 8 (F) months. The mean (±SEM) scotopic a-wave amplitude relative to baseline before a photobleach is shown. The grey area represents the mean±2SDs of the dark adaptation kinetics in WT mice. Recovery after photobleach was faster in 1-month-old compared to 4- and 8-months-old animals. Dark adaptation kinetics were similar in Abca4$^{-/-}$ and WT control mice.

5.4 Discussion

5.4.1 Functional relevance of increased fundus AF levels and A2E-accumulation

The most important finding from these ERG studies is that there was no relevant difference in scotopic and photopic light responses between pigmented *Abca4*$^{-/-}$ mice and WT controls up to an age of 12 months. Even in 18 months old animals, the difference was only marginal, although significant. This is in line with the similar photoreceptor layer thickness of those two mouse strains even at old age (see *Figure 4.6*). The finding is surprising when considering the high levels of fundus AF and A2E in *Abca4*$^{-/-}$ mice early in life (i.e. in 2-3 months old animals, see *Figure 4.5*). A2E may increase blue light cytotoxicity,[90, 91] induce lysosomal dysfunction[92, 93] and activate complement.[94] Thus the accumulation of A2E and other *bis*-retinoids that together constitute RPE lipofuscin is commonly discussed as a major risk factor for RPE cell death, with subsequent failure of photoreceptors. However, RPE cell death would be visible as qualitative changes on *in vivo* AF images. We have not found areas of RPE atrophy similar to those observed in Stargardt patients in *Abca4*$^{-/-}$ mice up to an age of 18 months, indirectly validating preserved retinal function.

Notably, an increase in 790 nm AF intensity preceded functional differences between *Abca4*$^{-/-}$ and WT mice and occurred before the appearance of small atrophy-resembling spots on 488 and 790 nm AF images. Alterations in the melanosomal compartment, as revealed by 790 nm AF imaging, might precede structurally and functionally relevant changes in the RPE. Quantitation of 790 nm AF may thus be a useful early marker for functionally relevant RPE alteration.

Others have identified photoreceptor loss as an indirect indicator for functional decline in the albino *Abca4*$^{-/-}$ mouse compared to albino controls.[103, 111] This difference might be explained by the higher levels of all-*trans*-retinal in the albino mouse eye, and thus might be independent from lipofuscin accumulation in the RPE. Although A2E levels are higher in pigmented compared to albino mice,[112] increased photoreceptor loss was not observed using pigmented mice, indicating lack of a direct causative relation between A2E accumulation and photoreceptor loss. This might also explain the paradox observed in heterozygote albino knockout (*Abca4*$^{+/-}$) mice, which show lipofuscin/A2E-measures similar to wild type controls while at the same time have photoreceptor loss similar to homozygous knockout (*Abca4*$^{-/-}$) mice.[111] The photoreceptor loss in *Abca4*$^{-/-}$ albino mice might be due to increased all-*trans*-retinal toxicity, while the increased lipofuscin/A2E levels would have no relevant effect on retinal structure and function. Notably, pigmented heterozygote Abca4$^{+/-}$ mice have A2E levels in between homozygous knockout (*Abca4*$^{-/-}$) and homozygous WT (*Abca4*$^{+/+}$) mice, without a difference in photoreceptor degeneration between the three genotypes.[113]

5.4.2 Dark adaptation kinetics

Assessment of dark adaptation revealed an effect of age in *Abca4*$^{-/-}$ and WT mice. This effect was similar between strains, suggesting that there is no relevant effect of the lack of Abca4. Notably, the change in dark adaptation rate from 1 month to 4 months of age was similar between strains despite the very steep increase of A2E and lipofuscin-related AF levels in *Abca4*$^{-/-}$ mice. This suggests that an inhibitory effect of A2E on RPE65 may not be an important contributor to delayed dark adaptation *in vivo*. It should be noted that protocols, background

strains, assessed parameters and analysis to describe the dark adaptation characteristics in *Abca4*$^{-/-}$ mice vary considerably in the literature (*Table 5.3*), which may be the reason heterogeneous and partly unreproducible results across studies. Additional variability may derive from different durations of dark adaptation before bleaching, use of control mice of a different background strain, and others. Our protocol assessing recovery of scotopic single flash amplitudes aimed at identifying differences in retinoid cycle kinetics after a photobleach. Although there might be a trend for a declining dark adaptation rate in aged *Abca4*$^{-/-}$ compared to WT controls (*Figure 5.3* F), the difference of this parameter would not be substantial and robust enough to assess treatment effects in preclinical studies. Paired-flash ERG-analysis, assessment of Rm_{P3} and similar protocols may identify reduced photoreceptor sensitivity states, for which the protocol used in this study might not be suitable.

Publication (1st author)	Background strain	Bleaching light	Bleaching duration	Reported parameter with significant difference
Weng [34]	129Sv	400 lux	5 min	Rm_{P3} *
Radu[37]	129Sv	1000 lux	25 sec	b-wave amplitude, Rm_{P3} *
Allocca[38]	BALB/c	300 cd/m^2	80 sec	b-wave amplitude
Kong[39]	BALB/c	No robust differences identified		
Radu[95]	not clear	1000 lux	1 min	b-wave amplitude
Han[114]	129Sv (?)	400 lux	5 min	a-wave

*Table 5.3: Variability of parameters in ERG studies reporting a strain difference between Abca4$^{-/-}$ mice an wild type controls. *derived from a computational model to provide estimates of photoreceptor activity*

5.5 Conclusion

High A2E levels can be tolerated by RPE cells over prolonged time periods, and additional factors such as high oxidative stress and/or the macular anatomy appear to be necessary to develop RPE atrophy with subsequent compromise of photoreceptor cells. The mouse model differs from Stargardt disease because many patients do not have two loss-of-function mutations. Rather, there appears to be a substantial number of mutations that result in an additional toxic gain-of-function,[115] which would not be reflected by a knockout mouse model with complete loss of function of the Abca4 protein.

There was no robust and pronounced functional phenotype of the *Abca4*$^{-/-}$ mouse on ERG testing. Differences compared to WT controls reported in the literature rely on specialized detection methods that would not easily be transferable to other labs for validation. In other instances, a functional phenotype of the *Abca4*$^{-/-}$ mouse is described using only small sample sizes without independent validation using the same protocol, and may thus be due to chance.

Overall, the lack of an evident functional phenotype on ERG testing suggests that such assessment would be unlikely to allow conclusions on efficiency of a potential phenotypic rescue. Thus, functional testing of the *Abca4*$^{-/-}$ mouse model for Stargardt disease in preclinical studies would rather be a read out parameter for evaluating safety of novel therapies

6 Fundus autofluorescence for evaluating a novel lipofuscin-lowering pharmacotherapy in the *Abca4*$^{-/-}$ mouse

6.1 Introduction

The initial step in the accumulation of RPE lipofuscin is the formation of vitamin A-derived *bis*-retinoids in photoreceptor outer sgements. Vitamin A is an integral molecule of visual pigment and cannot be depleted by dietary changes or pharmacologicaly without compromising visual function. However, the formation of *bis*-retinoids and subsequent lipofuscin-formation may be decreased by chemically engineering vitamin A. If higher energy is needed to form *bis*-retinoids, their formation becomes less probable. The latter has recently been achieved by exchanging a hydrogen for a deuterium atom at C20 of vitamin A (C20dVitA).[45, 46] It was shown in vitro that dimerization (and thus, *bis*-retinoid formation) of C20dVitA is considerable slower than of normal vitamin A. Moreover, the same authors could show that A2E accumulates less in eye cups of WT and *Abca4*$^{-/-}$ mice fed with a diet in which vitamin A had been replaced by C20dVitA.

It has not yet been investigated whether such treatment effects could be observed by fundus AF imaging. Therefore, the primary aim of this project was to determine if a C20dVitA diet would result in measurable differences of AF intensity in WT and *Abca4*$^{-/-}$ mice.

6.2 Methods

6.2.1 Diet

Diets were prepared by a commercial manufacturer. Control mice received a standard rodent diet (RM1; Special Diets Services, UK) which has vitamin A supplemented at a dose of 8,000 IU/kg. For the interventional group, C20dVitA was blended with sucrose and added to a purified diet instead of normal vitamin A at the same concentration (8,000 IU/kg diet). In the interventional group, normal diet was replaced by the C20dVitA diet when pups were born. All mice had food and water ad libitum throughout the study.

6.2.2 Fundus autofluorescence imaging and image analysis

Fundus AF imaging was performed in anesthetized animals following the standard protocol developed beforehand (see chapter 3.5). Only one eye per mouse was recorded. All images were recorded using the 55° lens (Heidelberg Engineering) of the Spectralis HRA.

For quantitative analysis of fundus AF, the mean grey level on mouse fundus AF images (acquired with standardized signal detector sensitivity, unprocessed, 1536x1536 pixels) was measured within a ring shaped area between 250 and 450 pixel radii from the optic disc center using ImageJ software (Version 1.43, National Institute of Health, http://rsb.info.nih.gov/ij), as outlined in chapter 3.2.3. The “electronic zero” was subtracted from each measured grey value to obtain the corrected grey level (cGL), which was used for all calculations.

6.2.3 Quantification of A2E

For A2E quantification, the cornea and lens were removed in phosphate buffered saline (PBS). Dissected eye cups were immediately snap frozen and stored at -80°C until further processing.

Quantification of A2E was performed by Ilyas Washington, Department of Ophthalmology, Columbia University Medical Center, New York, USA. The detailed method of *bis*-retinoids extraction and analysis has recently been published.[46]

6.2.4 Electroretinography

The general set up used for ERG testing is described in chapter 2.3. For dark-adapted testing, responses were elicited by brief flashes of white light on a dark background. Stimulus intensity was increased across ~7 log unit range (*Table 6.1*). For light-adapted testing, animals were pre-exposed to steady full-field white background illumination (30 cd/m^2) for 10 min.

In single flash ERGs, the b-wave amplitude (from a-wave trough to b-wave peak) was measured for all ERGs, whereas the a-wave amplitude (from baseline to a-wave trough) was measured only when recognizable as a distinct component (stimulus intensities ≥0.1 cd.s/m^2). Both amplitudes were measured in unfiltered recordings. Amplitudes of flicker ERGs were measured in recordings with 0-100 Hz bandpass and 50 Hz notch filters applied.

Flash intensity [cd.s/m^2]	Repetitions	Inter-stimulus interval [sec]	interval after intensity step [sec]	
0.000001	16	2	20	Scotopic testing
0.00001	16	2	20	
0.0001	16	5	20	
0.001	9	5	60	
0.01	9	10	60	
0.1	9	20	60	
1	4	40	60	
10	1	---	120	
25	1	---	120	
Pre-exposure: steady full-field white background illumination (30 cd/m2) for 10 min				
3	10	0.5		Photopic testing
10	10	0.5		
3	20 traces	20Hz flicker		
10	20 traces	20Hz flicker		

Table 6.1: Details of the ERG protocol.

6.3 Results

6.3.1 Treatment with C20dVitA reduces A2E- and autofluorescence levels

To test if C20D3-vitamin A may reduce lipofuscin formation, WT and *Abca4*$^{-/-}$ mice were fed C20D3-vitamin A from birth or received a normal diet. Effectiveness was assessed *in vivo* by lipofuscin- and melanin/melanolipofuscin-related fundus AF recordings in 9-month old *Abca4*$^{-/-}$ mice. A2E-concentrations were assessed post-mortem using UPLC.

A2E is a major fluorophore of lipofuscin in the RPE and thus may be used as a surrogate measure for lipofuscin accumulation. A2E increases about 8-fold in 9-month old *Abca4*$^{-/-}$ mice compared to WT controls (*Figure 6.1* A,B).

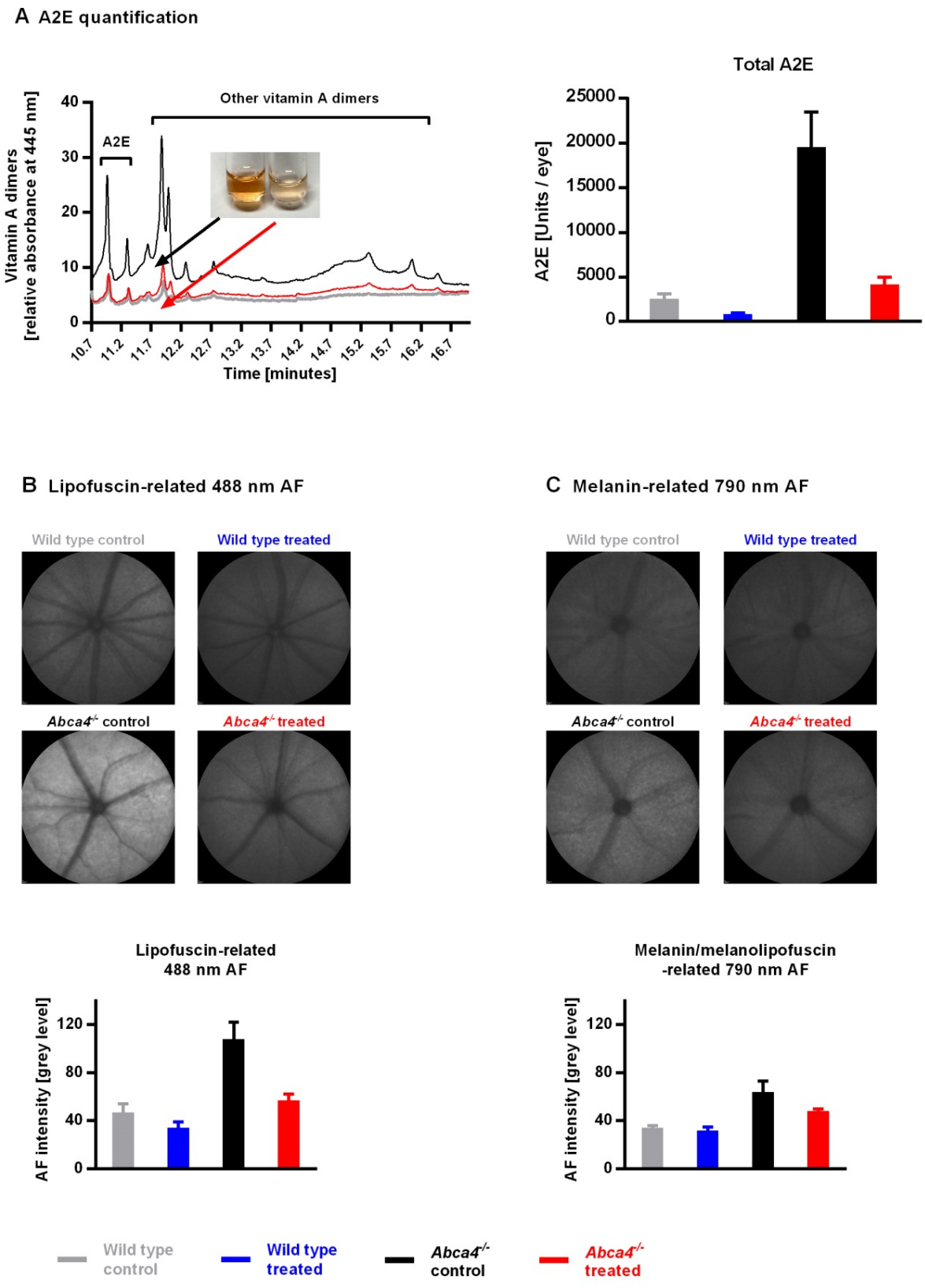
A A2E quantification
Other vitamin A dimers
A2E
Vitamin A dimers [relative absorbance at 445 nm]
Time [minutes]
Total A2E
A2E [Units / eye]
B Lipofuscin-related 488 nm AF
Wild type control
Wild type treated
Abca4-/- control
Abca4-/- treated
C Melanin-related 790 nm AF
Lipofuscin-related 488 nm AF
Melanin/melanolipofuscin -related 790 nm AF
AF intensity [grey level]
Wild type control
Wild type treated
Abca4-/- control
Abca4-/- treated

Figure 6.1 (previous page): Representative Ultra Performance Liquid Chromatography (UPLC) chromatograms (A) and fundus autofluorescence (AF) images (B, C) together with the corresponding quantitative analysis (mean±SD; n=10 in each group). All mice were 9-month old and treatment was started at birth.

A, left: UPLC chromatograms of treated and control Abca4$^{-/-}$ mice along with that of wild-type (WT) control mice. A2E and its geometric isomer, iso-A2E, eluted at 11.0 and 11.3 minutes. In addition to A2E, uncharacterized peaks eluting between 11.4 and 17.0 minutes with long-wavelength absorption (445 nm) were also observed. These later peaks were larger in eye extracts from Abca4$^{-/-}$ compared to WT control mice. Treatment with C20 deuterized vitamin A (C20dVitA) resulted in decreased formation of A2E and all compounds that eluted between 11.0 and 11.3 minutes. Thus compounds corresponding to those peaks are formed as a result of the Abca4 gene defect and this effect is counteracted by C20dVitA. A, right: A2E levels in Abca4$^{-/-}$ compared to WT control mice were increased ~8-fold. C20dVitA eliminated this increase almost completely and also significantly reduced A2E levels in WT mice.

B,C top: Representative original recordings of lipofuscin- and melanin/melanolipo-fuscin-related AF. B,C bottom: quantitative grey level analysis shows similar effects of the treatment as on A2E levels, although with smaller differences between groups. There was no significant effect of the treatment on melanin/melanolipofuscin-related AF levels in WT mice.

In untreated *Abca4*$^{-/-}$, treated *Abca4*$^{-/-}$ and treated WT 9-month old mice, the –fold difference compared to WT controls was 7.5x, 1.6x and 0.3x for total A2E, 2.3x, 1.2x and 0.7x for lipofuscin-related AF, and 1.9x, 1.4x and 1.0x for melanin / melanolipofuscin-related AF. In 3-month old animals, the -fold difference was 4.1x, 1.1x and 0.2x for total A2E, 2.1x, 1.0x and 0.8x for lipofuscin-related AF, and 1.4x, 1.1x and 1.0x for melanin / melanolipofuscin-related AF (*Figure 6.2*). Thus, at the age of 3 months, A2E- and AF-levels revealed similar changes as in 9-month old animals but at an overall lower level (*Table 6.2*).

		Wild type		*Abca4*$^{-/-}$	
	Age [months]	Control	Treated	Control	Treated
A2E-levels	3	1	0.2	4.1	1.1
	9	1	0.3	7.5	1.6
Lipofuscin-related AF	3	1	0.8	2.1	1
	9	1	0.7	2.3	1.2
Melanin-related AF	3	1	1	1.4	1.1
	9	1	1	1.9	1.4

Table 6.2: Effect of treatment over 3 or 9 months with C20dVitA on A2E-levels, lipofuscin-related- and melanin-related autofluorescence intensity. Numbers are fold-differences compared to untreated wild type control animals. In all three parameters, the treated Abca4$^{-/-}$ *mouse* shows a phenotype similar to untreated wild type control animals.

In a clinical setting, therapy would be initiated at various time points of the diseases course depending on the disease stage at which individual patients present, or therapy may be stopped for various reasons. To imitate such scenarios in the *Abca4*$^{-/-}$ mouse model, treatment with C20dVitA was initiated at different time points or was stopped after 3 months of therapy from birth (*Figure 6.3*). The advent of in vivo fundus AF imaging to repeatedly monitor AF levels in the same animals was used to assess therapeutic effectiveness at the age of 3, 6 and 9 months. At the final time point, the data set was supplemented by post mortem measures of eye cup A2E levels.

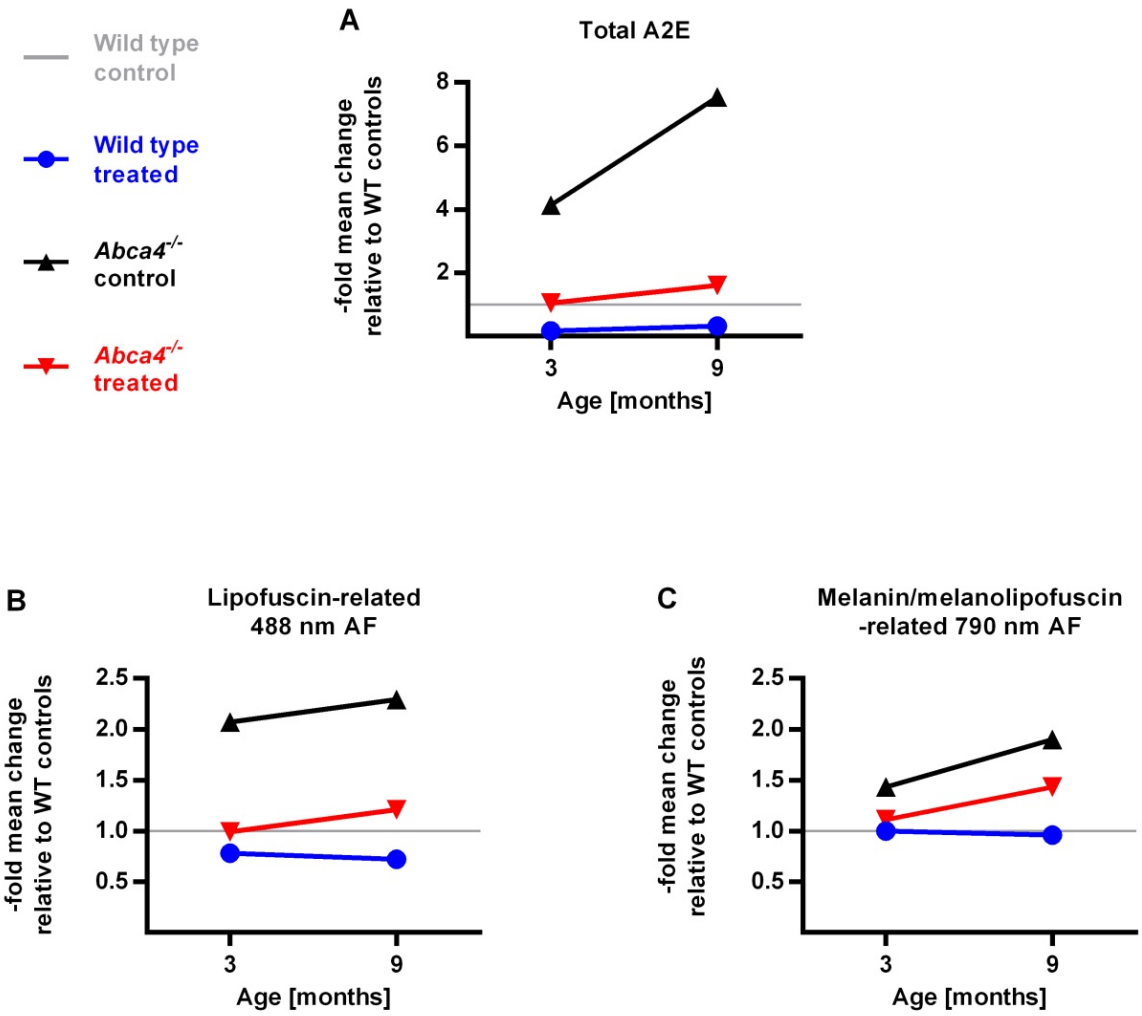

Figure 6.2: Difference of three parameters normalized to wild type (WT) controls (horizontal grey line; 1) in two different age groups. Data of 9-month old mice shown in figure 1 is re-plotted together with similar data from 3-month old mice. Measures of total A2E (A) show the highest –fold change in Abca4$^{-/-}$ mice compared to WT controls. Treatment effects of C20dVitA are qualitatively similar in measures of A2E and assessment of lipofuscin-related AF levels. Both parameters also reveal an effect of C20dVitA in WT mice. Melanin/melanolipofuscin-related AF is still relatively elevated in mice treated with C20dVitA over 9 months and shows no effect of the therapy in WT mice.

A2E levels assessed in 9 months old animals varied with the age of onset of therapy and thus with the duration of treatment (*Figure 6.3* A,B). Those with the longest treatment period revealed the lowest levels of A2E. Fundus AF levels at the same time point corroborated the biochemical data: levels of lipofuscin- and melanin / melanolipofuscin-related AF depended on the duration of treatment C20dVitA (*Figure 6.3* C,D; right graphs). To illustrate change of AF intensity over time, values were normalized to WT controls in order to control for potential changes between imaging sessions, such as fluctuation in laser power or change of pupil width with age. Both, 488 nm and 790 nm AF intensity levels changed over time depending on the presence of therapy (*Figure 6.3* C,D; left graphs).

Figure 6.3 (next page): Effect of age at initiation of treatment with C20D3-vitamin A on A2E accumulation and AF levels in Abca4$^{-/-}$ mice. A) Illustration of 5 different treatment intervals. A control group remained untreated throughout the experiment. B) A2E levels in 9 months old animals reveal a dose dependent effect. C) Longitudinal recordings of 488 nm AF levels were decreased depending on the presence of therapy (left). At 9 months of age fundus AF revealed changes in intensity levels similar to the changes in A2E concentration (right). D) Similar differences were observed in 790 nm recordings, although at an overall lower level compared to 488 nm AF

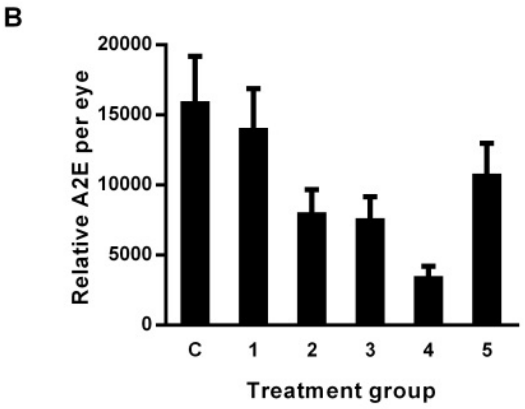

C Lipofuscin-related 488 nm AF

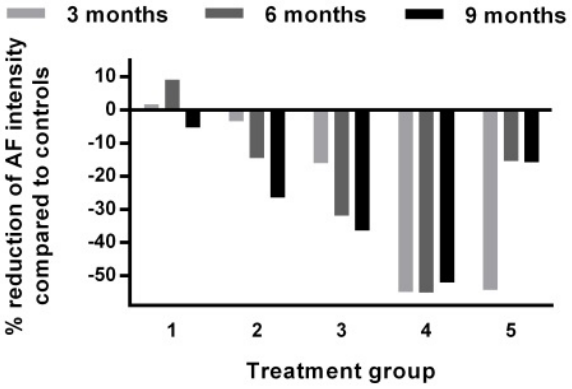

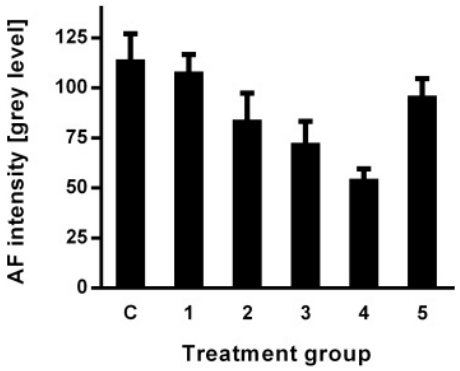

D Melanin-related 790 nm AF

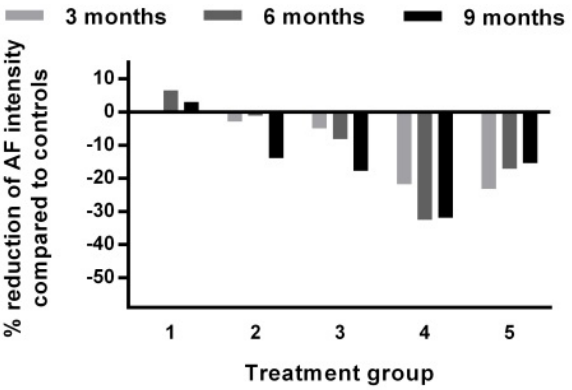

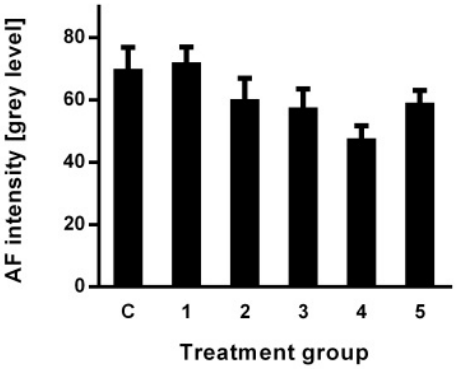

6.3.2 C20dVitA has no effect on retinal function

ERG recordings were performed in 9 month old WT and *Abca4*$^{-/-}$ mice which were fed throughout their life either with or without the C20dVitA therapy. Scotopic and photopic ERG responses were not different between WT and *Abca4*$^{-/-}$ mice on normal diet (*Figure 6.4*), confirming data from chapter 5. There was no effect of the diet on either scotopic or photopic ERG responses in *Abca4*$^{-/-}$ mice and WT controls (*Figure 6.5* and *Figure 6.6*).

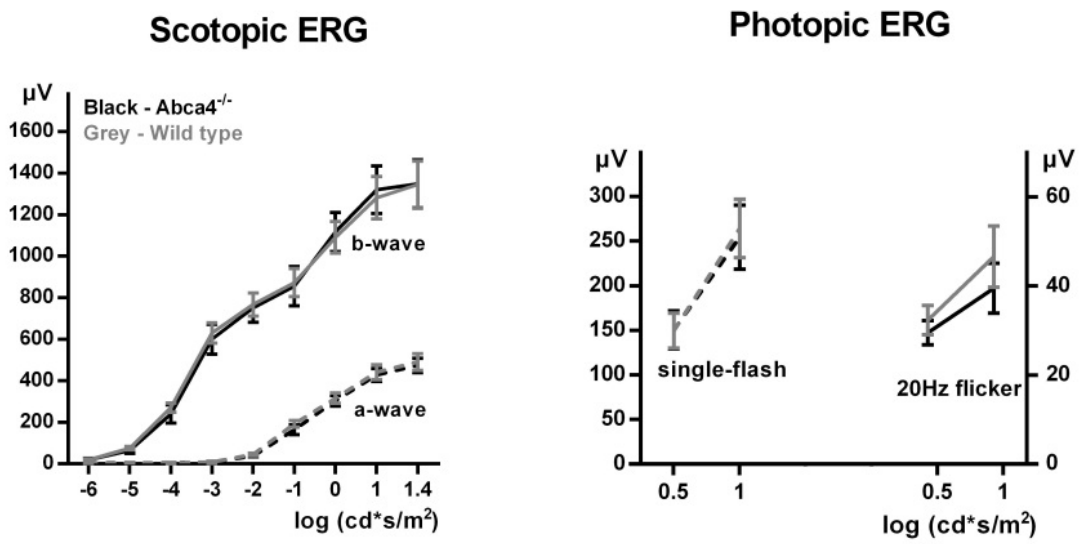

Figure 6.4: Comparison of scotopic (left) and photopic (right) ERG recordings in 9 month old WT and Abca4$^{-/-}$ *mice. All mice were on a normal diet throughout life. There is no difference between groups (n=10 each group).*

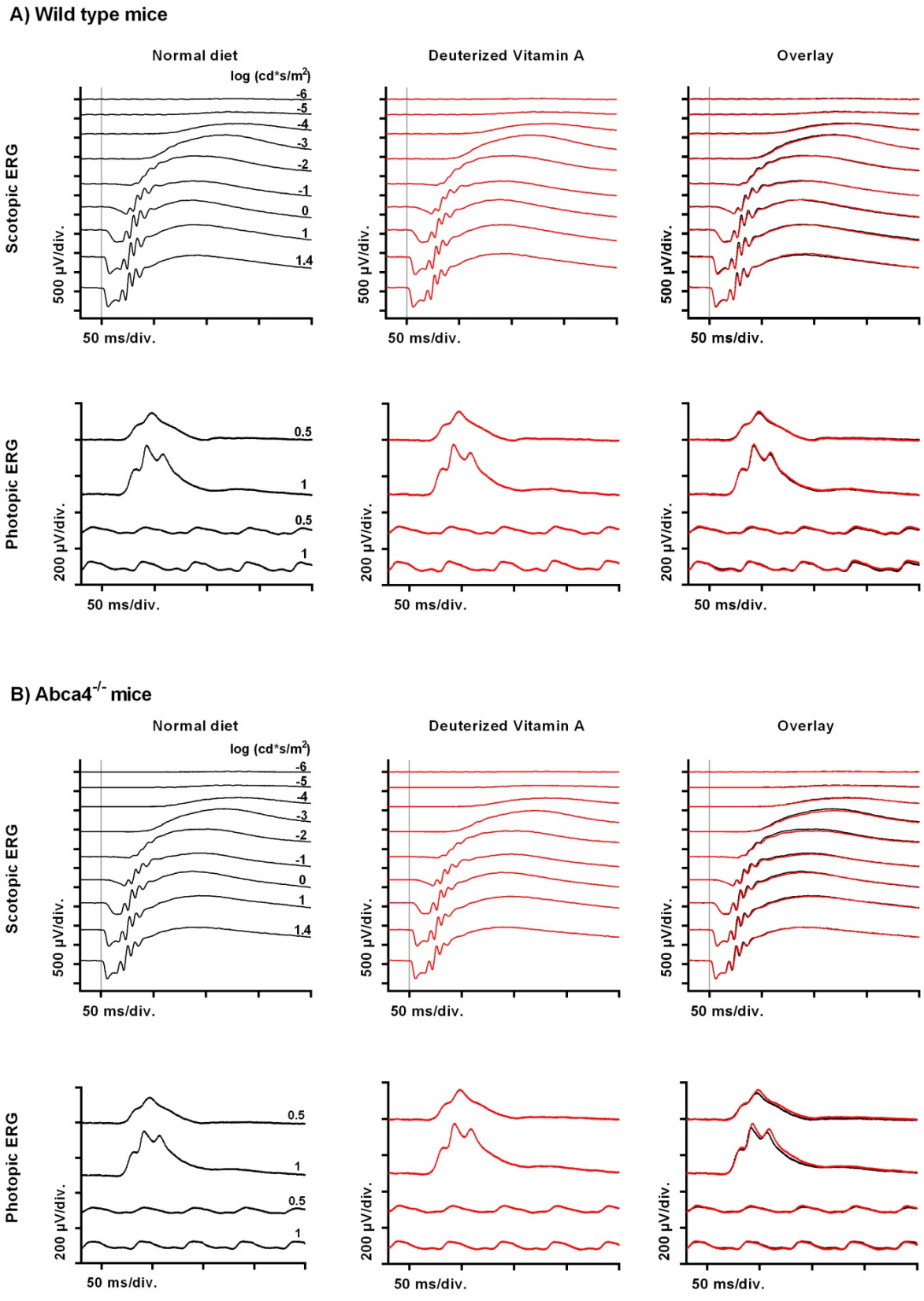
A) Wild type mice
Normal diet
Deuterized Vitamin A
Overlay
log (cd*s/m2)
-6
-5
-4
-3
-2
-1
0
1
1.4
Scotopic ERG
500 µV/div.
50 ms/div.
0.5
1
0.5
1
Photopic ERG
200 µV/div.
B) Abca4-/- mice

Figure 6.5 (previous page): Effect of C20dVitA on retinal function in 9 month old wild type (WT; A) and Abca4$^{-/-}$ (B) mice. Traces are means of 10 mice. Mice were either on a normal diet (black traces) or on a diet enriched with C20dVitA (red traces) throughout life. The dark-adapted (scotopic) single-flash ERG intensity series (upper row in A, B) shows no difference between groups. Visibility of the similarity is enhanced in the overlay (right). The vertical grey line indicates the timing of the light stimulus. Lower row in A, B: Light-adapted photopic single flash (upper two traces) and 20Hz flicker (lower two traces) at two different intensities also revealed no difference between treated and untreated WT and Abca4$^{-/-}$ mice.

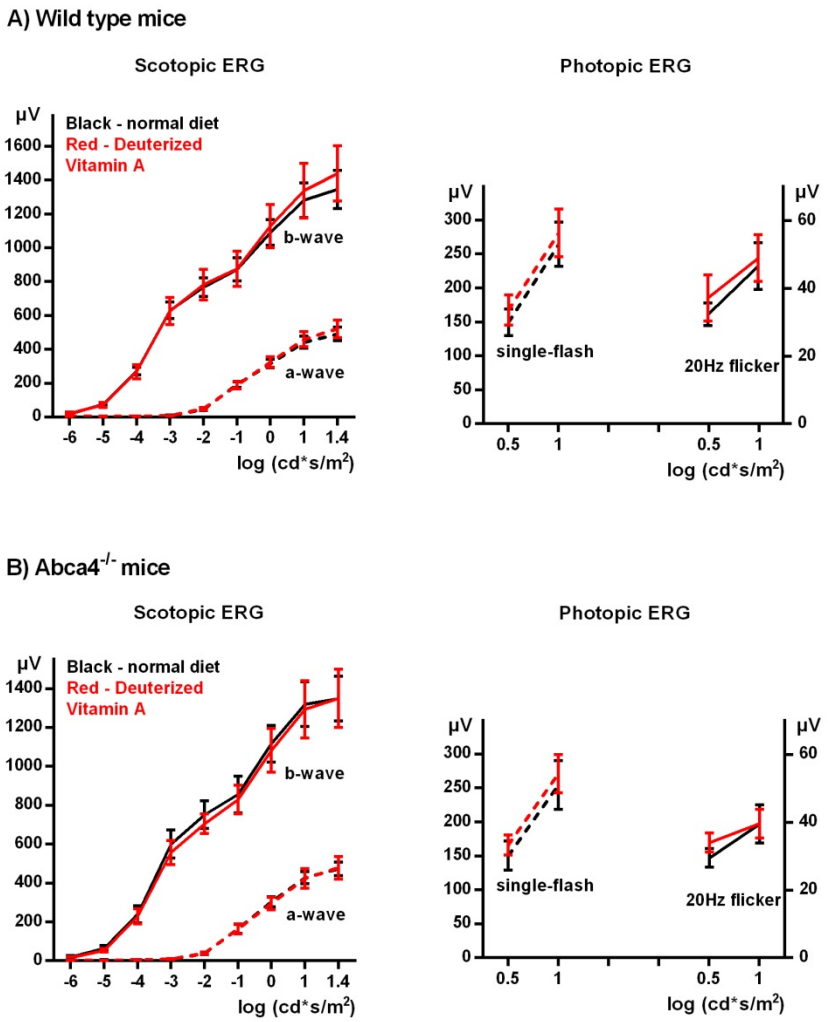

Figure 6.6: Quantitative illustration including error bars (mean±SD) for the data shown in Figure 6.5. Displayed are dose-response curves for the scotopic (left) and photopic function (right) for wild type (A) and Abca4$^{-/-}$ (B) mice.

6.4 Discussion

Herein, the ability of fundus AF imaging to detect treatment effects in the *Abca4*$^{-/-}$ mouse in vivo has been explored. The rationale for using this outcome measure was the analysis in chapters 4 and 5 defining increased fundus AF intensity as the most pronounced detectable phenotype of this mouse model.

C20dVitA has previously been shown to decrease accumulation of A2E in eyes of *Abca4*$^{-/-}$ mice. The experiments presented in this chapter show that changes in A2E-levels are paralleled by corresponding changes in lipofuscin-related fundus AF intensity, and that treatment effects of C20dVitA can be monitored with both, measurement of A2E and AF intensity. Observed differences were more pronounced in measures of A2E, most likely because other fluorophores contribute to the overall signal intensity on fundus AF images. However, the level of lipofuscin-related fundus AF intensity measures in mice treated from birth on was comparable to WT mice on a normal diet, suggesting a virtually complete rescue of the phenotype observed on fundus AF imaging.

Notably, a similar effect was observed when analyzing melanin-related fundus AF, suggesting that formation of melano-lipofuscin is reduced. Thus, the melanin compartment with its oxidative mechanisms appears to remain in a more physiological state.

The relatively large and robust effects observed on fundus AF signal intensity measures suggest that such analysis could also be applied in clinical studies using C20dVitA as therapy for patients with Stargardt disease. Notably, a technique to quantitatively assess fundus AF in humans has recently been optimized and is now ready for wider use in clinical trials.[77, 116]

The longitudinal analysis suggests that the earlier the therapy is started, the better treatment outcome may be. Notably, mice fed with the C20dVitA-enriched diet that were subsequently switched to normal diet approached similar A2E-levels as untreated mice. Thus, the therapeutic effect appears to last only while C20dVitA is supplemented.

There was the theoretical concern that dVitA could affect a hypothesized buffering mechanism for all-*trans* retinal, namely the binding of this photo-activation product to phosphatiyl-ethanolamine. The toxic properties of all-*trans* retinal could then potentially have caused photoreceptor cell death and thus declining function. However, there was no functional deterioration in mice fed with dVitA enriched diet, suggesting that such hypothesized protective mechanisms are not affected.

Deuterization of vitamin A has been used for decades to study the physiology of vitamin A in humans and specifically C20 deuterization has been suggested not to interfere with normal vitamin A metabolism.[45] We could not detect any negative effect on retinal function after 9 months of supplementation. Safety of C20dVitA may therefore be assumed, although this would have to be demonstrated in clinical trials. Very high safety standards will have to be applied because the therapy would likely be started early in life and taken over years, if not decades.

7 Towards gene therapy for Stargardt disease

7.1 Introduction

The monogenic recessive nature and chronicity of Stargardt disease makes it ideally suitable for gene replacement as a potential means to slow down or possibly even stop photoreceptor degeneration. The *Abca4*$^{-/-}$ mouse model can be used to assess possible gene therapy strategies for Stargardt disease. Challenges with *Abca4* gene delivery include the large size of the gene (~6.7kB) and the necessity to deliver it to photoreceptors (see chapter 1), where Abca4 is physiologically expressed and which are inherently more difficult to transduce than RPE cells in the previous RPE65 trials.

Required recombination mechanisms after viral transduction when delivering large genes, such as *Abca4*, limit the efficacy of transgene delivery (see chapter 1).[60] Thus, high levels of transduction using AAV would be required to aid recombination of two halves of a split *Abca4* transgene. Non-viral gene therapy has been envisaged as an alternative for delivering large genes to retinal cells. However, those efforts have as yet been unconvincing.[55]

Against this background there are ongoing efforts to improve efficiency of AAV-driven gene delivery and to improve vector tropism to specific retinal cell populations by modifying the capsid protein and/or the expression cassette. In the former case it has recently been shown that recombinant packaging of the AAV2 expression cassette into an AAV8 capsid (rAAV2/8) significantly enhanced transduction of primate photoreceptors when assessed by expression of GFP.[117] Furthermore the AAV5 capsid is known to transduce primate foveal cones

effectively, as evidenced by restoration of trichromatic color vision in the macaque following treatment of dichromats with rAAV2/5 vector encoding an opsin gene.[118]

The use of such recombinant vectors, in which a transgene cassette flanked by AAV2 inverted terminal repeats (ITR) is packaged into the capsid from another AAV serotype, is becoming established in retinal gene therapy. What has yet to be explored in detail, however, is how AAV vectors might behave if the capsid protein itself were a hybrid of several different serotypes, possibly combining beneficial effects of each for targeting photoreceptors.

The purpose of this study was therefore to explore if exchange of structural domains between capsids of different serotypes (vectors with hybrid recombinant capsids: rAAV2/Rec2 and rAAV2/Rec3), would confer greater infectivity or alter cellular tropism to photoreceptors compared to that of rAAV2/2 and rAAV2/5 after subretinal delivery in WT and *Abca4*$^{-/-}$ mice.

7.2 Methods

7.2.1 Viral vectors

The viral vectors were kindly supplied by Matthew J. During, Department of Molecular Medicine and Pathology, The University of Auckland, Auckland, New Zealand. The novel viral constructs were generated according to previously described techniques.[119, 120] In brief, to generate hybrid recombinant capsids for this study, fragments of capsid sequences of AAV8 and three newly identified recombinant serotypes were shuffled around by using known restriction sites. Resulting recombinant rAAV2/Rec vectors were assayed in a preliminary study by

During et al. in order to identify those with the greatest transduction efficiency for neuronal cells (unpublished). The serotypes, rAAV2/Rec2 and rAAV2/Rec3 were subsequently chosen for further experiments in the retina described herein.

The transgene cassette included GFP cloned into an AAV expression plasmid under the control of the CAG (hybrid CMV chicken b-actin) promoter and containing woodchuck hepatitis virus post-transcriptional regulatory element (WPRE), and bovine growth hormone (bGH) polyadenylation signal flanked by AAV2 ITRs. As control vectors, rAAV2/2 and rAAV2/5 expressed GFP under control of the same CAG promoter and included WPRE and bovine growth hormone polyadenylation signal as did the hybrid recombinant vectors.

7.2.2 Subretinal injection

Injections into the subretinal space were performed tangentially through the posterior sclera under the direct control of a surgical microscope with the tip of a 10-mm 34-gauge hypodermic needle (Hamilton RN needle (34/10/2) Pk6, product code 207434, Hamilton AG, Bonaduz, Switzerland) mounted on a 5 µl syringe (Hamilton 65 RN, Hamilton). The eye position was controlled and stabilized by holding the Musculus rectus superior or inferior with a toothed forceps when injecting into the superior or inferior quadrant, respectively. A circular cover glass (Ø6mm, VWR International, Lutterworth, UK) was applied onto the cornea with a carbomer coupling gel (Viscotears, Novartis, Frimley, UK) to ensure good visualization of the fundus. Retinal vessels overlying the beveled needle tip as well as control of the needles' reflectivity which increases in an intravitreal position helped to ensure correct placement in the subretinal space. The injected volume consisted of a 1µl solution and 0.5 µl air, and formation of a retinal bleb confirmed

subretinal delivery. 1 µl viral vector (1.0 x 10^{12} viral genoms/mL) was injected in each eye. The injection was performed rather rapidly in order to achieve a good separation of the neurosensory retina from the retinal pigment epithelium. The needle was left in position for additional 20-30 seconds and then withdrawn quickly to minimize reflux and to allow self-sealing of the scleral tunnel. The fundus was examined again to document the injection results on a worksheet which included information on the bleb size, any complications such as hemorrhage, the mouse number, date of birth, sex and amount of anesthesia. Besides a prominent retinal bleb, subretinal air was a sign for delivery into the subretinal space whereas air bubbles behind the lens (i.e. in the intravitreal space) were a sign for at least partial unintended intravitreal injection. Each animal received a different viral serotype in each eye, with different syringes and needles used for the different viruses. Between individual injections, the needle was flushed with sterile water.

7.2.3 Fundus *in vivo* imaging

Three weeks after intraocular injection, AF imaging was performed in anesthetized animals following the standard protocol developed before this study (see chapter 3.5). The protocol was modified in order to account for the much higher fluorescence signal due to expression of GFP. Images were recorded with a standardized detector sensitivity of 70 using the automated real time (ART) mode, without image normalization.

7.2.4 Immunohistology

Eyecups were cryosectioned into 16µm serial sections were affixed to poly-L-lysine coated glass slides (Polysine®; Thermo Scientific, Loughborough, UK). The sections were air-dried and then stored at -20°C until further histological

processing. After thawing, slides were dried at room temperature for about 30 minutes to ensure adhesion of the sections to the glass slide during the subsequent processing. If not stated otherwise, the following protocol for immunohistological staining was applied:

1. Wash slides 3x in 0.01M PBS on a shaker for 5 minutes
2. *Permeabilizion*: incubation in 0.4 % Triton X-100 (Sigma-Aldrich, Gillingham, UK) for 20 minutes
3. Wash slides 3x in 0.01M PBS on a shaker for 5 minutes
4. *Blocking* of unspecific binding: incubation of slides with normal goat serum (NGS; Invitrogen, Paisley, UK) block solution (10% NGS, 0.1% Triton X-100, 0.01M PBS, pH 7.2) to flat slides for 1 hour at room temperature
5. Wash slides 3x in 0.01M PBS on a shaker for 5 minutes
6. *Primary antibody* applied in 1% NGS, 0.1% Triton X-100, 0.01M PBS to flat slides and incubated for approximately 5 hours at 4°C.
7. Wash slides for 5mins 2x in a 0.05% solution of Tween-20 (VWR International, Lutterworth, UK) in PBS (0.01M PBS, pH 7.2) and 1x in 0.01M PBS
8. *Secondary antibody* applied in 1% NGS, 0.1% Triton X-100, 0.01M PBS to flat slides for 90-120 minutes at 4°C
9. Wash slides for 5 minutes 2x in a 0.05% solution of Tween-20 in PBS (0.01M PBS, pH 7.2) and 1x in 0.01M PBS
10. *Mounting* with an anti-fade reagent including DAPI as nuclear stain (ProLong®Gold+DAPI, Invitrogen, Paisley, UK)
11. Covering with a coverslip and sealed with nail vanish

As primary antibody for staining of cones, rabbit polyclonal anti-cone arrestin antibody (Millipore, Watford, UK; product code AB15282) was used at a dilution of 1:1000. Alexa Fluor 555 donkey anti-rabbit IgG (Invitrogen Ltd, Paisley, UK) was used as secondary antibody. For negative controls, the primary antibody was omitted.

7.2.5 Light microscopy

For the purpose of quantitative analysis of GFP expression, images were taken using the Leica DM IL inverted epifluorescence microscope. Images were obtained at x20 magnification using identical acquisition settings including exposure time, and were saved at a resolution of 1200 x 1600 pixels.

7.2.6 Image Analysis

Image analysis was performed on 8-bit images using ImageJ. Grey levels on cSLO images were measured within a circle of 300 pixel diameter. This area was placed within the region of vector delivery, avoiding the needle entry site where associated retinal damage often led to localized increased transduction.

Grey levels on histological fluorescence images were analyzed separately for the RPE, the photoreceptor layer, and the inner retina (including the outer plexiform layer and the inner nuclear layer). This allowed a quantitative analysis of GFP expression within individual retinal layers and thus to assess vector tropism. Retinal pigment epithelium (RPE) cells were always most efficiently transduced. Thus to ensure images were not overexposed, the exposure time for images analyzed for GFP fluorescence in the RPE was one quarter of that used for assessing transduction of neuronal cells. Regions of defined sizes (RPE: 20 x 200 pixels, outer nuclear layer: 50 x 250 pixels, inner retina: 100 x 250 pixels) were

analyzed within areas of highest GFP expression, and the mean grey level was calculated from a plot profile. In addition, the number of pixels above threshold was calculated from histogram analysis. The threshold was set conservatively using areas outside the injection site as reference.

7.2.7 Confocal microscopy

Retinal sections were viewed on a confocal microscope (LSM710; Zeiss, Jena, Germany). GFP-positive cells were located using epifluorescence illumination before taking a series of overlapping XY optical sections, of approximately 0.5 mm thickness. The fluorescence of DAPI, GFP and Alexa-555 were sequentially excited using 350 nm UV laser, 488 nm argon laser and the 543 nm HeNe laser, as appropriate. A stack was built to give an XY projection image as appropriate. Image processing was performed using Volocity (Perkin Elmer, Cambridge, UK) and Image J (Version 1.43, National Institute of Health, http://rsb.info.nih.gov/ij).

7.3 Results

7.3.1 *In vivo* measurement of fluorescence intensity

Three weeks after subretinal injection, GFP fluorescence was recorded within the area of subretinal vector injection using AF imaging. All vectors tested were capable of driving GFP expression in *Abca4*$^{-/-}$ mice and WT controls. GFP fluorescence did not extend noticeably outside the area of the bleb into which the vector was injected. However, clear differences in GFP fluorescence intensity were observed between mouse strains and rAAV serotypes (2-way ANOVA; $p<0.001$ for both strain and serotype; *Figure 7.1*). An interaction was detected

between strain and rAAV serotype (p=0.013), suggesting differing effects of the rAAV serotypes depending on retinal pathology.

Post hoc analysis showed that retinal GFP expression after viral transduction was lower in *Abca4*$^{-/-}$ mice than in WT controls (p<0.001). Furthermore, GFP fluorescence intensity was higher with the use of rAAV2/2 than with rAAV2/Rec2 and rAAV2/Rec3 (p<0.001 for both comparisons). Fluorescence was higher with rAAV2/5 than rAAV2/Rec3 (p=0.04) and showed a trend of superiority over AAV2/Rec2 (p=0.07). GFP fluorescence intensities after transduction with rAAV2/2 and rAAV2/5 were similar, as was the case when comparing rAAV2/Rec2 and rAAV2/Rec3.

7.3.2 Tropism of rAAV2/Rec2 and rAAV2/Rec3 in *Abca4*$^{-/-}$ and WT mice

Histology was analyzed to assess retinal cell tropism of the different rAAV serotypes. Retinal cell types were identified using immunocytochemistry and by morphology.

Following subretinal injection in WT mice, RPE cells were transduced by all serotypes tested (*Figure 7.2*). Photoreceptors were also transduced by all serotypes but GFP fluorescence intensity in this layer was higher using rAAV2/2 and rAAV2/5 than with rAAV2/Rec2 and rAAV2/Rec3. Sparse Müller cell transduction was seen with rAAV2/5 and rAAV2/Rec2, however good Müller transduction was noted with rAAV2/2 (*Table 7.1* and *Figure 7.2*).

The cell types transduced by all rAAV serotypes in *Abca4*$^{-/-}$ mice were similar to those in wild type mice, but transduction was generally less effective in this model (*Figure 7.3*).

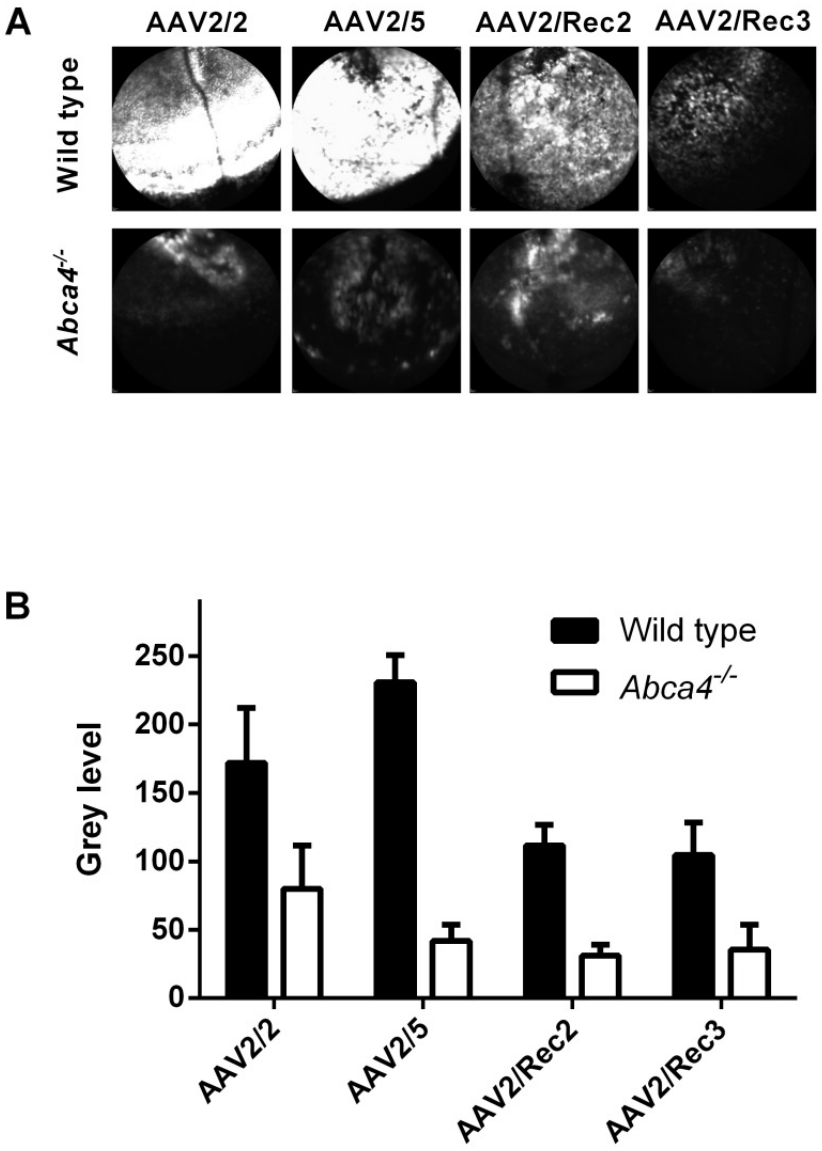

Figure 7.1: Analysis of in vivo measurement of fluorescence intensity 3 weeks after subretinal injection of different hybrid recombinant AAV serotypes expressing green fluorescent protein (mean±SEM). Besides wild type (WT) mice, a strain with strong lipofuscin accumulation in the retinal pigment epithelium (Abca4$^{-/-}$ mouse) was used. 4 to 8 eyes were analysed per group. (b) Representative topographical confocal scanning laser ophthalmoscopy (cSLO) 488 nmfluorescence images showing the range of fluorescence intensities that was found in the different groups.

	RPE cells	Photoreceptors	Müller cells
Wild type C57/BL6			
AAV2/2	++	++	+++
AAV2/5	+++	+++	+
AAV2/Rec2	++	++	+/-
AAV2/Rec3	++	+	+/-
Abca4$^{-/-}$			
AAV2/2	++	+	++
AAV2/5	+	+	+/-
AAV2/Rec2	+	+	+/-
AAV2/Rec3	+/-	+/-	+/-

Table 7.1: Summary of transduction efficiency in various mouse models (subretinal delivery) and ex-vivo primate retina of the tested recombinant AAV vectors rAAV2/Rec2 and rAAV2/Rec3 in comparison to rAAV2/2 and rAAV2/5.

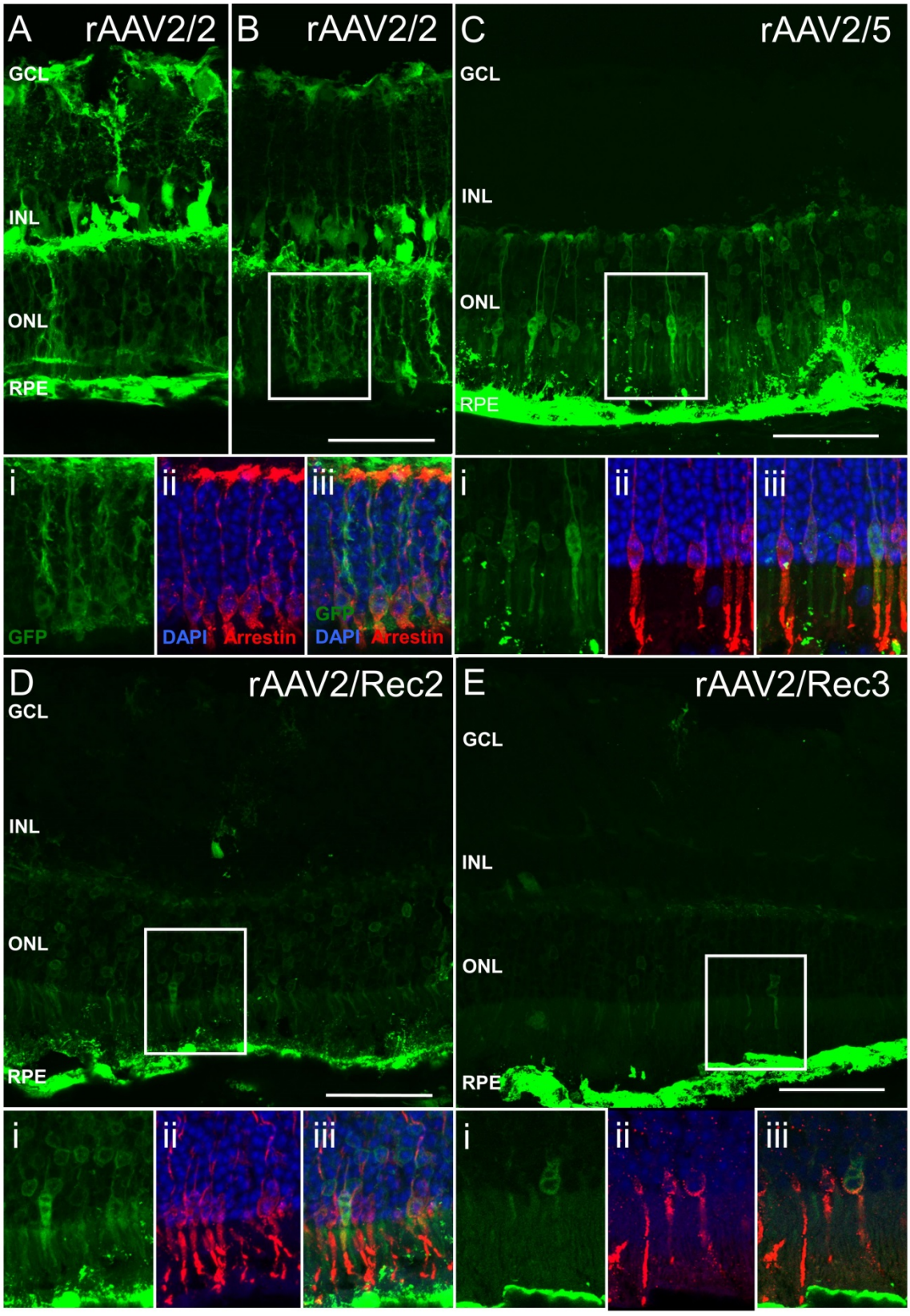
A rAAV2/2
B rAAV2/2
C rAAV2/5
GCL
INL
ONL
RPE
i
ii
iii
GFP
DAPI Arrestin
D rAAV2/Rec2
E rAAV2/Rec3

Figure 7.2 (previous page): Green fluorescent protein (GFP) fluorescence patterns of different recombinant AAV serotypes in wild type C57BL/6 mice following subretinal injection. The main images A–E are confocal stacks illustrating overall GFP expression patterns. Figure A illustrates transduction of the retinal pigment epithelium with rAAV2/2, whereas figure B demonstrates cone transduction. The boxed regions in images B–E are enlarged and shown as confocal slices in panels i-iii below for each serotype. GFP signal (green) and nuclear labeling with DAPI (blue) overlaid with immunostaining using cone arrestin (red) illustrate cone transduction using the different recombinant AAV serotypes. GCL = ganglion cell layer, INL = inner nuclear layer, ONL = outer nuclear layer, RPE = retinal pigment epithelium. Scale bar 50 mm.

7.3.3 Histological analysis of fluorescence intensity

In vivo fluorescence intensity measurements using topographic cSLO images reflect the combined fluorescence intensity at each location arising from all retinal layers. In order to quantify the transduction efficiency within retinal layers, fluorescence intensity was measured *post-mortem* on fixed histological sections (*Figure 7.3*) of eyes with subretinal vector delivery. The level of transgene (GFP) expression within the retinal pigment epithelium (RPE) layer, photoreceptor layer, and inner retina (including the outer plexiform layer and inner nuclear layer) was quantified by grey level analysis separately in each layer. In addition, the percentage of pixels above threshold was calculated from histogram analysis, to estimate the efficiency of viral transduction.

There were significant differences in GFP fluorescence intensity between mouse strains and rAAV serotypes on histological analysis, correlating with the cSLO *in vivo* data. Grey level analysis for the RPE layer (Figure 4A) again revealed an overall effect of viral capsid serotype on the resultant GFP fluorescence ($p<0.001$). Post hoc analysis showed that greater RPE fluorescence was achieved with rAAV2/5 than with rAAV2/Rec2 ($p=0.02$) and rAAV2/Rec3 ($p<0.001$). RPE fluorescence was more intense with rAAV2/2 than with rAAV2/Rec3 ($p<0.001$) and showed a trend of superiority compared to rAAV2/Rec2 ($p=0.06$). There was no significant difference in RPE fluorescence intensity when comparing rAAV2/Rec2 and rAAV2/Rec3. Fluorescence levels in *Abca4*$^{-/-}$ were significantly lower than in WT ($p<0.001$).

Analysing the fraction of pixels above threshold demonstrated that among the retinal laminae analyzed, the RPE layer was the most efficiently transduced (Figure 4D). rAAV2/2 and rAAV2/5 were each more effective at RPE transduction than either of the hybrid recombinant serotypes (Figure 3D). An interaction between strain and rAAV serotype ($p<0.001$) was seen due to the lower efficiency of rAAV2/Rec2 and rAAV2/Rec3 in transducing RPE cells in *Abca4*$^{-/-}$ mice (Figure 4D).

Analysis of transduction in the outer nuclear layer (ONL; Figure 4B,E) revealed significant differences in ONL transduction between strains and rAAV serotypes (2-way ANOVA; both, $p<0.01$). The ONL of *Abca4*$^{-/-}$ mice revealed a lower grey level ($p<0.01$; Figure 4B) a lower percentage of pixels above threshold intensity ($p<0.001$; Figure 4E) than in WT for all vectors. Comparing ONL grey level when using different vectors, rAAV2/2 was more effective than both rAAV2/Rec2

(p=0.01) and rAAV2/Rec3 (p<0.01; Figure 4B). This could be due to the high proportion of Müller cells transduced with rAAV2/2, whose processes traverse the ONL. The percentage of ONL pixels above threshold was significantly lower when using rAAV2/Rec3 than rAAV2/2 (p<0.01) and a trend of lower efficiency than rAAV2/5 (p=0.06), suggesting lower transduction efficiency of rAAV2/Rec3 in photoreceptors.

Analysing the effects of subretinal vector delivery within the inner retina (including the inner nuclear and inner plexiform layers), the grey level was significantly higher when using rAAV2/2 compared to all other viruses tested (all, p<0.001; Figure 4C,F). A significant difference was detected in the grey level of wild type mice in comparison with *Abca4*$^{-/-}$ mice (p<0.05).

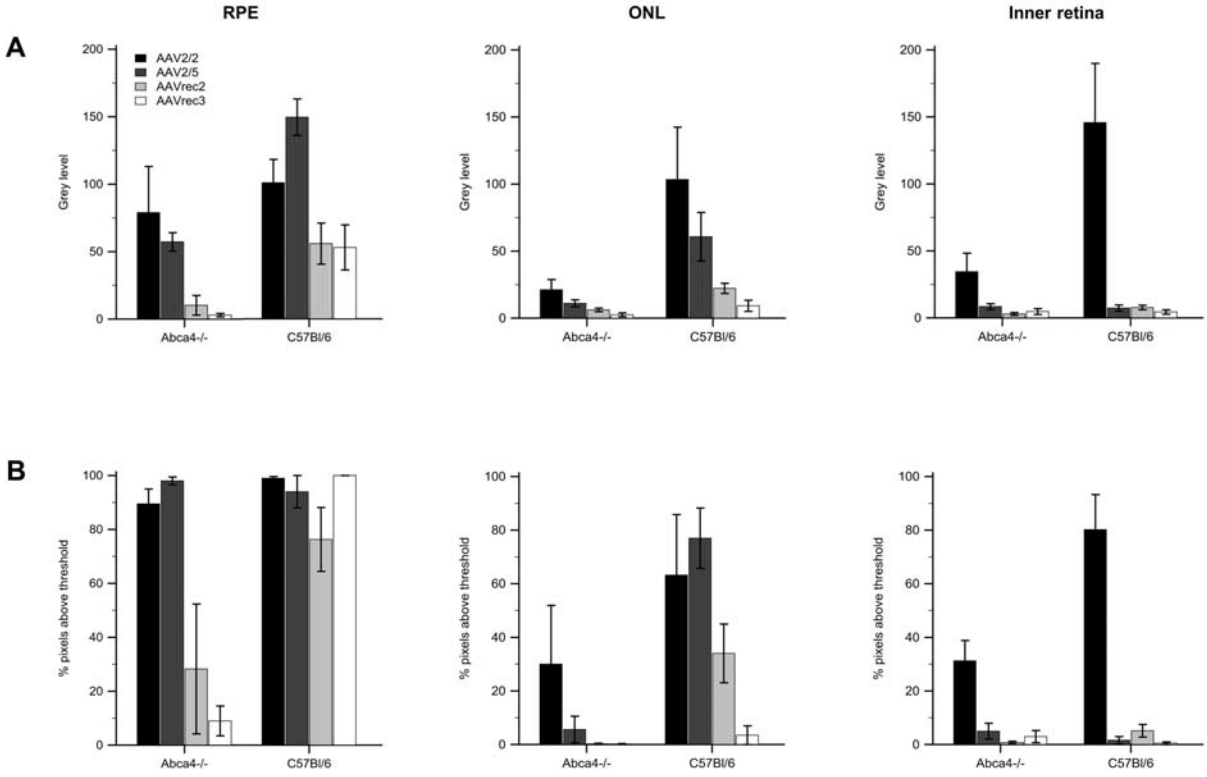

Figure 7.3: Quantitative analysis of green fluorescent protein (GFP) fluorescence intensity on histological sections in eyes that underwent subretinal injection of different recombinant AAV serotypes expressing GFP (mean±SEM). The mouse model for Stargardt disease is compared with wild type (WT) mice. Grey level analysis (upper row) represented an estimate for the level of transgene expression within transduced cells, whereas the percentage (%) of pixels above threshold (bottom row) represented an estimate of viral efficacy for cell transduction. 4 to 8 eyes were analysed per group. ONL = outer nuclear layer, RPE = retinal pigment epithelium.

7.4 Discussion

The retinal tropism and transduction efficiency of four recombinant AAV vectors was tested: two standard serotypes (rAAV2/2 and rAAV2/5) and two with novel hybrid recombinant capsids (rAAV2/Rec2 and rAAV2/Rec3). The data shows that it is possible to interchange viral capsid protein sequences between different AAV serotypes and that this still results in retinal transduction, albeit at a reduced efficiency compared to vectors pseudotyped with wildtype capsids. Although this pilot study did not show an increase in transduction efficiency or significant change in tropism with the hybrid recombinant vectors, it suggests that this approach in creating hybrid capsids may be a useful tool in generating any number of AAV capsid sequences in order to identify those with the greatest impact on transduction and cellular tropism.

In addition, shuffling specific capsid sequences may be of use in minimizing immune responses to AAV gene therapy. Previous studies have shown that high dose rAAV2/2 administration into the subretinal space in mice leads to production of neutralising antibodies to AAV, which may affect efficacy of treatment to the second eye [121]. In systemic gene therapy using rAAV2 for the treatment of haemophilia B, it has been postulated that the loss of factor IX transgene expression is due to proteasome-mediated cleaving of the AAV capsid, and presentation of capsid peptide sequences via the major histocompatibility complex. This would lead to recognition of transduced cells by CD8+ T cells, and their subsequent destruction [122]. In both cases, the ability to substitute specific capsid antigen sequences, by the technique of capsid shuffling, may be of use in avoiding the immune response to rAAV.

Several variations in AAV genome sequences have been isolated from a variety of body tissues, including the gut, lung and brain [119]. One principal drawback of our study is that the novel capsid sequences were identified in primate brain and not in the retina. This may be an unfavourable strategy to select the most efficient vectors for retinal gene therapy. Thus, in future it might therefore be prudent for retinal gene therapy to attempt isolation by PCR of AAV genome particles directly from primate retina.

Recent work has shown that modification of tyrosine residues can be exploited to significantly enhance AAV transduction in the retina [123]. In our study none of the recombined capsids included serotypes with modification of tyrosine residues, and the number of exposed surface tyrosine residues on rAAV2/Rec2 and Rec3 capsids is comparable to that of rAAV2/8. Hence, it is unlikely that the reduced transduction is due to increased ubiquitin-tagged proteasome-mediated degradation [124], as one might observe if greater numbers of tyrosine residues were present on the hybrid capsid.

Both rAAV2/Rec2 and rAAV2/Rec3 vectors use the C terminus of the VP3 region of rAAV2/8 which includes the HI loop, a critical sequence for genome packaging and capsid assembly [125]. Hence this region at least can be excluded as a cause for the reduced transduction seen.

It was also noted that the transduction of RPE cells and photoreceptors in the *Abca4*$^{-/-}$ mouse appears to be significantly lower with all viral serotypes assessed in this study. If this is also true of the human condition then it would also present a relative impediment in using AAV to treat Stargardt disease. Since the *ABCA4* transgene (at 6.7kb) is too large to be packaged into a single AAV vector capsid,

one current approach is to use two AAV genomes which can then recombine to form the full-length *ABCA4* transgene after cell entry [38, 57]. In order to achieve this it is likely that much higher levels of transduction will be necessary to compensate for a relatively low rate of transgene recombination. It is not entirely clear why *Abca4*$^{-/-}$ mice have reduced transduction with AAV. One explanation might be the different background strain (129S4v/SvJae) compared to the wild type control mice (C57/BL/6). Alternatively it is possible that loss of the transmembrane ABCA4 protein or the increased levels of phosphatidylethanolamine [34] reduce AAV entry into the photoreceptor cell. This explanation may also account for the poor RPE transduction observed, as the number of AAV particles entering RPE cells through phagocytosed outer segment discs would be low if the latter contained low amounts of AAV. It is also possible that the strong accumulation of lipofuscin, which mainly consists of visual cycle byproducts such as A2E and other bisretinoids, might somehow impair the transduction efficiency of AAV. Further studies will be required to address this question.

In summary the concept of pseudotyping viruses to alter retinal cell tropism by mixing capsid proteins was explored. Although the herein tested viruses may not be recommended for further studies due to their lower efficiency compared to established pseudotypes, the methodological approach might be used to identify hybrid rAAV vectors with specific retinal cell tropisms or increased efficiency in certain disease states.

8 General discussion

Stargardt disease due mutations in the *Abca4* gene is amongst the most common causes for severe vision loss in young visually disabled patients. With an estimated prevalence of 1:10,000 there would be approximately 75,000 Stargardt patients in Europe. This number, however, might even be higher considering that Stargardt disease may mimic certain forms of AMD,[2, 3] which is the overall most common cause for legal blindness in western countries. Currently, there is no cure and no therapy with proven benefit for patients with Stargardt disease and other retinal diseases associated with mutations in the *Abca4* gene.

Against this background, there is a strong need for identifying and evaluating novel therapies for Stargardt disease. Two key requirements for any given novel therapy are its safety and efficacy. Before those requirements can be addressed in clinical phase 1 and phase 2 studies, data from animal studies is needed to support a potential benefit for patients. Toxicity of novel drug compounds may certainly largely be tested in WT animals. However, efficacy needs to be tested in animal models mimicking the human disease. In the case of Stargardt disease, the only currently available animal is the *Abca4*$^{-/-}$ mouse.

For evaluating efficacy of a given therapy in the *Abca4*$^{-/-}$ mouse, detailed knowledge of its phenotype is necessary in order to define meaningful outcome measures in preclinical studies. Therefore, an in-depth phenotyping of the *Abca4*$^{-/-}$ mouse was intended. This subsequently allowed evaluating a novel pharmacotherapy in this mouse model using fundus AF imaging as a clinically meaningful outcome parameter. In addition, a novel gene therapy approach as

potentially causative treatment for the genetically driven disease process was investigated in the same mouse model.

8.1 Fundus autofluorescence imaging in mice

Histological analysis of tissue specimens obtained after sacrifice was once the only means by which to investigate retinal structure in animal models. Recently developed retinal imaging modalities, such as cSLO [73, 74] and optical coherence tomography,[76] may now be used for high-resolution *in vivo* assessment of retinal structure in small animals. Repeated *in vivo* assessments may be performed longitudinally in the same animal, reducing variability and, potentially, the number of animals required in some experiments.

Progressive changes on fundus AF imaging are observed in a large number of human retinal diseases, including AMD and most inherited retinal dystrophies, and such changes have been suggested as markers for disease progression. The use of the same in vivo imaging technique to assess animal models may allow investigation of the cellular and biochemical alterations underlying changes visible on fundus AF imaging, and may thus further the understanding of fundus AF in human retinal disease. Because Stargardt patients show pronounced alterations on fundus AF imaging, we hypothesized that fundus AF imaging in the *Abca4*$^{-/-}$ mouse might reveal similar alterations. However, although fundus AF imaging has been used in humans for over a decade in clinical routine, its use in mice had not been investigated systematically. Because of this lack of experience with the application of this imaging modality in mice, the first step was to optimize fundus

AF imaging for the mouse eye using the same cSLO-based fundus camera system which is amongst the devices most frequently used in clinical routine.

Controlling a large number of factors affecting fundus AF recordings in mice, it became possible to obtain reliable mouse fundus AF recordings that allowed a qualitative and quantitative image analysis. The feasability of such image analysis turned out to be useful not only for assessing lipofuscin accumulation in the *Abca4*$^{-/-}$ mouse, but also to assess effectiveness of therapeutic strategies making use of GFP as a reporter protein. GFP expression can be recorded because the commercially available cSLOs use excitation light and detect emitted light closely matching the characteristics for GFP. Consequently, application of fundus AF detection in mice include the assessment of a neuroprotective therapy in transgenic reporter mice that have fluorescent cones,[126] the evaluation of delivery and survival of transplanted GFP-positive photoreceptor precursors cells,[127] or the investigation of various viral vectors for effective gene delivery to the retina using GFP as reporter protein.[128]

Usefulness of this technique goes beyond the application in retinal research. The retina is a part of the central nervous system (CNS) where clear media allow direct visualization of CNS neurons in vivo. For instance, in vivo detection of the autofluorescent fibrillar tau protein was shown to be possible in the retina of a mouse model for Alzheimer disease, suggesting that this technique may suitable for longitudinally monitoring treatment effects in preclinical studies.[129] We investigated several transgenic mouse lines that express the reporter protein GFP under the control of different cell-specific promoters of the CNS (unpublished). Most studied mouse models revealed fluorescence of subpopulations of retinal

neurons, suggesting that specific neuronal populations could be followed longitudinally using fundus AF imaging. Importantly, GFP positive neurons frequently showed spacing large enough to count individual cells, allowing straight forward quantitative analysis. Moreover, fluorescent cells could be discerned as being located to the inner or outer retina due to the confocality of the system.

When comparing the performance of fundus AF imaging in mice with that in humans, it is clear that the image quality of the human eye is superior. There are several possible explanations for this circumstance: 1) The cSLO used is manufactured specifically for imaging the human eye and therefore is optimized for its anatomy, and 2) the mouse eye has several disadvantages including the small size with the small pupil aperture, a multifocal lens, and a high confocality.

Sparrow et al. have used a modified cSLO to overcome some of those challenges when imaging the mouse eye. They fitted the cSLO with a smaller pinhole limiting the diameter of the incident laser beam (normally 1.7 mm) and the detection pupil (normally 3.4 mm) to 0.98 mm. This should ensure equal amounts of light entering the small mouse eye across different animals and age groups, but is also associated with a decreased AF signal at the same laser power setting. Moreover, the reduced pinhole size should improve the validity of absolute AF measures because of signal intensity measures become more independent of pupil size. However, the reduced size of the pinhole would not correct for other age-dependent changes that might also modify fundus AF measures, such as eye size, lens absorption characteristics, or increasing contribution of other fluorophores.

In the work presented in this thesis it was not the aim to provide absolute quantitative AF measures that are comparable across different age groups. The focus was on investigating differences between strains within the same age group. Comparison with age-matched controls also corrected for age-dependent parameters potentially modifying AF measures that are not corrected for by using a smaller pinhole size.

Variability between measurements could be minimized by using an internal reference as described recently in a human study.[77] It would account for short-term (warm-up) and long-term changes in laser power, detector sensitivity fluctuations, and would provide a check for the consistent functioning of the camera resulting in improved reliability of fundus AF intensity measures. An internal reference would also permit the expression of fundus AF measurements in a format that can be compared with studies obtained with different cameras. However, the test-retest variability was only slightly better in the study by Sparrow *et al*. (coefficient of repeatability ±18.6% versus ±22% reported herein; 95% confidence interval). This suggests that other parameters influence quantitative AF measures in mice considerably more than in humans (coefficient of repeatability ±6%),[77] where fluctuations of laser power and detector sensitivity contribute noise of similar magnitude. These parameters may include the variation of fundus AF measurements between operators or suboptimal standardization of the recording procedure (e.g. differences in pupil dilation, camera alignment, control of media opacity). Thus, an internal reference would increase confidence in the functioning of the setup, but variability is likely to remain higher than in humans. In case laser power and detector sensitivity undergo long term changes such as a drop in laser

power, a reference fluorophore for mouse fundus AF imaging might be meaningful for longitudinal measures, provided changes of the reference are less than the combined fluctuations of laser power and detector sensitivity.

8.2 The phenotype of the *Abca4*$^{-/-}$ mouse

The *Abca4*$^{-/-}$ mouse model for Stargardt disease has been generated by insertional mutagenesis and has no residual expression of Abca4.[34] It therefore mimics bi-allelic loss of function in patients with retinopathies caused by mutations in *ABCA4*.

Mouse models are increasingly generated to study the pathophysiology of human retinal disease and are used to evaluate novel therapies. Therefore, thorough assessment of the rodent retinal morphology and function has become increasingly important in basic and preclinical research, and furthers the understanding of human retinal disease. There are, however, a number of prerequisites for determining efficiency in the preclinical evaluation of novel therapeutic approaches:

1. Any given disease model needs a phenotype, related to the human disease, which distinguishes it from WT animals.
2. The phenotypic difference should be of a relevant magnitude, robust throughout individual animals, consistent across independent studies, and quantifiable.
3. The phenotype should occur early in life in order to keep interventional studies within reasonable time frames

4. In the ideal scenario – the phenotype would be assessable in vivo so that a similar outcome measure could be used in subsequent clinical trials.

With regards to the *Abca4*$^{-/-}$ mouse model for Stargardt disease, no phenotype had been described that would fulfill those requirements.

8.2.1 The functional phenotype of the *Abca4*$^{-/-}$ mouse

Weng et al. had reported a decreasing retinal function with age.[34] However, we could not detect any relevant difference in scotopic and photopic retinal function up to an age of 18 months. Although retinal function was significantly reduced in the oldest age group, the magnitude of this impairment was marginal and would therefore not be a meaningful outcome measure. Using such a parameter, the power to detect relevant treatment effects in standard experiments would be very low. In other words, any given therapy would have to have very large effects and would have to be evaluated in a very large number of animals. *Abca4*$^{-/-}$ mice on an albino BALB/c background have consistently been reported to develop a more pronounced photoreceptor degeneration early in life compared to WT controls as surrogate marker for decreasing retinal function.[103] Photoreceptor degeneration in *Abca4*$^{-/-}$ albino mice might occur due to high levels of all-*trans* retinal which has been implicated in photoreceptor cell death. Formation of all-*trans* retinal is increased due to the higher light levels in the albino eye,[112] and its clearance is reduced due to defective ABCA4 function.[34] Because the pathophysiology of the retinal phenotype in *Abca4*$^{-/-}$ albino mice might involve additional pathophysiological pathways beyond dysfunction of Abca4, this model appears to be less relevant for extrapolating treatment effects for future clinical trials.

A second suggested functional phenotype of the *Abca4*$^{-/-}$ mouse is a delayed dark adaptation. However, as pointed out in chapter 5, protocols, background strains, assessed parameters and analysis to describe the dark adaptation characteristics in *Abca4*$^{-/-}$ mice varies considerably throughout the literature. Thus, it is not surprising that this functional phenotype has not consistently been identified. Although the assessment presented in chapter 5 would not rule out a mildly altered dark adaptation, such phenotype would not be robust enough for detecting treatment effects in preclinical studies. Moreover, it as yet remains unclear if delayed dark adaptation observed in Stargardt patients is primarily due to dysfunctional ABCA4 or occurs secondarily to progressive retinal degeneration.[99, 108]

8.2.2 The phenotype of the *Abca4*$^{-/-}$ mouse on fundus autofluorescence imaging

As shown in chapter 4, the phenotype of the *Abca4*$^{-/-}$ mouse on fundus AF imaging largely reflects the phenotype of patients with Stargardt disease, including an increased intensity of lipofuscin-related fundus AF and the development of hypo- and hyperfluorescent spots. Such a finding was hypothesized beforehand due to the known postmortem findings, such as increased levels of A2E and lipofuscin in the RPE of *Abca4*$^{-/-}$ mice. Notably, the magnitude of the difference in AF intensity was such that already at the age of approximately 2 months, no measurement in *Abca4*$^{-/-}$ mice was within the 95% confidence interval of WT controls, and this quantifiable difference was validated in independent experiments. Therefore, fundus AF intensity appeared to be an ideal parameter for assessing treatment effects in this animal model. Hypo- and hyperfluorescent

spots would be less suited because they occurred only later in life and are less well quantifiable.

Although less convenient as an outcome measure due to the later occurrence of a significant difference compared to WT animals, there was also an increase in melanin-related fundus AF intensity in *Abca4*$^{-/-}$ mice. The significance of this finding as yet needs to be explored, especially because equivalent changes also appear to occur in Stargardt patients, however, with only little data currently available from human studies.[10, 71] Oxidative changes of melanin and formation of melanolipofuscin-granules might be involved in the development of increased melanin-related AF. Due to antioxidant properties of melanin, those changes might precede RPE cell death with subsequent loss of retinal function. Future animal studies might explore the role of melanin in more detail, for instance by back-crossing the *Abca4*$^{-/-}$ mouse on background strains with different defects in melanin synthesis.

8.2.3 Comparison of the mouse phenotype with human disease

Cideciyan et al. have proposed 6 stages of the human disease sequence, where stage 1 is characterized by a normal retinal structure and function, and stage 6 by complete degeneration of photoreceptors and RPE cells with loss of function.[99] First detectable changes were described to occur on fundus AF imaging as an increase in intensity (stage 2) and texture (the spatial variation of fundus AF intensity; stage 3). Functional decline as surrogate for partial photoreceptor degeneration defines stage 4. Notably, slowing of the retinoid cycle (i.e. a prolonged dark adaptation) was not present beforehand, which is different to the somewhat inconsistent observations in the *Abca4*$^{-/-}$ mouse. In stage 5, functional

deficits increase, together with a decline in mean AF intensity.[99] Two studies have reported that loss of 790 nm AF precedes loss of 480 nm AF,[12, 71] and a model was suggested with decreasing 790 nm AF preceding similar changes on 488 nm AF imaging.

The *Abca4*$^{-/-}$ mouse model assessed herein mainly reflects the early stages of this proposed human disease sequence and may aid in adjusting suggested diseases models. There is an early diffuse increase in 488 nm fundus AF intensity due to lipofuscin accumulation, followed by an increase in texture, i.e. spatial variation of fundus AF and occurrence of fleck-like lesions. The mouse model suggests that preceding functional decline (as observed in 18 months old *Abca4*$^{-/-}$ mice, equivalent to the human disease stage 4) 790 nm fundus AF increases, most likely due to formation of melanolipofuscin. Higher long-wavelength AF intensity has been observed in humans irrespective of marked textural changes,[10] however, this phenotypic feature had not been placed into the context of the disease sequence. A fleck-like increase and subsequent decrease of 790 nm AF may precede similar changes on 488 nm AF, and functional decline ensues.

Progressive loss of cones starting in stage 2 has been shown by adaptive optics SLO imaging in the posterior fundus of patients with Stargardt disease,[130] and spectral domain OCT imaging has suggested that foveal photoreceptor damage may occur before occurrence of characteristic AF patterns.[131] In the *Abca4*$^{-/-}$ mouse, functional testing using ERG and histological analysis does not suggest significant photoreceptor loss at a similar disease stage. This discrepancy may be explained by the different anatomy of the human macula and the low number of cones in the mouse retina. The human macula with its particular

anatomy and physiology appears most vulnerable for the development of functionally relevant retinal atrophy in ABCA4-related retinal disease. The mouse model, however, might rather mimic the disease course in more peripheral human retina. Also, various human mutations have different effects on disease manifestation and progression,[115] and this may differ from the null-background in the *Abca4*$^{-/-}$ mouse.

Stargardt patients have been observed to have fundus AF intensity (excitation: 510 nm; emission: 620 nm) above the age-matched 99.99% confidence interval of normal control subjects.[11] As in our study, there appeared to be a trend that the increase of fundus AF in Stargardt patients is more pronounced at younger age,[11, 132] possibly with a ceiling effect later in life, while there appears to be a quasi linear increase with age in normals. The observed ~2-fold increase of AF intensity compared to wild type mice is in line with the data by Delori et al. in Stargardt patients. Normal or decreased fundus AF levels in patients with Stargardt diseases as reported by Lois et al. [133] might be due to assessment at various disease stages (see above), or may be explained by different mutational effects, gene-gene interactions, environmental modifiers and genetic heterogeneity.

8.3 Assessment of novel therapies for Stargardt disease

8.3.1 Pharmacotherapy using C20-deuterized Vitamin A

Dietary substitution of vitamin A by C20dVitA resulted in marked reduction of A2E accumulation and fundus AF intensity as a surrogate measure for lipofuscin deposition. Similar effects on A2E accumulation in the *Abca4*$^{-/-}$ mouse had been

reported after treatment with drugs reducing the availability of vitamin A to the RPE or inhibiting the visual cycle. Those approaches, however, have in common that they retard photopigment formation and thus reduce retinal function and dark adaptation kinetics. This is particularly disadvantageous in patients with a central scotoma due to their retinal disease in which pharmacotherapy diminishes peripheral retinal function in addition. In the *Abca4*$^{-/-}$ mouse model for Stargardt disease, retinal function was not compromised after 9 months supplementation with C20dVitA. Although there is no rationale for assuming that dark adaptation kinetics would be affected by C20dVitA, this was not formally investigated.

A human trial is currently being designed in order to test safety and efficacy of C20dVitA in Stargardt patients. It is likely that C20dVitA will be administered at a dose that exceeds the daily intake of vitamin A by about 10 to 20-fold. This would mean that 90-95% of all retinal in the visual cycle would eventually be replaced by C20dVitA. Mihai et al. recently addressed a theoretical concern if C20dVitA would replace retinal vitamin A stores of the RPE/retina within a reasonable time frame. Although there are relatively large amounts of vitamin A stored in the liver and the RPE, there appears to be a rapid assimilation within one month of the retinal C20dVitA concentration to C20dVitA blood levels, at least in a swine model.[134]

During the first clinical trials, it will be of uttermost importance to perform an extensive safety monitoring that also includes organs other than the eye and physiological functions which are dependent on or may be affected by the (dys-) function of vitamin A. Examples are gene transcription, skin health, fertility, hepatic function, or neurological symptoms ranging from irritability and reduced appetite to headaches and pain perceptions. Such monitoring will be particularly important because treatment might be best effective when started early in life and would

possibly have to be applied life-long, thus exposing the patient to considerable doses of the drug. Due to a known teratogenic effect of vitamin A, pregnant women will have to refrain from high doses of C20dVitA.

8.3.2 Gene therapy in the *Abca4*$^{-/-}$ mouse model for Stargardt disease

The monogenic recessive nature and chronicity of Stargardt disease makes it ideally suitable for gene replacement as a causal therapeutic concept to slow down or possibly even stop the disease process. The challenges, as outlined in section 1.3.4, include the size of the *Abca4*$^{-/-}$ gene and the necessity to transduce photoreceptors.

The two key requirements for any gene therapy approach are a safe and effective delivery of the therapeutic gene with its associated regulatory elements into the cell nucleus and the subsequent adequate and continuous expression of the gene product. AAV is the viral vector with most data with regard to safety in human trials and is capable of transducing photoreceptors. However, its packaging capability is limited and larger gene can only be transferred through packaging up to 5.1 kb transgene DNA as terminally truncated plus and minus strands into separate virions. The required re-annealing of the truncated genomes of opposite polarity after transduction decreases efficiency of the large gene transfer, thus necessitating even higher transduction efficiency.

The two viral constructs with novel hybrid recombinant capsids investigated were not more efficient than conventional viruses used in preclinical studies for retinal gene therapy. The arguably most interesting result from this study was the reduced efficiency in the *Abca4*$^{-/-}$ mouse compared to wild types, a comparison not previously reported. Assuming similar effects in Stargardt patients, this finding

would even increase further the required efficiency of the viral vectors for *ABCA4* gene delivery. Thus, further optimization steps might be necessary, such as the use of tyrosin-mutant AAV capsids which prevents ubiquitination and subsequent proteolysis of the capsid in the host cell, resulting in increased efficiency to transduce retinal cells including photoreceptors.[123]

An alternative approach for delivering large gene constructs would be the use of different viruses with a larger packaging capacity. During their evolution, a number of viruses have optimized strategies to transduce non-dividing neuronal cells, including some lentiviruses which have a larger packaging capacity. However, those viruses impose a higher risk for genomic insertional mutagenesis and the presence of a cell membrane envelope is likely to contribute to immune responses. Moreover, there is little evidence that currently available lentiviral constructs would efficiently transduce photoreceptors.[135] A commercial clinical trial using a lentiviral vector had been started in 2012 (clinical trials identifier: NCT01367444). However, published preclinical evidence for efficiency of this vector is low.[39]

Non-viral gene therapy also has been envisaged as an alternative for delivering large genes to retinal cells. However, those efforts have as yet been unconvincing.[55] For non-viral gene therapy approaches, nuclear localization and stable long-term transgene expression currently remain significant hurdles that need to be overcome.[136] A DNA plasmid has no vehicle to overcome the natural cellular barriers to viral infection and is itself exposed to intracellular nucleases which would result in rapid degradation of naked DNA. Barriers that need to be overcome before gene delivery results in protein expression include escape from extracellular DNA degradation and immune response, efficient cell entry of

plasmid DNA, its escape from the liposome or endosome, subsequent resistance from cytoplasmic degradative enzymes and passage through the nuclear envelope which is not possible during cell division in postmitotic retinal cells.[55] Agents or procedures used to assist and facilitate gene delivery to retinal cells must not be toxic for retinal structures. An additional fundamental problem remains even if the DNA was successfully delivered to the nucleus. Ideally, the gene would persist in the nucleus and continuously express the protein. However, DNA in postmitotic cells which is not integrated into the cell genome is usually silenced and degraded. Therefore, DNA delivery has to be complemented with methods that aid its passage through the cell membrane and ideally also help to overcome further barriers and silencing. Such methods have been developed in vitro and in vivo, and many including electroporation,[137-139] iontophoresis,[140-142] liposomes,[138] polymers [143] and compacted nanoparticles [114, 144-146] have also been tried to deliver DNA to the outer retina. In summary, despite many potential advantages of non-viral retinal gene therapy, success has been limited to date. It remains difficult to target photoreceptor cells and to achieve high and persistent transgene expression without causing harm to the sensitive neuronal tissue by using physical or chemical transfections methods.

8.4 The therapeutic window

It remains noteworthy that the marked accumulation of A2E and lipofuscin in the *Abca4*$^{-/-}$ mouse within the first three months of age remains without relevant functional impact for at least another 9 months. Assuming similar processes in the human eye, this opens a window for interventions between the accumulation of

lipofuscin and photoreceptor death. Lipofuscin accumulation may be detected by clinical examination or with higher sensitivity using fundus AF imaging. The presence of disease in those at risk, e.g. siblings of patients affected by Stargardt disease with the same genotype in *ABCA4*, may now even be detected earlier before occurrence of first symptoms. This has become possible through predictive genetic testing, and possibly, quantitative AF which has recently been developed for clinical use may allow a similar early diagnosis. This would allow starting non-invasive therapy such as supplementation with C20dVitA early on. Notably, in such disease stages which have no retinal atrophy and no functional decline, quantitative AF measures might be used for evaluating therapeutic effectiveness, and the ability of this technique to detect and measure treatment effects has been shown in chapter 6. If disease nevertheless progresses to be functionally relevant, gene therapy could be an alternative as a more invasive escalation.

Alterations in the melanin compartment might play a role for defining the optimal time point for interventions. For instance, cell damage might approach a “point of no return” once certain anti-oxidative mechanisms such as those fulfilled by melanin become increasingly compromised. The fate of cell death would then be predetermined, independent of therapeutic intervention. Therefore, melanin-related AF measures need to be included in future clinical trials in order to determine if such associations exist.

8.5 Comment on masked assessment in preclinical studies

Novel rational and promising treatment approaches are usually tested in animal models for a human disease to assess their safety and effectiveness before the therapy is tested in human clinical trials. Therefore, such preclinical studies are important to limit clinical trials to a minimum of the most promising treatments to reduce patient burden and to safe costs. However, only about 5-10% of drugs tested in clinical trials prove to be successful.[147] Possible explanations are manifold: Besides limitations such as species differences in effectiveness, or unforeseen side effects in humans, there is considerable concern that preclinical studies are not performed to the high standards applied in clinical studies.[147]

In the presented work, principles such as the use of a relevant animal model, characterization of animal properties at baseline, assessment of outcome measures that may be translated into clinical settings, and randomization of animals to treatment were followed where applicable. However, measurements and analysis were rarely performed blinded, although blinding is a well-known procedure to reduce bias. Reasons may be a lack of human resources (more than one researcher would be needed for an experiment), a lack of adaption to such principles in research laboratories, and others. Future preclinical studies investigating promising compounds close to translation into clinical trials should aim at following suggested guidelines [147] in order to increase confidence in the provided preclinical data.

9 Conclusions

- Fundus AF in mice is feasible using the same technique as in humans and allows quantitative and qualitative image analysis.
- The *Abca4*$^{-/-}$ mouse model for Stargardt disease reflects the human phenotype on AF imaging. Functional measures in this animal model are not reliable for evaluating treatment effects.
- Pharmacotherapy using C20dVitA is a promising intervention to prevent lipofuscin accumulation, a relevant step in the pathogenesis of Stargardt disease
- Gene therapy using AAV vectors requires further optimization before being efficiently applied in clinical trials.

References

1. Stargardt K. Über familiäre, progressive Degenerationen in der Maculagegend des Auges. *Graefes ArchClinExpOphthalmol* 1909;71:534-550.
2. Westeneng-van Haaften SC, Boon CJ, Cremers FP, Hoefsloot LH, den Hollander AI, Hoyng CB. Clinical and genetic characteristics of late-onset Stargardt's disease. *Ophthalmology* 2012;119:1199-1210.
3. Fritsche LG, Fleckenstein M, Fiebig BS, et al. A subgroup of age-related macular degeneration is associated with mono-allelic sequence variants in the ABCA4 gene. *Investigative ophthalmology & visual science* 2012;53:2112-2118.
4. Allikmets R, Singh N, Sun H, et al. A photoreceptor cell-specific ATP-binding transporter gene (ABCR) is mutated in recessive Stargardt macular dystrophy. *NatGenet* 1997;15:236-246.
5. Cremers FP, van de Pol DJ, van Driel M, et al. Autosomal recessive retinitis pigmentosa and cone-rod dystrophy caused by splice site mutations in the Stargardt's disease gene ABCR. *HumMolGenet* 1998;7:355-362.
6. Martinez MA, Paloma E, Allikmets R, et al. Retinitis pigmentosa caused by a homozygous mutation in the Stargardt disease gene ABCR. *NatGenet* 1998;18:11-12.
7. Maugeri A, Klevering BJ, Rohrschneider K, et al. Mutations in the ABCA4 (ABCR) gene are the major cause of autosomal recessive cone-rod dystrophy. *AmJHumGenet* 2000;67:960-966.
8. Klevering BJ, Deutman AF, Maugeri A, Cremers FP, Hoyng CB. The spectrum of retinal phenotypes caused by mutations in the ABCA4 gene. *Graefes ArchClinExpOphthalmol* 2005;243:90-100.
9. Allikmets R. Further evidence for an association of ABCR alleles with age-related macular degeneration. The International ABCR Screening Consortium. *AmJHumGenet* 2000;67:487-491.
10. Cideciyan AV, Swider M, Aleman TS, et al. Reduced-illuminance autofluorescence imaging in ABCA4-associated retinal degenerations. *J Opt Soc Am A Opt Image Sci Vis* 2007;24:1457-1467.
11. Delori FC, Staurenghi G, Arend O, Dorey CK, Goger DG, Weiter JJ. In vivo measurement of lipofuscin in Stargardt's disease--Fundus flavimaculatus. *Invest Ophthalmol VisSci* 1995;36:2327-2331.
12. Cukras CA, Wong WT, Caruso R, Cunningham D, Zein W, Sieving PA. Centrifugal Expansion of Fundus Autofluorescence Patterns in Stargardt Disease Over Time. *Arch Ophthalmol* 2011.
13. von Rückmann A, Fitzke FW, Bird AC. Distribution of fundus autofluorescence with a scanning laser ophthalmoscope. *BrJOphthalmol* 1995;79:407-412.
14. McBain VA, Townend J, Lois N. Progression of retinal pigment epithelial atrophy in stargardt disease. *American journal of ophthalmology* 2012;154:146-154.
15. Chen B, Tosha C, Gorin MB, Nusinowitz S. Analysis of autofluorescent retinal images and measurement of atrophic lesion growth in Stargardt disease. *Experimental eye research* 2010;91:143-152.

16. Tang PH, Kono M, Koutalos Y, Ablonczy Z, Crouch RK. New insights into retinoid metabolism and cycling within the retina. *Progress in retinal and eye research* 2013;32:48-63.
17. Chen Y, Okano K, Maeda T, et al. Mechanism of all-trans-retinal toxicity with implications for stargardt disease and age-related macular degeneration. *The Journal of biological chemistry* 2012;287:5059-5069.
18. Sparrow JR, Fishkin N, Zhou J, et al. A2E, a byproduct of the visual cycle. *Vision res* 2003;43:2983-2990.
19. Eldred GE, Katz ML. Fluorophores of the human retinal pigment epithelium: separation and spectral characterization. *Exp Eye Res* 1988;47:71-86.
20. Eldred GE, Lasky MR. Retinal age pigments generated by self-assembling lysosomotropic detergents. *Nature* 1993;361:724-726.
21. Ben-Shabat S, Parish CA, Hashimoto M, Liu J, Nakanishi K, Sparrow JR. Fluorescent pigments of the retinal pigment epithelium and age-related macular degeneration. *Bioorg Med Chem Lett* 2001;11:1533-1540.
22. Birnbach CD, Jarvelainen M, Possin DE, Milam AH. Histopathology and immunocytochemistry of the neurosensory retina in fundus flavimaculatus. *Ophthalmology* 1994;101:1211-1219.
23. Allikmets R, Gerrard B, Hutchinson A, Dean M. Characterization of the human ABC superfamily: isolation and mapping of 21 new genes using the expressed sequence tags database. *Human molecular genetics* 1996;5:1649-1655.
24. Illing M, Molday LL, Molday RS. The 220-kDa rim protein of retinal rod outer segments is a member of the ABC transporter superfamily. *J BiolChem* 1997;272:10303-10310.
25. Sun H, Nathans J. Stargardt's ABCR is localized to the disc membrane of retinal rod outer segments. *NatGenet* 1997;17:15-16.
26. Anderson DH, Fisher SK, Steinberg RH. Mammalian cones: disc shedding, phagocytosis, and renewal. *Investigative ophthalmology & visual science* 1978;17:117-133.
27. Young RW. The renewal of rod and cone outer segments in the rhesus monkey. *J Cell Biol* 1971;49:303-318.
28. Jonnal RS, Besecker JR, Derby JC, et al. Imaging outer segment renewal in living human cone photoreceptors. *Optics express* 2010;18:5257-5270.
29. Young RW. The renewal of photoreceptor cell outer segments. *J Cell Biol* 1967;33:61-72.
30. Beharry S, Zhong M, Molday RS. N-retinylidene-phosphatidylethanolamine is the preferred retinoid substrate for the photoreceptor-specific ABC transporter ABCA4 (ABCR). *The Journal of biological chemistry* 2004;279:53972-53979.
31. Travis GH, Golczak M, Moise AR, Palczewski K. Diseases caused by defects in the visual cycle: retinoids as potential therapeutic agents. *Annu Rev Pharmacol Toxicol* 2007;47:469-512.
32. Sun H. Membrane receptors and transporters involved in the function and transport of vitamin A and its derivatives. *Biochimica et biophysica acta* 2012;1821:99-112.
33. Chen C, Thompson DA, Koutalos Y. Reduction of all-trans-retinal in vertebrate rod photoreceptors requires the combined action of RDH8 and RDH12. *The Journal of biological chemistry* 2012;287:24662-24670.
34. Weng J, Mata NL, Azarian SM, Tzekov RT, Birch DG, Travis GH. Insights into the function of Rim protein in photoreceptors and etiology of Stargardt's disease from the phenotype in abcr knockout mice. *Cell* 1999;98:13-23.
35. Rivas MA, Vecino E. Animal models and different therapies for treatment of retinitis pigmentosa. *HistolHistopathol* 2009;24:1295-1322.
36. Radu RA, Han Y, Bui TV, et al. Reductions in serum vitamin A arrest accumulation of toxic retinal fluorophores: a potential therapy for treatment of lipofuscin-based retinal diseases. *Invest OphthalmolVisSci* 2005;46:4393-4401.

37. Radu RA, Mata NL, Nusinowitz S, Liu X, Sieving PA, Travis GH. Treatment with isotretinoin inhibits lipofuscin accumulation in a mouse model of recessive Stargardt's macular degeneration. *ProcNatlAcadSciUSA* 2003;100:4742-4747.
38. Allocca M, Doria M, Petrillo M, et al. Serotype-dependent packaging of large genes in adeno-associated viral vectors results in effective gene delivery in mice. *J Clin Invest* 2008;118:1955-1964.
39. Kong J, Kim SR, Binley K, et al. Correction of the disease phenotype in the mouse model of Stargardt disease by lentiviral gene therapy. *Gene therapy* 2008;15:1311-1320.
40. Grey AC, Crouch RK, Koutalos Y, Schey KL, Ablonczy Z. Spatial localization of A2E in the retinal pigment epithelium. *Investigative ophthalmology & visual science* 2011;52:3926-3933.
41. Webb RH, Hughes GW, Delori FC. Confocal scanning laser ophthalmoscope. *Applied optics* 1987;26:1492-1499.
42. Schmitz-Valckenberg S, Holz FG, Bird AC, Spaide RF. Fundus autofluorescence imaging: review and perspectives. *Retina* 2008;28:385-409.
43. Dobri N, Qin Q, Kong J, et al. A1120, a nonretinoid RBP4 antagonist, inhibits formation of cytotoxic bisretinoids in the animal model of enhanced retinal lipofuscinogenesis. *Investigative ophthalmology & visual science* 2013;54:85-95.
44. Maeda T, Maeda A, Matosky M, et al. Evaluation of potential therapies for a mouse model of human age-related macular degeneration caused by delayed all-trans-retinal clearance. *Investigative ophthalmology & visual science* 2009;50:4917-4925.
45. Ma L, Kaufman Y, Zhang J, Washington I. C20-D3-vitamin A slows lipofuscin accumulation and electrophysiological retinal degeneration in a mouse model of Stargardt disease. *J Biol Chem* 2011;286:7966-7974.
46. Kaufman Y, Ma L, Washington I. Deuterium enrichment of vitamin A at the C20 position slows the formation of detrimental vitamin A dimers in wild-type rodents. *The Journal of biological chemistry* 2011;286:7958-7965.
47. Bainbridge JW, Smith AJ, Barker SS, et al. Effect of gene therapy on visual function in Leber's congenital amaurosis. *NEnglJMed* 2008;358:2231-2239.
48. Maguire AM, Simonelli F, Pierce EA, et al. Safety and efficacy of gene transfer for Leber's congenital amaurosis. *N Engl J Med* 2008;358:2240-2248.
49. Hauswirth WW, Aleman TS, Kaushal S, et al. Treatment of leber congenital amaurosis due to RPE65 mutations by ocular subretinal injection of adeno-associated virus gene vector: short-term results of a phase I trial. *Hum Gene Ther* 2008;19:979-990.
50. Simonelli F, Maguire AM, Testa F, et al. Gene therapy for Leber's congenital amaurosis is safe and effective through 1.5 years after vector administration. *Mol Ther* 2010;18:643-650.
51. Cideciyan AV, Hauswirth WW, Aleman TS, et al. Human RPE65 gene therapy for Leber congenital amaurosis: persistence of early visual improvements and safety at 1 year. *Hum Gene Ther* 2009;20:999-1004.
52. Cideciyan AV, Hauswirth WW, Aleman TS, et al. Vision 1 year after gene therapy for Leber's congenital amaurosis. *N Engl J Med* 2009;361:725-727.
53. Cideciyan AV, Aleman TS, Boye SL, et al. Human gene therapy for RPE65 isomerase deficiency activates the retinoid cycle of vision but with slow rod kinetics. *Proc Natl Acad Sci U S A* 2008;105:15112-15117.
54. Jacobson SG, Cideciyan AV, Ratnakaram R, et al. Gene Therapy for Leber Congenital Amaurosis Caused by RPE65 Mutations: Safety and Efficacy in 15 Children and Adults Followed Up to 3 Years. *Arch Ophthalmol* 2011.
55. Charbel Issa P, Maclaren RE. Non-viral retinal gene-therapy: a review. *Clin Experiment Ophthalmol* 2011;40:39-47.

56. Berns KI. Paroviridae: the viruses and their replication. *In: Fields, BN (Ed), Fundamental Virology Lippincott-Raven, Philadelphia, New York* 1996;1017-1042.
57. Hirsch ML, Agbandje-McKenna M, Samulski RJ. Little vector, big gene transduction: fragmented genome reassembly of adeno-associated virus. *Mol Ther* 2010;18:6-8.
58. Wu Z, Yang H, Colosi P. Effect of genome size on AAV vector packaging. *Mol Ther* 2010;18:80-86.
59. Lai Y, Yue Y, Duan D. Evidence for the failure of adeno-associated virus serotype 5 to package a viral genome > or = 8.2 kb. *Molecular therapy : the journal of the American Society of Gene Therapy* 2010;18:75-79.
60. Dong B, Nakai H, Xiao W. Characterization of genome integrity for oversized recombinant AAV vector. *Mol Ther* 2010;18:87-92.
61. Humphries MM, Rancourt D, Farrar GJ, et al. Retinopathy induced in mice by targeted disruption of the rhodopsin gene. *Nat Genet* 1997;15:216-219.
62. Sagdullaev BT, DeMarco PJ, McCall MA. Improved contact lens electrode for corneal ERG recordings in mice. *Documenta ophthalmologica Advances in ophthalmology* 2004;108:181-184.
63. Delori FC, Dorey CK, Staurenghi G, Arend O, Goger DG, Weiter JJ. In vivo fluorescence of the ocular fundus exhibits retinal pigment epithelium lipofuscin characteristics. *Invest Ophthalmol VisSci* 1995;36:718-729.
64. von Rückmann A, Fitzke FW, Bird AC. Fundus autofluorescence in age-related macular disease imaged with a laser scanning ophthalmoscope. *Invest OphthalmolVisSci* 1997;38:478-486.
65. Lorenz B, Wabbels B, Wegscheider E, Hamel CP, Drexler W, Preising MN. Lack of fundus autofluorescence to 488 nanometers from childhood on in patients with early-onset severe retinal dystrophy associated with mutations in RPE65. *Ophthalmology* 2004;111:1585-1594.
66. Charbel Issa P, Bolz HJ, Ebermann I, Domeier E, Holz FG, Scholl HP. Characterization of Severe Rod-Cone Dystrophy in a Consanguineous Family with a Splice Site Mutation in the MERTK Gene. *Br J Ophthalmol* 2009;93:920-925.
67. Sergouniotis PI, Sohn EH, Li Z, et al. Phenotypic variability in RDH5 retinopathy (Fundus Albipunctatus). *Ophthalmology* 2011;118:1661-1670.
68. Keilhauer CN, Delori FC. Near-infrared autofluorescence imaging of the fundus: visualization of ocular melanin. *Invest Ophthalmol Vis Sci* 2006;47:3556-3564.
69. Gibbs D, Cideciyan AV, Jacobson SG, Williams DS. Retinal pigment epithelium defects in humans and mice with mutations in MYO7A: imaging melanosome-specific autofluorescence. *Invest Ophthalmol Vis Sci* 2009;50:4386-4393.
70. Schmitz-Valckenberg S, Lara D, Nizari S, et al. Localisation and significance of in vivo near-infrared autofluorescent signal in retinal imaging. *Br J Ophthalmol* 2011;95:1134-1139.
71. Kellner S, Kellner U, Weber BH, Fiebig B, Weinitz S, Ruether K. Lipofuscin- and melanin-related fundus autofluorescence in patients with ABCA4-associated retinal dystrophies. *Am J Ophthalmol* 2009;147:895-902, 902 e891.
72. Kellner U, Kellner S, Weber BH, Fiebig B, Weinitz S, Ruether K. Lipofuscin- and melanin-related fundus autofluorescence visualize different retinal pigment epithelial alterations in patients with retinitis pigmentosa. *Eye (Lond)* 2009;23:1349-1359.
73. Paques M, Simonutti M, Roux M, et al. High resolution fundus imaging by confocal scanning laser ophthalmoscopy in the mouse. *Vision Research* 2006;46:1336-1345.
74. Seeliger MW, Beck SC, Pereyra-Muñoz N, et al. In vivo confocal imaging of the retina in animal models using scanning laser ophthalmoscopy. *Vision Research* 2005;45:3512-3519.
75. Helb HM, Charbel Issa P, Fleckenstein M, et al. Clinical evaluation of simultaneous confocal scanning laser ophthalmoscopy imaging combined with high-resolution spectral-domain optical coherence tomoggraphy. *Acta Ophthalmologica* 2010;88:842-849.

76. Fischer MD, Huber G, Beck SC, et al. Noninvasive, in vivo assessment of mouse retinal structure using optical coherence tomography. *PLoS One* 2009;4:e7507.
77. Delori F, Greenberg JP, Fischer J, et al. Quantitative measurements of autofluorescence with the scanning laser ophthalmoscope. *Invest Ophthalmol Vis Sci* 2011;52:9379-9390.
78. Abramoff MD, Magalhães PJ, Ram SJ. Image processing with ImageJ. *Biophotonics International* 2004;11:36-42.
79. Schmucker C, Schaeffel F. A paraxial schematic eye model for the growing C57BL/6 mouse. *Vision Res* 2004;44:1857-1867.
80. Ridder W, 3rd, Nusinowitz S, Heckenlively JR. Causes of cataract development in anesthetized mice. *Exp Eye Res* 2002;75:365-370.
81. Theelen T, Berendschot TT, Boon CJ, Hoyng CB, Klevering BJ. Analysis of visual pigment by fundus autofluorescence. *ExpEye Res* 2008;86:296-304.
82. Remtulla S, Hallett PE. A schematic eye for the mouse, and comparisons with the rat. *Vision Res* 1985;25:21-31.
83. Geng Y, Schery LA, Sharma R, et al. Optical properties of the mouse eye. *Biomed Opt Express* 2011;2:717-738.
84. Gabriele ML, Ishikawa H, Schuman JS, et al. Reproducibility of spectral-domain optical coherence tomography total retinal thickness measurements in mice. *Invest Ophthalmol Vis Sci* 2010;51:6519-6523.
85. Srinivasan VJ, Ko TH, Wojtkowski M, et al. Noninvasive volumetric imaging and morphometry of the rodent retina with high-speed, ultrahigh-resolution optical coherence tomography. *Invest Ophthalmol Vis Sci* 2006;47:5522-5528.
86. Weinberger AW, Lappas A, Kirschkamp T, et al. Fundus near infrared fluorescence correlates with fundus near infrared reflectance. *Invest OphthalmolVisSci* 2006;47:3098-3108.
87. Morgan JI, Hunter JJ, Masella B, et al. Light-induced retinal changes observed with high-resolution autofluorescence imaging of the retinal pigment epithelium. *Invest Ophthalmol Vis Sci* 2008;49:3715-3729.
88. Morgan JI, Hunter JJ, Merigan WH, Williams DR. The reduction of retinal autofluorescence caused by light exposure. *Invest Ophthalmol Vis Sci* 2009;50:6015-6022.
89. Grimm C, Reme CE, Rol PO, Williams TP. Blue light's effects on rhodopsin: photoreversal of bleaching in living rat eyes. *Invest Ophthalmol Vis Sci* 2000;41:3984-3990.
90. Schütt F, Davies S, Kopitz J, Holz FG, Boulton ME. Photodamage to human RPE cells by A2-E, a retinoid component of lipofuscin. *Invest OphthalmolVisSci* 2000;41:2303-2308.
91. Sparrow JR, Nakanishi K, Parish CA. The lipofuscin fluorophore A2E mediates blue light-induced damage to retinal pigmented epithelial cells. *Invest OphthalmolVisSci* 2000;41:1981-1989.
92. Bergmann M, Sch tt F, Holz FG, Kopitz J. Inhibition of the ATP-driven proton pump in RPE lysosomes by the major lipofuscin fluorophore A2-E may contribute to the pathogenesis of age-related macular degeneration. *FASEB J* 2004;18:562-564.
93. Holz FG, Schütt F, Kopitz J, et al. Inhibition of lysosomal degradative functions in RPE cells by a retinoid component of lipofuscin. *Invest OphthalmolVisSci* 1999;40:737-743.
94. Zhou J, Jang YP, Kim SR, Sparrow JR. Complement activation by photooxidation products of A2E, a lipofuscin constituent of the retinal pigment epithelium. *ProcNatlAcadSciUSA* 2006;103:16182-16187.
95. Radu RA, Yuan Q, Hu J, et al. Accelerated accumulation of lipofuscin pigments in the RPE of a mouse model for ABCA4-mediated retinal dystrophies following Vitamin A supplementation. *Investigative Ophthalmology & Visual Science* 2008;49:3821-3829.
96. Kim SR, Fishkin N, Kong J, Nakanishi K, Allikmets R, Sparrow JR. Rpe65 Leu450Met variant is associated with reduced levels of the retinal pigment epithelium lipofuscin fluorophores A2E and iso-A2E. *Proc Natl Acad Sci U S A* 2004;101:11668-11672.

97. Radu RA, Hu J, Yuan Q, et al. Complement system dysregulation and inflammation in the retinal pigment epithelium of a mouse model for Stargardt macular degeneration. *The Journal of biological chemistry* 2011;286:18593-18601.
98. Charbel Issa P, Singh MS, Lipinski DM, et al. Optimization of in vivo confocal autofluorescence imaging of the ocular fundus in mice and its application to models of human retinal degeneration. *Invest Ophthalmol Vis Sci* 2012;53:1066-1075.
99. Cideciyan AV, Aleman TS, Swider M, et al. Mutations in ABCA4 result in accumulation of lipofuscin before slowing of the retinoid cycle: a reappraisal of the human disease sequence. *Hum Mol Genet* 2004;13:525-534.
100. Boyer NP, Higbee D, Currin MB, et al. Lipofuscin and N-retinylidene-N-retinylethanolamine (A2E) accumulate in retinal pigment epithelium in absence of light exposure: their origin is 11-cis-retinal. *The Journal of biological chemistry* 2012;287:22276-22286.
101. Kayatz P, Thumann G, Luther TT, et al. Oxidation causes melanin fluorescence. *Investigative ophthalmology & visual science* 2001;42:241-246.
102. Sarna T, Burke JM, Korytowski W, et al. Loss of melanin from human RPE with aging: possible role of melanin photooxidation. *Experimental eye research* 2003;76:89-98.
103. Wu L, Nagasaki T, Sparrow JR. Photoreceptor cell degeneration in Abcr (-/-) mice. *Adv Exp Med Biol* 2010;664:533-539.
104. Rozanowski B, Burke JM, Boulton ME, Sarna T, Rozanowska M. Human RPE melanosomes protect from photosensitized and iron-mediated oxidation but become pro-oxidant in the presence of iron upon photodegradation. *Invest Ophthalmol Vis Sci* 2008;49:2838-2847.
105. Fujinami K, Lois N, Davidson AE, et al. A longitudinal study of stargardt disease: clinical and electrophysiologic assessment, progression, and genotype correlations. *American journal of ophthalmology* 2013;155:1075-1088 e1013.
106. Zahid S, Jayasundera T, Rhoades W, et al. Clinical phenotypes and prognostic full-field electroretinographic findings in Stargardt disease. *American journal of ophthalmology* 2013;155:465-473 e463.
107. Oh KT, Weleber RG, Stone EM, Oh DM, Rosenow J, Billingslea AM. Electroretinographic findings in patients with Stargardt disease and fundus flavimaculatus. *Retina* 2004;24:920-928.
108. Fishman GA, Farbman JS, Alexander KR. Delayed rod dark adaptation in patients with Stargardt's disease. *Ophthalmology* 1991;98:957-962.
109. Kang Derwent JJ, Derlacki DJ, Hetling JR, et al. Dark adaptation of rod photoreceptors in normal subjects, and in patients with Stargardt disease and an ABCA4 mutation. *Investigative ophthalmology & visual science* 2004;45:2447-2456.
110. Moiseyev G, Nikolaeva O, Chen Y, Farjo K, Takahashi Y, Ma JX. Inhibition of the visual cycle by A2E through direct interaction with RPE65 and implications in Stargardt disease. *Proceedings of the National Academy of Sciences of the United States of America* 2010;107:17551-17556.
111. Sparrow JR, Blonska A, Flynn E, et al. Quantitative fundus autofluorescence in mice: correlation with HPLC quantitation of RPE lipofuscin and measurement of retina outer nuclear layer thickness. *Investigative ophthalmology & visual science* 2013;54:2812-2820.
112. Radu RA, Mata NL, Bagla A, Travis GH. Light exposure stimulates formation of A2E oxiranes in a mouse model of Stargardt's macular degeneration. *Proc Natl Acad Sci U S A* 2004;101:5928-5933.
113. Mata NL, Tzekov RT, Liu X, Weng J, Birch DG, Travis GH. Delayed dark-adaptation and lipofuscin accumulation in abcr+/- mice: implications for involvement of ABCR in age-related macular degeneration. *Invest Ophthalmol Vis Sci* 2001;42:1685-1690.

114. Han Z, Conley SM, Makkia RS, Cooper MJ, Naash MI. DNA nanoparticle-mediated ABCA4 delivery rescues Stargardt dystrophy in mice. *The Journal of clinical investigation* 2012;122:3221-3226.
115. Cideciyan AV, Swider M, Aleman TS, et al. ABCA4 disease progression and a proposed strategy for gene therapy. *Hum Mol Genet* 2009;18:931-941.
116. Greenberg JP, Duncker T, Woods RL, Smith RT, Sparrow JR, Delori FC. Quantitative fundus autofluorescence in healthy eyes. *Investigative ophthalmology & visual science* 2013;54:5684-5693.
117. Vandenberghe LH, Bell P, Maguire AM, et al. Dosage thresholds for AAV2 and AAV8 photoreceptor gene therapy in monkey. *Sci Transl Med* 2011;3:88ra54.
118. Mancuso K, Hauswirth WW, Li Q, et al. Gene therapy for red-green colour blindness in adult primates. *Nature* 2009;461:784-787.
119. Gao G, Vandenberghe LH, Alvira MR, et al. Clades of Adeno-associated viruses are widely disseminated in human tissues. *J Virol* 2004;78:6381-6388.
120. Lawlor PA, Bland RJ, Mouravlev A, Young D, During MJ. Efficient gene delivery and selective transduction of glial cells in the mammalian brain by AAV serotypes isolated from nonhuman primates. *Mol Ther* 2009;17:1692-1702.
121. Barker SE, Broderick CA, Robbie SJ, et al. Subretinal delivery of adeno-associated virus serotype 2 results in minimal immune responses that allow repeat vector administration in immunocompetent mice. *J Gene Med* 2009;11:486-497.
122. Mingozzi F, High KA. Immune responses to AAV in clinical trials. *Curr Gene Ther* 2011;11:321-330.
123. Petrs-Silva H, Dinculescu A, Li Q, et al. High-efficiency transduction of the mouse retina by tyrosine-mutant AAV serotype vectors. *Mol Ther* 2009;17:463-471.
124. Zhong L, Li B, Mah CS, et al. Next generation of adeno-associated virus 2 vectors: point mutations in tyrosines lead to high-efficiency transduction at lower doses. *Proc Natl Acad Sci U S A* 2008;105:7827-7832.
125. DiPrimio N, Asokan A, Govindasamy L, Agbandje-McKenna M, Samulski RJ. Surface loop dynamics in adeno-associated virus capsid assembly. *J Virol* 2008;82:5178-5189.
126. Aslam SA, Davies WI, Singh MS, et al. Cone Photoreceptor Neuroprotection Conferred by CNTF in a Novel In Vivo Model of Battlefield Retinal Laser Injury. *Investigative ophthalmology & visual science* 2013;54:5456-5465.
127. Singh MS, Charbel Issa P, Butler R, et al. Reversal of end-stage retinal degeneration and restoration of visual function by photoreceptor transplantation. *Proceedings of the National Academy of Sciences of the United States of America* 2013;110:1101-1106.
128. Charbel Issa P, De Silva SR, Lipinski DM, et al. Assessment of tropism and effectiveness of new primate-derived hybrid recombinant AAV serotypes in the mouse and primate retina. *PloS one* 2013;8:e60361.
129. Schön C, Hoffmann NA, Ochs SM, et al. Long-term in vivo imaging of fibrillar tau in the retina of P301S transgenic mice. *PloS one* 2012;7:e53547.
130. Chen Y, Ratnam K, Sundquist SM, et al. Cone photoreceptor abnormalities correlate with vision loss in patients with Stargardt disease. *Invest Ophthalmol Vis Sci* 2011;52:3281-3292.
131. Gomes NL, Greenstein VC, Carlson JN, et al. A comparison of fundus autofluorescence and retinal structure in patients with Stargardt disease. *Invest Ophthalmol Vis Sci* 2009;50:3953-3959.
132. von Rückmann A, Fitzke FW, Bird AC. In vivo fundus autofluorescence in macular dystrophies. *ArchOphthalmol* 1997;115:609-615.
133. Lois N, Halfyard AS, Bird AC, Holder GE, Fitzke FW. Fundus autofluorescence in Stargardt macular dystrophy-fundus flavimaculatus. *Am J Ophthalmol* 2004;138:55-63.

134. Mihai DM, Jiang H, Blaner WS, Romanov A, Washington I. The retina rapidly incorporates ingested C20-D(3)-vitamin A in a swine model. *Molecular vision* 2013;19:1677-1683.
135. Lipinski DM, Thake M, MacLaren RE. Clinical applications of retinal gene therapy. *Progress in retinal and eye research* 2013;32:22-47.
136. Kumar Singh R. Barriers for retinal gene therapy: Separating fact from fiction. *Vision Research* 2008;48:1671-1680.
137. Matsuda T, Cepko CL. Electroporation and RNA interference in the rodent retina in vivo and in vitro. *Proc Natl Acad Sci U S A* 2004;101:16-22.
138. Kachi S, Oshima Y, Esumi N, et al. Nonviral ocular gene transfer. *Gene Ther* 2005;12:843-851.
139. Johnson CJ, Berglin L, Chrenek MA, Redmond TM, Boatright JH, Nickerson JM. Technical brief: subretinal injection and electroporation into adult mouse eyes. *Mol Vis* 2008;14:2211-2226.
140. Davies JB, Ciavatta VT, Boatright JH, Nickerson JM. Delivery of several forms of DNA, DNA-RNA hybrids, and dyes across human sclera by electrical fields. *Mol Vis* 2003;9:569-578.
141. Souied EH, Reid SN, Piri NI, Lerner LE, Nusinowitz S, Farber DB. Non-invasive gene transfer by iontophoresis for therapy of an inherited retinal degeneration. *Exp Eye Res* 2008;87:168-175.
142. Andrieu-Soler C, Doat M, Halhal M, et al. Enhanced oligonucleotide delivery to mouse retinal cells using iontophoresis. *Mol Vis* 2006;12:1098-1107.
143. Horbinski C, Stachowiak MK, Higgins D, Finnegan SG. Polyethyleneimine-mediated transfection of cultured postmitotic neurons from rat sympathetic ganglia and adult human retina. *BMC Neurosci* 2001;2:2.
144. Cai X, Conley SM, Nash Z, Fliesler SJ, Cooper MJ, Naash MI. Gene delivery to mitotic and postmitotic photoreceptors via compacted DNA nanoparticles results in improved phenotype in a mouse model of retinitis pigmentosa. *FASEB J* 2010;24:1178-1191.
145. Cai X, Nash Z, Conley SM, Fliesler SJ, Cooper MJ, Naash MI. A partial structural and functional rescue of a retinitis pigmentosa model with compacted DNA nanoparticles. *PLoS One* 2009;4:e5290.
146. Ding XQ, Quiambao AB, Fitzgerald JB, Cooper MJ, Conley SM, Naash MI. Ocular delivery of compacted DNA-nanoparticles does not elicit toxicity in the mouse retina. *PLoS One* 2009;4:e7410.
147. Henderson VC, Kimmelman J, Fergusson D, Grimshaw JM, Hackam DG. Threats to validity in the design and conduct of preclinical efficacy studies: a systematic review of guidelines for in vivo animal experiments. *PLoS Med* 2013;10:e1001489.

Appendix

Optimization of In Vivo Confocal Autofluorescence Imaging of the Ocular Fundus in Mice and Its Application to Models of Human Retinal Degeneration

Peter Charbel Issa,[*,1] *Mandeep S. Singh,*[1] *Daniel M. Lipinski,*[1] *Ngaihang V. Chong,*[1] *François C. Delori,*[2] *Alun R. Barnard,*[1] *and Robert E. MacLaren*[*,1,3]

Purpose. To investigate the feasibility and to identify sources of experimental variability of quantitative and qualitative fundus autofluorescence (AF) assessment in mice.

Methods. Blue (488 nm) and near-infrared (790 nm) fundus AF imaging was performed in various mouse strains and disease models (129S2, C57Bl/6, *Abca4*$^{-/-}$, C3H-*Pde6b*$^{rd1/rd1}$, *Rho*$^{-/-}$, and BALB/c mice) using a commercially available scanning laser ophthalmoscope. Gray-level analysis was used to explore factors influencing fundus AF measurements.

Results. A contact lens avoided cataract development and resulted in consistent fundus AF recordings. Fundus illumination and magnification were sensitive to changes of the camera position. Standardized adjustment of the recorded confocal plane and consideration of the pupil area allowed reproducible recording of fundus AF from the retinal pigment epithelium with an intersession coefficient of repeatability of ±22%. Photopigment bleaching occurred during the first 1.5 seconds of exposure to 488 nm blue light (~10 mW/cm^2), resulting in an increase of fundus AF. In addition, there was a slight decrease in fundus AF during prolonged blue light exposure. Fundus AF at 488 nm was low in animals with an absence of a normal visual cycle, and high in BALB/c and *Abca4*$^{-/-}$ mice. Degenerative alterations in *Pde6b*$^{rd1/rd1}$ and *Rho*$^{-/-}$ were reminiscent of findings in human retinal disease.

Conclusions. Investigation of retinal phenotypes in mice is possible in vivo using standardized fundus AF imaging. Correlation with postmortem analysis is likely to lead to further understanding of human disease phenotypes and of retinal degenerations in general. Fundus AF imaging may be useful as an outcome measure in preclinical trials, such as for monitoring effects aimed at lowering lipofuscin accumulation in the retinal pigment epithelium. (*Invest Ophthalmol Vis Sci.* 2012; 53:1066–1075) DOI:10.1167/iovs.11-8767

Retinal research, including the investigation of novel therapies for retinal degenerative or neovascular diseases, relies heavily on the use of animal models. Small rodents constitute the majority of disease models that have been developed to date.[1] Therefore, assessment of the rodent retina has become increasingly important in basic and preclinical research and furthers the understanding of human retinal disease.

Histologic analysis of tissue specimens obtained after euthanasia was once the only means by which to investigate retinal structure in animal models. Recently developed retinal imaging modalities, such as confocal scanning laser ophthalmoscopy (cSLO)[2,3] and optical coherence tomography (OCT),[4] may now be used for high-resolution in vivo assessment of retinal structure in small animals. Repeated in vivo assessments may be performed longitudinally in the same animal, reducing variability and, potentially, the number of animals required in some experiments.

Fundus autofluorescence (AF) imaging allows noninvasive assessment of retinal disease. In humans, fundus AF findings may inform disease diagnosis, characterization, prognostication, and monitoring.[5] Currently, a 488 nm laser light source is most commonly used for AF excitation. At this excitation wavelength, the main fluorophore in the human fundus is lipofuscin.[6] Lipofuscin is a natural byproduct of the visual cycle and is composed of compounds that normally accumulate in the retinal pigment epithelium (RPE) with age.[6,7] Retinal disease may be associated with abnormally increased[8] or decreased[9–11] 488 nm AF, specific alterations of the AF pattern,[5] or both. Near-infrared (NIR) light using a 790 nm laser has also been used for fundus AF imaging. The AF signal at this excitation wavelength appears to originate from melanin in the RPE and choroid[12–14]; 790 nm AF may show similar, but distinct, alterations in retinal diseases compared with 488 nm AF, possibly because of changes in the melanosome compartment.[15–17]

A high-resolution, high-contrast image of fundus AF distribution in humans can be visualized with cSLO. The use of cSLO imaging in animal models has been described.[2,3] Despite these pioneering advances in this field, cSLO AF imaging of the ocular fundus in mice has not been investigated systematically. Herein, we aimed to explore factors influencing fundus AF imaging in mice and to optimize the technique to be able to

From the [1]Nuffield Laboratory of Ophthalmology and Oxford Eye Hospital Biomedical Research Centre, University of Oxford, John Radcliffe Hospital, Oxford, United Kingdom; [2]Schepens Eye Research Institute and Department of Ophthalmology, Harvard Medical School, Boston, Massachusetts; and [3]Moorfields Eye Hospital, London, United Kingdom.

Presented in part at the annual meeting of the Association for Research in Vision and Ophthalmology, Fort Lauderdale, Florida, May 2011.

Supported by The European Commission, FP7, Marie Curie Intra-European Fellowship 237238; Fight for Sight, Wellcome Trust Grant 086868/Z/08/Z; Oxford Stem Cell Institute; Health Foundation; Royal College of Surgeons of Edinburgh, NIHR Oxford and Moorfields Biomedical Research Centers.

Submitted for publication October 7, 2011; revised November 18, 2011; accepted November 30, 2011.

Disclosure: **P. Charbel Issa**, None; **M.S. Singh**, None; **D.M. Lipinski**, None; **N.V. Chong**, None; **F.C. Delori**, None; **A.R. Barnard**, None; **R.E. MacLaren**, None

*Each of the following is a corresponding author: Peter Charbel Issa, Nuffield Laboratory of Ophthalmology, University of Oxford, John Radcliffe Hospital, OX3 9DU, United Kingdom; enquiries@eye.ox.ac.uk.

Robert E. MacLaren, Nuffield Laboratory of Ophthalmology, University of Oxford, John Radcliffe Hospital, OX3 9DU, United Kingdom; enquiries@eye.ox.ac.uk.

apply fundus AF imaging in a standardized, consistent, and reproducible way. cSLO imaging was subsequently used to characterize 488 nm and 790 nm fundus AF in different wild-type (WT) mice and in retinal disease models. These data provide evidence that a standardized approach to fundus AF imaging allows the recognition of disease-related changes of AF patterns (i.e., qualitative changes) and the determination of fundus AF intensity (i.e., quantitative changes) in vivo as an alternative to postmortem measurements of lipofuscin components.

METHODS

Mice

Pigmented WT 129S2/SvHsd (WT129) and C3H/HeNHsd-*Pde6b*^{rd1} (*Pde6b*$^{rd1/rd1}$) were purchased from Harlan Laboratories (Hillcrest, UK). WT C57Bl/6 and albino BALB/c mice were provided by the Biomedical Sciences division of the University of Oxford. Pigmented *Abca4* knockout mice (129S4/SvJae-*Abca4*^{tm1Gbt} [*Abca4*$^{-/-}$])[18] were provided by Gabriel Travis (David Geffen School of Medicine, University of California, Los Angeles, CA). Rhodopsin knockout mice (B6.129S1- *Rho*^{tm1Pbm} [*Rho*$^{-/-}$])[19] were a kind gift obtained under MTA from Jane Farrar (Trinity College Dublin, Ireland). Mice expressing the fluorescent reporter protein DsRed under a modified actin promoter (Tg(CAG-DsRed*MST)1Nagy/J) were purchased from The Jackson Laboratory (Bar Harbor, ME).

Animals were kept in a 12-hour light (<100 lux)/12-hour dark cycle, with food and water available ad libitum. All procedures were performed under the approval of local and national ethical and legal authorities and in accordance with the ARVO Statement for the Care and Use of Animals in Ophthalmic and Vision Research.

Animal Preparation for Imaging Procedures

Mice were anesthetized by intraperitoneal injection of 1 mg/kg medetomidine (Dormitor 1 mg/mL; Pfizer, Sandwich, UK) and 60 mg/kg ketamine (Ketaset 100 mg/kg; Fort Dodge, Southampton, UK). Their pupils were dilated with tropicamide (Mydriaticum 1%; Bausch & Lomb, Kingston-on-Thames, UK) and phenylephrine (phenylephrine hydrochloride 2.5%; Bausch & Lomb) eyedrops. A custom-made contact lens was used for all recordings (except where stated otherwise) to prevent corneal desiccation and subsequent cataract formation and to improve image quality (PMMA mouse lens, back optic zone radius of 1.7 mm, total diameter of 3.2 mm, center thickness of 0.4 mm, straight sides; Cantor and Nissel, Brackley, UK). Lubricating eyedrops (Hypromellose BPC 0.3%; Matindale Pharmaceuticals, Romford, UK) were used as viscous coupling fluid between the contact lens and the cornea. For image acquisition, the animal was placed on a platform mounted on the chin rest of the imaging device so that its eyes were positioned approximately at the level of the marking for a human patients' eye position. If prolonged imaging is required, a heat mat can be used to maintain body temperature. In selected cases, mice with dilated pupils can be assessed with the cSLO with only brief physical restraint, without general anesthesia and without a contact lens placed on the cornea. For consistent recordings across animals allowing gray-level (GL) analysis, imaging was performed under anesthesia throughout this study.

Fundus Imaging Using a Confocal Scanning Laser Ophthalmoscope

cSLO imaging was performed with a device commercially available for human fundus imaging (Spectralis HRA; Heidelberg Engineering, Heidelberg, Germany).[20] Fluorescence was excited using laser diodes centered at approximately 488 nm and 788 nm. Emission was recorded between 500 and 700 nm or above 805 nm, respectively. The beam powers were approximately 280 μW and 2.6 mW, respectively.

The NIR reflectance mode (820 nm laser) was used for camera alignment to obtain an evenly illuminated fundus image and to focus on the confocal plane of interest. A confocal reference plane of high reflectivity could be consistently identified in the outer retina using the NIR reflectance mode with slight overexposure. Signals beyond the dynamic range of the detector were highlighted as red pixels by the software. This feature assisted the user in detecting the areas of highest reflectivity and, therefore, the confocal plane with the largest overexposed area. Using this technique the dioptric focus was adjusted and the camera aligned so that the highest fundus NIR reflectivity was paracentral (uniform illumination in the entire 55° field of the mouse fundus is usually not possible using the Spectralis HRA). If the paracentral overexposure characteristic appeared similar in consecutive planes (sometimes spanning a range of up to 6 diopters [D]), the middle focus setting was chosen. Cross-sectional OCT imaging, using a wavelength similar to that of NIR reflectance, shows highest reflective bands at the approximate level of the RPE,[4] suggesting that the highly reflective confocal NIR reflectance reference plane corresponds to anatomic structures at or close to the RPE.

The alignment for obtaining an optimal signal also ensured that the camera was aligned such that its "scan pupil" and its "detection pupil" were centered in the dilated pupil of the mouse and were in focus in the plane of the mouse's iris. The scan pupil is the area in the pupil plane in which the incident laser beam oscillates as it scans the fundus, and the detection pupil is the area through which the fundus AF is detected. Both pupils are conjugated to the scan mirrors in the camera and are concentric with each other. It is important to monitor the diameter of the dilated pupil during measurements because it may obstruct the scan pupil and the detection pupil and, thus, influence fundus AF measurements.

Images were usually recorded using the automatic real-time (ART) mode, which was able to track slight movements of the fundus (e.g., caused by respiration) based on fundus landmarks with high contrast. This allowed up to 100 consecutive frames to be averaged in real time and improved the signal-to-noise ratio. Single-averaged images were recorded with an intensity resolution of 8 bits/pixel, a 1536 × 1536 pixel resolution (high-resolution mode), and a frame rate of 4.8 frames/s. Rapid nonaveraged image sequences (high-speed mode, 768 × 768 pixel resolution, 8.9 frames/s) were used only for capturing photopigment bleaching effects.

For quantitative analysis, nonnormalized images were recorded in a dimmed room. Experiments on photopigment bleaching were performed in a dark room under dim red light after a minimum of 6 hours of dark adaptation. Normalized images (i.e., automatic software enhancement of contrast by histogram stretching) were only used if high contrast was aimed at (Fig. 10B). No further image processing was performed unless stated otherwise. The full angle of view using the 55° lens (Spectralis HRA) was displayed.

The detector sensitivity setting of the Spectralis HRA can be adjusted between 31 and 107, resulting in a nonlinear increase in detector gain by a factor of approximately 3600. Because detected AF levels in mice are low, a sensitivity of 100 was used to acquire all mouse images (except for the DsRed mouse, in which lower sensitivity settings are appropriate because of the expression of a fluorescent reporter protein). At this sensitivity, the zero-corrected GL (cGL) linear range extends up to approximately 150 GLs.[21] In human subjects with healthy eyes, such sensitivity settings would usually result in nonlinear effects (i.e., GL > 150) and partial saturation, which is only rarely observed in mice. Although mouse fundus AF images may appear dark at a sensitivity ≤100, higher sensitivity settings were avoided because of an increasing contribution of noise and a decreasing linear range with increasing sensitivity.[21]

Quantitative Gray-Level Image Analysis

Quantitative GL analysis of nonnormalized and unprocessed fundus AF images (recorded with the same detector sensitivity) was performed using ImageJ software (developed by Wayne Rasband, National Insti-

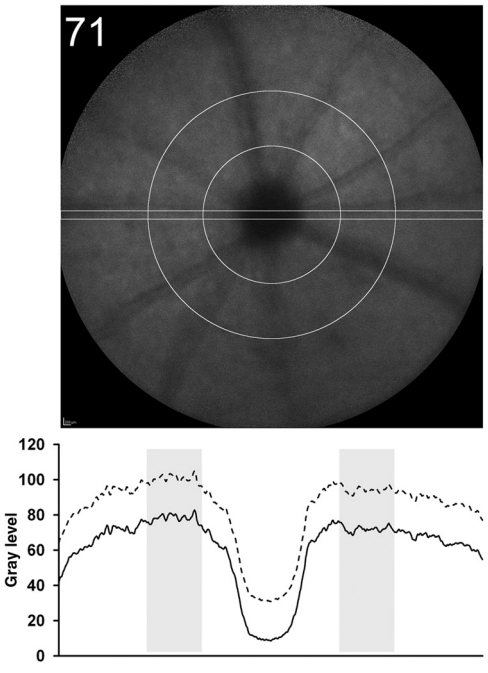

FIGURE 1. Quantitative gray level (GL) analysis of fundus autofluorescence (AF) images. The *dashed line* in the graph (*bottom*) represents the GL profile along the horizontal 30 pixels wide band (*top*). The *continuous line* in the graph represents the corrected GL (cGL), which results after subtracting the zero-GL and which is used for all comparisons. The mean cGL within an annular area, concentric to the optic disc center, defined by *circles* with 250 and 450 pixels radius (*gray background*, *bottom graph*), was used for all quantitative GL measurements (indicated in the *left upper* corner; range 0–255 minus zero-GL). This sampling area avoids the optic disc and the more peripheral part of the image, where darkening and distortion are usually observed.

tutes of Health, Bethesda, MD; available at http://rsb.info.nih.gov/ij/index.html).[22] After applying a standard Gaussian blur with a 3-pixel radius (σ) to reduce image noise, analysis included a plot of the mean GL profile within a 30-pixel-wide horizontal band through the optic nerve head and a measurement of the mean GL within the midperipheral fundus (Fig. 1). All measured GLs were corrected for the zero-GL, which is automatically recorded for individual images ("Grey value offset (0-level)" in the Image Information panel). This zero-signal is measured with the laser switched off but the detector on and thus is potentially affected by room light (dimmed room light was used for experiments). The resultant corrected GL (cGL) represented mean fundus AF and allowed comparisons between animals on the assumption that detector gain and laser diode power were both relatively constant and did not vary significantly in the ~12-month duration of this study.

Recording of the Pupil Diameter

The dilated pupil diameter in mice was usually larger than the diameter of the scan pupil, resulting in no relevant loss of the incident excitation light. However, the dilated pupil diameter was generally smaller than the diameter of the detection pupil, causing a loss of AF detection. To monitor this we measured the pupil diameter from an image of the pupil captured before each fundus AF image or each sequence of images. Each time, the focus was set at +50D, and the pupil was brought into focus by adjusting the *z*-position of the camera, with the eye in the center of the image to avoid distortions. This approach standardized the distance between camera and pupil plane and, hence, the magnification factor. The pupil diameter was measured in pixels using ImageJ after fitting a circular area to the largest pupil diameter. A scale factor of 83 pixels/1 mm, based on measurements of the image of the diameter of the contact lens centered in the iris image, allowed conversion to millimeters. The refraction at the anterior segment of the mouse eye, and especially at the interface air/contact lens, resulted in a magnification of the image of the pupil plane, acquired at a refraction setting of +50 D. This magnification was estimated by Zemax simulation to be in the order of 16% (Dr. Jörg Fischer, Heidelberg Engineering, data on file) and may explain differences of our measurements compared with smaller postmortem measurements of the pupil.[23] This magnification factor also affected the optical path. Thus, the calculated sizes of the scan pupil and the detection pupil (1.7 mm and 3.4 mm, respectively, for the 55° field lens; HRA2 55° Objective User Information, Heidelberg Engineering) were reduced to approximately 1.4 mm and 2.9 mm, respectively.

RESULTS

Image Acquisition

Contact Lens. Anesthetized mice with dilated pupils may develop cataract within few minutes, which may be related to corneal desiccation.[24] To investigate the optimal strategy to maintain clear ocular media throughout, fundus AF images were recorded using a contact lens (with Hypromellose coupling fluid as described earlier), artificial tears (Hypromellose) alone, or with neither of these protective measures (Fig. 2). The lack of corneal protection consistently resulted in cataract formation and reduced fundus AF signal intensity in minutes. Contact lens placement was found to be a reliable means to avoid this. Application of artificial tears alone also resulted in a protective effect, though this was more variable than with the contact lens.

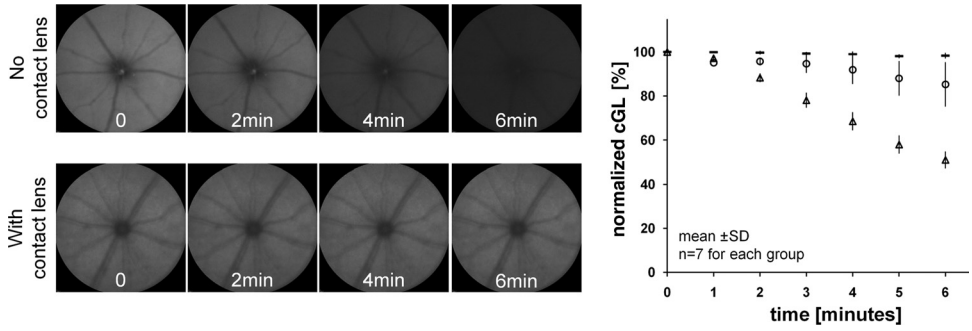

FIGURE 2. Prevention of media opacity using a contact lens. Cataract development in anesthetized mice with dilated pupils, without measures to prevent corneal desiccation, results in image deterioration within minutes (*upper row*). Quantification of the decreasing fundus AF (normalized to the first measurement at 0 minutes) is shown in the graph (*triangles*). Such media opacity can be avoided by protecting the cornea from drying using a contact lens (*lower row*, *horizontal bars*). A similar but less consistent effect can be achieved using a corneal lubricant (*circles*). cGL, corrected gray level.

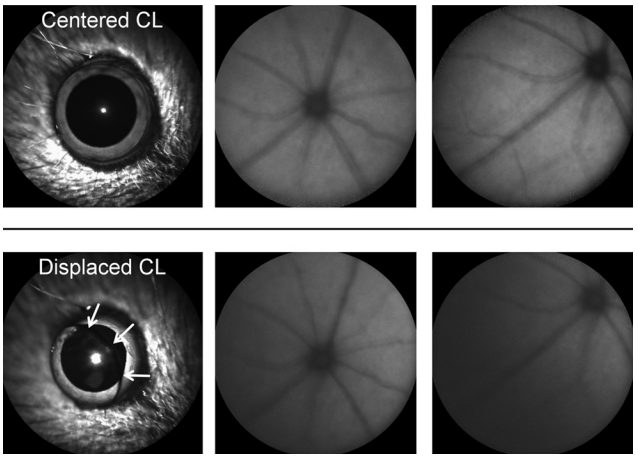

FIGURE 3. Correct placement of the contact lens (CL) is necessary for recording images with even illumination of the fundus (*upper row*). Displacement of the contact lens results in shadowing of the fundus image (*lower row*; *arrows* mark lens margin). Adequate lens position can be controlled using the cSLO image focused on the anterior segment (e.g., +50 D).

We found that contact lens use allowed better comparability between animals because of the consistent curvature of the contact lens. Additionally, the small eyes of very young mice could be imaged with the contact lens application. The contact lens may lead to a change in magnification and thus a more or less wider fundus area displayed.

For optimal recordings of the posterior pole, the contact lens had to be placed exactly on the corneal center (Fig. 3). Off-center lens position caused shadowing in the direction of lens displacement. However, when imaging the peripheral retina, deliberate displacement of the lens toward the incident light beam usually improved peripheral fundus illumination.

Camera Position. Uneven retinal illumination may also be caused by poor camera alignment with the pupillary axis and plane and improper camera position along the *z*-axis (Fig. 4, upper row). Notably, the latter factor also significantly affected image magnification. Translation of camera *z*-position by only 4 mm resulted in an approximate doubling of the apparent optic disc diameter (Fig. 4, bottom row).

Focus. After aligning the camera using the NIR reflectance mode (820 nm laser), a dioptric shift of approximately +8 D to +10 D (due to chromatic aberration) is needed to refocus the 488 nm fundus AF image on the same retinal plane as the NIR image (Fig. 5). Focusing on other layers of the retina then necessitates additional dioptric shifts. The shorter focal length of the mouse eye results in greater confocality than in humans. Thus, a large change of approximately +30 D to +40 D was necessary to change the focus from the outer retinal reference plane (see Methods) to the nerve fiber layer of the inner retina in adult wild-type mice. With the contact lens in place and maximal pupil dilation, a focus setting of about +30 D was often a good estimated initial configuration to identify the outer retinal reference plane in adult mice. However, mouse strain, age, and pupil dilation may considerably affect the nature of the dioptric adjustments necessary for optimal focus.

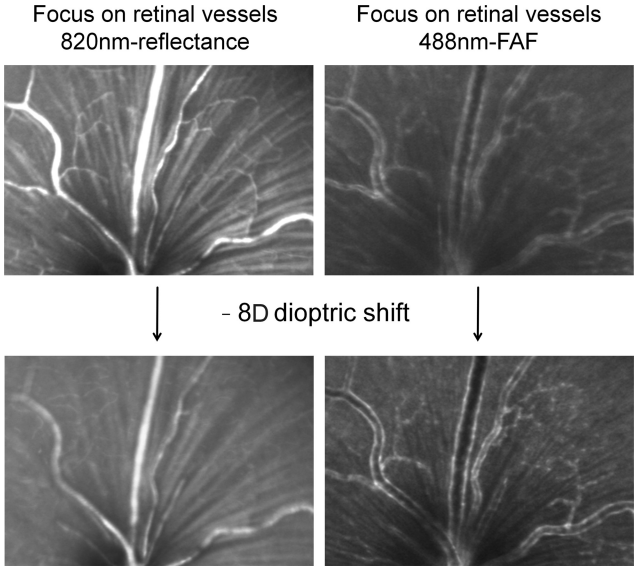

FIGURE 5. Dioptric shift with change in illumination wavelength. When using the 820 nm reflectance image for positioning of the camera and locating the confocal plane of interest (*upper left*), the 488 nm fundus AF image is not in focus (*upper right*; the vascular walls are visible because of expression of the fluorescent reporter protein DsRed under control of the actin promoter). The confocal plane must be corrected by approximately 8 D. Images are cropped from images recorded with the 55° field lens.

Pupil Diameter. The pupil size in mice after dilation with tropicamide and phenylephrine varies greatly with age (exem-

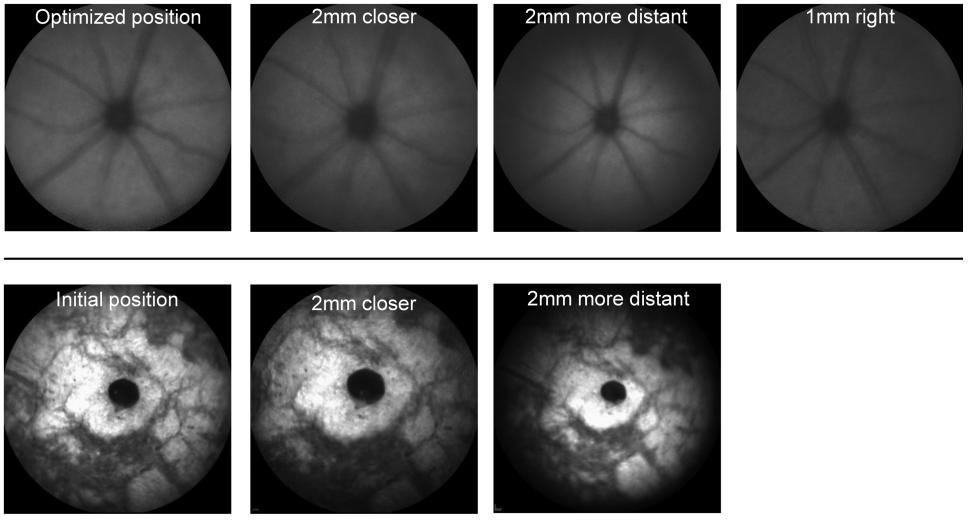

FIGURE 4. Influence of camera position on fundus shadowing and magnification. Misalignment from an optimized camera position results in peripheral image shadowing (*upper row*). Changes of the camera position in the *z*-axis led to significant changes in image magnification and thus influenced the scale factor (*bottom row*). The focus was readjusted for each camera position. A degenerated retina was recorded using the NIR reflectance mode because of the superior visibility of the disc margin.

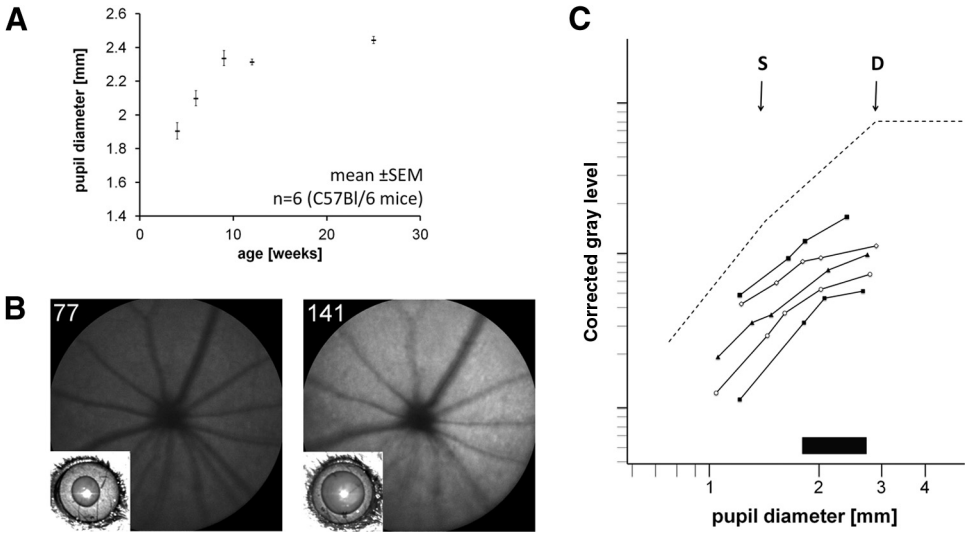

Figure 6. (**A**) Pupil size increases with age, especially during the first 3 months of life. (**B**) Effect of different pupil diameters on AF measurement, exemplified in a 5-month-old *Abca4*$^{-/-}$ mouse. The midperipheral cGL was measured (indicated in the *upper left corner* of each fundus image). *Insets*: NIR iris images recorded immediately after the AF image. (**C**) Log-log plots showing the variation of fundus AF with pupil diameter for five eyes (different symbols, minimum of four measures per eye). The curves were slightly displaced vertically for clarity (≤5%). *Interrupted line*: theoretical prediction of how AF would change with change in pupil diameter in the assumptions those pupils are concentric with the iris, that the laser irradiance in the scan pupil is uniform, and that the pupil diameter is recorded at the same time as the fundus AF image. *Arrows*: diameters of the scan pupil (S) and the detection pupil (D), respectively. *Black horizontal bar*: range of pupil diameters for all other instances in this study.

plified for C57Bl/6 mice in Fig. 6A). The dilated pupil diameters measured in this study ranged from 1.9 mm to 2.3 mm (Fig. 6C, black bar) and thus remained below the diameter of the detection pupil. To assess the effect of pupil size on AF measurement, repetitive combined measurements of pupil size and fundus AF intensity were obtained during successive pharmacologic pupil dilation (phenylephrine in fellow eye, tropicamide in recorded eye, additional phenylephrine in recorded eye). The focus of the reference plane (see Methods) changed slightly for each pupil diameter (most likely because of spherical aberrations) and thus was adjusted for each fundus AF image. Figure 6B illustrates the effect of increasing pupil size in the same eye on fundus AF. Measurements in our study were at pupil diameters between that of the scan pupil and that of the detection pupil (Fig. 6C). The time needed to refocus and reposition the camera between fundus and pupil imaging, and the relatively fast pupil dilation in mice, remained sources of imprecision in our study when attempting to correlate pupil diameter with fundus AF measurements.

Recording and Quantifying Autofluorescence from the RPE

cGL analysis of fundus AF images from the reference plane (see Methods) and adjacent confocal planes suggested that the reference plane was a good approximate position from which to record the highest AF signal originating from the RPE (Fig. 7A). The deviation of the mean cGL from the mean maximum cGL was ≤5% within ±4 D defocus and ≤10% within ±8 D defocus from the reference plane. The highest fundus AF signal was always measured within ±6 D defocus from the reference plane. More severe defocus further reduced the AF signal detected (Fig. 7A).

The test-retest variability of RPE AF measurements was assessed in 31 eyes of 31 animals (C57Bl/6 and *Abca4*$^{-/-}$). After the reference plane was identified, a 488 nm fundus AF image was recorded (test 1). The mouse was then taken off the platform, and the contact lens was removed. Hypromellose eyedrops were applied again, the contact lens was replaced

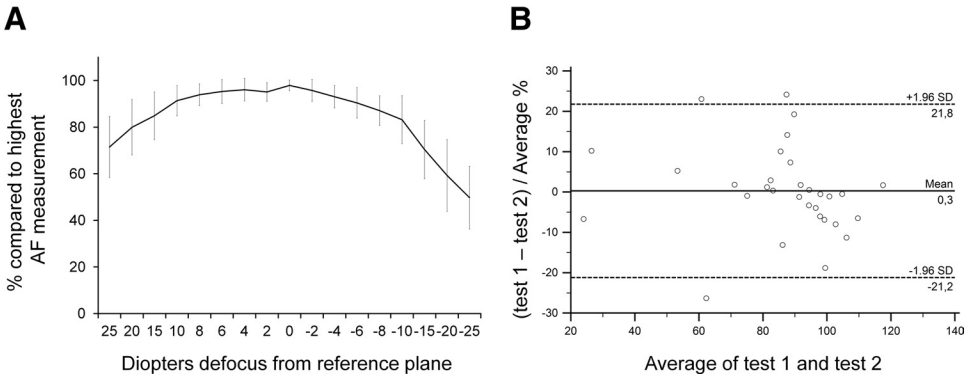

Figure 7. Recording AF from the RPE in mice. (**A**) Effect of defocus from a reference plane, defined as the confocal plane with the highest reflectivity in the NIR reflectance mode. AF images were recorded in 2 D steps in a range of ±10 D defocus from the reference plane and 5 D steps outside this range up to ±25 D defocus; $n = 13$. Mean ± SD. (**B**) Bland-Altman plot of percentage difference against mean for quantitative fundus AF measurements (cGL). *Continuous line*: mean difference; *dashed lines*: 95% limits of agreement.

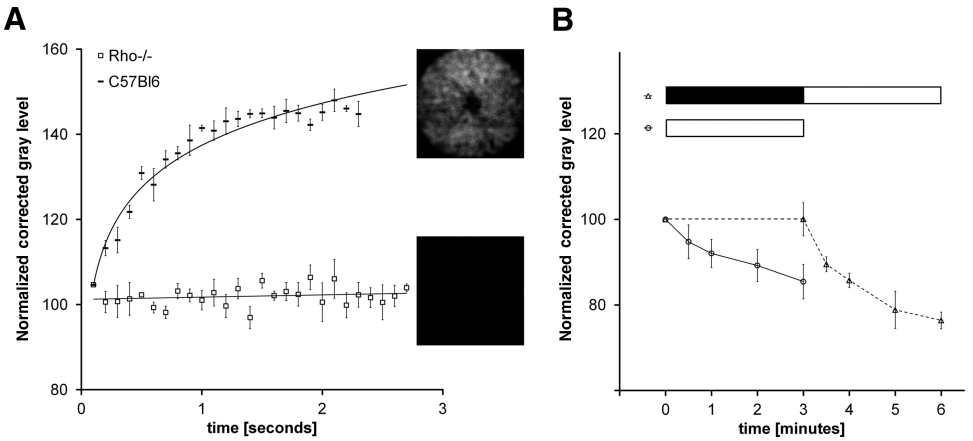

FIGURE 8. Effect of blue light exposure on the measured fundus AF signal. (**A**) Photopigment bleaching increases fundus AF considerably within the first 1.5 seconds of blue light exposure in wild-type C57Bl/6 mice. This increase is not seen in *Rho*$^{-/-}$ mice that lack photopigment. The mean ± SEM of four independent measurements is shown. (*insets*) Enhanced fundus differential maps (at 2 seconds minus baseline) in wild-type (*top*) and *Rho*$^{-/-}$ mice (*bottom*). (**B**) During continuous light exposure over 3 minutes (*lower horizontal white bar*), there is an approximately 15% decrease in measured fundus AF (*circles, solid line*). A similar change was observed after a 3-minute interval without light exposure, during which AF remained stable (*upper black and white horizontal bar*). The mean ± SEM of four independent measurements in C57Bl/6 mice is shown.

and imaging was performed (test 2) as in test 1. Midperipheral cGL was measured as described earlier in the Methods. Measures from test 1 and test 2 were not significantly different (P = 0.93, paired t-test). The intersession coefficient of repeatability (1.96 × SD of the differences between the two measurements) was approximately ±22% (95% confidence interval; Fig. 7B).

Bleaching Experiments

Bleaching of rhodopsin in photoreceptors changes its absorption maximum (λ_{max}) from ~500 nm to ~330 nm, which leads to decreased 488 nm light absorption by the photoreceptor layer. This results in higher 488 nm light exposure of the RPE layer and thus an increased excitation of RPE AF.[21,25]

Because of the high retinal irradiance (~30 times what is used in human with the 30° lens; see Discussion) and no possibility to reduce the excitation light through the user interface, we predicted that bleaching would occur much more rapidly than the ~30 seconds it takes in humans.[21] Therefore, the "high-speed" movie mode was started and the laser activated while the optical path was manually occluded with black card. Rapid removal of the occluder allowed immediate high speed image sequence acquisition from the moment of 488 nm laser bleaching onset. There was an ~40% increase in fundus AF in the first 1.5 seconds it laser illumination in 2-month-old C57Bl/6 mice that leveled off thereafter (Fig. 8A). In age-matched *Rho*$^{-/-}$ mice, in which rhodopsin as the major photopigment in the retina is absent, no change in fundus AF intensity was noted. Photopigment bleaching and thus photopigment distribution can be mapped topographically by subtraction of unbleached from a bleached fundus AF image (Fig. 8A).

In addition to photopigment bleaching, we observed a slow decrease of fundus AF during several minutes of blue light exposure. Continuous exposure to the excitation light over 3 minutes resulted in lower fundus AF measurements. If a 3-minute control interval preceded the continuous light exposure, there was no change during the initial dark phase.

Fundus Autofluorescence Imaging in Wild-Type Mice and Disease Models

Figure 9 compares 488 nm and 790 nm fundus AF pattern and intensity in three mouse strains (WT129, C57Bl/6, BALB/c) commonly used in retinal research and in the *Abca4*$^{-/-}$ mouse, a model of Stargardt disease. Patients with Stargardt disease have increased 488 nm fundus AF[8] because of excessive accumulation of lipofuscin in the RPE.

Fundus AF at 488 nm was lowest in the two wild-type strains, WT129 and C57Bl/6. In BALB/c mice, the dots of increased AF may represent subretinal photoreceptor debris[3] or lipofuscin-containing macrophages and/or microglia cells, as described in another mouse model with a similar phenotype.[26] Notably, the resultant jagged gray level profile shows a higher background signal compared with the two wild-type strains, possibly because of the increased accumulation of lipofuscin fluorophores or, alternatively, the increased excitation light from the lack of iris and fundus pigmentation. The cGL in the *Abca4*$^{-/-}$ mouse was approximately twice the level in the wild-type strains. There was a pattern of focally increased AF in the *Abca4*$^{-/-}$ mouse, revealing a faint flecked phenotype similar to the flecked fundus AF appearance in Stargardt patients.

AF at 790 nm is thought to originate from melanin in the RPE and choroid. Accordingly, the AF signal was almost absent in the nonpigmented BALB/c mouse when compared with pigmented mouse strains. Fundus AF 790 nm intensity in the *Abca4*$^{-/-}$ mouse on a WT129 background was about twice as high as in WT129 mice.

Figure 10 shows fundus AF images from two mouse models of retinal dystrophies. *Pde6b*$^{rd1/rd1}$ mice homozygous for the *rd1* mutation have an early-onset, fast retinal degeneration with loss of all rods within the first month of life.[27] *Rho*$^{-/-}$ mice have an absence of rod function caused by the lack of rhodopsin. At 3 months of age, photoreceptor degeneration is essentially complete.[19]

Both animal models show a marked reduction in 488 nm fundus AF intensity at the age of 3 months compared with wild-type animals (Fig. 10A). This finding is consistent with a lack of lipofuscin accumulation from the absence of a normal visual cycle. Fundus AF at 790 nm was lower in the *Pde6b*$^{rd1/rd1}$ mouse than in the wild-type mouse but was slightly higher in the *Rho*$^{-/-}$ mouse. Only after normalization by histogram stretching did both imaging modalities reveal an altered pattern

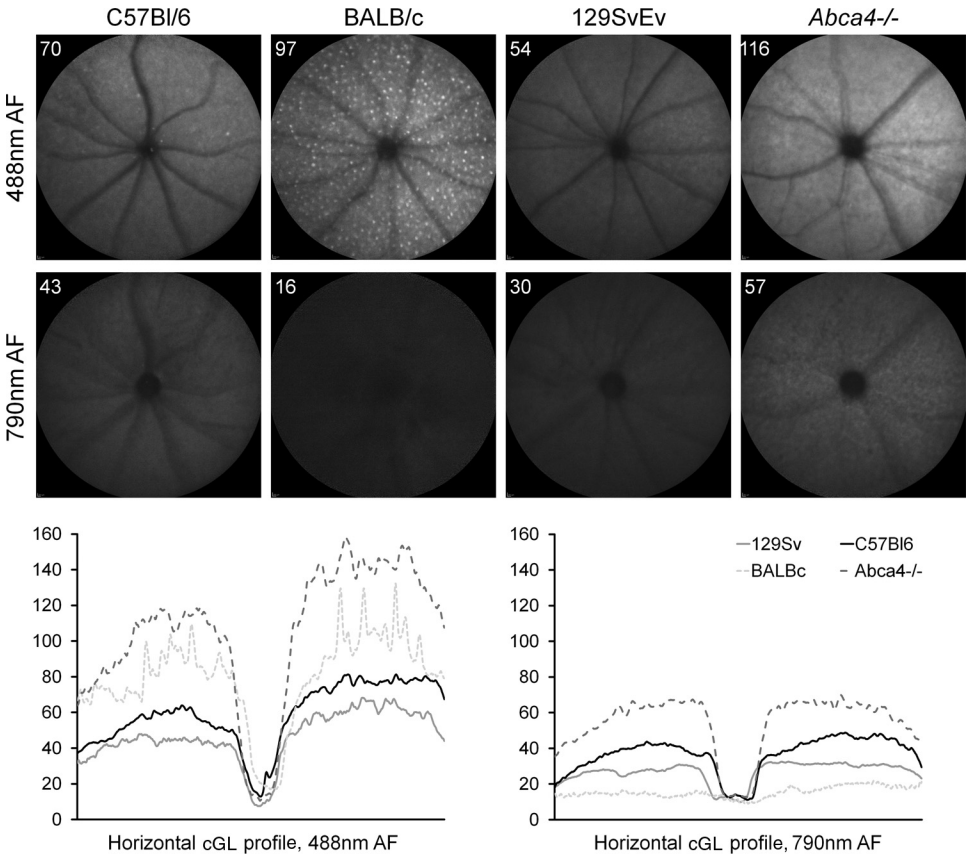

Figure 9. Pattern and corrected gray level (cGL; representing fundus AF intensity) on 488 nm and 790 nm fundus AF images in three wild-type mouse strains and an *Abca4*$^{-/-}$ mouse at 6 months of age. Standardized image acquisition and detector settings allow quantification and comparison of the AF intensity. The numbers in the *left upper corner* of each fundus image represent the mean cGL measured in the midperiphery. The horizontal cGL profile through the optic disc is shown in the *bottom* line plots for 488 nm (*left*) and 790 nm (*right*) fundus AF images. Pupil diameter was 2.2, 2.33, and 2.26 mm in the WT129, C57Bl/6, and *Abca4*$^{-/-}$ mice, respectively, and was not recorded in the BALB/c mouse because of the translucent iris.

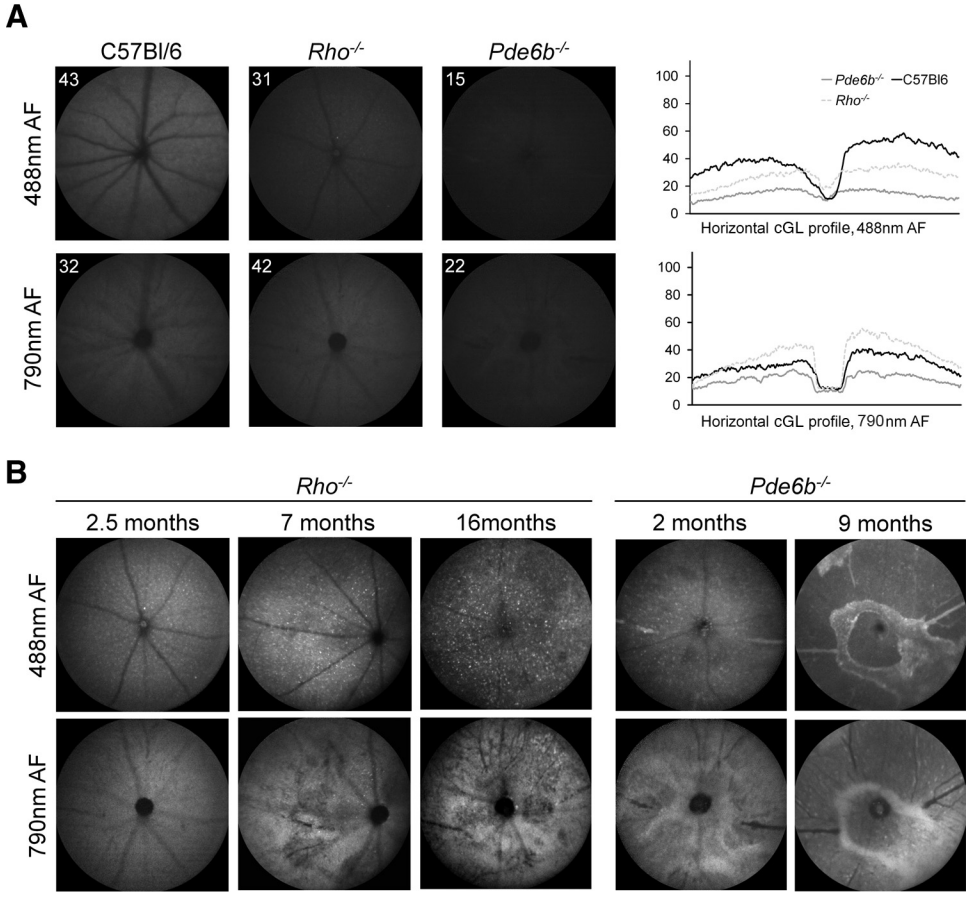

Figure 10. GL (**A**) and pattern (**B**, contrast enhanced) fundus AF images in two mouse models for retinal dystrophies. (**A**) Both models have a lack of photoreceptor outer segment shedding and thus do not accumulate lipofuscin, resulting in a reduced AF compared with an age-matched wild-type mouse. Pupil diameter was 2.23, 2.28, and 2.30 mm in the *C57Bl/6, Rho*$^{-/-}$, and *Pde6b*$^{rd1/rd1}$ mouse, respectively. cGL, corrected gray level. (**B**) Histogram stretching and contrast enhancement reveals a pattern of further decreased AF that first appears on 790 nm AF images. All alterations occur earlier in the faster progressing *Pde6b*$^{rd1/rd1}$ model. *Rho*$^{-/-}$, rhodopsin knockout mouse. *Pde6b*$^{rd1/rd1}$, nonsense mutation in Pde6b.

compared with normal (Fig. 10B). The slow progressive degeneration in the $Rho^{-/-}$ mouse revealed a multitude of fluorescent spots on 488 nm AF, possibly representing activated microglia,[28] which appeared to increase in number with age. At 7 months, large patches with a decreased signal were visible only on 790 nm AF. In a 16-month-old $Rho^{-/-}$ mouse, these areas were also faintly visible on 488 nm fundus AF images. In the $Pde6b^{rd1/rd1}$ mouse, onset of similar phenotypic observations occurred at earlier time points; at 2 months there were areas of reduced 790 nm AF signal that subsequently became apparent on 488 nm AF. $Pde6b^{rd1/rd1}$ mice demonstrated higher AF signal intensity (relative to adjacent areas) at the border of atrophic areas, which was not seen in $Rho^{-/-}$ mice.

Discussion

In this study, the parameters affecting fundus AF imaging in mice were studied so the procedure could be optimized and standardized to allow quantitative assessment of FA. A standard protocol for fundus AF imaging in mice has been designed (Supplementary Material, http://www.iovs.org/lookup/suppl/doi:10.1167/iovs.11-8767/-/DCSupplemental) and was subsequently applied to mouse models for retinal diseases.

Image Acquisition

Considerable improvement in image quality may be achieved by using a contact lens (Fig. 2). Media opacities decrease the detectable signal and the signal-to-noise ratio of the already low fundus AF signal in mice. The contact lens prevents the development of cataract and ensures a consistent surface profile across different mice. It also enables recording from very small eyes in young animals in which adjustment of the confocal plane can otherwise be very difficult.

A scale factor would allow the conversion of cSLO fundus image measurements in pixels into actual size. Differences in the optical properties and sizes of the human and mouse eyes render current software algorithms unsuitable for use in mice. Assuming a full angle of view of the murine fundus with the 55° lens, a 1.1- to 1.2-μm/pixel scale factor may be calculated based on the number of pixels per degree (1536 pixels per 55° fundus image = 28 pixels/1° visual angle) and estimates of the lateral measure of the visual angle on the mouse retina (1° visual angle = 31 to 34 μm[23,29]). The exposed circular retinal area can thus be calculated as $3.14 \times (1.1\text{- to } 1.2\text{-}\mu\text{m/pixel} \times 768 \text{ pixels} \times 10^{-3} \text{ mm/}\mu\text{m})^2$ or 2.2 to 2.7 mm^2.

We observed that small changes in camera *z*-position resulted in large effects on image magnification (Fig. 4, bottom), a finding not usually obvious in humans. Tests with graph paper (not shown) revealed that this effect increases with high positive focus settings as used in mice, which are rarely needed in patients. The dependency of magnification on the distance between the retina and the camera, and thus on eye growth, implies that fixed scales for cSLO images of the mouse fundus will remain imprecise. Possible effects of image magnification on AF measurements were therefore not accounted for in this study.

Both the dioptric shift necessary to correct for chromatic aberrations (Fig. 5) and the high confocality of the mouse eye are in line with previous reports,[2,30] with the latter allowing for excellent discrimination between retinal planes. Retinal thickness measurements in vivo revealed variable results in mice, ranging from ~200 μm to ~300 μm.[31,32] Based on the +30 to 40 D change necessary to focus from the outer to the inner retinal border, an effect of ~5 to 10 μm change per diopter change in focus may be estimated. A lower dioptric range between inner and outer retina may suggest retinal atrophy.

Recording and Quantifying Autofluorescence from RPE

Fundus AF originates mainly from fluorophores in the RPE[6] and therefore from a defined plane between Bruch's membrane and the neurosensory retina. Reliable localization of this confocal plane while recording fundus AF is difficult to achieve in mice because of the lack of fluorescent structures or landmarks with high contrast or signal intensity, and only minor effects on measured AF with small focus changes in the outer retinas of mice (Fig. 7A). A reference plane of highest NIR reflectivity may instead be used to approximate the plane of highest fundus AF (Fig. 7A). An origin of the high NIR reflectance from the Bruch's membrane/RPE complex is supported by human cSLO reflectance studies that suggest higher reflectivity caused by melanin[33] and by the high reflectivity from the Bruch's membrane/RPE complex on OCT recordings using a similar wavelength in the NIR range. Small dioptric shifts between highest AF signal and reference plane may be attributed to slightly different planes of origin, chromatic aberrations, and minor measurement errors. The only small changes of measured AF with defocusing ±4 D from the reference plane may be explained by the high confocality in the mouse eye, resulting in a change of only ±20 to 40 μm across the RPE.

Measurement of fundus AF in mice is substantially affected by the small size of the dilated pupil in mice, restricting the detection pupil and thus underestimating the fundus AF (Fig 6). The scan pupil was generally smaller than the dilated pupil. When pupil diameter was varied in the same animal, we found a near-exponential relationship between fundus zero-cGL and pupil diameter (log-log plot; Fig. 6C). The slopes for the five animals varied between 1.4 and 2.8 (mean, 2.0 ± 0.4), indicating that the cGL was roughly proportional to the area of the pupil aperture (the data for the largest diameter were removed because these might have been equal to or larger than the diameter of the detection pupil). This suggests that correction for loss of AF because of pupil obstruction may be feasible, but further experiments are needed to confirm these somewhat variable data. Smaller custom-made cSLO apertures may be used in future studies to reduce both the size of the scan pupil and the detection pupil, though at the expense of resolution and signal strength.

When measuring fundus AF in mice, the procedure as performed in this study has limitations. To allow comparison between mice with different pupil diameters (e.g., in longitudinal observations and when comparing fundus AF between mice of different ages), a correction for variation in pupil diameter would be needed. Such correction was not implemented in this study because pupil diameters were about equal when AF measurements were compared (Figs. 9, 10). Furthermore, variability between measurements could be minimized by using an internal reference, as described recently in a human study.[21] It would account for short-term (warm-up) and long-term changes in laser power and detector sensitivity fluctuations and would provide a check for the consistent functioning of the camera. An internal reference would also permit expression of fundus AF measurements in a format that can be compared among studies obtained with different cameras. However, variation in fundus AF measurements between operators and because of suboptimal standardization of the recording procedure (e.g., differences in pupil dilation, camera alignment, control of media opacity) appear to have a higher impact on fundus AF measurements in mice than in humans. Thus, an internal reference would increase confidence on the functioning of the setup, but variability is likely to remain higher than in humans.

Bleaching Experiments

An effect of photopigment bleaching on fundus AF in mice was observed within the first 1.5 seconds of exposure to the excitation light using the 55° cSLO lens (Fig. 8A), which is much faster than in human AF imaging using the 30° cSLO lens (20–30 seconds[21,25]). The difference can be explained by the fact that approximately the same beam power (~260 μW) is used to scan a smaller retinal area in mouse (2.2–2.7 mm^2) than in human imaging (79 mm^2, with a 30° field). As a result, the retinal irradiance occurring in mouse imaging is approximately 30 times higher than in human imaging (488 nm AF imaging using the Spectralis HRA; ~10 mW/cm^2 and 0.3 mW/cm^2 for mice and humans, respectively, ignoring media-related light loss).

In addition, a slight decrease of fundus AF over time was observed during continuing blue light exposure. A photochemical effect of relevant fluorophores or a masking of fluorophores by photochemical generation of additional absorbers might explain this finding. A reversible decrease in fundus AF ("fading") has been observed in monkeys after exposure to 5 to 210 J/cm^2 with 568 nm light over long exposure periods (15 minutes).[34,35] The lower end of the range observed in monkeys would just approximate the 1.8 J/cm^2 retinal radiant exposure during 488 nm cSLO AF imaging in mice (retinal irradiance of 10 mW/cm^2 for 3 minutes). More experimental evidence is needed here to ascertain whether this represents the same process.

Photoreversal of bleaching is a process by which rhodopsin is photochemically regenerated within photoreceptors during intense blue light exposure. The reported kinetics appears to be in line with our experiments. The effect was observed in rats with a retinal irradiance of 300 $\mu W/cm^2$ using 403 nm light,[36] which is ~2 log units below the irradiance during 488 nm AF imaging (Spectralis HRA) in mice. If photoreversal of bleaching underlies the observed decrease in fundus AF, the higher irradiance might compensate for a mismatch of the 488 nm excitation light with the absorption maximum of the suggested photoreversible intermediate.

Fundus Autofluorescence Imaging in Different Mouse Strains and Models of Retinal Disease

Light at 488 nm is close to the excitation maximum of lipofuscin,[6] of which major components accumulate extensively in the *Abca4*$^{-/-}$ mouse.[18] Consistent with this, we observed 488 nm AF to be much higher in the *Abca4*$^{-/-}$ mouse than in wild-type animals (Fig. 10). Additionally, mice with retinal degenerations, in which a lack of visual cycle byproducts would be expected to result in less A2E accumulation (*Pde6b*$^{rd1/rd1}$ and *Rho*$^{-/-}$ mouse), had a much lower fundus AF (Fig. 10A). Such quantitative AF measurements may be useful in humans to classify retinal dystrophies according to their AF levels. This may suggest certain genetic defects or pathophysiological pathways, as exemplified previously for patients with mutations in *ABCA4*, *RPE65, RDH5,* or *MERTK*.[8–11] Furthermore, excitation at 790 nm, which has been suggested to excite melanin fluorescence,[12–14] results in a higher fluorescence signal in highly pigmented mice and only very low signals in albino mice (BALB/c). Interestingly, the *Abca4*$^{-/-}$ mouse showed the highest 790 nm fundus AF. Longitudinal and histopathologic studies may shed light on the nature of this finding, which is in line with human data that have thus far remained unexplained.[15]

Histogram stretching and contrast enhancement of AF images in *Rho*$^{-/-}$ and *Pde6b*$^{rd1/rd1}$ mice produced images reminiscent of human retinal dystrophies (Fig. 10B). In early stages, there was a pattern of spotted relatively increased AF. Histologic studies suggest that such foci of increased AF may correlate with lipofuscin-containing macrophages, microglia cells, or both.[26,28,37] A progressive localized loss of fundus AF develops over time. The faster progressing phenotype (*Pde6b*$^{rd1/rd1}$ mouse) revealed areas of increased AF surrounding areas of presumed atrophy, which was not observed in the slowly progressing phenotype (*Rho*$^{-/-}$ mouse). Similar phenomena have been described in patients, in whom increased AF surrounding atrophy may be a marker for disease progression.[5,38] Notably, in the *Rho*$^{-/-}$ and the *Pde6b*$^{rd1/rd1}$ mouse, only contrast enhancement made these patterns visible against a very low fluorescent background. Thus, such patterns are not necessarily indicative of abnormal and potentially cytotoxic lipofuscin accumulation but might rather reflect multilayered RPE cells, photooxidized fluorophores, or impaired photoreceptors.[39] Moreover, changes appear to be visible earlier on 790 nm AF, which is in line with findings in patients in whom 790 nm fundus AF often shows larger affected areas than other imaging modalities, including 488 nm fundus AF.[16,17]

Conclusion

We have shown that consistent and reproducible fundus AF imaging is feasible in mice through adherence to key principles such as the prevention of media opacities and standardization camera position and confocal plane during image acquisition. Fundus AF, now increasingly accepted as a meaningful clinical outcome measure, may allow noninvasive and longitudinal assessment in preclinical models, potentially reducing the number of research animals needed. Furthermore, phenotypic similarities with fundus AF findings in patients suggest that animal models for retinal diseases may be used to investigate further the correlation between histopathology and disease-related AF phenomena. Our findings support the clinical use of AF imaging in the definition of different phenotypes of retinal degeneration in monitoring disease progression and the possible response to innovative treatments.

Acknowledgments

The authors thank Jörg Fischer (Heidelberg Engineering, Heidelberg, Germany) for helpful discussions.

References

1. Rivas MA, Vecino E. Animal models and different therapies for treatment of retinitis pigmentosa. *Histol Histopathol.* 2009;24:1295–1322.
2. Paques M, Simonutti M, Roux M, et al. High resolution fundus imaging by confocal scanning laser ophthalmoscopy in the mouse. *Vision Res.* 2006;46:1336–1345.
3. Seeliger MW, Beck SC, Pereyra-Muñoz N, et al. In vivo confocal imaging of the retina in animal models using scanning laser ophthalmoscopy. *Vision Res.* 2005;45:3512–3519.
4. Fischer MD, Huber G, Beck SC, et al. Noninvasive, in vivo assessment of mouse retinal structure using optical coherence tomography. *PLoS One.* 2009;4:e7507.
5. Schmitz-Valckenberg S, Holz FG, Bird AC, Spaide RF. Fundus autofluorescence imaging: review and perspectives. *Retina.* 2008;28:385–409.
6. Delori FC, Dorey CK, Staurenghi G, Arend O, Goger DG, Weiter JJ. In vivo fluorescence of the ocular fundus exhibits retinal pigment epithelium lipofuscin characteristics. *Invest Ophthalmol VisSci.* 1995;36:718–729.
7. von Rückmann A, Fitzke FW, Bird AC. Fundus autofluorescence in age-related macular disease imaged with a laser scanning ophthalmoscope. *Invest Ophthalmol Vis Sci.* 1997;38:478–486.
8. Delori FC, Staurenghi G, Arend O, Dorey CK, Goger DG, Weiter JJ. In vivo measurement of lipofuscin in Stargardt's disease-fundus flavimaculatus. *Invest Ophthalmol Vis Sci.* 1995;36:2327–2331.

9. Lorenz B, Wabbels B, Wegscheider E, Hamel CP, Drexler W, Preising MN. Lack of fundus autofluorescence to 488 nanometers from childhood on inpatients with early-onset severe retinal dystrophy associated with mutations in RPE65. *Ophthalmology.* 2004; 111:1585–1594.
10. Charbel Issa P, Bolz HJ, Ebermann I, Domeier E, Holz FG, Scholl HP. Characterization of severe rod-cone dystrophy in a consanguineous family with a splice site mutation in the *MERTK* gene. *Br J Ophthalmol.* 2009;93:920–925.
11. Sergouniotis PI, Sohn EH, Li Z, et al. Phenotypic variability in RDH5 retinopathy (*Fundus albipunctatus*). *Ophthalmology.* 2011;118:1661–1670.
12. Keilhauer CN, Delori FC. Near-infrared autofluorescence imaging of the fundus: visualization of ocular melanin. *Invest Ophthalmol Vis Sci.* 2006;47:3556–3564.
13. Gibbs D, Cideciyan AV, Jacobson SG, Williams DS. Retinal pigment epithelium defects in humans and mice with mutations in MYO7A: imaging melanosome-specific autofluorescence. *Invest Ophthalmol Vis Sci.* 2009;50:4386–4393.
14. Schmitz-Valckenberg S, Lara D, Nizari S, et al. Localisation and significance of in vivo near-infrared autofluorescent signal in retinal imaging. *Br J Ophthalmol.* 2011;95:1134–1139.
15. Cideciyan AV, Swider M, Aleman TS, et al. Reduced-illuminance autofluorescence imaging in ABCA4-associated retinal degenerations. *J Opt Soc Am A Opt Image Sci Vis.* 2007;24:1457–1467.
16. Kellner S, Kellner U, Weber BH, Fiebig B, Weinitz S, Ruether K. Lipofuscin- and melanin-related fundus autofluorescence in patients with ABCA4-associated retinal dystrophies. *Am J Ophthalmol.* 2009;147:895–902, e891.
17. Kellner U, Kellner S, Weber BH, Fiebig B, Weinitz S, Ruether K. Lipofuscin- and melanin-related fundus autofluorescence visualize different retinal pigment epithelial alterations in patients with retinitis pigmentosa. *Eye.* 2009;23:1349–1359.
18. Weng J, Mata NL, Azarian SM, Tzekov RT, Birch DG, Travis GH. Insights into the function of Rim protein in photoreceptors and etiology of Stargardt's disease from the phenotype in abcr knockout mice. *Cell.* 1999;98:13–23.
19. Humphries MM, Rancourt D, Farrar GJ, et al. Retinopathy induced in mice by targeted disruption of the rhodopsin gene. *Nat Genet.* 1997;15:216–219.
20. Helb HM, Charbel Issa P, Fleckenstein M, et al. Clinical evaluation of simultaneous confocal scanning laser ophthalmoscopy imaging combined with high-resolution spectral-domain optical coherence tomography. *Acta Ophthalmol.* 2010;88:842–849.
21. Delori F, Greenberg JP, Fischer J, et al. Quantitative measurements of autofluorescence with the scanning laser ophthalmoscope. *Invest Ophthalmol Vis Sci.* 2011;52:9379–9390.
22. Abramoff MD, Magalhães PJ, Ram SJ. Image processing with ImageJ. *Biophotonics Int.* 2004;11:36–42.
23. Schmucker C, Schaeffel F. A paraxial schematic eye model for the growing C57BL/6 mouse. *Vision Res.* 2004;44:1857–1867.
24. Ridder W 3rd, Nusinowitz S, Heckenlively JR. Causes of cataract development in anesthetized mice. *Exp Eye Res.* 2002;75:365–370.
25. Theelen T, Berendschot TT, Boon CJ, Hoyng CB, Klevering BJ. Analysis of visual pigment by fundus autofluorescence. *Exp Eye Res.* 2008;86:296–304.
26. Luhmann UF, Robbie S, Munro PM, et al. The drusenlike phenotype in aging Ccl2-knockout mice is caused by an accelerated accumulation of swollen autofluorescent subretinal macrophages. *Invest Ophthalmol Vis Sci.* 2009;50:5934–5943.
27. Noell WK. Differentiation, metabolic organization, and viability of the visual cell. *AMA Arch Ophthalmol.* 1958;60:702–731; discussion 731–703.
28. Xu H, Chen M, Manivannan A, Lois N, Forrester JV. Age-dependent accumulation of lipofuscin in perivascular and subretinal microglia in experimental mice. *Aging Cell.* 2008;7:58–68.
29. Remtulla S, Hallett PE. A schematic eye for the mouse, and comparisons with the rat. *Vision Res.* 1985;25:21–31.
30. Geng Y, Schery LA, Sharma R, et al. Optical properties of the mouse eye. *Biomed Opt Expr.* 2011;2:717–738.
31. Gabriele ML, Ishikawa H, Schuman JS, et al. Reproducibility of spectral-domain optical coherence tomography total retinal thickness measurements in mice. *Invest Ophthalmol Vis Sci.* 2010;51: 6519–6523.
32. Srinivasan VJ, Ko TH, Wojtkowski M, et al. Noninvasive volumetric imaging and morphometry of the rodent retina with high-speed, ultrahigh-resolution optical coherence tomography. *Invest Ophthalmol Vis Sci.* 2006;47:5522–5528.
33. Weinberger AW, Lappas A, Kirschkamp T, et al. Fundus near infrared fluorescence correlates with fundus near infrared reflectance. *Invest Ophthalmol Vis Sci.* 2006;47:3098–3108.
34. Morgan JI, Hunter JJ, Masella B, et al. Light-induced retinal changes observed with high-resolution autofluorescence imaging of the retinal pigment epithelium. *Invest Ophthalmol Vis Sci.* 2008;49: 3715–3729.
35. Morgan JI, Hunter JJ, Merigan WH, Williams DR. The reduction of retinal autofluorescence caused by light exposure. *Invest Ophthalmol Vis Sci.* 2009;50:6015–6022.
36. Grimm C, Reme CE, Rol PO, Williams TP. Blue light's effects on rhodopsin: photoreversal of bleaching in living rat eyes. *Invest Ophthalmol Vis Sci.* 2000;41:3984–3990.
37. Wang NK, Fine HF, Chang S, et al. Cellular origin of fundus autofluorescence in patients and mice with a defective *NR2E3* gene. *Br J Ophthalmol.* 2009;93:1234–1240.
38. Holz FG, Bindewald-Wittich A, Fleckenstein M, Dreyhaupt J, Scholl HP, Schmitz-Valckenberg S. Progression of geographic atrophy and impact of fundus autofluorescence patterns in age-related macular degeneration. *Am J Ophthalmol.* 2007;143: 463–472.
39. Sparrow JR, Yoon KD, Wu Y, Yamamoto K. Interpretations of fundus autofluorescence from studies of the bisretinoids of the retina. *Invest Ophthalmol Vis Sci.* 2010;51:4351–4357.

Optimization of *in vivo* confocal autofluorescence imaging of the ocular fundus in mice and its application to models of human retinal degeneration

Peter Charbel Issa [1], Mandeep S. Singh [1], Daniel M. Lipinski [1], Ngaihang V. Chong [1], Alun R. Barnard [1], Robert E. MacLaren [1,2] *

[1] Nuffield Laboratory of Ophthalmology and Oxford Eye Hospital Biomedical Research Centre, University of Oxford, John Radcliffe Hospital, Oxford, United Kingdom

[2] Moorfields Eye Hospital, London, United Kingdom

Supplementary material

Standard protocol: Recording fundus autofluorescence (AF) in mice using a confocal scanning laser ophthalmoscope (cSLO[1])

1. Apply tropicamide and phenylephrine eye drops. Allow sufficient time for full pupil dilation.
2. Dab away dilating eye drops and apply Hypermellose eye drops 0.3% as viscous coupling between the contact lens and cornea. Don't let the cornea become dry
3. Place a contact lens [2] to prevent corneal drying and to improve image quality
4. Place mouse on a platform in front of the cSLO camera so that the eyes are positioned approximately at the level of the marking for a patients' eye position
5. Set focus to 50dptr. and align contact lens on the corneal center under infrared reflectance (labeled "IR" on the SpectralisHRA control panel) image control
6. Record an image with the pupil in the confocal plane for documentation of the pupil dilation
7. Move cSLO camera forward to visualize the fundus
8. Adjust focus to the outer retina (high reflectivity) in the IR-reflectance mode [3]
9. Optimize camera position, moving it slightly forward, backwards and side to side. Use the position with the least shadowing at the image margins.
10. Slightly overexpose the image and adjust the focus to the confocal plane of highest reflectivity [3]
11. Switch to fundus AF mode (labeled "FA" on the SpectralisHRA control panel) [4] and darken room light
12. Expose retina to excitation light for a standardized time interval (e.g. 30 or 60sec) to ensure standardized bleaching
13. Acquire an averaged fundus AF image [5] with standardized detector settings [6]
14. If required, acquire near-infrared fundus AF (labeled "ICG" on the SpectralisHRA control panel; much lower signal!) images with standardized detector settings

1. SpectralisHRA (Heidelberg Engineering, Heidelberg, Germany) used in this study.
2. PMMA mouse lens used in this study: see methods
3. This protocol is for recording AF from the retinal pigment epithelium. Confocal plane and detector setting have to be adjusted if fluorescence from other retinal planes need to be recorded, e.g. when imaging mice expressing fluorescent reporter proteins in retinal cells.
4. Default settings: high resolution (1536x1536 pixels). Normalization switched off.
5. Either by recording a movie of 9+ images and averaging all adequate images post-acquisition, or by using the ART mode of the SpectralisHRA.
6. If the SpectralisHRA is used, don't exceed a detector setting of 100 (see methods). Contact manufacturer for details of other cSLO devices.

OPEN ACCESS Freely available online

PLOS ONE

Assessment of Tropism and Effectiveness of New Primate-Derived Hybrid Recombinant AAV Serotypes in the Mouse and Primate Retina

Peter Charbel Issa[1☯¤a], Samantha R. De Silva[1☯], Daniel M. Lipinski[1], Mandeep S. Singh[1], Alexandre Mouravlev[2], Qisheng You[1¤b], Alun R. Barnard[1], Mark W. Hankins[1], Matthew J. During[2,3], Robert E. MacLaren[1,4,5]*

1 Nuffield Laboratory of Ophthalmology, Nuffield Department of Clinical Neurosciences, University of Oxford, Oxford, United Kingdom, **2** Department of Molecular Medicine and Pathology, The University of Auckland, Auckland, New Zealand, **3** Department of Molecular Virology, Immunology and Medical Genetics, Ohio State University, Columbus, Ohio, United States of America, **4** Moorfields Eye Hospital Foundation Trust and UCL Institute of Ophthalmology National Institute for Health Research Biomedical Research Centre, London, United Kingdom, **5** Oxford Eye Hospital, Oxford University Hospitals NHS Trust and National Institute for Health Research Biomedical Research Centre, Oxford, United Kingdom

Abstract

Adeno-associated viral vectors (AAV) have been shown to be safe in the treatment of retinal degenerations in clinical trials. Thus, improving the efficiency of viral gene delivery has become increasingly important to increase the success of clinical trials. In this study, structural domains of different rAAV serotypes isolated from primate brain were combined to create novel hybrid recombinant AAV serotypes, rAAV2/rec2 and rAAV2/rec3. The efficacy of these novel serotypes were assessed in wild type mice and in two models of retinal degeneration (the *Abca4*$^{-/-}$ mouse which is a model for Stargardt disease and in the *Pde6b*$^{rd1/rd1}$ mouse) in vivo, in primate tissue ex-vivo, and in the human-derived SH-SY5Y cell line, using an identical AAV2 expression cassette. We show that these novel hybrid serotypes can transduce retinal tissue in mice and primates efficiently, although no more than AAV2/2 and rAAV2/5 serotypes. Transduction efficiency appeared lower in the *Abca4*$^{-/-}$ mouse compared to wild type with all vectors tested, suggesting an effect of specific retinal diseases on the efficiency of gene delivery. Shuffling of AAV capsid domains may have clinical applications for patients who develop T-cell immune responses following AAV gene therapy, as specific peptide antigen sequences could be substituted using this technique prior to vector re-treatments.

Citation: Charbel Issa P, De Silva SR, Lipinski DM, Singh MS, Mouravlev A, et al. (2013) Assessment of Tropism and Effectiveness of New Primate-Derived Hybrid Recombinant AAV Serotypes in the Mouse and Primate Retina. PLoS ONE 8(4): e60361. doi:10.1371/journal.pone.0060361

Editor: Anneke I. d e n Hollander, Radboud University Nijmegen Medical Centre, The Netherlands

Received August 4, 2012; **Accepted** February 26, 2013; **Published** April 9, 2013

Funding: This work was supported by Wellcome Trust Grant 086868/Z/08/Z and 094448/Z/10/Z; Oxford Stem Cell Institute; Health Foundation; Royal College of Surgeons of Edinburgh, NIHR Oxford and Moorfields Biomedical Research Centers, The European Commission, FP7, Marie Curie Intra-European Fellowship 237238; Fight for Sight. The funders had no role in study design, data collection and analysis, decision to publish, or preparation of the manuscript.

Competing Interests: The authors have declared that no competing interests exist.

* E-mail: enquiries@eye.ox.ac.uk

¤a Current address: Department of Ophthalmology, University of Bonn, Bonn, Germany
¤b Current address: Beijing Institute of Ophthalmology, Beijing Tongren Hospital, Capital Medical University, Beijing, China

☯ These authors contributed equally to this work.

Introduction

Inherited retinal dystrophies such as retinitis pigmentosa (RP) have until recently been untreatable. Recent developments in retinal gene therapy have led to the successful treatment of patients with Leber's congenital amaurosis (LCA) due to mutations in *RPE65* [1,2,3,4,5,6,7]. Although the studies were designed to investigate safety, lasting functional improvements in vision have been detected in some patients [1,6]. Importantly, these proof-of-principle studies have not suggested any relevant safety concerns with adeno-associated viral (AAV) vectors. Indeed, an AAV clinical trial has recently been started to treat choroideremia, which involves vector delivery to the fovea whilst it is still healthy, in order to prevent degeneration (NCT01461213).

While current retinal gene therapy trials have shown AAV vectors to be safe, there remain ongoing efforts to improve efficiency of gene delivery and to restrict vector tropism to specific retinal cell populations by modifying the capsid protein and/or the expression cassette. In the former case it has recently been shown that recombinant packaging of the AAV2 expression cassette into an AAV8 capsid (rAAV2/8) significantly enhanced transduction of primate photoreceptors when assessed by expression of green fluorescent protein (GFP) [8]. Furthermore the AAV5 capsid is known to transduce primate foveal cones effectively, as evidenced by restoration of trichromatic color vision in the macaque following treatment of dichromats with rAAV2/5 vector encoding the long (L) opsin gene [9].

The use of these recombinant vectors, in which a transgene cassette flanked by AAV2 inverted terminal repeats (ITR) is packaged into the capsid from another AAV serotype, is becoming established in retinal gene therapy. What has yet to be explored in detail, however, is how AAV vectors might

behave if the capsid protein itself were a hybrid of several different serotypes, possibly combining beneficial effects of each for targeting a specific class of retinal cell. Furthermore, the ability to shuffle or remove antigenic capsid sequences that may induce an immune response, would be of benefit in systemic gene therapy where high vector doses are used, or in treating the second eye in ocular gene therapy.

Since the discovery of AAV8 through PCR-based screening of human and primate tissues, several further AAV serotypes have been identified. [10] Analysis of the infectivity of these new serotypes in the mouse brain identified three serotypes (cy5, rh20 and rh39) that had similar tropism to, but greater infectivity than, rAAV2/8 [11].

The purpose of this pilot study was therefore to explore the possibility that structural domains might be exchanged between capsids of different serotypes in order to confer greater infectivity or to alter cellular tropism. Fragments of capsid sequences from the newly discovered primate serotypes were combined with AAV8 to create vectors with hybrid recombinant capsids (rAAV2/Rec2 and rAAV2/Rec3), and their tropism in mouse and primate retina was compared to that of rAAV2/2 and rAAV2/5. In addition to subretinal and intravitreal delivery in wild type (WT) C57BL/6 mice, subretinal injections were performed in the *Abca4*$^{-/-}$ mouse (a model for Stargardt disease) and in the *Pde6b*$^{rd1/rd1}$ mouse. The latter has no photoreceptors in advanced stages of degeneration and therefore presents a model for optobionic strategies to restore vision. In these models, high levels of AAV transduction would most likely be required to aid recombination of two halves of a split transgene (*Abca4*), or to target bipolar cells which are poorly transduced by most AAV serotypes. We also assessed tropism in the primate retina in an *in vitro* system which facilitates long term preservation of photoreceptors [12]. Finally, we tested the ability of the same viral vectors to transduce the human derived neuroblastoma cell line SH-SY5Y *in vitro*, under culture conditions that induce neuron-specific differentiation.

Results

In vivo Measurement of Fluorescence Intensity

Three weeks after subretinal injection, GFP fluorescence was recorded within the area of subretinal vector injection using *in vivo* confocal scanning laser ophthalmoscopy (cSLO) imaging. All vectors tested were capable of driving GFP expression in all of the mouse strains used. GFP fluorescence did not extend noticeably outside the area of the bleb into which the vector was injected. However, clear differences in GFP fluorescence intensity were observed between mouse strains and rAAV serotypes (2-way ANOVA; $p<0.001$ for both strain and serotype; Figure 1). An interaction was detected between strain and rAAV serotype ($p = 0.013$), suggesting differing effects of the rAAV serotypes depending on retinal pathology.

Post hoc analysis showed that retinal GFP expression after viral transduction was lower in *Pde6b*$^{rd1/rd1}$ mice than in WT controls ($p = 0.02$), and lowest in the *Abca4*$^{-/-}$ mice ($p<0.001$ when compared to both other strains). Furthermore, GFP fluorescence intensity was higher with the use of rAAV2/2 than with rAAV2/Rec2 and rAAV2/Rec3 ($p<0.001$ for both comparisons). Fluorescence was higher with rAAV2/5 than rAAV2/Rec3 ($p = 0.04$) and showed a trend of superiority over AAV2/Rec2 ($p = 0.07$). GFP fluorescence intensities after transduction with rAAV2/2 and rAAV2/5 were similar, as was the case when comparing rAAV2/Rec2 and rAAV2/Rec3.

Tropism of rAAV2/Rec2 and rAAV2/Rec3 in WT Mice and Disease Models

Histology was analyzed to assess retinal cell tropism of the different rAAV serotypes. Retinal cell types were identified using immunocytochemistry and by morphology.

Following subretinal injection in WT mice, RPE cells were transduced by all serotypes tested (Figure 2). Photoreceptors were also transduced by all serotypes but GFP fluorescence intensity in this layer was higher using rAAV2/2 and rAAV2/5 than with rAAV2/Rec2 and rAAV2/Rec3. Sparse Müller cell transduction was seen with rAAV2/5 and rAAV2/Rec2, however good horizontal, Müller and ganglion cell transduction was noted with rAAV2/2 (Table 1 and Figure 2).

Following intravitreal injection, ganglion cell and Müller cell transduction was demonstrated with rAAV2/2, but there was no significant retinal transduction with rAAV2/5, rAAV2/Rec2 or rAAV2/Rec3 (data not shown).

In the degenerate retina of *Pde6b*$^{rd1/rd1}$ mice, all serotypes transduced RPE, horizontal cells, Müller cells and ganglion cells (Figure 3). GFP fluorescence was less overall when using rAAV2/Rec3 than other serotypes and especially so for RPE and Müller cells. No bipolar cell transduction was seen with any serotype.

The cell types transduced by all rAAV serotypes in *Abca4*$^{-/-}$ mice were similar to those in wild type mice, but transduction was generally less effective in this model (Figure 4).

Histological Analysis of Fluorescence Intensity

In vivo fluorescence intensity measurements using topographic cSLO images reflect the combined fluorescence intensity at each location arising from all retinal layers. In order to quantify the transduction efficiency within retinal layers, fluorescence intensity was measured *post-mortem* on fixed histological sections (Figure 4) of eyes with subretinal vector delivery. The level of transgene (GFP) expression within the retinal pigment epithelium (RPE) layer, photoreceptor layer, and inner retina (including the outer plexiform layer and inner nuclear layer) was quantified by grey level analysis separately in each layer. In addition, the percentage of pixels above threshold was calculated from histogram analysis, to estimate the efficiency of viral transduction.

There were significant differences in GFP fluorescence intensity between mouse strains and rAAV serotypes on histological analysis, correlating with the cSLO *in vivo* data. Grey level analysis for the RPE layer (Figure 4A) again revealed an overall effect of viral capsid serotype on the resultant GFP fluorescence ($p<0.001$). Post hoc analysis showed that greater RPE fluorescence was achieved with rAAV2/5 than with rAAV2/Rec2 ($p = 0.02$) and rAAV2/Rec3 ($p<0.001$). RPE fluorescence was more intense with rAAV2/2 than with rAAV2/Rec3 ($p<0.001$) and showed a trend of superiority compared to rAAV2/Rec2 ($p = 0.06$). There was no significant difference in RPE fluorescence intensity when comparing rAAV2/Rec2 and rAAV2/Rec3. Fluorescence levels were similar in *Abca4*$^{-/-}$ and *Pde6b*$^{rd1/rd1}$ mice, but both were significantly lower than WT ($p<0.001$).

Analysing the fraction of pixels above threshold demonstrated that among the retinal laminae analyzed, the RPE layer was the most efficiently transduced (Figure 4D). We found that rAAV2/2 and rAAV2/5 were each more effective at RPE transduction than either of the hybrid recombinant serotypes (Figure 3D). An interaction between strain and rAAV serotype ($p<0.001$) was seen due to the lower efficiency of rAAV2/Rec2 and rAAV2/Rec3 in transducing RPE cells in *Abca4*$^{-/-}$ mice (Figure 4D).

Analysis of transduction in the outer nuclear layer (ONL; Figure 4B,E) was performed only in *Abca4*$^{-/-}$ and WT mice as the ONL was almost completely degenerated in *Pde6b*$^{rd1/rd1}$ mice.

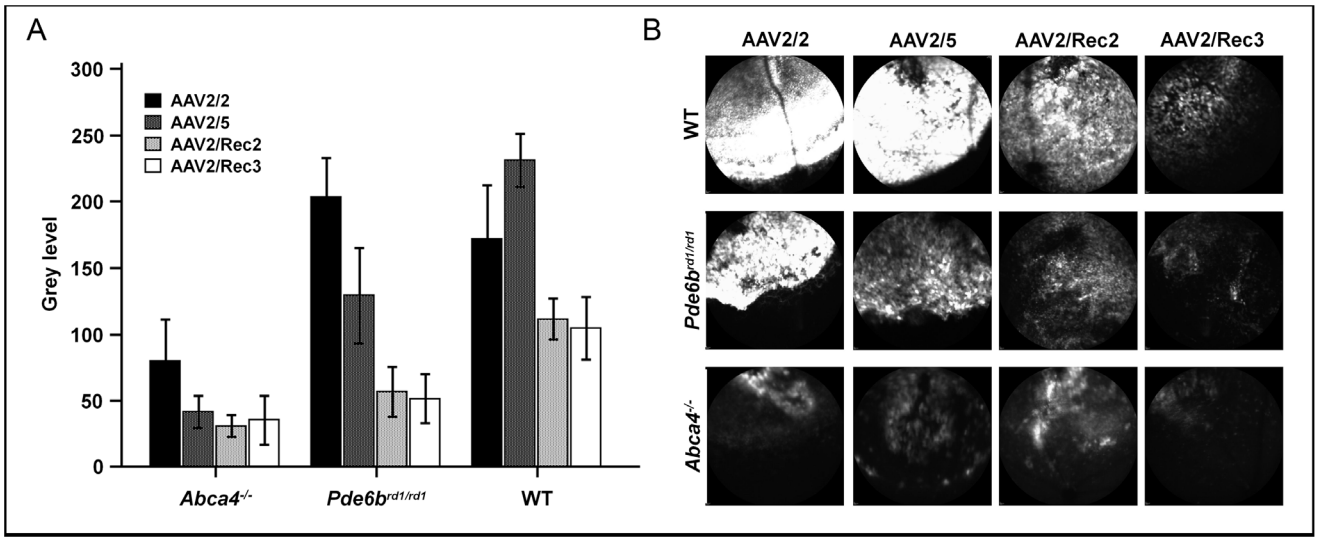

Figure 1. (a) Analysis of *in vivo* measurement of fluorescence intensity 3 weeks after subretinal injection of different hybrid recombinant AAV serotypes expressing green fluorescent protein (mean±SEM). Besides wild type (WT) mice, a strain with totally degenerate retina (Pde6b$^{rd1/rd1}$ mouse) as well as a strain with strong lipofuscin accumulation in the retinal pigment epithelium (*Abca4*$^{-/-}$ mouse) were used. 4 to 8 eyes were analysed per group. (**b**) Representative topographical confocal scanning laser ophthalmoscopy (cSLO) 488 nm-fluorescence images showing the range of fluorescence intensities that was found in the different groups.
doi:10.1371/journal.pone.0060361.g001

There were significant differences in ONL transduction between strains and rAAV serotypes (2-way ANOVA; both, $p<0.01$). The ONL of *Abca4*$^{-/-}$ mice revealed a lower grey level ($p<0.01$; Figure 4B) a lower percentage of pixels above threshold intensity ($p<0.001$; Figure 4E) than in WT for all vectors. Comparing ONL grey level when using different vectors, rAAV2/2 was more effective than both rAAV2/Rec2 ($p = 0.01$) and rAAV2/Rec3 ($p<0.01$; Figure 4B). This could be due to the high proportion of Müller cells transduced with rAAV2/2, whose processes traverse the ONL. The percentage of ONL pixels above threshold was significantly lower when using rAAV2/Rec3 than rAAV2/2 ($p<0.01$) and a trend of lower efficiency than rAAV2/5 ($p = 0.06$), suggesting lower transduction efficiency of rAAV2/Rec3 in photoreceptors.

Analysing the effects of subretinal vector delivery within the inner retina (including the inner nuclear and inner plexiform layers), the grey level was significantly higher when using rAAV2/2 compared to all other viruses tested (all, $p<0.001$; Figure 4C,F). A significant difference was detected in the grey level of wild type mice in comparison with *Abca4*$^{-/-}$ and *Pde6b*$^{rd1/rd1}$ mice ($p<0.05$).

Tropism of rAAV2/Rec2 and rAAV2/Rec3 Serotypes in *ex vivo* Primate Retinal Culture

Ex vivo culture of macaque retinal explants was used as an alternative to *in vivo* administration to assess the tropism of novel rAAV2/Rec2 and rAAV2/Rec3 serotypes in the primate retina. GFP expression was observed in explants cultured with rAAV2/Rec2 and rAAV2/Rec3 by day 3 (data not shown). *Ex vivo* fluorescence imaging of rAAV2/Rec2-cultured explants revealed limited transduction of cells on the inner retinal aspect (Figure 5A); analysis of histological sections showed these cells to be localized in the ganglion cell layer (Figure 5B–C).

Imaging of rAAV2/Rec3-cultured explants showed widespread transduction of cells on the inner retinal aspect with processes extending the width of the tissue (Figure 5D). Transduced cells were predominantly observed at the edge of the explanted retinal tissue, indicating that cellular access is restricted in the tissue's center. This is potentially due to the presence of an intact inner limiting membrane, which is disrupted by dissection at the periphery of the tissue. The processes of transduced cells were parallel, which is suggestive of ganglion cell axons (Figure 5D). Histological analysis confirmed that rAAV2/Rec3 primarily transduced cells located in the ganglion cell layer, in addition to Müller glia (data not shown). No significant transduction of cells was observed in the ONL. Transduced cell types were determined by morphology and location within the retina.

Measurement of GFP Fluorescence Intensity in SH-SY5Y Cells *in vitro*

In the human derived neuroblastoma cell line SH-SY5Y, GFP fluorescence intensity as measure for transduction efficiency was significantly different between rAAV serotypes ($p = 0.0006$; Figure 6B). Grey value analysis showed reduced fluorescence with rAAV2/Rec2 compared to rAAV2/2 ($p<0.05$) and rAAV2/5 ($p<0.05$). rAAV2/Rec3 also showed reduced fluorescence compared to rAAV2/2 ($p<0.01$) and rAAV2/5 ($p<0.01$). There was no significant difference in pairwise comparisons between rAAV2/2 and rAAV2/5 or between rAAV2/Rec2 and rAAV2/Rec3. Examining pixels above threshold (Figure 6C), rAAV2/Rec2 showed lower transduction efficiency for SH-SY5Y cells than rAAV2/2 ($p<0.01$) and rAAV2/5 ($p<0.01$). This was also the case for rAAV2/Rec3 compared to rAAV2/2 and rAAV2/5 ($p<0.001$ in both). Nuclear count was without significant difference between groups, ensuring similar confluence of the cell layers (Figure 6D).

Discussion

In this study we have assessed the retinal tropism and transduction efficiency of four recombinant AAV vectors: two standard serotypes (rAAV2/2 and rAAV2/5) and two with novel hybrid recombinant capsids (rAAV2/Rec2 and rAAV2/Rec3). *In vivo* mouse experiments (WT mice and two models of retinal degeneration) were combined with *ex vivo* testing of primate retinal

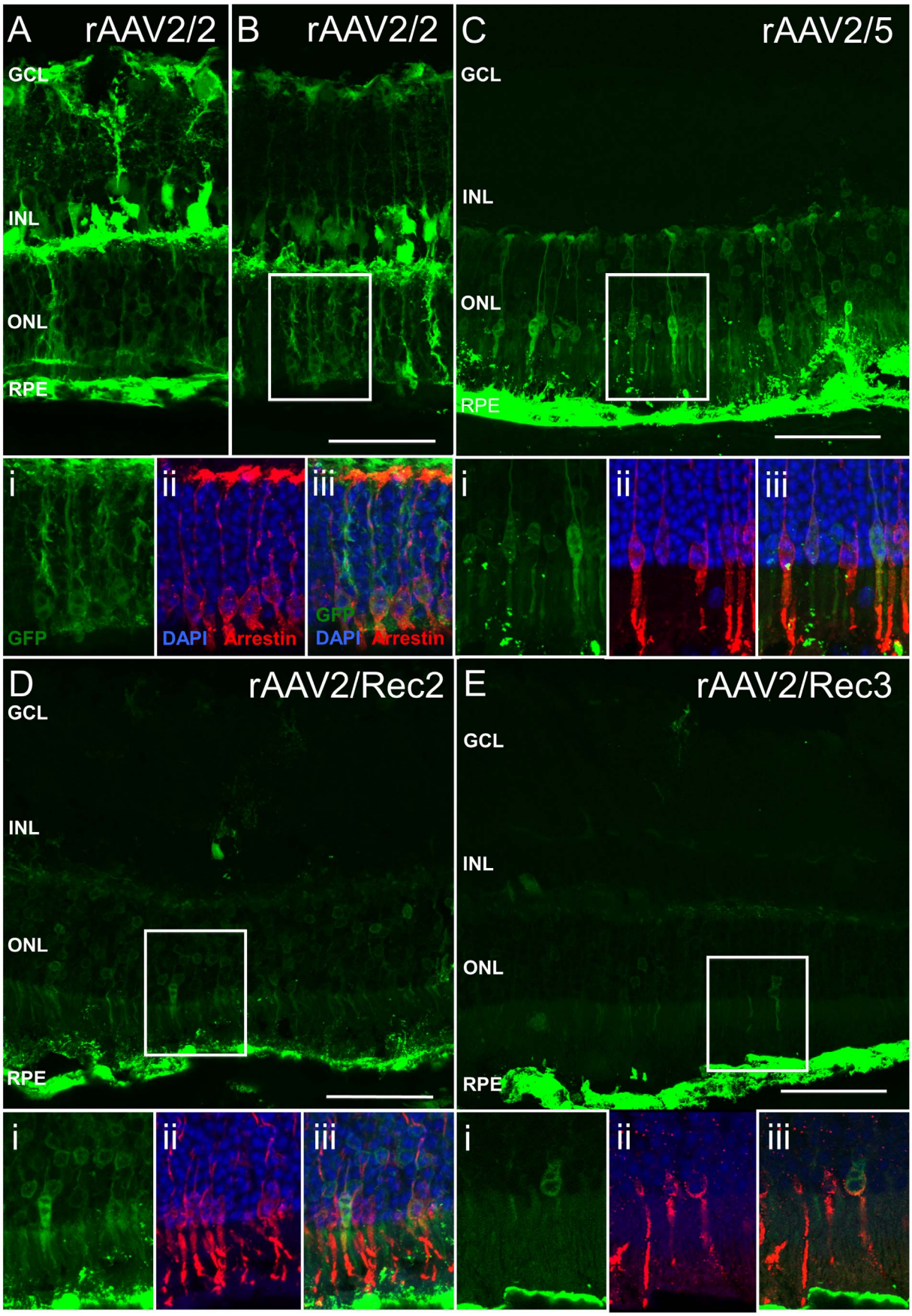
A rAAV2/2
B rAAV2/2
C rAAV2/5
GCL
INL
ONL
RPE
i
ii
iii
GFP
DAPI
Arrestin
D rAAV2/Rec2
E rAAV2/Rec3

Figure 2. Green fluorescent protein (GFP) fluorescence patterns of different recombinant AAV serotypes in wild type C57BL/6 mice following subretinal injection. The main images A–E are confocal stacks illustrating overall GFP expression patterns. Figure A illustrates transduction of the retinal pigment epithelium with rAAV2/2, whereas figure B demonstrates cone transduction. The boxed regions in images B–E are enlarged and shown as confocal slices in panels i-iii below for each serotype. GFP signal (green) and nuclear labeling with DAPI (blue) overlaid with immunostaining using cone arrestin (red) illustrate cone transduction using the different recombinant AAV serotypes. GCL = ganglion cell layer, INL = inner nuclear layer, ONL = outer nuclear layer, RPE = retinal pigment epithelium. Scale bar 50 μm.
doi:10.1371/journal.pone.0060361.g002

explants and *in vitro* investigation in a human-derived neural cell line (SH-SY5Y). The construction of vectors with hybrid capsids involved recombination of structural domains from vectors of different serotypes previously isolated from primate brain together with AAV8 to create vectors with novel capsids (see methods). We provide data showing that it is possible to interchange viral capsid protein sequences between different AAV serotypes and that this still results in retinal transduction, albeit at a reduced efficiency compared to vectors pseudotyped with wildtype capsids. Although in this pilot study we did not show an increase in transduction efficiency or significant change in tropism with the hybrid recombinant vectors, we propose that this approach in creating hybrid capsids may be a useful tool in generating any number of AAV capsid sequences in order to identify those with the greatest impact on transduction and cellular tropism.

In addition, shuffling specific capsid sequences may be of use in minimizing immune responses to AAV gene therapy. Previous studies have shown that high dose rAAV2/2 administration into the subretinal space in mice leads to production of neutralising antibodies to AAV, which may affect efficacy of treatment to a second eye [13]. In systemic gene therapy using rAAV2 for the treatment of haemophilia B, it has been postulated that the loss of factor IX transgene expression is due to proteasome-mediated cleaving of the AAV capsid, and presentation of capsid peptide sequences via the major histocompatibility complex. This would lead to recognition of transduced cells by CD8+ T cells, and their subsequent destruction [14]. In both cases, the ability to substitute specific capsid antigen sequences, by the technique of capsid shuffling, may be of use in avoiding the immune response to rAAV.

Several variations in AAV genome sequences have been isolated from a variety of body tissues, including the gut, lung and brain [10]. One principal drawback of our study is that the novel capsid sequences (cy5, rh20 and rh39) were identified in primate brain and not in the retina. It was interesting to note that rAAV2/Rec3 which had the highest transduction in neural tissue also showed greatest tropism for retinal ganglion cells in primate retinal explants. This is a similar finding with rAAV2/2 which also has been shown to effectively target brain and retinal ganglion cells [15,16]. In contrast, rAAV2/8 targets photoreceptors highly efficiently but ganglion cells relatively poorly [17]. In future it might therefore be prudent for retinal gene therapy to attempt isolation by PCR of AAV genome particles directly from primate retina.

AAV2/Rec2 and AAV2/Rec3 were effective in transducing ganglion cells following subretinal vector delivery in the *Pde6b*$^{rd1/rd1}$ mouse, and the primate retinal explants. No ganglion cell transduction was seen when these vectors were administered subretinally or intravitreally in WT mice. The former is likely due to the lack of penetration of these vectors to the ganglion cell layer in the presence of a thick ONL, and the latter may be due to an intact inner limiting membrane (ILM), which is known to affect

Table 1. Summary of transduction efficiency in various mouse models (subretinal delivery) and ex-vivo primate retina of the tested recombinant AAV vectors rAAV2/Rec2 and rAAV2/Rec3 in comparison to rAAV2/2 and rAAV2/5.

	RPE cells	Photoreceptors	Bipolar cells	Horizontal cells	Müller cells	RGCs
Wild type C57/bl6						
AAV2/2	++	++	−	++	+++	+
AAV2/5	+++	+++	−	−	+	−
AAV2/Rec2	++	++	−	−	+/−	−
AAV2/Rec3	++	+	−	−	+/−	−
***Abca4*$^{-/-}$**						
AAV2/2	++	+	−	++	++	+
AAV2/5	+	+	−	−	+/−	−
AAV2/Rec2	+	+	−	−	+/−	−
AAV2/Rec3	+/−	+/−	−	−	+/−	−
***Pde6b*$^{rd1/rd1}$**						
AAV2/2	+++	n.a.	−	+	+++	+
AAV2/5	+++	n.a.	−	+	+++	+
AAV2/Rec2	+++	n.a.	−	+	+++	+
AAV2/Rec3	+	n.a.	−	+	+	+
Primate retina (ex vivo)						
AAV2/Rec2	n.a.	−	−	−	−	+
AAV2/Rec3	n.a.	+	−	−	+	+++

n.a. = not applicable. RPE = retinal pigment epithelium. RGCs = retinal ganglion cells.
doi:10.1371/journal.pone.0060361.t001

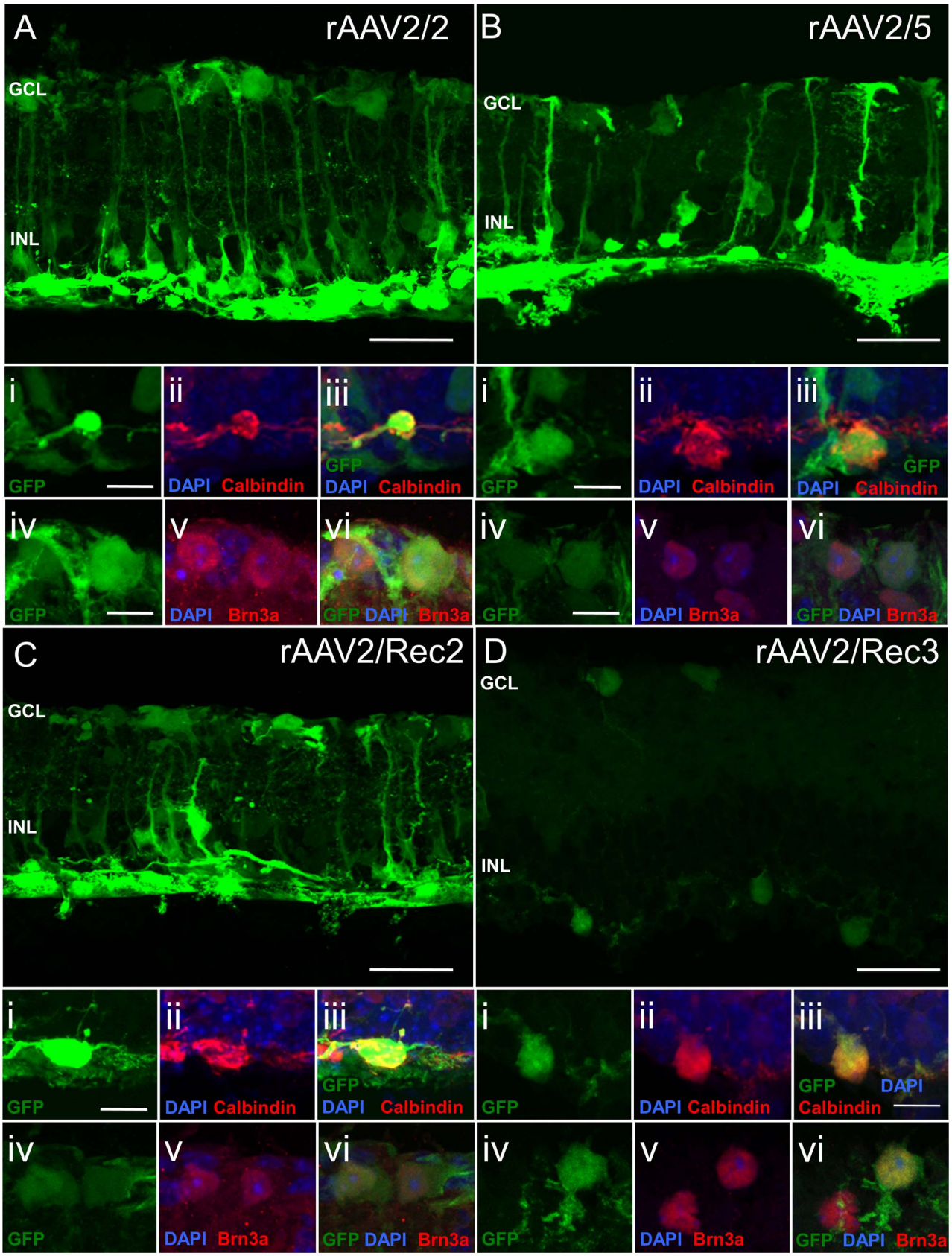

Figure 3. Green fluorescent protein (GFP) fluorescence patterns of different recombinant AAV serotypes in the degenerate retina of *Pde6b*$^{rd1/rd1}$ mice following subretinal injection. The main images a–d are confocal stacks illustrating overall GFP expression patterns. For each serotype, images i–iii are confocal slices showing GFP expression (green), nuclear labeling (blue) and immunostaining with calbindin identifying

horizontal cells (red). Colocalisation of signals indicates horizontal cell transduction. Images iv–vi show colocalisation of GFP (green) in ganglion cells identified by Brn-3a immunostaining (red) demonstrating ganglion cell transduction. GCL = ganglion cell layer, INL = inner nuclear layer, RPE = retinal pigment epithelium. Scale bar: 30 μm for images a–d, 10 μm for images i–vi.
doi:10.1371/journal.pone.0060361.g003

viral transduction. [18] Indeed, the presence of an intact ILM may explain the fact that transduced cells were predominantly observed at the edge of the primate retinal explants, where the ILM would have been disrupted by tissue dissection. rAAV2/Rec2 and rAAV2/Rec3 only weakly transduced photoreceptors. These observations show some of the limitation of *in vitro* experiments. However, the data may provide an effective means before deciding whether to conduct *in vivo* experiments in non-human primates.

Recent work has shown that modification of tyrosine residues can be exploited to significantly enhance AAV transduction in the retina [19]. In our study none of the recombined capsids included serotypes with modification of tyrosine residues, and the number of exposed surface tyrosine residues on rAAV2/Rec2 and Rec3 capsids is comparable to that of rAAV2/8. Hence, it is unlikely that the reduced transduction is due to increased ubiquitin-tagged proteasome-mediated degradation [20], as one might observe if greater numbers of tyrosine residues were present on the hybrid capsid. Both rAAV2/Rec2 and rAAV2/Rec3 vectors use the C terminus of the VP3 region of rAAV2/8 which includes the HI loop, a critical sequence for genome packaging and capsid assembly [21]. Hence this region at least can be excluded as a cause for the reduced transduction seen. It is however possible that impaired synthesis of the viral capsid might result in impaired genome packaging and increase the number of truncated transgenes which might not be detected in the PCR assay used to determine titer. In order to confirm that the hybrid recombinant capsids are able to rearrange into an appropriate AAV structure, it would be necessary to perform more complex analyses of AAV geometry such as X-ray crystallography. However, this technique would only give detail as to the structure of fully matured virions and would be unlikely to highlight issues relating to improper genome packaging or capsid maturation.

None of the four vectors assessed in this study were able to transduce bipolar cells. This is perhaps not a surprising finding because vectors which are highly efficient at transducing photoreceptors, such as rAAV2/5, can achieve high levels of gene expression in the innermost rod photoreceptors but fail to label cells of the adjacent inner nuclear layer [22]. In the *Pde6b*$^{rd1/rd1}$ mouse model used here, virtually the entire ONL (i.e. the photoreceptors) had degenerated and hence the failure to target bipolar cells cannot be due to the failure of AAV to access this layer. Ubiquitination of AAV particles may be an important mechanism preventing successful AAV transduction of bipolar cells. This is suggested by the recently achieved effective transduction of bipolar cells using the capsid mutant rAAV2/8 [23] which has one less tyrosine residue at position 503, resulting in reduced ubiquitination compared to the serotypes explored in this study. However, due to the design of our study, such

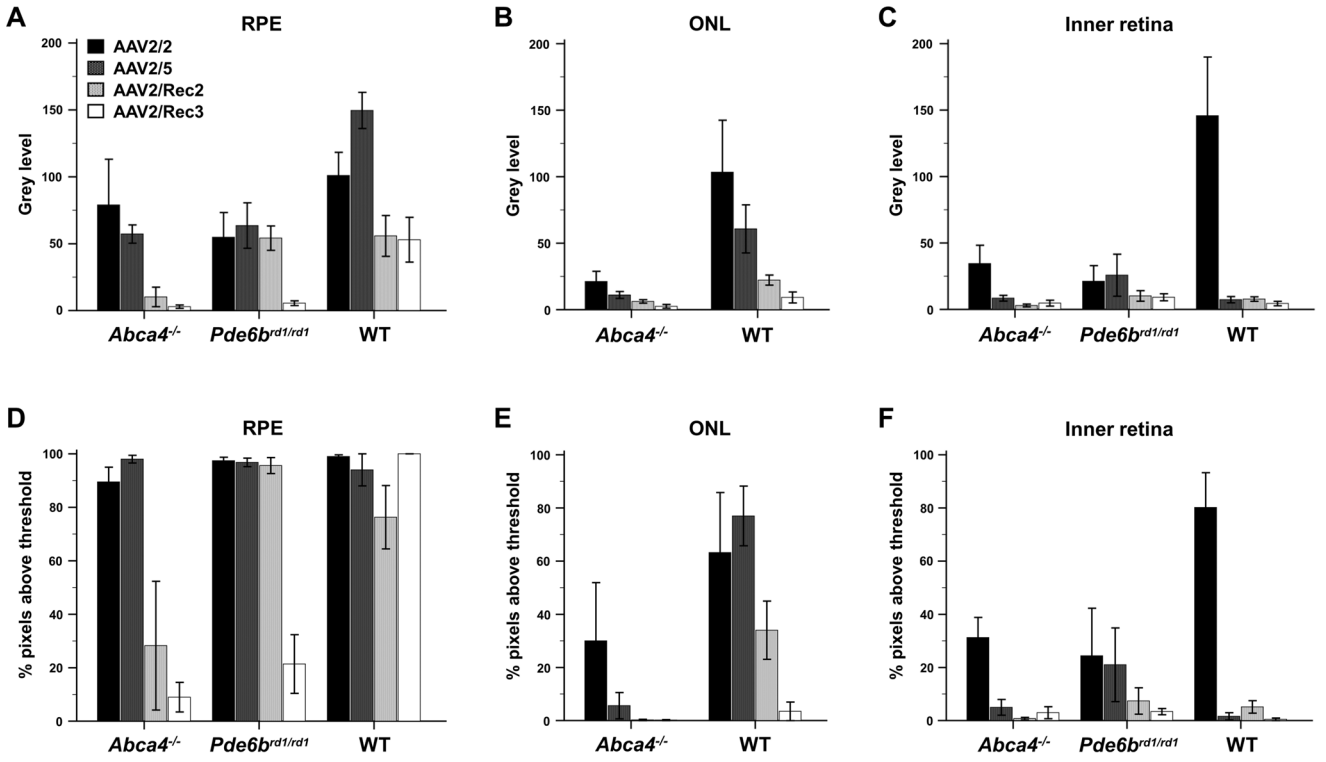

Figure 4. Quantitative analysis of green fluorescent protein (GFP) fluorescence intensity on histological sections in eyes that underwent subretinal injection of different recombinant AAV serotypes expressing GFP (mean±SEM). Two mouse models for retinal degeneration (*Abca4*$^{-/-}$ and *Pde6b*$^{rd1/rd1}$ mice) are compared with wild type (WT) mice. Grey level analysis (upper row) represented an estimate for the level of transgene expression within transduced cells, whereas the percentage (%) of pixels above threshold (bottom row) represented an estimate of viral efficacy for cell transduction. 4 to 8 eyes were analysed per group. ONL = outer nuclear layer, RPE = retinal pigment epithelium.
doi:10.1371/journal.pone.0060361.g004

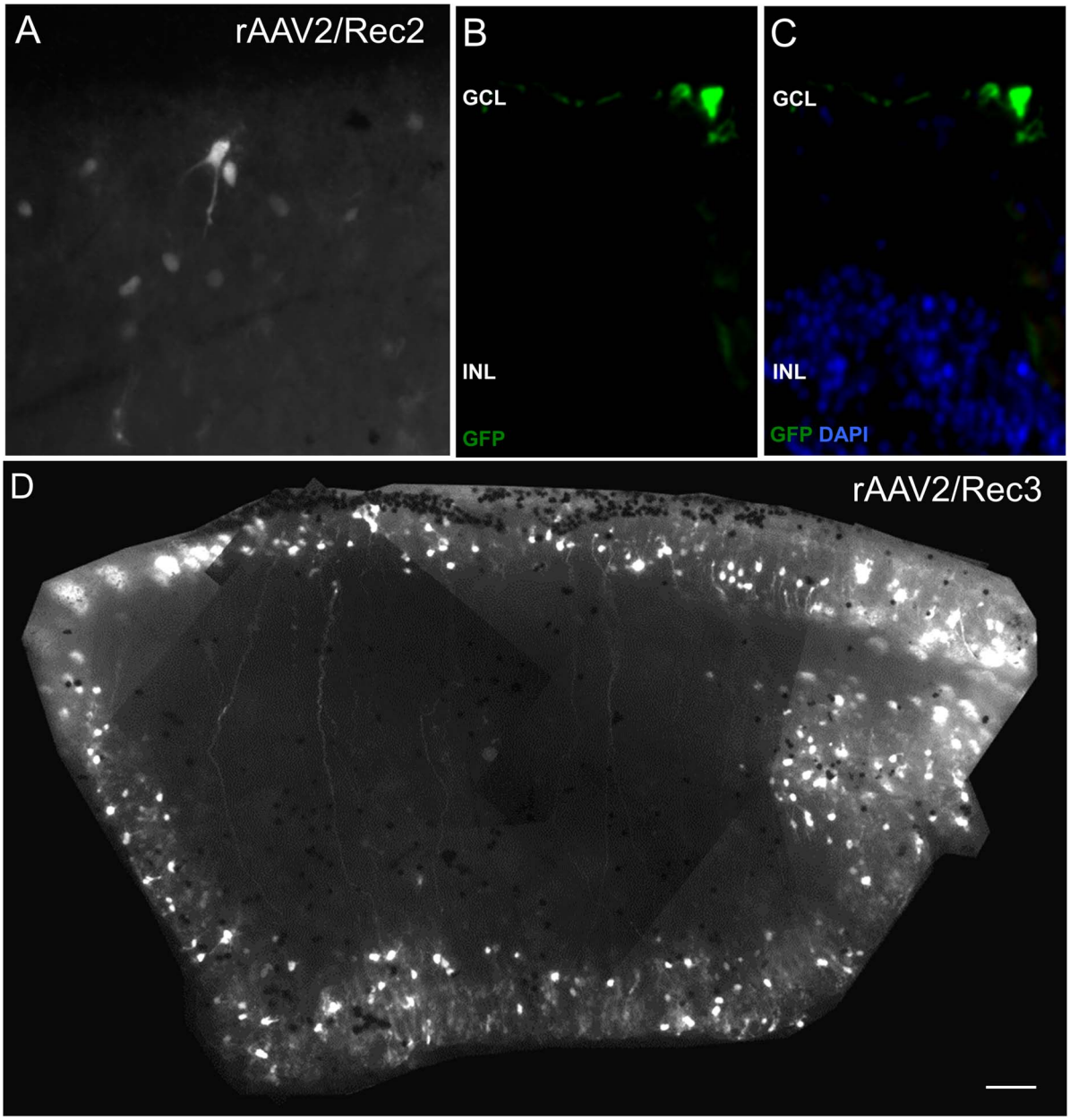

Figure 5. Green fluorescent protein (GFP) fluorescence following *ex vivo* administration of hybrid recombinant AAV vectors. GFP expression in macaque explants following rAAV2/Rec2 transduction (A) and histology of cross-sectional specimens showing expression of GFP (green) in the ganglion cell layer (B,C). Image D shows GFP expression in macaque explants following rAAV2/Rec3 transduction. GCL = ganglion cell layer; INL = inner nuclear layer.
doi:10.1371/journal.pone.0060361.g005

conclusions on the lack of bipolar cell transduction remain speculative.

It was also noted that the transduction of RPE cells and photoreceptors in the *Abca4*$^{-/-}$ mouse appears to be significantly lower with all viral serotypes assessed in this study. If this is also true of the human condition then it would also present a relative impediment in using AAV to treat Stargardt disease. Since the *ABCA4* transgene (at 6.7kb) is too large to be packaged into a single AAV vector capsid, one current approach is to use two AAV genomes which can then recombine to form the full-length *ABCA4* transgene after cell entry [24,25]. In order to achieve this it is likely that much higher levels of transduction will be necessary to compensate for a relatively low rate of transgene recombination. It is not entirely clear why *Abca4*$^{-/-}$ mice have reduced transduction with AAV. One explanation might be the different background strain (129S4v/SvJae) compared to the wild type control mice (C57/BL/6). Alternatively it is possible that loss of the transmembrane ABCA4 protein or the increased levels of phosphatidylethanolamine [26] reduce AAV entry into the photoreceptor cell. This explanation may also account for the poor RPE transduction observed, as the number of AAV particles entering RPE cells through phagocytosed outer segment discs would be low if the latter contained low amounts of AAV. It is also possible that the strong accumulation of lipofuscin, which mainly consists of visual

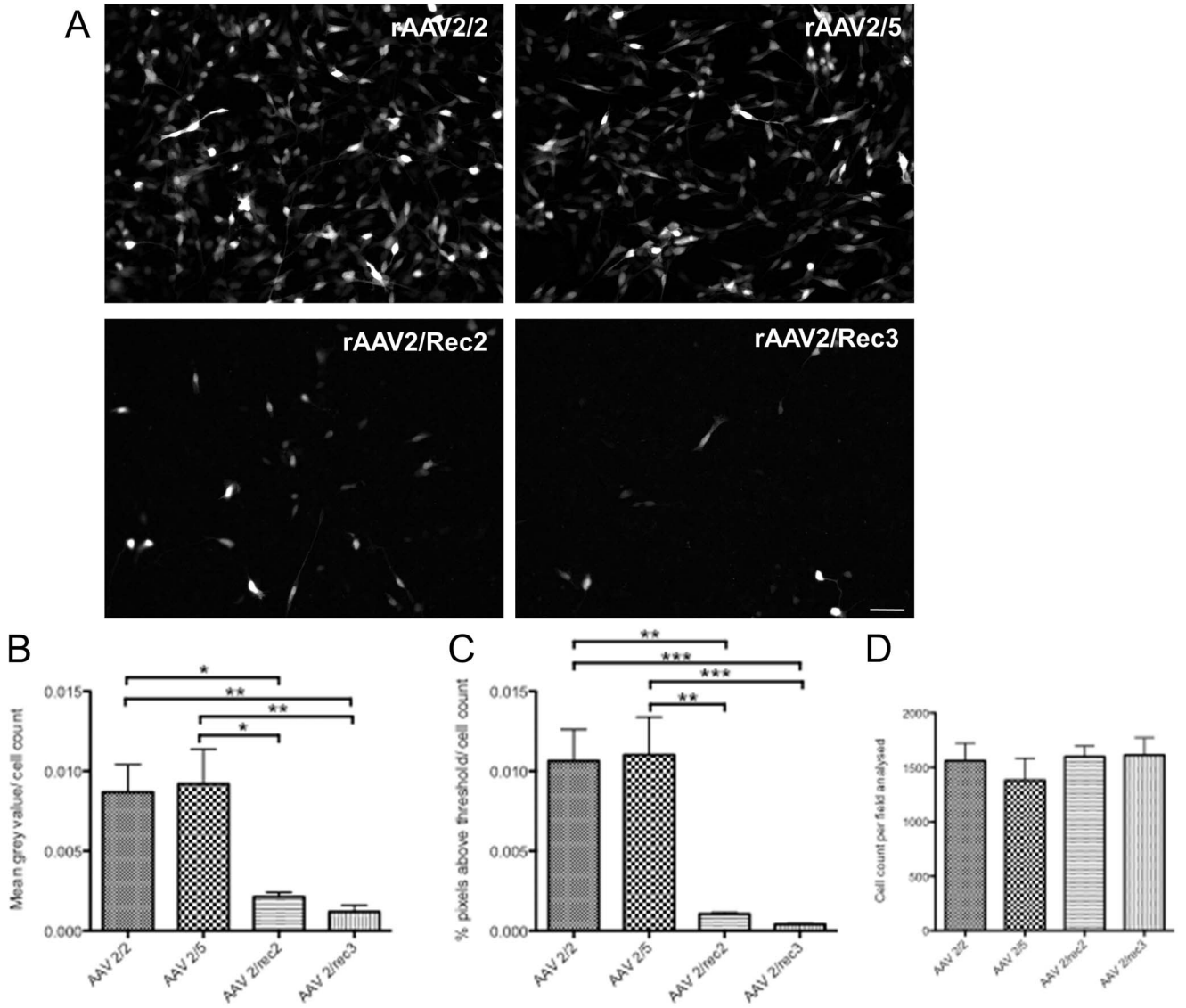

Figure 6. Analysis of Green fluorescent protein (GFP) fluorescence intensity measurement of SH-SY5Y cells *in vitro* 9 days after transfection using different recombinant AAV serotypes. Representative images are shown of GFP fluorescence following transduction with rAAV2/2, rAAV2/5, rAAV2/Rec2 and rAAV2/Rec3 (A). Analysis of grey value (B) and percentage of pixels above threshold (C) are shown in the bottom row, demonstrating significant differences between standard rAAV2/2 and rAAV2/5 serotypes and hybrid recombinant vectors (*$p<0.05$, **$p<0.01$, ***$p<0.001$). In order to ensure levels of cell confluence did not differ between groups and affect transduction, Hoechst-labeled nuclei were counted in each field analyzed, with no significant difference between groups (D). Scale bar 50 μm.
doi:10.1371/journal.pone.0060361.g006

cycle byproducts such as N-retinylidene-N-retinyl-ethanolamine (A2E) and other bisretinoids, might somehow impair the transduction efficiency of AAV. Further studies will be required to address this question.

In summary we further explored the concept of pseudotyping viruses to alter retinal cell tropism by mixing capsid proteins. Although the herein tested viruses may not be recommended for further studies due to their lower efficiency compared to established pseudotypes, our methodological approach might be used to identify hybrid rAAV vectors with specific retinal cell tropisms or increased efficiency in certain disease states.

Methods

Viral Vectors

Three new recombinant serotypes previously identified, with greater transduction efficiency than rAAV8, were cloned into AAV helper plasmids as previously described [11]. These are termed cy5 (cynomolgus macaque – variant 5), rh20 (rhesus macaque – variant 20) and rh39 and were originally supplied by Guang-Ping Gao and the Gene Therapy Program Vector Core, Department of Medicine, University of Pennsylvania, where further details of the identification of these sequences is available [10].

For the generation of hybrid recombinant capsids, fragments of capsid sequences that matched in all three vectors and AAV8 were shuffled around by using known restriction sites. Particular

attention was made to use restriction enzymes that facilitated mixing of the three viral protein (VP) sequences, between the novel primate vectors and AAV8. The N-terminus of the VP1 protein is known to affect AAV infectivity. Hence one of the fragments chosen was derived by HindIII-StuI restriction digest which codes for the first 80 amino acids of VP1 including the phospholipase (PL) A2 site (Figure S2 in File S1). The HindIII-StuI fragments from cy5 were incorporated into Rec1, 3 and 4, whereas the restriction fragments from rh20 or rh39 (which are identical) created a different VP1 for Rec2, 5 and 6. The restriction enzyme MluI cuts nearly in half the coding region for VP2 and VP3 in rh20 and AAV8. SmaI does the same for cy5 and rh20. This allowed the creation of Rec1, 2 and Rec5, 6. Restriction enzyme BamHI cuts off a smaller C-terminal fragment containing the HI loop in rh20, rh39 and AAV8. This allowed the generation of the Rec3 and Rec4 constructs (Figure S1 in File S1).

In a preliminary study the rAAV2/Rec vectors were assayed using standard in vivo protocols comparing transduction efficiency to rAAV2/8. With intravenous infusion, rAAV2/Rec2 showed the greatest transduction of the target tissue (cardiac muscle), and with direct intracerebral administration, rAAV2/Rec3 led to the greatest neuronal cell transduction (unpublished data, Matthew J. During). These vectors (referred to as rAAV2/Rec2 and rAAV2/Rec3) were therefore selected for this study.

To generate hybrid AAV vectors, GFP was cloned into an AAV expression plasmid under the control of the CAG (hybrid CMV-chicken β-actin) promoter and containing woodchuck hepatitis virus post-transcriptional regulatory element (WPRE), and bovine growth hormone (bGH) polyadenylation signal flanked by AAV2 inverted terminal repeats. Human embryonic kidney 293 cells were co-transfected with three plasmids–AAV plasmid, appropriate helper plasmid encoding rep and cap (Rec2 and 3) genes, and adenoviral helper pF Δ6–using standard CaPO4 transfection. rAAV vectors were purified from the cell lysate by ultracentrifugation through an iodixanol density gradient, as previously described [11]. Vectors were titered using real-time PCR (ABI Prism 7700; Applied Biosystems, Foster City, CA) and diluted to 1.0×10^{12} vector genomes (vg)/mL prior to subretinal or intravitreal injection.

rAAV2/2 and rAAV2/5 expressed GFP under control of the same CAG promoter and included WPRE and bovine growth hormone polyadenylation signal as did the hybrid recombinant vectors. The alignment of the rAAV2/Rec2 and rAAV2/Rec3 sequences in comparison to AAV5 and AAV2 is shown in the supporting information (Figure S2 in File S1).

Mice

Wild type (WT) C57BL/6 mice were provided by the Biomedical Sciences division, University of Oxford. C3H/HeNHsd-*Pde6b*^{rd1} (herein referred to as *Pde6b*$^{rd1/rd1}$) mice were purchased from Harlan Laboratories (Hillcrest, UK). Founder *Abca4* knockout mice (129S4/SvJae-*Abca4*^{tm1Ght}, herein referred to as *Abca4*$^{-/-}$) were provided by Gabriel Travis, David Geffen School of Medicine, University of California, Los Angeles, USA. [26] and bred locally at the University of Oxford.

Animals were kept in a 12 hour light (<100 lux)/dark cycle, with food and water available *ad libitum*. All procedures were performed under the approval of local and national ethical and legal authorities and in accordance with the Association for Research in Vision and Ophthalmology statements on the care and use of animals in ophthalmic research. The study was approved by the Faculty of Clinical Medicine Ethical Review Committee, and was then assessed, approved and covered by UK Home Office Project licence (number: 30/2808). All procedures were perfomed under general anesthesia, and all efforts were made to minimize suffering.

At the time of intraocular injection, mice were between 6 and 8 weeks old. For surgery and *in vivo* imaging procedures, animals were anesthetized by intraperitoneal injection of 1 mg/kg medetomidine (Dormitor 1 mg/ml, Pfizer, Sandwich, UK) and 60 mg/kg ketamine (Ketaset 100 mg/kg, Fort Dodge, Southampton, UK) and pupils fully dilated with tropicamide 1% eye drops (Bausch & Lomb, Kingston-Upon-Thames, UK) and, for the imaging procedure, phenylephrine eye hydrochloride 2.5% drops (Bausch & Lomb, Kingston-Upon-Thames, UK).

Intraocular Injections

Intra-ocular injections were performed tangentially through the sclera with a 10 mm 34-gauge needle (Hamilton; Hamilton AG, Bonaduz, Switzerland) mounted on a 5 µl syringe (Hamilton 65 RN, Hamilton AG) under direct visual control using a surgical microscope. A circular cover glass (Ø6 mm, VWR International, Lutterworth, UK) was applied onto the cornea with a carbomer coupling gel (Viscotears, Novartis, Frimley, UK) to ensure good visualization of the fundus. The eye position was controlled and stabilized by holding the superior or inferior rectus muscle with a notched forceps. 1 µl viral vector (1.0×10^{12} vg/mL) was injected in each eye, and complete subretinal or intravitreal delivery was confirmed by direct visualization. After injection, the needle was left in position for an additional 20–30 seconds and then withdrawn quickly to minimize reflux and to allow self-sealing of the scleral tunnel. Each animal received a different viral serotype in each eye, with different syringes and needles used for the different viruses. Between individual injections, the needle was flushed with sterile water.

Fundus Imaging using a Confocal Scanning Laser Ophthalmoscope

Three weeks after intraocular injection, confocal scanning laser ophthalmoscope (cSLO; Spectralis HRA, Heidelberg Engineering, Heidelberg, Germany) imaging was performed under general anesthesia (as above) according to a modified protocol that has been described in detail previously [27]. In brief, the pupils were fully dilated and a contact lens applied on the cornea. The near-infrared (NIR) reflectance mode (820 nm laser) was used for camera alignment. For recordings from the outer retina, the plane of highest NIR reflectivity or the plane of the nerve fibre layer was identified, respectively. After switching to the autofluorescence mode (excitation wavelength: 488 nm, emission recorded between 500 and 700 nm) and slight focus adjustments (due to the dioptric shift between the different wavelengths), images were recorded with a standardized detector sensitivity of 70 using the automated real time (ART) mode, without image normalization. All images were recorded in the high-resolution mode (1536×1536 pixels) using a 55 degree lens.

Tissue Collection and Processing

After the imaging procedure, mice were perfusion fixed using 4% paraformaldehyde (PFA, Thermo Fisher, Loughborough, UK) in PBS. After enucleation, the cornea and lens were removed under direct visualisation with an operating microscope in 4% PFA in PBS. After fixation overnight, the eyecups were cryoprotected using a 10–30% sucrose gradient. Eyecups were embedded in optimal cutting temperature (OCT) compound (Tissue-Tek, Sakura Finetek, The Netherlands), frozen on dry ice and stored at −80°C until sectioning. Eyecups were cryosectioned into 16 µm sections and affixed to poly-L-lysine coated glass slides

(Polysine®; Thermo Scientific, Loughborough, UK). The sections were air-dried and then stored at −20°C until further histological processing.

Retinal Explant Culture

Eyes were enucleated from a 12-year-old rhesus macaque (*Macaca mulatta*) immediately *post-mortem* and transferred into room temperature complete culture media consisting of Neurobasal A, L-glutamine (0.08 mM), penicillin (100 U/mL), streptomycin (100 U/mL) and serum free supplements B27 (2%) and N2 (1%, all Invitrogen Ltd, Paisley, UK). The anterior segment and lens were removed and the retina detached from the RPE. Subsequently, the retina was divided into 2–3 mm segments and transferred into an organotypic system for long term culture, as described previously [12,28] One day post explantation (D1), 20 µl rAAV2/Rec2 (1.0×10^{12} vg/mL) and rAAV2/Rec3 (1.0×10^{12} vg/mL) vectors were applied to the retinal explants during media change. Media (700 µL) was refreshed every third day and GFP expression evaluated using an inverted epifluorescence microscope (Leica DM IL, Leica, Wetzlar, Germany). Images of live explants were acquired at D10 after removal of media to ensure that explants remained flat on the tissue culture membranes and that background autofluorescence due to the presence of media was minimal. Following imaging, explants were removed from tissue culture and fixed for 40 min in 4% PFA followed by incubation overnight at 4°C in 30% sucrose. Explants were subsequently embedded in OCT, frozen on dry ice and stored at −80°C until sectioning.

Histology and Immunohistochemistry

After hydration and 3×5 min washes in 0.01 M PBS, retinal sections were blocked for 1 hour at room temperature in PBS +0.1% Triton X-100+10% donkey serum. After 3×5 min washes, the sections were incubated at 4°C overnight with the primary antibody and subsequently for 2 hours at room temperature with the species–appropriate secondary antibody (both in PBS +0.1% Triton X-100+1% serum). After each step, sections were rinsed for 2×5 min in PBS +0.05% Tween20, followed by 1×5 min in PBS alone. All sections were counter-stained with Hoechst 33342 (Invitrogen) 1:5000 and mounted with an antifade reagent (Prolong Gold; Invitrogen). All antibodies used for immunohistochemistry are specified in table 2. Alexa Fluor 555 donkey anti-rabbit IgG and Alexa Fluor 568 donkey anti-goat IgG (Invitrogen) were used as secondary antibodies as appropriate.

Confocal Microscopy

Retinal sections were viewed on a confocal microscope (LSM710; Zeiss, Jena, Germany). GFP-positive cells were located using epifluorescence illumination before taking a series of overlapping XY optical sections, of approximately 0.5 µm thickness. The fluorescence of Hoechst, GFP and Alexa-555 or 568 were sequentially excited using 350 nm UV laser, 488 nm argon laser and the 543 nm HeNe laser, as appropriate. A stack was built to give an XY projection image as appropriate. Image processing was performed using Volocity (Perkin Elmer, Cambridge, UK) and Image J (Version 1.43, National Institute of Health, http://rsb.info.nih.gov/ij).

Light Microscopy

For the purpose of quantitative analysis of GFP expression, images were taken using the Leica DM IL inverted epifluorescence microscope. Images were obtained at x20 magnification using identical acquisition settings including exposure time, and were saved at a resolution of 1200×1600 pixels.

Image Analysis

Image analysis was performed on 8-bit images using ImageJ. Grey levels on cSLO images were measured within a circle of 300 pixel diameter. This area was placed within the region of vector delivery, avoiding the needle entry site where associated retinal damage often led to localized increased transduction.

Grey levels on histological fluorescence images were analyzed separately for the RPE, the photoreceptor layer, and the inner retina (including the outer plexiform layer and the inner nuclear layer). This allowed a quantitative analysis of GFP expression within individual retinal layers and thus to assess vector tropism. Retinal pigment epithelium (RPE) cells were always most efficiently transduced. Thus to ensure images were not over-exposed, the exposure time for images analyzed for GFP-fluorescence in the RPE was one quarter of that used for assessing transduction of neuronal cells. Regions of defined sizes (RPE: 20×200 pixels, outer nuclear layer: 50×250 pixels, inner retina: 100×250 pixels) were analyzed within areas of highest GFP expression, and the mean grey level was calculated from a plot profile. In addition, the number of pixels above threshold was calculated from histogram analysis. The threshold was set conservatively using areas outside the injection site as reference.

Cell Culture and in vitro Transduction

SH-SY5Y cells (obtained from the American tissue culture collection) were cultured in complete RPMI-1640 media containing L-glutamine (2 nM), penicillin (100 units/mL), streptomycin (100 µg/mL) all from Sigma-Aldrich UK, and 10% fetal calf serum (GIBCO, Invitrogen, UK). Cells were maintained at 37°C in a 5% CO2 environment.

Cells were seeded in 96 well culture dishes at a density of 5×10^4 cells per well. One day after plating, media was changed to that containing 1.6×10^{-8} M Tetradecanoylphorbol-13-acetate (TPA)

Table 2. Details of primary antibodies used for immunohistochemistry.

Staining	Antigen	Host	Source (product code)	Dilution
Cone arrestin	Synthetic linear peptide	Rabbit	Millipore (AB15282)	1:1000
Calbindin	28kDa calbindin-D protein purified from rat kidney	Rabbit	Abcam (ab11426)	1:1000
GFAP	GFAP isolated from cow spinal cord	Rabbit	Abcam (ab7779)	1:1000
PKCα	C-terminus of human PKCα	Rabbit	Epitomics (1510-1)	1:1000
Brn-3a	N-terminus of human Brn-3a	Goat	Santa Cruz (sc-31984)	1:250

Milipore, Billerica, MA. Abcam, Cambridge, UK. Epitomics, Burlingame, CA. Santa Cruz Biotechnology, Santa Cruz, CA.
doi:10.1371/journal.pone.0060361.t002

and 10^{-5} M retinoic acid (RA) to induce neuron-specific differentiation and morphological changes in the SH-SY5Y cells as previously shown [29].

After 48 hours, media was changed and 1 μL of virus (1.0×10^{12} vg/mL) was added per well, giving an overall multiplicity of infection (MOI) of approximately 2×10^{4} vg/cell. The media was changed every 48 hours and RA and TPA were maintained in the media throughout.

Cells were imaged daily to detect GFP expression using an inverted epifluorescence microscope (Leica DM IL). Images were obtained at x20 magnification using identical acquisition settings including exposure time, and were saved at a resolution of 1200×1600 pixels. 9 days after transfection, cells were fixed using 4% paraformaldehyde in PBS and Hoechst 33342 was used for nuclear staining.

Post-fixation images were taken as above, and 8-bit images were analyzed using Image J software. The mean grey level of each image was calculated from a plot profile and the number of pixels above threshold calculated from histogram analysis. Control values (from images taken of wells where no virus was added) were subtracted from the data points to minimize background and also were used to set the threshold. The number of Hoechst-labelled cell nuclei in each field analysed were counted, and grey level and pixel above threshold values were adjusted accordingly, to ensure that any difference in cell number was accounted for.

Statistical Analysis

Mean grey levels on cSLO and histological fluorescence images were compared using two-way ANOVA using strain and rAAV serotype as factors. Mean GFP fluorescence intensity in SH-SY5Y cells in vitro was compared using one-way ANOVA. The Bonferroni post hoc test was applied in all instances, and the significance level was set at 0.05.

Supporting Information

File S1 Supporting Information.
(DOC)

Author Contributions

Conceived and designed the experiments: MWH MJD REM. Performed the experiments: PCI SRDS DML MSS AM QY ARB. Analyzed the data: PCI SRDS DML MSS AM ARB. Contributed reagents/materials/analysis tools: PCI SRDS DML AM REM. Wrote the paper: PCI SRDS DML AM MJD REM.

References

1. Simonelli F, Maguire AM, Testa F, Pierce EA, Mingozzi F, et al. (2010) Gene therapy for Leber's congenital amaurosis is safe and effective through 1.5 years after vector administration. Mol Ther 18: 643–650.
2. Bainbridge JW, Smith AJ, Barker SS, Robbie S, Henderson R, et al. (2008) Effect of gene therapy on visual function in Leber's congenital amaurosis. NEnglJMed 358: 2231–2239.
3. Cideciyan AV, Hauswirth WW, Aleman TS, Kaushal S, Schwartz SB, et al. (2009) Human RPE65 gene therapy for Leber congenital amaurosis: persistence of early visual improvements and safety at 1 year. Hum Gene Ther 20: 999–1004.
4. Cideciyan AV, Hauswirth WW, Aleman TS, Kaushal S, Schwartz SB, et al. (2009) Vision 1 year after gene therapy for Leber's congenital amaurosis. N Engl J Med 361: 725–727.
5. Cideciyan AV, Aleman TS, Boye SL, Schwartz SB, Kaushal S, et al. (2008) Human gene therapy for RPE65 isomerase deficiency activates the retinoid cycle of vision but with slow rod kinetics. Proc Natl Acad Sci U S A 105: 15112–15117.
6. Jacobson SG, Cideciyan AV, Ratnakaram R, Heon E, Schwartz SB, et al. (2011) Gene Therapy for Leber Congenital Amaurosis Caused by RPE65 Mutations: Safety and Efficacy in 15 Children and Adults Followed Up to 3 Years. Arch Ophthalmol.
7. Maguire AM, Simonelli F, Pierce EA, Pugh EN, Jr., Mingozzi F, et al. (2008) Safety and efficacy of gene transfer for Leber's congenital amaurosis. N Engl J Med 358: 2240–2248.
8. Vandenberghe LH, Bell P, Maguire AM, Cearley CN, Xiao R, et al. (2011) Dosage thresholds for AAV2 and AAV8 photoreceptor gene therapy in monkey. Sci Transl Med 3: 88ra54.
9. Mancuso K, Hauswirth WW, Li Q, Connor TB, Kuchenbecker JA, et al. (2009) Gene therapy for red-green colour blindness in adult primates. Nature 461: 784–787.
10. Gao G, Vandenberghe LH, Alvira MR, Lu Y, Calcedo R, et al. (2004) Clades of Adeno-associated viruses are widely disseminated in human tissues. J Virol 78: 6381–6388.
11. Lawlor PA, Bland RJ, Mouravlev A, Young D, During MJ (2009) Efficient gene delivery and selective transduction of glial cells in the mammalian brain by AAV serotypes isolated from nonhuman primates. Mol Ther 17: 1692–1702.
12. Lipinski DM, Singh MS, MacLaren RE (2011) Assessment of cone survival in response to CNTF, GDNF, and VEGF165b in a novel ex vivo model of end-stage retinitis pigmentosa. Invest Ophthalmol Vis Sci 52: 7340–7346.
13. Barker SE, Broderick CA, Robbie SJ, Duran Y, Natkunarajah M, et al. (2009) Subretinal delivery of adeno-associated virus serotype 2 results in minimal immune responses that allow repeat vector administration in immunocompetent mice. J Gene Med 11: 486–497.
14. Mingozzi F, High KA (2011) Immune responses to AAV in clinical trials. Curr Gene Ther 11: 321–330.
15. Yin L, Greenberg K, Hunter JJ, Dalkara D, Kolstad KD, et al. (2011) Intravitreal injection of AAV2 transduces macaque inner retina. Invest Ophthalmol Vis Sci 52: 2775–2783.
16. Kells AP, Hadaczek P, Yin D, Bringas J, Varenika V, et al. (2009) Efficient gene therapy-based method for the delivery of therapeutics to primate cortex. Proc Natl Acad Sci U S A 106: 2407–2411.
17. Natkunarajah M, Trittibach P, McIntosh J, Duran Y, Barker SE, et al. (2008) Assessment of ocular transduction using single-stranded and self-complementary recombinant adeno-associated virus serotype 2/8. Gene Ther 15: 463–467.
18. Dalkara D, Kolstad KD, Caporale N, Visel M, Klimczak RR, et al. (2009) Inner limiting membrane barriers to AAV-mediated retinal transduction from the vitreous. Mol Ther 17: 2096–2102.
19. Petrs-Silva H, Dinculescu A, Li Q, Min SH, Chiodo V, et al. (2009) High-efficiency transduction of the mouse retina by tyrosine-mutant AAV serotype vectors. Mol Ther 17: 463–471.
20. Zhong L, Li B, Mah CS, Govindasamy L, Agbandje-McKenna M, et al. (2008) Next generation of adeno-associated virus 2 vectors: point mutations in tyrosines lead to high-efficiency transduction at lower doses. Proc Natl Acad Sci U S A 105: 7827–7832.
21. DiPrimio N, Asokan A, Govindasamy L, Agbandje-McKenna M, Samulski RJ (2008) Surface loop dynamics in adeno-associated virus capsid assembly. J Virol 82: 5178–5189.
22. Lebherz C, Maguire A, Tang W, Bennett J, Wilson JM (2008) Novel AAV serotypes for improved ocular gene transfer. J Gene Med 10: 375–382.
23. Doroudchi MM, Greenberg KP, Liu J, Silka KA, Boyden ES, et al. (2011) Virally delivered channelrhodopsin-2 safely and effectively restores visual function in multiple mouse models of blindness. Mol Ther 19: 1220–1229.
24. Allocca M, Doria M, Petrillo M, Colella P, Garcia-Hoyos M, et al. (2008) Serotype-dependent packaging of large genes in adeno-associated viral vectors results in effective gene delivery in mice. J Clin Invest 118: 1955–1964.
25. Hirsch ML, Agbandje-McKenna M, Samulski RJ (2010) Little vector, big gene transduction: fragmented genome reassembly of adeno-associated virus. Mol Ther 18: 6–8.
26. Weng J, Mata NL, Azarian SM, Tzekov RT, Birch DG, et al. (1999) Insights into the function of Rim protein in photoreceptors and etiology of Stargardt's disease from the phenotype in abcr knockout mice. Cell 98: 13–23.
27. Charbel Issa P, Singh MS, Lipinski DM, Chong NV, Barnard AR, et al. (2012) Optimization of in vivo confocal autofluorescence imaging of the ocular fundus in mice and its application to models of human retinal degeneration. InvestOphthalmol VisSci.
28. Johnson TV, Martin KR (2008) Development and characterization of an adult retinal explant organotypic tissue culture system as an in vitro intraocular stem cell transplantation model. Invest Ophthalmol Vis Sci 49: 3503–3512.
29. You Q, Brown LA, McClements M, Hankins MW, Maclaren RE (2012) Tetradecanoylphorbol-13-acetate (TPA) significantly increases AAV2/5 transduction of human neuronal cells in vitro. Exp Eye Res 97: 148–153.

Assessment of tropism and effectiveness of new primate derived hybrid recombinant AAV serotypes in the mouse and primate retina

- Supporting information -

Figure S1

Recombinant AAV capsid (Rec) serotypes

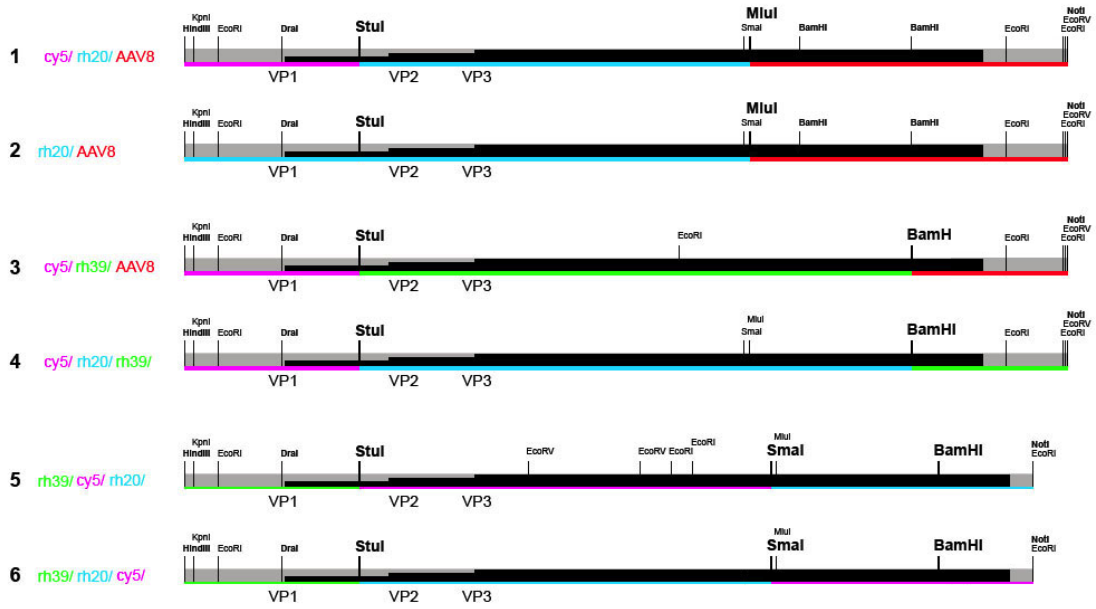

Structure of the six recombinant capsid (Rec) serotypes initially screened showing regions of overlap and restriction sites. The position of the wildtype viral protein (VP) 1-3 sequences are shown in black. The C-terminal half of the VP1 and VP2 proteins includes both the area that corresponds to the heparin binding domain in AAV2 and the HI loop. Whereas, the N-terminal half contains the nuclear localization signal like sequence, as well as several other highly variable domains. Rec2 and Rec3 showed greatest transduction efficacy in cardiac muscle and brain respectively and were selected for this study in the retina.

Figure S2

Rec2/ Rec3/ AAV2/ AAV5 VP protein alignment

```
Rec2   MAADGYLPDWLEDNLSEGIREWWDLKPGAPKPKANQQKQDDGRGLVLPGYKYLGPFNGLD   60
Rec3   MAADGYLPDWLEGNLSEGIREWWDLKPGAPKPKANQQKQDDGRGLVLPGYRYLGPFNGLD   60
AAV2   MAADGYLPDWLEDTLSEGIRQWWKLKPGPPPPKPAERHKDDSRGLVLPGYKYLGPFNGLD   60
AAV5   MSFVDHPPDWLE-EVGEGLREFLGLEAGPPKPKPNQQHQDQARGLVLPGYNYLGPGNGLD   59
       VP1

                        StuI
Rec2   KGEPVNAADAAALEHDKAYDQQLKAGDNPYLRYNHADAEFQERLQEDTSFGGNLGRAVFQ   120
Rec3   KGEPVNEADAAALEHDKAYDQQLKAGDNPYLRYNHADAEFQERLQEDTSFGGNLGRAVFQ   120
AAV2   KGEPVNEADAAALEHDKAYDRQLDSGDNPYLKYNHADAEFQERLKEDTSFGGNLGRAVFQ   120
AAV5   RGEPVNRADEVAREHDISYNEQLEAGDNPYLKYNHADAEFQEKLADDTSFGGNLGKAVFQ   119
                     PLA2                                  VP2

Rec2   AKKRVLEPLGLVEEGAKTAPGKKRPVEPSPQRSPDSSTGIGKTGQQPAKKRLNFGQTGDS   180
Rec3   AKKRVLEPLGLVEEAAKTAPGKKRPVEPSPQRSPDSSTGIGKKGQQPAKKRLNFGQTGDS   180
AAV2   AKKRVLEPLGLVEEPVKTAPGKKRPVEHSPV-EPDSSSGTGKAGQQPARKRLNFGQTGDA   179
AAV5   AKKRVLEPFGLVEEGAKTAPTGKRIDDHFPKRKKART----EEDSKPS-------TSSDA   168
                                                      NLS

Rec2   ESVPDPQPIGEPPAGP-SGLGSGTMAAGGGAPMADNNEGADGVGSSSGNWHCDSTWLGDRV   240
Rec3   ESVPDPQPIGEPPAGP-SGLGSGTMAAGGGAPMADNNEGADGVGSSSGNWHCDSTWLGDRV   240
AAV2   DSVPDPQPLGQPPAAP-SGLGTNTMATGSGAPMADNNEGADGVGNSSGNWHCDSTWMGDRV   239
AAV5   EAGPSGSQQLQIPAQPASSLGADTMSAGGGGPLGDNNQGADGVGNASGDWHCDSTWMGDRV   229
                              VP3

Rec2   ITTSTRTWALPTYNNHLYKQISNGTSGGSTNDNTYFGYSTPWGYFDFNRFHCHFSPRDWQ   300
Rec3   ITTSTRTWALPTYNNHLYKQISNGTSGGSTNDNTYFGYSTPWGYFDFNRFHCHFSPRDWQ   300
AAV2   ITTSTRTWALPTYNNHLYKQISSQ-S-GASNDNHYFGYSTPWGYFDFNRFHCHFSPRDWQ   297
AAV5   VTKSTRTWVLPSYNNHQYREIKSGSVDGS-NANAYFGYSTPWGYFDFNRFHSHWSPRDWQ   288

Rec2   RLINNNWGFRPKRLNFKLFNIQVKEVTQNEGTKTIANNLTSTIQVFTDSEYQLPYVLGSA   360
Rec3   RLINNNWGFRPKRLSFKLFNIQVKEVTQNEGTKTIANNLTSTIQVFTDSEYQLPYVLGSA   360
AAV2   RLINNNWGFRPKRLNFKLFNIQVKEVTQNDGTTTIANNLTSTVQVFTDSEYQLPYVLGSA   357
AAV5   RLINNYWGFRPRSLRVKIFNIQVKEVTVQDSTTTIANNLTSTVQVFTDDDYQLPYVVGNG   348

Rec2   HQGCLPPFPADVFMIPQYGYLTLN--NGSQAVGRSSFYCLEYFPSQMLRTGNNFEFSYQFED   420
Rec3   HQGCLPPFPADVFMIPQYGYLTLN--NGSQAVGRSSFYCLEYFPSQMLRTGNNFEFSYTFED   420
AAV2   HQGCLPPFPADVFMVPQYGYLTLN--NGSQAVGRSSFYCLEYFPSQMLRTGNNFTFSYTFED   417
AAV5   TEGCLPAFPPQVFTLPQYGYATLNRDNTENPTERSSFFCLEYFPSKMLRTGNNFEFTYNFEE   410

Rec2   VPFHSSYAHSQSLDRLMNPLIDQYLYYLSRTQSTGGTAGTQQLLFSQAGPNNMSAQAKNW   480
Rec3   VPFHSSYAHSQSLDRLMNPLIDQYLYYLSRTQSTGGTQGTQQLLFSQAGPANMSAQAKNW   480
AAV2   VPFHSSYAHSQSLDRLMNPLIDQYLYYLSRTNTPSGTTTQSRLQFSQAGASDIRDQSRNW   477
AAV5   VPFHSSFAPSQNLFKLANPLVDQYLYRFVSTNNTGG------VQFNKNLAGRYANTYKNW   464

            MluI
Rec2   LPGPCYRQQRVSTTTGQNNNSNFAWTAGTKYHLNGRNSLANPGIAMATHKDDEERFFPSN   540
Rec3   LPGPCYRQQRVSTTLSQNNNSNFAWTGATKYHLNGRDSLVNPGVAMATHKDDEERFFPSS   540
AAV2   LPGPCYRQQRVSKTSADNNNSEYSWTGATKYHLNGRDSLVNPGPAMASHKDDEEKFFPQS   537
AAV5   FPGPMGRTQGWNLGSGVNRASVSAFATTNRMELEGASYQVPPQPNGMTNNLQGSNTYALE   524

Rec2   GILIFGKQNA-ARDNADY-SDVML-TSEEEIKTTNPVATEEYGIVADNLQQQNTAPQIGTVNS   600
Rec3   GVLMFGKQGA-GRDNVDY-SSVML-TSEEEIKTTNPVATEQYGVVADNLQQTNTGPIVGNVNS   600
AAV2   GVLIFGKQGS-EKTNVDI-EKVMI-TDEEEIRTTNPVATEQYGSVSTNLQRGNRQAATADVNT   597
```

```
AAV5   NTMIFNSQPANPGTTATYLEGNMLITSESETQPVNRVAYNVGGQMATNNQSSTTAPATGTYNL  587

       R 484, 487, 585, 588 and K 532 - heparin binding domain

                                                                  BamHI
Rec2   QGALPGMVWQNRDVYLQGPIWAKIPHTDGNFHPSPLMGGFGLKHPPPQILIKNTPVPADP   660
Rec3   QGALPGMVWQNRDVYLQGPIWAKIPHTDGNFHPSPLMGGFGLKHPPPQILIKNTPVPADP   660
AAV2   QGVLPGMVWQDRDVYLQGPIWAKIPHTDGHFHPSPLMGGFGLKHPPPQILIKNTPVPANP   657
AAV5   QEIVPGSVWMERDVYLQGPIWAKIPETGAHFHPSPAMGGFGLKHPPPMMLIKNTPVPGN-   647

Rec2   PTTFNQSKLNSFITQYSTGQVSVEIEWELQKENSKRWNPEIQYTSNYYKSTSVDFAVNTE   720
Rec3   PTTFNQSKLNSFITQYSTGQVSVEIEWELQKENSKRWNPEIQYTSNYYKSTSVDFAVNTE   720
AAV2   STTFSAAKFASFITQYSTGQVSVEIEWELQKENSKRWNPEIQYTSNYYKSTSVDFAVNTE   717
AAV5   ITSFSDVPVSSFITQYSTGQVTVEMEWELKKENSKRWNPEIQYTNNYNDPQFVDFAPDST   706
       HI loop

Rec2   GVYSEPRPIGTRYLTRNL  738
Rec3   GVYSEPRPIGTRYLTRNL  738
AAV2   GVYSEPRPIGTRYLTRNL  735
AAV5   GEYRTTRPIGTRYLTRPL  724
```

Critical residues are in **bold**: PLA2 – phospholipase A2 site (endosomal release); NLS – nuclear localization signal; HI Loop – protein sequence connecting the H and I beta-strands of the VP3 subunit (genome packaging and assembly). Restriction sites are shown above sequences. Changes between the sequences are highlighted in red. Note that most of the sequence variation of Rec2 and Rec3 is with AAV5, whereas they are not as dissimilar with AAV8.

Fundus Autofluorescence in the *Abca4*$^{-/-}$ Mouse Model of Stargardt Disease—Correlation With Accumulation of A2E, Retinal Function, and Histology

Peter Charbel Issa,[1,2] Alun R. Barnard,[1] Mandeep S. Singh,[1] Emma Carter,[1] Zhichun Jiang,[3] Roxana A. Radu,[3] Ulrich Schraermeyer,[4] and Robert E. MacLaren[1,5]

[1]Oxford Eye Hospital and Nuffield Laboratory of Ophthalmology, University of Oxford, Oxford, United Kingdom
[2]Department of Ophthalmology, University of Bonn, Bonn, Germany
[3]Jules Stein Eye Institute, Department of Ophthalmology, University of California at Los Angeles School of Medicine, Los Angeles, California
[4]University Eye Hospital, University of Tübingen, Tübingen, Germany
[5]Moorfields Eye Hospital and University College London Institute of Ophthalmology Biomedical Research Centre, London, United Kingdom

Correspondence: Peter Charbel Issa, Nuffield Laboratory of Ophthalmology, University of Oxford, John Radcliffe Hospital, OX3 9DU, UK; enquiries@eye.ox.ac.uk.
Robert E. MacLaren, Nuffield Laboratory of Ophthalmology, University of Oxford, John Radcliffe Hospital, OX3 9DU, UK; enquiries@eye.ox.ac.uk.

Submitted: January 18, 2013
Accepted: June 2, 2013

Citation: Charbel Issa P, Barnard AR, Singh MS, et al. Fundus autofluorescence in the *Abca4*$^{-/-}$ mouse model of Stargardt disease—correlation with accumulation of A2E, retinal function, and histology. *Invest Ophthalmol Vis Sci.* 2013;54:5602–5612. DOI: 10.1167/iovs.13-11688

Purpose. To investigate fundus autofluorescence (AF) characteristics in the *Abca4*$^{-/-}$ mouse, an animal model for AMD and Stargardt disease, and to correlate findings with functional, structural, and biochemical assessments.

Methods. Blue (488 nm) and near-infrared (790 nm) fundus AF images were quantitatively and qualitatively analyzed in pigmented *Abca4*$^{-/-}$ mice and wild type (WT) controls in vivo. Functional, structural, and biochemical assessments included electroretinography (ERG), light and electron microscopic analysis, and A2E quantification. All assessments were performed across age groups.

Results. In *Abca4*$^{-/-}$ mice, lipofuscin-related 488 nm AF increased early in life with a ceiling effect after 6 months. This increase was first paralleled by an accumulation of typical lipofuscin granules in the retinal pigment epithelium (RPE). Later, lipofuscin and melanin granules decreased in number, whereas melanolipofuscin granules increased. This increase in melanolipofuscin granules paralleled an increase in melanin-related 790 nm AF. Old *Abca4*$^{-/-}$ mice revealed a flecked fundus AF pattern at both excitation wavelengths. The amount of A2E, a major lipofuscin component, increased 10- to 12-fold in 6- to 9-month-old *Abca4*$^{-/-}$ mice compared with controls, while 488 nm AF intensity only increased 2-fold. Despite pronounced lipofuscin accumulation in the RPE of *Abca4*$^{-/-}$ mice, ERG and histology showed a slow age-related thinning of the photoreceptor layer similar to WT controls up to 12 months.

Conclusions. Fundus AF can be used to monitor lipofuscin accumulation and melanin-related changes in vivo in mouse models of retinal disease. High RPE lipofuscin may not adversely affect retinal structure or function over prolonged time intervals, and melanin-related changes (melanolipofuscin formation) may occur before the decline in retinal function.

Keywords: fundus autofluorescence, mouse model, *Abca4*, A2E

Mutations in the gene coding for the ATP-binding cassette A4 (ABCA4) transmembrane transporter cause autosomal recessive Stargardt disease, cone–rod dystrophy or retinitis pigmentosa.[1–5] Mutations in *ABCA4* are among the most common causes for inherited retinal dystrophies and may, in addition, modify the phenotype of other genetic and/or multifactorial retinal diseases, including AMD.[5–7]

Stargardt disease[8] is the phenotype most commonly caused by *ABCA4* mutations. A hallmark of the disease is an increased fundus autofluorescence (AF) exhibiting the fluorescence characteristics of lipofuscin in the retinal pigment epithelium (RPE).[9,10] Later, atrophy of the central retina develops, which spreads centrifugally over time.[11]

Based on findings in *Abca4*$^{-/-}$ mice, the lack of ABCA4 function results in marked accumulation of the bisretinoid N-retinylidene-N-retinylethanolamine (A2E) in the RPE.[12] A2E is a major component of RPE lipofuscin and appears to have a role in retinal disease pathophysiology. This includes its potential to increase blue light cytotoxicity,[13,14] induce lysosomal dysfunction,[15,16] and activate complement.[17] Increased RPE lipofuscin has been shown in postmortem specimens of *Abca4*$^{-/-}$ mice.[12,18–20] However, it is not known if this increase in lipofuscin/A2E levels is indeed correlated with increased fundus AF measured in vivo in *Abca4*$^{-/-}$ mice.

We recently showed the feasibility, reproducibility, and utility of standardized qualitative and quantitative fundus AF assessment in mice.[21] Being able to monitor A2E/lipofuscin accumulation using noninvasive fundus AF imaging would allow longitudinal in vivo assessment when evaluating potential treatments for Stargardt disease and other potentially lipofuscin-related retinopathies such as AMD. Moreover, studying this clinically meaningful imaging modality in the *Abca4*$^{-/-}$ mouse

along with further structural, biochemical, and functional parameters may have implications for interpreting the human retinal disease phenotype and natural history.

The aim of this study was to investigate quantitative and qualitative fundus AF characteristics in *Abca4*$^{-/-}$ mice at various ages compared with age-matched wild type (WT) controls. In addition to conventional fundus AF with short wavelength excitation (488 nm light), near-infrared (NIR) excitation (790 nm light) was also used. Results were correlated with tissue A2E levels, histologic findings, and retinal function using electroretinography (ERG).

Methods

Mice

Pigmented *Abca4*$^{-/-}$ mice (129S4/SvJae-*Abca*^{4tm1Gbt})[12] were provided by Gabriel Travis (David Geffen School of Medicine, University of California, Los Angeles, CA) and bred in the Biomedical Sciences division, University of Oxford. Pigmented WT control mice (129S2/SvHsd) were purchased from Harlan Laboratories (Hillcrest, UK). All experiments were conducted in female mice. The animals were kept in a 12 hour light (<100 lux)/dark cycle, with food and water available ad libitum. All animal breeding and experimental procedures were performed under approval of local and national ethical and legal authorities, and were conducted in compliance with the ARVO Statement for the Use of Animals in Ophthalmic and Vision Research. *Abca4*$^{-/-}$ and WT mice were homozygous for the (Leu450) allele of *Rpe65* (Supplementary Fig. S1).

Fundus Autofluorescence Imaging

Mouse fundus AF imaging was performed using a confocal scanning laser ophthalmoscope (cSLO; SpectralisHRA, Heidelberg Engineering, Heidelberg, Germany), according to a previously described standardized protocol.[21] Fluorescence was excited using a 488 nm argon laser or a 790 nm diode laser and emission was recorded at 500 to 700 or greater than 810 nm, respectively.

Animals were anesthetized by intraperitoneal injection of 1 mg/kg medetomidine (Dormitor 1 mg/mL; Pfizer, Sandwich, UK) and 60 mg/kg ketamine (Ketaset 100 mg/mL; Fort Dodge, Southampton, UK), and pupils fully dilated with tropicamide eye drops (Mydriaticum 1%; Bausch & Lomb, Kingston-Upon-Thames, UK) and phenylephrine eye drops (phenylephrine hydrochloride 2.5%, Bausch & Lomb). A custom made contact lens was placed on the cornea with hypromellose eye drops (Hypromellose eye drops BPC 0.3%; Matindale Pharmaceuticals, Romford, UK) as viscous coupling fluid. For image acquisition, the mouse was positioned on a platform mounted on the chin rest of the cSLO device. Only one eye per mouse was recorded.

All images were recorded using the 55° lens (Heidelberg Engineering) of the Spectralis HRA. The NIR reflectance image (820 nm diode laser) was used to align the fundus camera relative to the pupil and to focus on the confocal plane of highest reflectivity in the outer retina.[21] Images were recorded using the "automatic real time" (ART) mode, which is able to track ocular movement (e.g., due to respiration) based on high contrast landmarks. The ART mode allows averaging of up to 100 consecutive images in real time, resulting in an improved signal-to-noise ratio.

Image Analysis

For quantitative analysis of fundus AF, the mean grey level on mouse fundus AF images (acquired with standardized signal detector sensitivity, unprocessed, 1536 × 1536 pixels) was measured within a ring shaped area between 250 and 450 pixel radii from the optic disc center (Supplementary Fig. S2) using ImageJ software (Version 1.43, National Institutes of Health, Bethesda, MD; http://rsb.info.nih.gov/ij). The "electronic zero" was subtracted from each measured grey value to obtain the corrected grey level (cGL), which was used for all calculations.

Electroretinography

Animals were dark adapted for at least 6 hours before ERG responses were recorded from one eye. The other eye remained undilated and was protected by a contact lens to facilitate subsequent cSLO imaging. A DTL-type silver-coated nylon thread active electrode (DTL Plus Electrode; Diagnosys LLC, Cambridge, UK) was modified to include a custom-made contact lens of clear Aclar film (Honeywell International, Inc., supplied by Agar Scientific, Stansted, UK). This was positioned concentrically on the cornea using hypromellose eye drops (1% methylcellulose solution) for coupling. Platinum needles in the scruff and at the base of the tail served as reference and ground electrodes, respectively. Signals were differentially amplified and digitized at a rate of 5 kHz using an Espion E2 system (Diagnosys LLC, Cambridge, UK). The amplitude and latency of major ERG components were measured with the Espion software (Diagnosys LLC) using automated and manual methods. Brief (4 ms) single flash stimuli were delivered in a Ganzfeld dome. Animals were placed on a heated platform, maintained at 38°C using a circulating pump-water bath. All recordings were made in a custom-made light-tight Faraday cage.

For dark-adapted testing, responses were elicited by brief flashes of white light on a dark background. Stimulus intensity was increased across an approximately 5 log unit range (Supplementary Table S1). For light-adapted testing, animals were preexposed to steady full-field white background illumination (30 cd/m^2) for 10 minutes. The recovery of dark-adapted function was measured after a 30 second exposure to 1000-lux white light. For this latter experiment, *Abca4*$^{-/-}$ mice were crossed with WT mice and the heterozygote progeny intercrossed to obtain littermate homozygous *Abca4*$^{-/-}$ and WT mice. Further details of the ERG protocols are provided in Supplementary Tables S1 and S2.

In single flash ERGs, the b-wave amplitude (from a-wave trough to b-wave peak) was measured for all ERGs, whereas the a-wave amplitude (from baseline to a-wave trough) was measured only when recognizable as a distinct component (stimulus intensities $\geq$ 0.1 cd.s/m^2). Both amplitudes were measured in unfiltered recordings. Amplitudes of flicker ERGs were measured in recordings with 0 to 100 Hz bandpass and 50 Hz notch filters applied.

Preparation and Embedding for Light and Electron Microscopy

After enucleation, the eyes were cleaned of orbital tissue and, after removal of the cornea, were fixed overnight at 4°C in 2% glutaraldehyde in 0.1 M cacodylate buffer (pH 7.4) containing 100 mM sucrose. After washing with cacodylate buffer, areas of interest in flat mount preparations were excised and post-fixed with 1% osmium tetroxide in 0.1 M cacodylate buffer at room temperature for 1 hour. Dehydration was then started by a series of incubations in 30%, 50%, and 70% ethanol. The samples were stained with saturated uranyl acetate. Dehydration was continued by incubations in 70%, 80%, 95% ethanol, absolute ethanol, and propylene oxide. The samples were then embedded in Epon (SPI-Pon812 Epoxy Embedding Kit; SPI

Investigative Ophthalmology & Visual Science

supplies, West Chester, PA). For light and fluorescence microscopy, staining with osmium and uranylacetate was omitted.

Electron Microscopy and Pigment Granule Quantification

Ultrathin Epon sections (70 nm) from WT control eyes and *Abca4*$^{-/-}$ eyes were post stained with lead citrate and investigated under a transmission electron microscope (TEM; Model 902 A; Carl Zeiss, Oberkochen, Germany). For statistical analysis, the areas occupied by different types of pigment granules were quantified in 5 to 8 micrographs from each group. As lipofuscin is somewhat unusual in *Abca4*$^{-/-}$ mice, the morphologic definition we used in this study of the RPE was as follows: lipofuscin in *Abca4*$^{-/-}$ mice is a type of intracellular granule, which appears in the electron microscope as a membrane bound body with heterogeneous staining and very variable shape generally darker than the cytosol. Melanin granules are easily and reliably distinguished from lipofuscin in the electron microscope, in that melanosomes are uniformly electron dense (black), are not fused with other organelles and appear spindle shaped, ovoid, or round. Melanosomes that are fused with lipofuscin are considered as melanolipofuscin and were included in the combined category of lipofuscin and melanolipofuscin. For lipofuscin and melanolipofuscin quantification, image analysis software (iTEM; Olympus Soft Imaging Solutions, Münster, Germany) was used. For each image, the total area of RPE cytoplasm was determined. Nuclei were not included in this measurement. Apical microvilli and extracellular space in the region of the basal infoldings were also excluded. The included area totaled from approximately 50 to 100 μm^2 per image. The area fraction of lipofuscin/melanolipofuscin is expressed as area in squared micrometers occupied by lipofuscin per 1000 μm^2 RPE cytoplasm.

Fluorescence Microscopy

Autofluorescent lipofuscin and melanolipofuscin granules were photographed in semi-thin sections using a fluorescence microscope (Zeiss Axioplan 2; Carl Zeiss, Jena, Germany; excitation 370/36 nm, emission 575/15 nm, 40× objective) connected to a computer equipped with a CCD camera (Orca-ER; Hamamatsu Photonics, Hamamatsu, Japan). Since the granules could not clearly be separated from each other and lipofuscin cannot be differentiated from melanolipofuscin, the quantification of lipofuscin granules was only performed using electron microscopy.

Outer Nuclear Layer Count

Eyes were dissected in 4% paraformaldehyde (Thermo Fisher, Loughborough, UK) in PBS. After fixation for 30 to 45 minutes, the eyecups were transferred to 30% sucrose for cryoprotection and kept at 4°C overnight. Eyecups were embedded in optimal cutting temperature (OCT) compound (Tissue-Tek, Sakura Finetek, The Netherlands) and frozen on dry ice. Serial 16-μm thick cryosections were affixed to poly-L-lysine–coated glass slides (Polysine; Thermo Scientific, Loughborough, UK), air dried and then stored at −20°C until further histologic processing. Outer nuclear layer (ONL) count was performed after nuclear staining using Hoechst 33342 (Invitrogen Ltd., Paisley, UK) 1:5000 at three eccentricities, 500 and 1000 μm from the optic disc center, and 500 μm from the ora serrata. Nuclei were counted manually within a box of fixed width (20 pixels ≈ 19.6 μm) placed over the ONL. To present data as number of nuclear layers, the total ONL nuclear count was divided by the number of nuclei along the width of the box. Per eye, results from three sections and both sides of the optic nerve head were averaged.

Quantification of A2E

For A2E quantification, the cornea and lens were removed in PBS. Dissected eye cups were immediately snap frozen and stored at −80°C until further processing. The detailed method of *bis*-retinoids extraction and analysis is described in the paper by Radu et al.[22]

Statistical Analysis

PRISM (Version 6.02; GraphPad Software, La Jolla, CA) was used for statistical analysis. Two-way ANOVA was performed to detect significant differences between *Abca4*$^{-/-}$ mice and WT controls, using strain and age as factors. The Holm-Sidak or Bonferroni method was applied in all instances to correct for multiple testing (e.g., in pairwise comparisons). The significance level was set at 0.05.

Results

Longitudinal Recordings of 488 and 790 nm Fundus AF Intensity

Repeated recordings in the same animals were performed between the ages of 1 and 9 months in *Abca4*$^{-/-}$ mice and WT controls to investigate the change in fundus AF levels over time. 488 and 790 nm fundus AF in *Abca4*$^{-/-}$ mice were similar to WT at 1 month (Figs. 1A, 1B). Thereafter, 488 nm fundus AF rose significantly faster in *Abca4*$^{-/-}$ mice compared with WT, leveling off at 6 months (Fig. 1A). Following a different time course, 790 nm AF in *Abca4*$^{-/-}$ mice increased relative to WT only after 3 months of age (Fig. 1B). 488 nm fundus AF levels in all 9-week-old or older *Abca4*$^{-/-}$ mice studied were higher than the 95% confidence interval (CI) of WT measurements. The same applied for 790 nm AF in *Abca4*$^{-/-}$ mice aged 6 and 9 months.

Pupil size, which has a major impact on measured fundus AF in mice,[21] significantly increased with age in both strains to a similar degree (Supplementary Fig. S3). Thus, differences in pupil size would not explain the differences between strains.

Fundus AF levels in *Abca4*$^{-/-}$ mice were normalized to that in age-matched WTs to control for possible age-related confounders including pupil size, and, thus, to allow a better estimation of the effect of *Abca4* deficiency on AF levels over time (Fig. 1C). 488 nm AF rose from 1.2× that of WT at 1 month, to 2× by 3 months, to a maximum of approximately of 2.2×, thereafter showing a ceiling effect. 790 nm AF was 1× WT level in the first 3 months, increased to 1.7× from 3 to 6 months, and to 1.9× by 9 months.

Cross-Sectional Recordings of 488 and 790 nm Fundus AF

To investigate AF in aged animals naïve to any imaging that may have influenced A2E levels, separate cohorts of *Abca4*$^{-/-}$and WT control mice were assessed cross sectionally at 3, 6, 9, 12, and 18 months of age. Eyes of these animals were used to correlate fundus AF levels with postmortem A2E measurements and histology (see below). Quantitative fundus AF assessment in animals 12 months and older was hampered by suspected incident cataract in *Abca4*$^{-/-}$ and WT mice. AF levels in animals aged 3, 6, and 9 months from this independent cross-sectional cohort confirmed the findings of the longitudinal assessment (Supplementary Table S3), and suggested that repeated cSLO imaging in the longitudinally observed animals did not

Investigative Ophthalmology & Visual Science

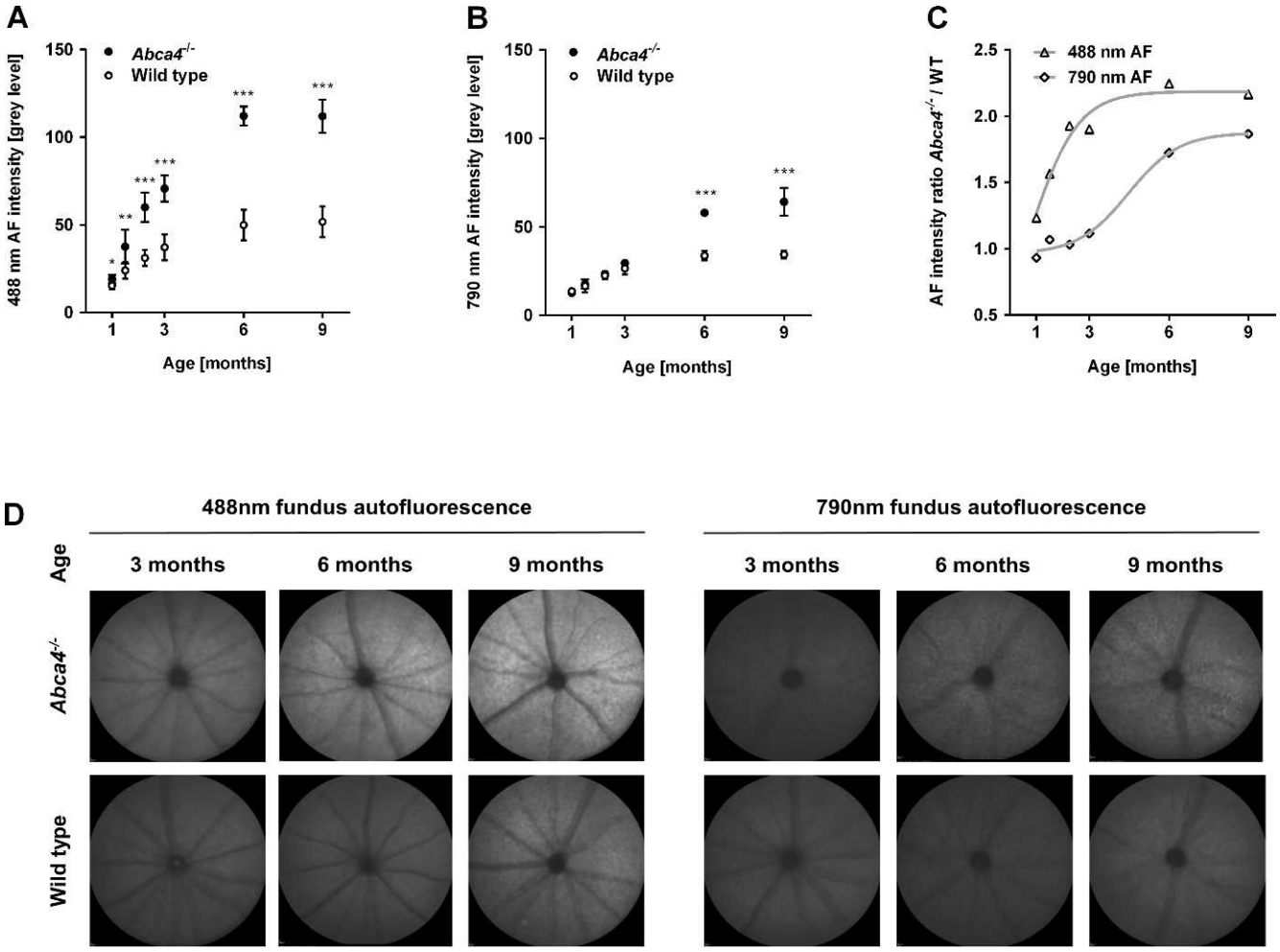

Figure 1. (**A–C**) Longitudinal measurements of fundus AF intensity in the *Abca4*$^{-/-}$ mouse ($n = 5$) and WT ($n = 8$) controls between 1 to 9 months of age. To distinguish lipofuscin- and melanin-related fundus AF, 488 (**A**) and 790 nm (**B**) wavelengths were used for excitation, respectively. Levels of fundus AF (mean ± SD) were significantly different between strains and between age groups ($P < 0.01$, two-way ANOVA) for 488 and 790 nm fundus AF. $^{*}P < 0.05$; $^{**}P < 0.01$; $^{***}P < 0.001$. (**C**) Using the ratio of mean fundus AF between *Abca4*$^{-/-}$ and WT mice controlled for age-related factors potentially affecting AF intensity measures. Curves were fitted to illustrate the time course of AF increase in *Abca4*$^{-/-}$ relative to WT at the two different excitation wavelengths. (**D**) Unprocessed representative recordings of fundus AF excited at 488 and 790 nm in *Abca4*$^{-/-}$ and WT control mice (cross-sectional cohort). Overall, the AF signal was higher with 488 nm compared with 790 nm excitation light. At 3, 6, and 9 months, 488 nm AF in *Abca4*$^{-/-}$ mice is higher than in WT, with a larger difference in older animals. 790 nm AF was only significantly different in 6 and 9 months old animals, where *Abca4*$^{-/-}$ mice show a higher AF level than controls.

significantly modify AF levels over time. Representative recordings with an age- and strain-dependent increase of fundus AF intensity are shown in Figure 1D.

Qualitatively, flecks of increased or decreased 488 nm AF were obvious in 6-month-old *Abca4*$^{-/-}$ mice (Fig. 2A), whereas in WT these appeared later at 9 months and were noticeably less distinct. On 790 nm AF, a fleck pattern was consistently observed in *Abca4*$^{-/-}$ mice 6 months and older. Flecks on 790 nm AF were not seen in WT controls up to the age of 18 months.

Large areas of geographic atrophy, as typically observed in patients with Stargardt disease, were not observed. However, in *Abca4*$^{-/-}$ mice 12 months and older, there were spots of decreased AF. Such loss of fluorophores may suggest focal damage and/or incident atrophy of the RPE. Overall, this was observed more frequently in 790 nm AF, sometimes in presence of near-normal 488 nm AF pattern (Figs. 2B, 2C). In a few eyes the opposite pattern occurred (i.e., that a reduced 488 nm AF was more obvious alongside near-normal 790 nm AF [Fig. 2D]).

Comparison of Fundus AF Recordings and A2E Measurements

A2E is regarded as a major fluorophore of lipofuscin at the ocular fundus. Therefore, we assessed if A2E levels in *Abca4*$^{-/-}$ and WT control mice increased in parallel with 488 nm AF levels (cross-sectional data set). AF ratios between *Abca4*$^{-/-}$ and WT mice confirmed results from the longitudinal data set. 488 nm AF levels in *Abca4*$^{-/-}$ mice were approximately 1.8-fold higher than controls at 3 months and approximately 2-fold at 6 and 9 months (Fig. 3A). In contrast, A2E levels in 3-month-old *Abca4*$^{-/-}$ mice were 8 times higher than controls and increased to approximately 12-fold at 9 months (Fig. 3B).

Electroretinography

In *Abca4*$^{-/-}$ and WT control mice, scotopic a-wave and b-wave amplitudes depended on age and stimulus intensity (Supplementary Fig. S4, Figs. 4A, 4B; two-way ANOVA, all $P < 0.001$). a- and b-wave amplitudes depended on stimulus intensity in all age groups, but only in 18-month-old animals were affected by

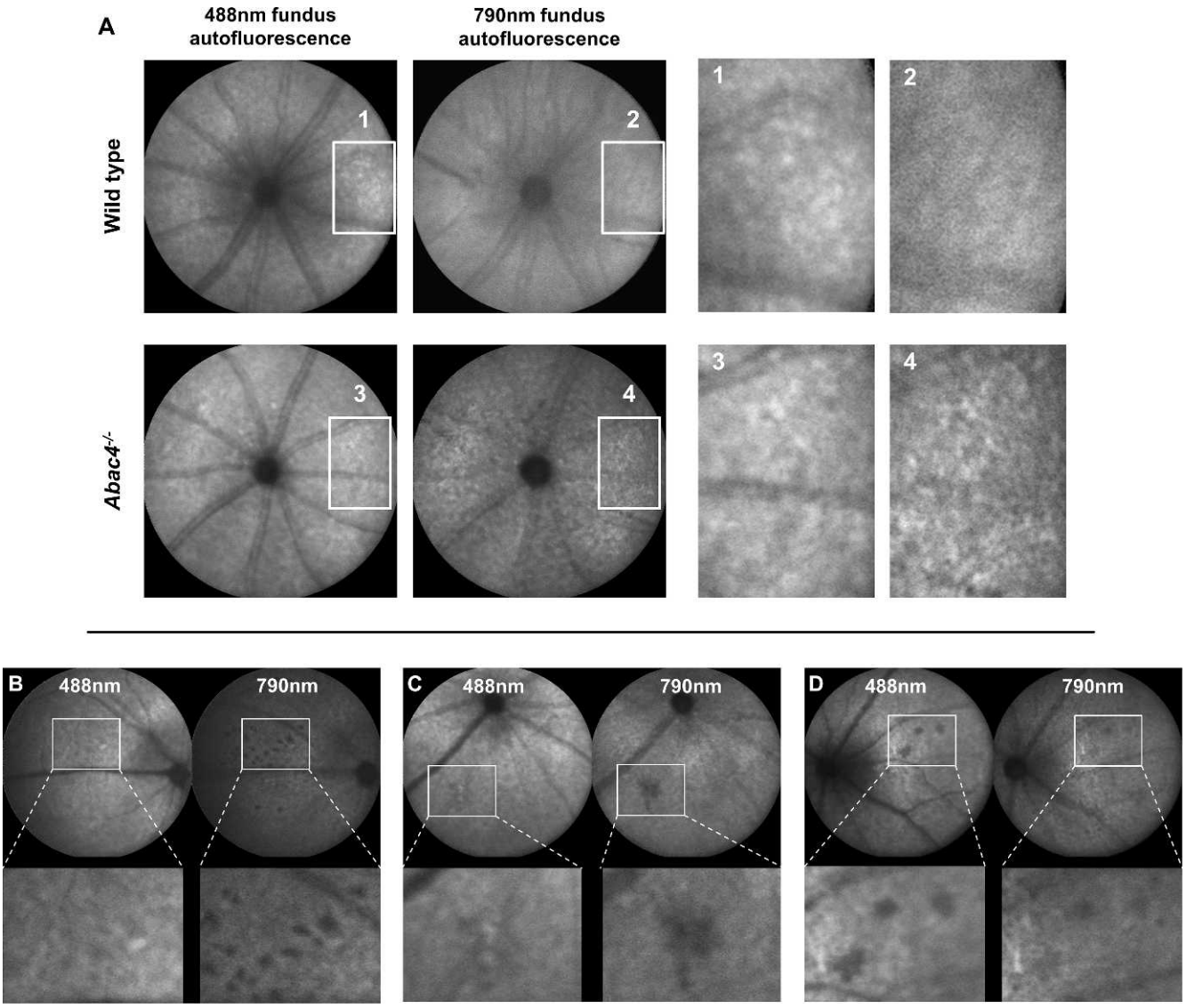

Figure 2. (**A**) Representative AF fleck patterns in a 12-month-old *Abca4*$^{-/-}$ mouse and an age-matched control (images processed for contrast). Flecks on 488 nm AF images were visible in both mice but were more pronounced in the *Abca4*$^{-/-}$ mouse. On 790 nm AF, a fleck pattern was only visible in the *Abca4*$^{-/-}$ mouse, but not in the WT control. (**B**–**D**) Dark areas on fundus AF imaging suggesting focal damage of the RPE in aged *Abca4*$^{-/-}$mice. (**B**, **C**) 488 nm fundus AF (*left*) in a 12- (**B**) and 18- (**C**) month-old mouse showing fleck-like increased AF and faint spots of reduced AF. The latter are also hypofluorescent on the 790 nm AF image (*right*). (**D**) Rarely, spots of markedly reduced AF were more obvious on 488 nm AF images. These lesions were not seen in similarly aged WT mice.

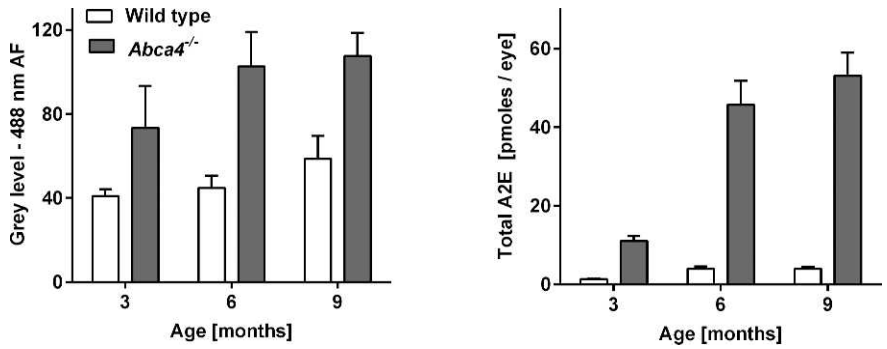

Figure 3. Difference of mean ± SD fundus AF intensity and A2E-levels between *Abca4*$^{-/-}$ and WT control mice aged 3, 6, and 9 months. While fundus AF intensity approximately doubles in *Abca4*$^{-/-}$ mice compared with controls (*left*), A2E levels are 10 and 12 times higher in *Abca4*$^{-/-}$ mice aged 6 and 9 months, respectively (*right*).

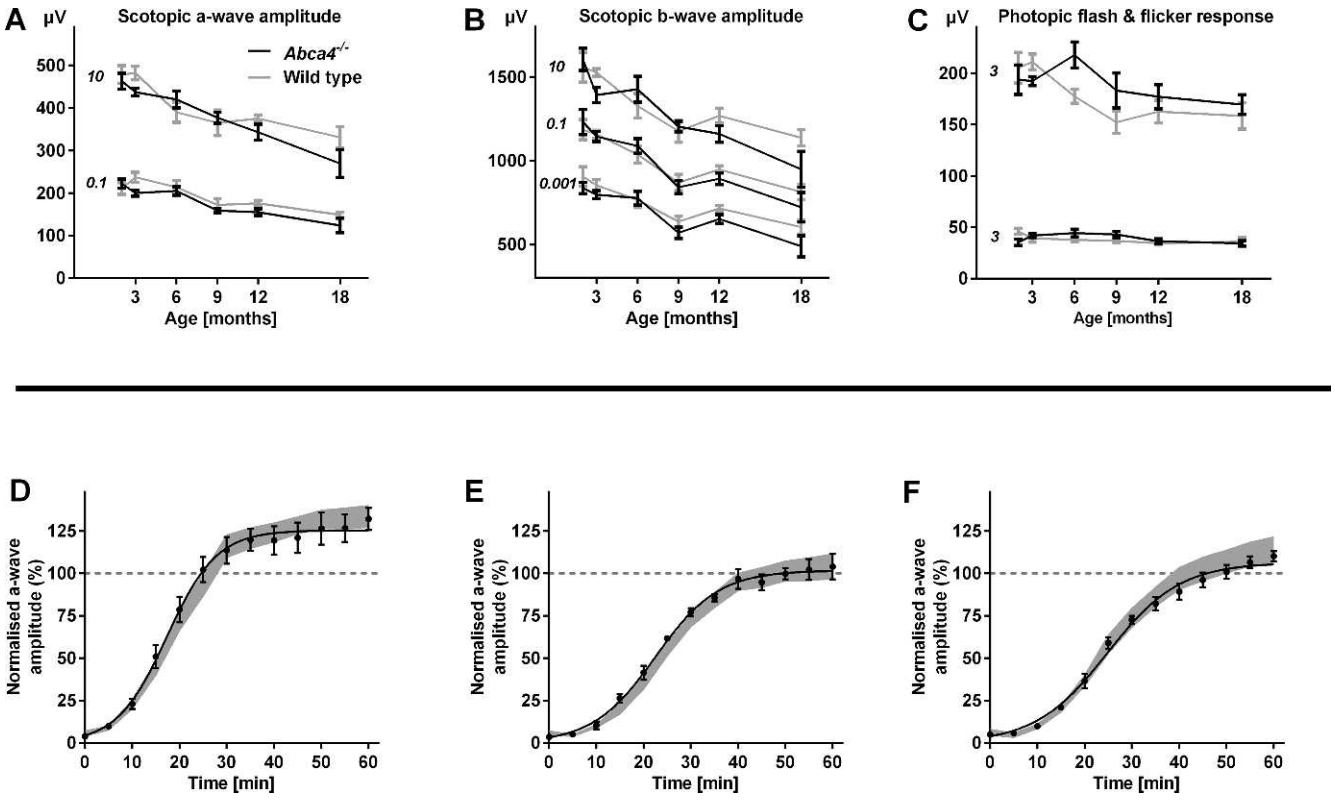

Figure 4. Functional testing by means of electroretinography in *Abca4*$^{-/-}$ and WT control mice. (**A–C**) Mean scotopic and photopic amplitudes ± SEM across all tested ages for representative flash intensities (for full range of mean traces see Supplementary Fig. S4). Numbers in italics indicate flash intensity in cd/m^2. The only significant difference between *Abca4*$^{-/-}$ mice and WT controls was observed in the scotopic testing of 18-month-old animals. *n* equals 5 to 8 in each group, except *n* equals 4 for 18-month-old WTs. (**D–F**) Kinetics of dark adaptation in *Abca4*$^{-/-}$ compared with WT control mice ($n = 5$–7 in each group) aged 1 (**D**), 4 (**E**), and 8 (**F**) months. The mean (±SEM) scotopic a-wave amplitude relative to baseline before a photobleach is shown. The *grey area* represents the mean ± 2SDs of the dark adaptation kinetics in WT mice. Recovery after photobleach was faster in 1-month-old compared with 4- and 8-month-old animals. Dark adaptation kinetics were similar in *Abca4*$^{-/-}$ and WT control mice.

genotype (two-way ANOVA, $P < 0.05$). Scotopic and photopic flicker ERG as well as photopic flash ERG were no different in *Abca4*$^{-/-}$ compared with WT mice (Supplementary Fig. S4, Fig. 4C).

The mean EC50 (as a sensitivity parameter) and mean hill slope (as a parameter for the dynamic range) on curve-fitted a-wave recordings in *Abca4*$^{-/-}$ mice were similar to WT mice, and did not vary with age (two-way ANOVA) at all intensities. Mean V_{max} (the maximum amplitude) varied with age ($P < 0.001$) but not genotype (two-way ANOVA). Bonferroni-corrected post hoc analysis revealed significant differences between animals aged 18 and 2 ($P < 0.001$), 3 ($P < 0.001$), and 6 ($P < 0.01$) months, as well as between mice aged 2 and 9 ($P < 0.05$), and 12 ($P < 0.001$) months.

Based on previous reports of an inhibitory effect of A2E on RPE65,[23] a key enzyme in the visual cycle, we hypothesized that dark adaptation after a photobleach as a functional measure for visual cycle efficiency would be slowed down with age (thus, significantly increased A2E-levels) in the *Abca4*$^{-/-}$ mouse compared with age-matched WT controls. Baseline a-wave amplitudes before the photobleach decreased with age, but were not different between strains (Supplementary Fig. S5), recapitulating the above results in a separate set of animals. Dark adaptation after a photobleach was slower in 4- and 8-month-old *Abca4*$^{-/-}$ mice than at age 1 month (Supplementary Fig. S5, Figs. 4D–F). This age effect was similar in WT mice.

Bright Light and Fluorescence Microscopy

In line with the functional ERG data, quantification of the photoreceptor layer thickness revealed loss of photoreceptors with age in *Abca4*$^{-/-}$ mice similar to WT controls up to 18 months (Supplementary Fig. S6). Semithin sections (Fig. 5A) qualitatively illustrate the similarity between retinas of *Abca4*$^{-/-}$ and WT mice even in 18-month-old animals. In contrast, the RPE of *Abca4*$^{-/-}$ mice showed marked structural differences compared with WT controls, with bright dots representing extensively accumulated lipofuscin granules (arrowhead in Fig. 5A). Also vacuolisation of RPE cells was observed focally in 18-month-old *Abca4*$^{-/-}$ mice (Supplementary Fig. S7). Under fluorescent light, lipofuscin was virtually absent in 3-month-old WT mice and increased little in animals aged 12 and 18 months (Fig. 5B). In contrast, fluorescent granules accumulated extensively with age in *Abca4*$^{-/-}$ mice.

Ultrastructural Observations in the TEM

The retina, RPE, and choroid tissues were examined to determine ultrastructural differences in *Abca4*$^{-/-}$ mice and WT controls. Prominent differences were only detected in the RPE. In young *Abca4*$^{-/-}$ mice, electron-opaque homogeneous granules as shown in Figure 6A were frequent, but significantly reduced in number in 12-month-old *Abca4*$^{-/-}$ mice. These granules had the typical appearance that has been described in aged human or monkey RPE and were nearly completely absent in WT mice. With increasing age in *Abca4*$^{-/-}$ mice,

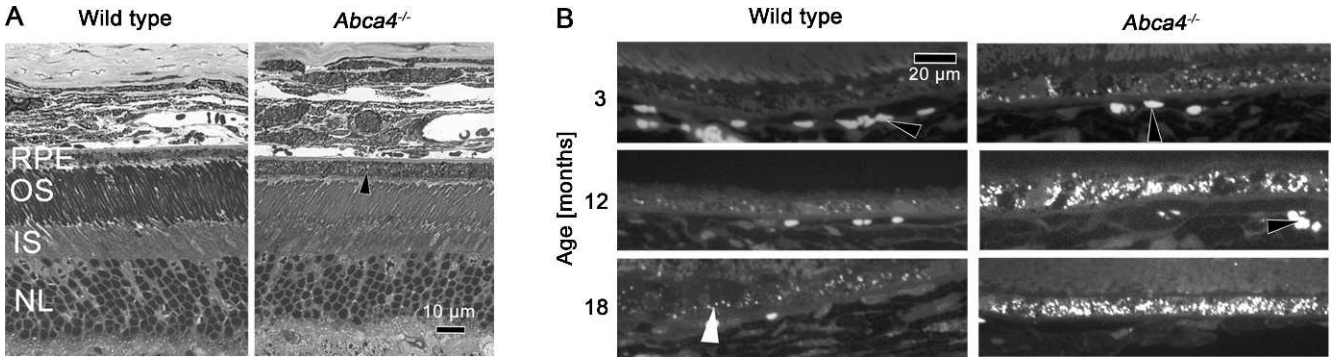

Figure 5. (**A**) Bright light microscopy of semithin sections of eyes from *Abca4*$^{-/-}$ and WT mice. In the RPE of 18-month-old *Abca4*$^{-/-}$mice bright dots (*arrowhead*) representing lipofuscin are detected, but are lacking in the age-matched WT control. Retinal morphology is otherwise similar. (**B**) Under fluorescent light, lipofuscin AF is virtually absent in WT mice at age 3 months and increased only little at 12 and 18 months. In contrast a strong accumulation of fluorescent granules with age occurred in *Abca4*$^{-/-}$ mice. Individual lipofuscin granules are indicated by a *white arrowhead*. Red blood cells also are somewhat autofluorescent (*black arrowheads*). OS, photoreceptor outer segments; IS, photoreceptor inner segments; NL, photoreceptor nuclear layer.

unusual material accumulated in the cytoplasm of RPE cells (Fig. 6), irregular in shape and electron dense. This type of organelle was nearly absent from WT mice. Although it is possible that these organelles are similar to the typical membrane bound lipofuscin granule, membranes were difficult to detect. The latter organelles showed a tendency to fuse with each other and occasionally with melanosomes (Fig. 6B). Eighteen-month-old mice of both groups contained electron opaque material between Bruch's membrane and basal infoldings (asterisks in Fig. 6A).

Quantification of Lipofuscin Granules by Electron Microscopy

The total areas (μm^2) occupied by lipofuscin and melanolipofuscin per 1000 μm^2 sectioned RPE cytoplasm was significantly higher in *Abca4*$^{-/-}$ mice at 12 and 18 months (53.4 $\pm$ 39.2 μm^2 and 115.6 $\pm$ 18.8 μm^2) compared with age-matched WT mice (2.2 $\pm$ 3.9 μm^2 and 0.5 $\pm$ 1.1 μm^2; Fig. 6C). This increase was statistically significant at 12 and 18 months of age ($P < 0.001$, Dunnett's test) but not at 3 months. The classical lipofuscin granules shown in Figure 6A occupied 16.1 $\pm$ 6.9 μm^2 in 3-month- and 5.7 $\pm$ 6.6 μm^2 in 12-month-old *Abca4*$^{-/-}$ mice ($P < 0.02$). They were virtually absent in 18-month-old *Abca4*$^{-/-}$ mice.

Discussion

488 and 790 nm Fundus AF: Its Relation to A2E Accumulation and Subcellular RPE Alterations

Quantitative analysis of AF intensity was performed in animals aged up to 9 months, when *Abca4*$^{-/-}$ mice were not different from WT controls in function and photoreceptor count, and without media opacity that could influence AF measurement. Because fundus AF quantification in mice is influenced by various factors that change with age, such as pupil width, eye size, and optical magnification,[21] AF measures in *Abca4*$^{-/-}$ mice were normalized to WT controls. This should control for age-related changes in knock-out and control mouse strains.

The ratio of 488 nm AF measurements between *Abca4*$^{-/-}$ and WT mice increased steeply within the first 3 months of life to approximately two, followed by a ceiling effect with only a minor further increase until age 9 months. These values are similar to those previously reported in patients with Stargardt disease compared with healthy controls.[24,25] Although the ratio of A2E levels between *Abca4*$^{-/-}$ and WT mice changed with a similar time course, its increase was considerably higher. One hypothesis to explain this discrepancy (assuming *Abca4*$^{-/-}$ mice had *bis*-retinoid and AF levels similar to WT mice at birth) would be that a substantial fraction of the 488-nm fundus AF signal in WT mice derives from fluorophores other than A2E and related *bis*-retinoids that do not vary considerably between WT and *Abca4*$^{-/-}$ mice (e.g., connective tissue flavoproteins, retinoids that do not depend on functional ABCA4; Fig. 7). A large increase in A2E content would then be necessary before relevant changes of 488 nm AF may be detected. Thus, increased 488 nm fundus AF levels parallel the accumulation of A2E in the RPE of *Abca4*$^{-/-}$ mice, but may not quantitatively represent its accumulation in direct proportion. Such "incongruence" was also reported based on post mortem experiments by Boyer et al. who found a lack of correspondence in the rates of increase between lipofuscin-related AF in eyecups and quantification of A2E.[26] Similar to our data, AF and A2E-levels in eyes from aged *Abca4*$^{-/-}$ mice (background strain: 129Sv) compared with WT controls were approximately 2- and 10-fold higher, respectively.[26] The same authors also reported incongruence between lipofuscin-related AF and A2E levels across different WT mouse strains: while eyecup AF intensity in the C57BL/6 strain was higher compared with the 129Sv strain, A2E-levels were lower. Such differences of AF intensity based on genetic background were also observed in our experiments (not reported in detail; Supplementary Fig. S8) and may be of interest when interpreting quantitative AF measures in humans.[27] Boyer et al.[26] also challenged the current hypothesis on the function of ABCA4 by providing evidence that light exposure and thus all-*trans*-retinal formation is not necessary for accumulation of A2E- and lipofuscin in the RPE. Assessment of AF intensity in vivo in dark-reared animals was not performed in our study, but would complement those findings.

An additional explanation for the faster increase of A2E-levels compared with AF levels would be an interaction between lipofuscin-accumulation and fundus AF intensity. Lipofuscin located in the apical RPE cell compartment may absorb excitation light and, thus, reduce the contribution to the AF signal from more basally located lipofuscin.

Melanin-related 790-nm AF levels also revealed a pronounced but considerably later increase compared with 488 nm AF. The major fluorophore for NIR excitation and thus the origin of 790 nm AF at the ocular fundus appears to be melanin.[28] Oxidative stress on the RPE has been suggested to play a pathophysiologic role in a variety of retinal diseases, and

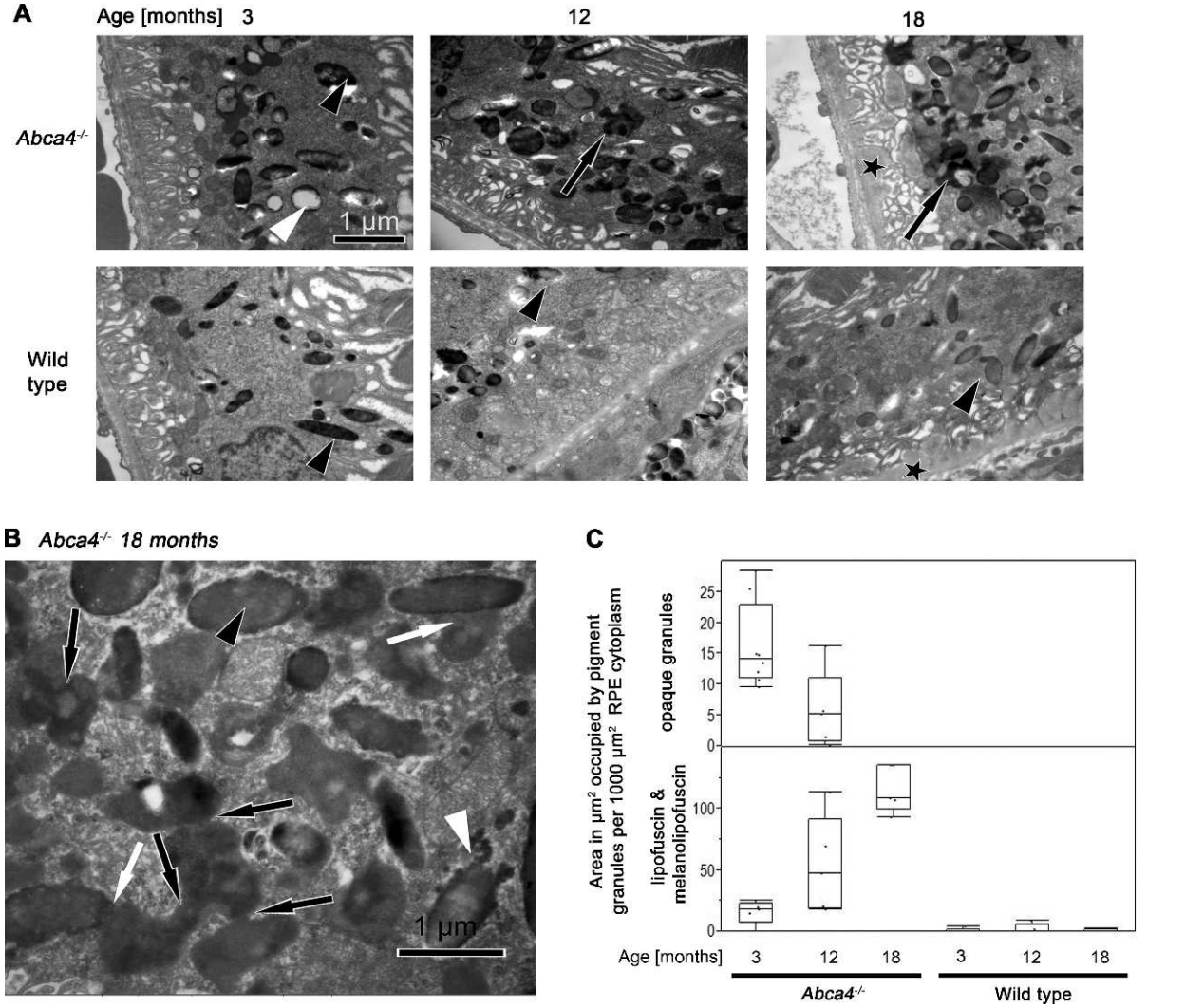

Figure 6. (**A**) TEM micrographs of RPE cells of from *Abca4*$^{-/-}$ and WT mice at ages 3, 12, and 18 months. In 3-month-old *Abca4*$^{-/-}$ mice electron-opaque homogeneous granules are labeled by a *white* and a melanosome by a *black arrowhead*. The granule labeled by the *white arrowhead* represents the more classical type of lipofuscin. With progression of age, unusual granules of irregular shape and electron density (*black arrows*) accumulate in the RPE cytoplasm of 12- and 18-month-old *Abca4*$^{-/-}$ mice. This type of organelle is nearly absent from WT mice. Melanosomes are indicated by *black arrowheads*. Eighteen-month-old mice of both groups contain electron opaque material (*asterisks*) between Bruch's membrane and basal infoldings. (**B**) TEM micrograph of the RPE from an 18-month-old *Abca4*$^{-/-}$ mouse at high magnification. With progression of age, unusual granules accumulated in the cytoplasm of RPE cells. A melanosome is marked by an *arrowhead* and Bruch's membrane by an *asterisk*. The material accumulated in the cytoplasm is irregular in shape and electron dense (*black arrows*). These granules appear to fuse with each other (*black arrows*) and with melanosomes (*white arrows*). The electron density of these confluent granules is occasionally as dense as in melanosomes (*black arrowhead*). A melanosome in a state of disintegration is indicated by a *white arrowhead* and were also present in WT mice. (**C**) Quantification of lipofuscin and melanolipofuscin granules by electron microscopy. The total areas (μm^2) occupied by lipofuscin and melanolipofuscin per 1000 μm^2 sectioned RPE cytoplasm increased significantly in *Abca4*$^{-/-}$ mice at 12 and 18 months compared with age-matched WTs. The area occupied by the classic (*opaque*) lipofuscin granules in *Abca4*$^{-/-}$ mice declined with age.

oxidation of melanin has been shown to increase its autofluorescence.[29,30] The observed time course of 790 nm AF could therefore be explained by increased oxidative stress in RPE cells after pronounced A2E accumulation. Based on electron microscopy findings, a significant increase in melanin-related AF due to an increase in melanin granules appears unlikely. However, melanin granules revealed marked morphologic alteration with a similar time course as the increase in 790 nm AF. Oxidative stress increases in RPE cells with increased lipofuscin load, possibly leading to melanin oxidation and formation of melanolipofuscin granules. Thus, altered AF properties of melanin (e.g., through oxidation or fusion with lipofuscin granules) appear to be the most likely explanation for the increased 790 nm AF. It is notable that in contrast to the results of this study, in albino *Abca4*$^{-/-}$ mice there is a progressive photoreceptor cell loss that is detectable at 8 months of age and worsens at 11 and 13 months.[31] Because melanin has an antioxidative capacity[32] the formation of melanolipofuscin as observed in the present study may reduce the formation of oxidative damage caused by lipofuscin alone.

No larger areas of RPE atrophy similar to those observed in Stargardt patients were observed in animals up to an age of 18 months. However, small patches of AF loss suggestive for RPE damage were observed in some *Abca4*$^{-/-}$ mice 9 months and older, but were never present in WT mice of similar age.

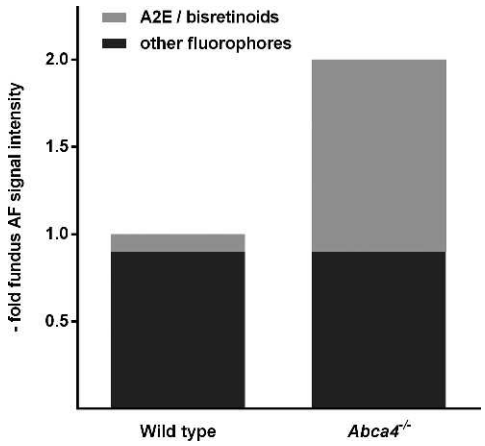

Figure 7. Model to explain the discrepancy between the approximate 2-fold higher fundus AF levels and approximate 10-fold higher A2E levels in *Abca4*$^{-/-}$ mice compared with WT controls. There may be only a low contribution of A2E and related bis-retinoids to fundus AF intensity in WT mice.

Besides RPE cell atrophy and/or a change in fluorophores, vacuolization within the RPE (Supplementary Fig. S7) might contribute to this finding. Loss of 790 nm AF often appeared to precede loss of 488 nm AF. Those findings suggest that high A2E levels may not be the direct cause of damage within the RPE, which appears to develop after an increase in melanin-related AF. If oxidation products of A2E are causing the changes in the melanin compartment and/or are cytotoxic, increased light exposure might lead to earlier development of the observed changes.

Functional Relevance of Increased Fundus AF Levels and A2E Accumulation

Despite the high levels of fundus AF and A2E in *Abca4*$^{-/-}$ mice early in life (i.e., in 2- to 3- month-old animals), no areas of atrophy similar to those observed in Stargardt patients were observed up to 18 months of age. Also, such high lipofuscin contents in the RPE remained without functionally relevant damage over prolonged time intervals, as shown by ERG testing. Thus, high A2E levels can be tolerated by RPE cells over prolonged time periods, and additional factors such as high oxidative stress or the macular anatomy appear to be necessary to develop RPE atrophy.

Notably, an increase in 790-nm AF intensity preceded functional differences between *Abca4*$^{-/-}$ and WT mice and occurred before the appearance of small atrophy-resembling spots on AF images. Thus, alterations in the melanosomal compartment, as revealed by 790-nm AF imaging, seem to precede structurally and functionally relevant changes in the RPE.

Assessment of dark adaptation revealed an effect of age in *Abca4*$^{-/-}$ and WT mice. This effect was similar between strains, suggesting that there is no relevant effect of the lack of ABCA4. Notably, the change in dark adaptation rate from 1 to 4 months of age was similar between strains despite the very steep increase of A2E and lipofuscin-related AF levels in *Abca4*$^{-/-}$ mice. This suggests that an inhibitory effect of A2E on RPE65 may not be an important contributor to delayed dark adaptation in vivo. It should be noted that protocols, background strains, assessed parameters, and analysis to describe the dark adaptation characteristics in *Abca4*$^{-/-}$ mice vary considerably in the literature,[12,33–36] which may be the reason heterogeneous and partly unreproducible results across studies. Our protocol assessing recovery of scotopic single flash amplitudes aimed at identifying differences in retinoid cycle kinetics after a photobleach. Although there might be a trend for a declining dark-adaptation rate in aged *Abca4*$^{-/-}$ compared with WT controls (Fig. 4F), the difference of this parameter might not be substantial and robust enough to assess treatment effects in preclinical studies. Paired-flash ERG analysis and similar protocols may identify reduced photoreceptor sensitivity states, for which the protocol used in this study would not be suitable.

Comparison With Human Disease

Cideciyan et al. have proposed six stages of the human disease sequence, where stage 1 is characterized by a healthy retinal structure and function, and stage 6 by complete degeneration of photoreceptors and RPE cells with loss of function.[25] The first detectable changes were described occurring in fundus AF imaging as an increase in intensity (stage 2) and texture (the spatial variation of fundus AF intensity; stage 3). Functional decline, as surrogate for partial photoreceptor degeneration, defines stage 4. Notably, slowing of the retinoid cycle (i.e., a prolonged dark adaptation) was not present beforehand, which is in in contrast to the somewhat inconsistent observations in the *Abca4*$^{-/-}$ mouse. In stage 5, functional deficits increase together with a decline in mean AF intensity.[25] Two studies have reported that loss of 790 nm AF precedes loss of 480 nm AF,[11,37] and a model was suggested with decreasing 790 nm AF preceding similar changes on 488-nm AF imaging.

The *Abca4*$^{-/-}$ mouse model assessed herein mainly reflects the early stages of this proposed human disease sequence and may aid in adjusting suggested diseases models. There is an early diffuse increase in 488-nm fundus AF intensity due to lipofuscin accumulation, followed by an increase in texture (i.e., spatial variation of fundus AF and occurrence of fleck-like lesions). The mouse model suggests that preceding functional decline (as observed in 18-month-old *Abca4*$^{-/-}$ mice, equivalent to the human disease stage 4) 790-nm fundus AF increases, most likely due to formation of melanolipofuscin. Higher long-wavelength AF intensity has been observed in humans irrespective of marked textural changes[9]; however, this phenotypic feature had not been placed into the context of the disease sequence. A fleck-like increase and subsequent decrease of 790 nm AF may precede similar changes on 488 nm AF, and functional decline ensues.

Progressive loss of cones starting in stage 2 has been shown by adaptive optics SLO imaging in the posterior fundus of patients with Stargardt disease,[38] and spectral domain OCT imaging has suggested that foveal photoreceptor damage may occur before occurrence of characteristic AF patterns.[39] In the *Abca4*$^{-/-}$ mouse, functional testing using ERG and histologic analysis does not suggest significant photoreceptor loss at a similar disease stage. This discrepancy may be explained by the different anatomy of the human macula and the low number of cones in the mouse retina. The human macula with its particular anatomy and physiology appears most vulnerable to the development of functionally relevant retinal atrophy in ABCA4-related retinal disease. The mouse model, however, might rather mimic the disease course in more peripheral human retina. Also, various human mutations have different effects on disease manifestation and progression,[40] and this may differ from the null-background in the *Abca4*$^{-/-}$ mouse.

Stargardt patients have been observed to have fundus AF intensity (excitation: 510 nm; emission: 620 nm) above the age-matched 99.99% CI of healthy control subjects.[10] As in our study, there appeared to be a trend that the increase of fundus AF in Stargardt patients is more pronounced at younger age,[10,41] possibly with a ceiling effect later in life, while there

appears to be a quasi linear increase with age in healthy controls. The observed approximate 2-fold increase of AF intensity compared with WT mice is in line with the data by Delori et al.[10] in Stargardt patients. Normal or decreased fundus AF levels in patients with Stargardt diseases as reported by Lois et al.[42] might be due to assessment at various disease stages (see above), or may be explained by different mutational effects, gene–gene interactions, environmental modifiers, and genetic heterogeneity.

Conclusions

Progressive changes in fundus AF are observed in a large number of human retinal diseases, including AMD and most inherited retinal dystrophies, and such changes have been suggested as markers for disease progression. The use of the same in vivo imaging technique to assess animal models allows investigation of the cellular and biochemical alterations underlying changes visible on fundus AF imaging, and may, thus, further the understanding of fundus AF in human retinal disease.

We show that quantitative and qualitative changes in fundus AF can be assessed in the *Abca4*$^{-/-}$ mouse. Increased fundus AF intensity (488 nm excitation light) is related to an increase in lipofuscin and one of its major constituents, A2E, and may therefore be used as a surrogate marker for monitoring efficacy of drug or gene therapy treatments aimed at lowering RPE-lipofuscin. Using similar imaging techniques in patients, results from preclinical studies may be directly translated into clinical trials. Of note, increased lipofuscin-associated AF alone did not result in functional decline. However, quantitation of 790 nm AF may be a useful early marker for functionally relevant RPE alteration. Increased 790 nm AF follows lipofuscin accumulation, is associated with changes in the melanosome compartment and might precede functionally relevant cell loss.

Note after acceptance of the manuscript: During the review of this manuscript, a paper with partly similar content was published by Sparrow et al.[43] in the same journal. A discussion relating to their findings can be found in the Supplementary Material.

Acknowledgments

The authors thank Sylvia Bolz for her excellent technical assistance (Section of Experimental Vitreoretinal Surgery; Centre of Ophthalmology, Institute for Ophthalmic Research, Tübingen, Germany).

Supported by The European Commission, FP7, Marie Curie Intra-European Fellowship 237238; ProRetina; Fight for Sight; Wellcome Trust Grant 086868/Z/08/Z; Health Foundation; Royal College of Surgeons of Edinburgh; and National Institute for Health Research Oxford and Moorfields Biomedical Research Centres.

Disclosure: **P. Charbel Issa**, None; **A.R. Barnard**, None; **M.S. Singh**, None; **E. Carter**, None; **Z. Jiang**, None; **R.A. Radu**, None; **U. Schraermeyer**, None; **R.E. MacLaren**, None

References

1. Allikmets R, Singh N, Sun H, et al. A photoreceptor cell-specific ATP-binding transporter gene (ABCR) is mutated in recessive Stargardt macular dystrophy. *Nat Genet*. 1997;15:236–246.
2. Cremers FP, van de Pol DJ, van Driel M, et al. Autosomal recessive retinitis pigmentosa and cone-rod dystrophy caused by splice site mutations in the Stargardt's disease gene ABCR. *Hum Mol Genet*. 1998;7:355–362.
3. Martinez MA, Paloma E, Allikmets R, et al. Retinitis pigmentosa caused by a homozygous mutation in the Stargardt disease gene ABCR. *Nat Genet*. 1998;18:11–12.
4. Maugeri A, Klevering BJ, Rohrschneider K, et al. Mutations in the ABCA4 (ABCR) gene are the major cause of autosomal recessive cone-rod dystrophy. *Am J Hum Genet*. 2000;67:960–966.
5. Klevering BJ, Deutman AF, Maugeri A, Cremers FP, Hoyng CB. The spectrum of retinal phenotypes caused by mutations in the ABCA4 gene. *Graefes Arch Clin Exp Ophthalmol*. 2005;243:90–100.
6. Allikmets R, Shroyer NF, Singh N, et al. Mutation of the Stargardt disease gene (ABCR) in age-related macular degeneration. *Science*. 1997;277:1805–1807.
7. Poloschek CM, Bach M, Lagreze WA, et al. ABCA4 and ROM1: implications for modification of the PRPH2-associated macular dystrophy phenotype. *Invest Ophthalmol Vis Sci*. 2010;51:4253–4265.
8. Stargardt K. Über familiäre, progressive Degenerationen in der Maculagegend des Auges. *Graefes Arch Clin Exp Ophthalmol*. 1909;71:534–550.
9. Cideciyan AV, Swider M, Aleman TS, et al. Reduced-illuminance autofluorescence imaging in ABCA4-associated retinal degenerations. *J Opt Soc Am A Opt Image Sci Vis*. 2007;24:1457–1467.
10. Delori FC, Staurenghi G, Arend O, Dorey CK, Goger DG, Weiter JJ. In vivo measurement of lipofuscin in Stargardt's disease–Fundus flavimaculatus. *Invest Ophthalmol Vis Sci*. 1995;36:2327–2331.
11. Cukras CA, Wong WT, Caruso R, Cunningham D, Zein W, Sieving PA. Centrifugal expansion of fundus autofluorescence patterns in Stargardt disease over time. *Arch Ophthalmol*. 2012;130:171–179.
12. Weng J, Mata NL, Azarian SM, Tzekov RT, Birch DG, Travis GH. Insights into the function of Rim protein in photoreceptors and etiology of Stargardt's disease from the phenotype in abcr knockout mice. *Cell*. 1999;98:13–23.
13. Schütt F, Davies S, Kopitz J, Holz FG, Boulton ME. Photodamage to human RPE cells by A2-E, a retinoid component of lipofuscin. *Invest Ophthalmol Vis Sci*. 2000;41:2303–2308.
14. Sparrow JR, Nakanishi K, Parish CA. The lipofuscin fluorophore A2E mediates blue light-induced damage to retinal pigmented epithelial cells. *Invest Ophthalmol Vis Sci*. 2000;41:1981–1989.
15. Bergmann M, Schütt F, Holz FG, Kopitz J. Inhibition of the ATP-driven proton pump in RPE lysosomes by the major lipofuscin fluorophore A2-E may contribute to the pathogenesis of age-related macular degeneration. *FASEB J*. 2004;18:562–564.
16. Holz FG, Schütt F, Kopitz J, et al. Inhibition of lysosomal degradative functions in RPE cells by a retinoid component of lipofuscin. *Invest Ophthalmol Vis Sci*. 1999;40:737–743.
17. Zhou J, Jang YP, Kim SR, Sparrow JR. Complement activation by photooxidation products of A2E, a lipofuscin constituent of the retinal pigment epithelium. *Proc Natl Acad Sci U S A*. 2006;103:16182–16187.
18. Grey AC, Crouch RK, Koutalos Y, Schey KL, Ablonczy Z. Spatial localization of A2E in the retinal pigment epithelium. *Invest Ophthalmol Vis Sci*. 2011;52:3926–3933.
19. Radu RA, Han Y, Bui TV, et al. Reductions in serum vitamin A arrest accumulation of toxic retinal fluorophores: a potential therapy for treatment of lipofuscin-based retinal diseases. *Invest Ophthalmol Vis Sci*. 2005;46:4393–4401.
20. Radu RA, Yuan Q, Hu J, et al. Accelerated accumulation of lipofuscin pigments in the RPE of a mouse model for ABCA4-mediated retinal dystrophies following vitamin A supplementation. *Invest Ophthalmol Vis Sci*. 2008;49:3821–3829.
21. Charbel Issa P, Singh MS, Lipinski DM, et al. Optimization of in vivo confocal autofluorescence imaging of the ocular fundus in mice and its application to models of human retinal degeneration. *Invest Ophthalmol Vis Sci*. 2012;53:1066–1075.

Investigative Ophthalmology & Visual Science

22. Radu RA, Hu J, Yuan Q, et al. Complement system dysregulation and inflammation in the retinal pigment epithelium of a mouse model for Stargardt macular degeneration. *J Biol Chem*. 2011;286:18593–18601.
23. Moiseyev G, Nikolaeva O, Chen Y, Farjo K, Takahashi Y, Ma JX. Inhibition of the visual cycle by A2E through direct interaction with RPE65 and implications in Stargardt disease. *Proc Natl Acad Sci U S A*. 2010;107:17551–17556.
24. Delori FC, Dorey CK, Staurenghi G, Arend O, Goger DG, Weiter JJ. In vivo fluorescence of the ocular fundus exhibits retinal pigment epithelium lipofuscin characteristics. *Invest Ophthalmol Vis Sci*. 1995;36:718–729.
25. Cideciyan AV, Aleman TS, Swider M, et al. Mutations in ABCA4 result in accumulation of lipofuscin before slowing of the retinoid cycle: a reappraisal of the human disease sequence. *Hum Mol Genet*. 2004;13:525–534.
26. Boyer NP, Higbee D, Currin MB, et al. Lipofuscin and N-retinylidene-N-retinylethanolamine (A2E) accumulate in retinal pigment epithelium in absence of light exposure: their origin is 11-cis-retinal. *J Biol Chem*. 2012;287:22276–22286.
27. Delori F, Greenberg JP, Fischer J, et al. Quantitative measurements of autofluorescence with the scanning laser ophthalmoscope. *Invest Ophthalmol Vis Sci*. 2011;52:9379–9390.
28. Keilhauer CN, Delori FC. Near-infrared autofluorescence imaging of the fundus: visualization of ocular melanin. *Invest Ophthalmol Vis Sci*. 2006;47:3556–3564.
29. Kayatz P, Thumann G, Luther TT, et al. Oxidation causes melanin fluorescence. *Invest Ophthalmol Vis Sci*. 2001;42:241–246.
30. Sarna T, Burke JM, Korytowski W, et al. Loss of melanin from human RPE with aging: possible role of melanin photooxidation. *Exp Eye Res*. 2003;76:89–98.
31. Wu L, Nagasaki T, Sparrow JR. Photoreceptor cell degeneration in Abcr (–/–) mice. *Adv Exp Med Biol*. 2010;664:533–539.
32. Rozanowski B, Burke JM, Boulton ME, Sarna T, Rozanowska M. Human RPE melanosomes protect from photosensitized and iron-mediated oxidation but become pro-oxidant in the presence of iron upon photodegradation. *Invest Ophthalmol Vis Sci*. 2008;49:2838–2847.
33. Pawar AS, Qtaishat NM, Little DM, Pepperberg DR. Recovery of rod photoresponses in ABCR-deficient mice. *Invest Ophthalmol Vis Sci*. 2008;49:2743–2755.
34. Allocca M, Doria M, Petrillo M, et al. Serotype-dependent packaging of large genes in adeno-associated viral vectors results in effective gene delivery in mice. *J Clin Invest*. 2008;118:1955–1964.
35. Han Z, Conley SM, Makkia RS, Cooper MJ, Naash MI. DNA nanoparticle-mediated ABCA4 delivery rescues Stargardt dystrophy in mice. *J Clin Invest*. 2012;122:3221–3226.
36. Kong J, Kim SR, Binley K, et al. Correction of the disease phenotype in the mouse model of Stargardt disease by lentiviral gene therapy. *Gene Therapy*. 2008;15:1311–1320.
37. Kellner S, Kellner U, Weber BH, Fiebig B, Weinitz S, Ruether K. Lipofuscin- and melanin-related fundus autofluorescence in patients with ABCA4-associated retinal dystrophies. *Am J Ophthalmol*. 2009;147:895–902. 902 e891.
38. Chen Y, Ratnam K, Sundquist SM, et al. Cone photoreceptor abnormalities correlate with vision loss in patients with Stargardt disease. *Invest Ophthalmol Vis Sci*. 2011;52:3281–3292.
39. Gomes NL, Greenstein VC, Carlson JN, et al. A comparison of fundus autofluorescence and retinal structure in patients with Stargardt disease. *Invest Ophthalmol Vis Sci*. 2009;50:3953–3959.
40. Cideciyan AV, Swider M, Aleman TS, et al. ABCA4 disease progression and a proposed strategy for gene therapy. *Hum Mol Genet*. 2009;18:931–941.
41. von Rückmann A, Fitzke FW, Bird AC. In vivo fundus autofluorescence in macular dystrophies. *Arch Ophthalmol*. 1997;115:609–615.
42. Lois N, Halfyard AS, Bird AC, Holder GE, Fitzke FW. Fundus autofluorescence in Stargardt macular dystrophy-fundus flavimaculatus. *Am J Ophthalmol*. 2004;138:55–63.
43. Sparrow JR, Blonska A, Flynn E, et al. Quantitative fundus autofluorescence in mice: correlation with HPLC quantitation of RPE lipofuscin and measurement of retina outer nuclear layer thickness. *Invest Ophthalmol Vis Sci*. 2013;54:2812–2820.

Investigative Ophthalmology & Visual Science

Fundus Autofluorescence in the *Abca4*$^{-/-}$ Mouse Model of Stargardt Disease – Correlation with Accumulation of A2E, Retinal Function and Histology

- Supplementary figures and tables -

Peter Charbel Issa [1,2], Alun R. Barnard [1], Mandeep Singh [1], Emma Carter [1], Zhichun Jiang[3], Roxana A. Radu [3], Ulrich Schraermeyer [4], Robert E. MacLaren [1,5 *]

1. Oxford Eye Hospital and Nuffield Laboratory of Ophthalmology, University of Oxford, Oxford, UK
2. Department of Ophthalmology, University of Bonn, Bonn, Germany
3. Jules Stein Eye Institute, Department of Ophthalmology, University of California at Los Angeles School of Medicine, Los Angeles, California, USA
4. University Eye Hospital, University of Tübingen, Tübingen, Germany
5. Moorfields Eye Hospital and UCL Institute of Ophthalmology Biomedical Research Centre, London, UK

Supplementary figure 1: RPE65 genotyping

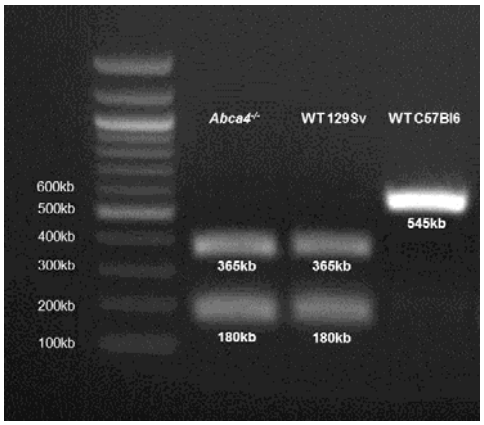

Rpe65 was sequenced by the PCR restriction fragment length polymorphism method according to Kim et al.[1] Genomic DNA was extracted from ear biopsies and PCR-amplified with the forward 5'-ACCAGAAATTTGGAGGGAAAC-3' and reverse 5'-CCCTTCCATTCAGAGCTTCA-3' primers. The Leu-450 variant introduces a Mwo1 restriction site in the resulting 545-bp product, leading to 180 and 365 bp products. *Abca4*$^{-/-}$ mice (129S4/SvJae-*Abca*^{4tm1Ght}) and wild type controls (129S2/SvHsd) showed presence of the Leu-450 variant which is associated with a higher A2E-accumulation compared to the Met-450 variant. The latter is present in the C57BL6 strain which is shown for comparison.

Supplementary figure 2: Image analysis

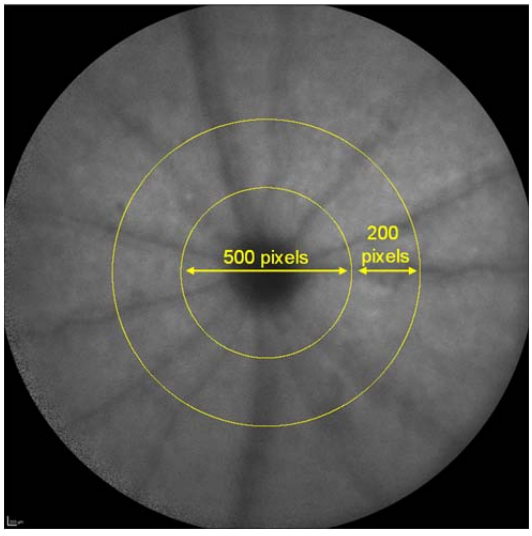

The mean grey level on mouse fundus autofluorescence images (unprocessed, 1536x1536 pixels) was measured within a ring shaped area (delineated by the two yellow circles) between 250 and 450 pixels eccentricity from the optic disc center using ImageJ software (Version 1.43, National Institute of Health, http://rsb.info.nih.gov/ij). The midperipheral area of the fundus was chosen to avoid influence of peripheral shadowing and the optic disc with the surrounding vascular crowding on the measured grey value.

Supplementary figure 3: Pupil width in *Abca4*$^{-/-}$ and wild type controls.

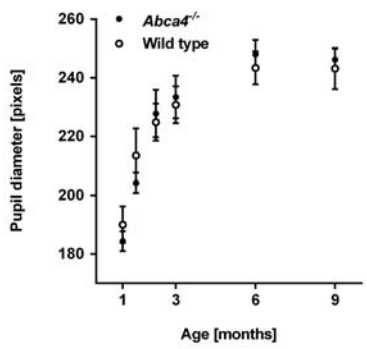

The pupil diameter (mean±SD), which strongly influences autofluorescence intensity measurements in mice,[2] increased with age ($p<0.001$) but was not different between strains (2-way ANOVA).

Supplementary figure 4: Electroretinography responses in *Abca4*$^{-/-}$ and wild type mice aged 12 and 18 months.

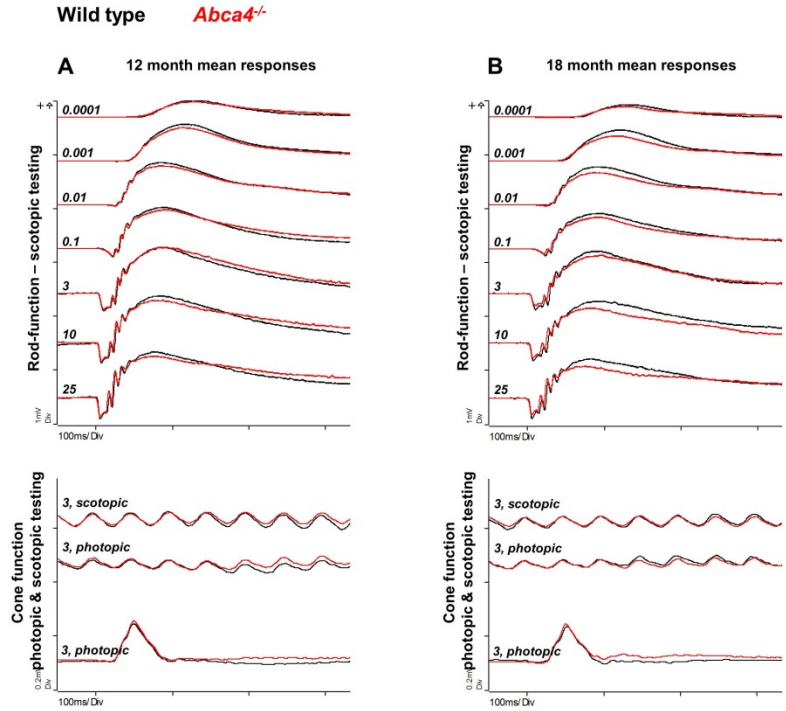

Mean responses (full range of mean traces) in animals aged 12 months (A; n=8 *Abca4*$^{-/-}$; n=6 wild type) and 18 months (B; n=5 *Abca4*$^{-/-}$; n=4 wild type). Slightly lower a- and b-wave amplitudes are present in the 18 month old *Abca4*$^{-/-}$ mice compared to wild types. There is no difference in cone function. Numbers in italics indicate flash intensity in cd.s/m^2.

Supplementary figure 5: Dark adaptation kinetics

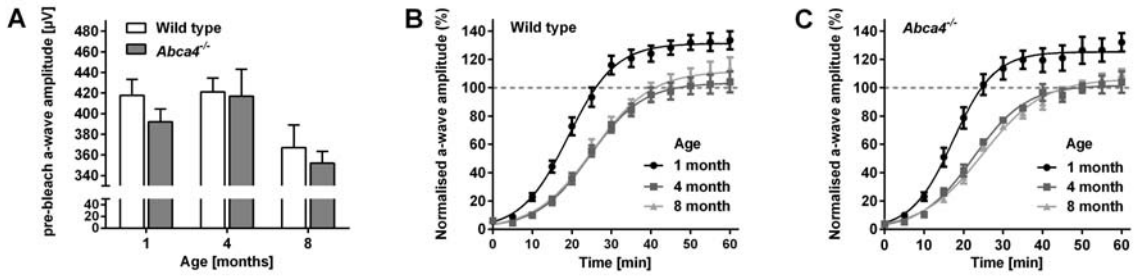

A: Before the photobleach, dark adapted a-wave amplitudes were similar between *Abca4*$^{-/-}$ and wild type (WT) animals at all ages tested. B,C: The mean scotopic a-wave amplitude (±SEM) relative to baseline before a photobleach is shown. Dark adaptation after the photobleach was slower in 4- and 8-months-old animals compared to 1-month-old mice. This age-effect was observed in both, WT (B) and *Abca4*$^{-/-}$ (C) mice. n=5-7 in each group

Supplementary figure 6: Quantitative analysis of the photoreceptor layer

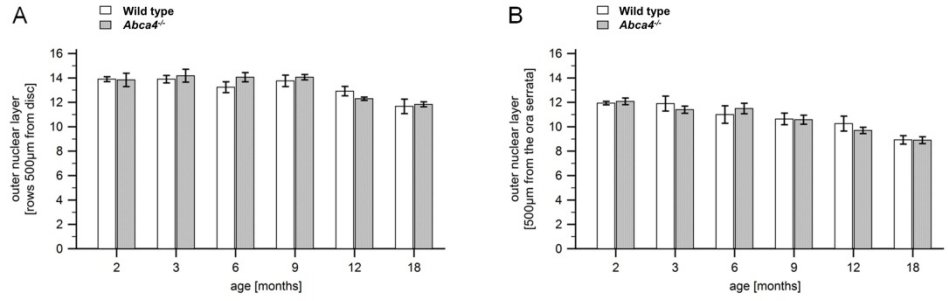

age [months]	2	3	6	9	12	18
2	-	1.0	1.0	0.03	0,03	<0.001
3		-	1.0	1.0	<0.01	<0.001
6			-	1.0	0.14	<0.001
9				-	0.02	<0.001
12					-	0.54
18						-

age [months]	2	3	6	9	12	18
2	-	1.0	1.0	1.0	<0.001	<0.001
3		-	1.0	0.3	<0.01	<0.001
6			-	1.0	0.08	<0.001
9				-	1	<0.01
12					-	0.32
18						-

Age-related loss of photoreceptors in the central (A) and peripheral (B) retina of *Abca4*$^{-/-}$ and wild type control mice. At all ages, there was no significant difference in photoreceptor layers (mean ± SEM) between the two strains in the central and peripheral retina. However, there was a significant change with age which was most pronounced after 9 months of age (tables, 2-way ANOVA). Similar results were found in the midperipheral retina 1000µm from the disc (data not shown). n=5 for each data point, except n=4 for 18 months old wild types.

Supplementary figure 7: Vacuolization of RPE in the *Abca4*$^{-/-}$ mouse.

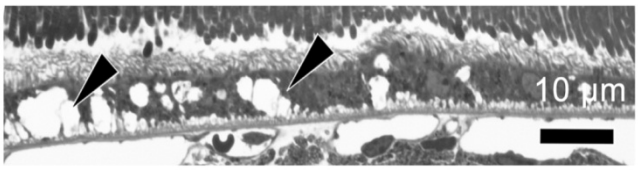

Vacuolization of RPE cells is indicated by arrowheads in the RPE of an 18 month old *Abca4*$^{-/-}$ mouse (bright light microscopy of a semithin section).

Supplementary figure 8: Difference in fundus autofluorescence intensity in different wild type strains compared to *Abca4*$^{-/-}$ mice.

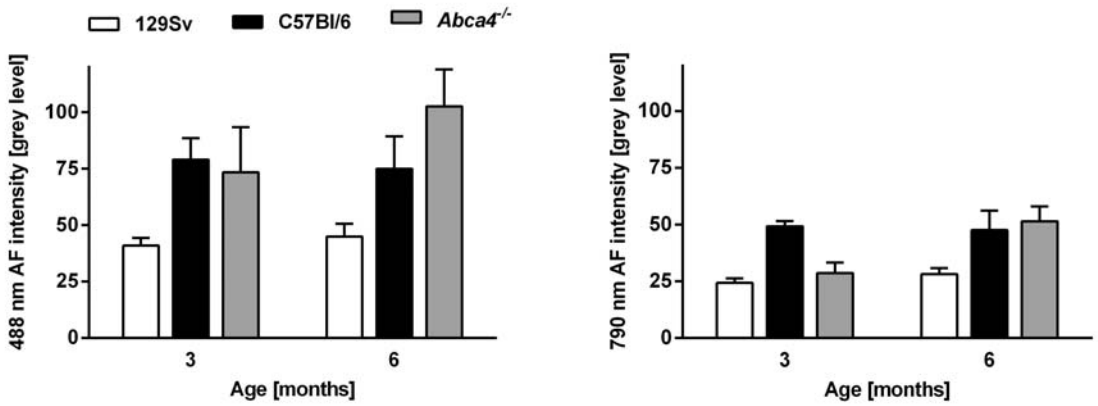

Comparison of 488 nm (left) and 790 nm (right) autofluorescence (AF) intensity in C57BL/6 wild type (WT) mice with *Abca4*$^{-/-}$ and WT control mice of the same background strain (129Sv). Fundus AF intensity was higher in C57BL/6 WT compared to 129Sv WT mice, although C57BL/6 have the Met-450 variant in *RPE65* which is associated with less A2E-accumulation compared to the Leu-450 variant present in the 129Sv strains used (A2E-levels were not determined in C57BL/6 mice for this experiment).[1, 3] Note that the AF levels for both excitation lights do not change considerably between 3 and 6 month-old WT animals of both background strains, while there is a substantial increase in *Abca4*$^{-/-}$ mice. The difference in AF intensity between the two WT strains is in line with previous post-mortem data.[3]

Supplementary table 1: Details of the ERG protocol.

Flash intensity [cd.s/m^2]	Repetitions	Inter-stimulus interval [sec]	interval after intensity step [sec]	
0.0001	10	5	20	Scotopic testing
0.001	10	5	20	
0.01	10	5	20	
0.1	5	20	60	
3	5	20	60	
10	5	20	60	
25	5	20	120	
3	20 traces	20Hz flicker		
Pre-exposure: steady full-field white background illumination (30 cd/m^2) for 10 min				
3	10	0.5		Photopic testing
10	10	0.5		
3	20 traces	20Hz flicker		
10	20 traces	20Hz flicker		

The scotopic dose-response curve results of the three highest intensities were not averaged and only the first flash response was analyzed, because incomplete recovery between stimuli was noted.

Supplementary table 2: Details of ERG protocol to test recovery of dark-adapted function.

Flash intensity [cd.s/m^2]	Repetitions	Interval between sets [sec]	interval after intensity step [sec]	
0.001	3, applied as set	120	1-2 (manual)	After ≥6 hours dark adaptation
10				
Photobleach (400 cd/m^2) for 30 sec				
0.001	1	300	1-2 (manual)	Dark re-adaptation
10				

The results of the three baseline measures were not averaged and only the first flash response was analyzed because incomplete recovery between set of stimuli was noted.

Supplementary Table 3: Quantitative measurements of fundus autofluorescence

Age [months]	*Abca4*$^{-/-}$		Wild type	
	Longitudinal	Cross sectional	longitudinal	Cross sectional
3	71 [±7.5] (n=5)	73 [±20.0] (n=7)	37 [±7.4] (n=8)	41 [±3.4] (n=7)
6	112 [±5.6] (n=5)	103 [±16.3] (n=6)	50 [±8.7] (n=8)	45 [±5.7] (n=6)
9	112 [±9.6] (n=5)	108 [±11.0] (n=5)	52 [±9.6] (n=8)	59 [±10.9] (n=6)

Comparisons of data derived from longitudinally recorded animals (same data as in Figure 1 of the main manuscript) and from a separate cross sectional data set. Mean levels of fundus autofluorescence (AF) [±SD] are presented. The two different experiments confirm each other, providing evidence for the reliability of the method of quantitative analysis of fundus AF intensity in mice. Also, the data suggested that repeated assessments did not significantly modify AF levels over time.

Supplementary discussion

During the review of this manuscript, a paper with partly similar content was published by Sparrow *et al*. in the same journal (IOVS 2013; 54:2812-2820).[4] These authors aimed at correlating quantitative measures of fundus autofluorescence (AF) with quantitation of A2E and measurements of outer nuclear layer thickness. Our work includes a number of additional investigations, such as longitudinal and near-infrared AF imaging, qualitative analysis of AF images, functional testing, and extensive light and electron microscopy.

There are a number of common findings that mutually confirm each other's results. We have previously published a paper looking at factors which affect *in vivo* AF imaging in mice.[2] Sparrow *et al*. largely confirmed those findings in the first part of their results. In the second part of their results they reported that the increase in A2E concentration is steeper than the increase in AF intensity, which is similar to the findings reported in our current paper. In line with our discussion, they argued that this may point to other fluorophores contributing to the baseline fundus AF signal in mice (i.e. the signal without age-dependent accumulation of A2E). Also, the extent of AF intensity increase in *Abca4*$^{-/-}$ mice relative to wild type controls is of similar magnitude in both studies.

However, there are also some obvious differences between the two studies that merit further detailed discussion.

1. *Modification of the confocal scanning laser ophthalmoscope (cSLO)*

The cSLO used in the study by Sparrow *et al*. was fitted with a smaller pinhole limiting the diameter of the incident laser beam (normally 1.7 mm) and the detection pupil (normally 3.4 mm) to 0.98 mm. This should ensure equal amounts of light entering the small mouse eye (pupil size only up to ~2 mm depending on age and strain) across different animals and age groups. A small pinhole size is associated with a decreased AF signal at the same laser power setting. This, together with the overall lower A2E accumulation of the mouse strain used by Sparrow *et al*. (see below) may explain the darker appearance of their fundus AF images of *Abca4*$^{-/-}$ mice (e.g. their figure 2) compared to our observations (e.g. figures 1D, 2A). Moreover, th modification of the cSLO used by Sparrow et al. should improve the validity of associations between AF measures and quantification of A2E. However,

the reduced size of the pinhole would not correct for other age-dependent changes that might also modify fundus AF measures, such as eye size, lens absorption characteristics, or increasing contribution of other fluorophores (for example the due to the age-dependent occurrence of hyper-autofluorescent spots in albino mice).

In our study, we did not aim at providing quantitative AF measures that are comparable across different age groups. We focused on investigating differences between strains within the same age group. Comparison with age-matched controls also corrects for age-dependent parameters potentially modifying AF measures (as mentioned above) that are not corrected for by using a smaller pinhole size. We plotted ratios between age-matched *Abca4*$^{-/-}$ and wild type control animals, assuming similar changes of age-dependent parameters between strains, which we have exemplarily shown for pupil width.

A second modification of the cSLO used by Sparrow *et al*. was the use of an internal fluorescent reference, as described elsewhere [5], to correct for fluctuations in laser power and detector sensitivity and thereby improve reliability of fundus AF intensity measures. However, the test-retest variability was only slightly better in the study by Sparrow *et al*. (coefficient of repeatability ±18.6% versus ±22% using our method [2]; 95% confidence interval). This suggests that other parameters influence quantitative AF measures in mice considerably more than in humans (coefficient of repeatability ±6%),[5] where fluctuations of laser power and detector sensitivity contribute noise of similar magnitude. In case the latter parameters undergo long term changes such as a drop in laser power, a reference fluorophore for mouse fundus AF imaging might be meaningful for longitudinal measures, provided changes of the reference are less than the combined fluctuations of laser power and detector sensitivity.

2. Different mouse strain genetic backgrounds used: the importance of pigment.

Sparrow *et al*. used albino mice (*BALB/c*) whereas we used pigmented mice (*129S4/Sv*). *Abca4*$^{-/-}$ albino mice accumulate less A2E compared with pigmented *Abca4*$^{-/-}$ mice.[6] This slower accumulation of the A2E/bis-retinoids observed in ageing *Abca4*$^{-/-}$ albino mice may be due to increased oxidation of the bisretinoids in the albino eye followed by some clearance and/or due to photoreceptor degeneration with subsequently reduced bisretinoid formation. Photoreceptor degeneration in

Abca4$^{-/-}$ albino mice might occur due to high levels of all-*trans*-retinal which has been implicated in photoreceptor cell death. Formation of all-*trans*-retinal is increased due to the higher light levels in the albino eye,[6] and its clearance is reduced due to defective ABCA4 function.[7]

Sparrow *et al.* found increasing A2E levels in *Abca4*$^{-/-}$ albino mice up to the age of 8 months and declining levels thereafter, whereas AF levels continuously increased up to the age of 12 months – the latest time point reported. Compared to wild type controls, the photoreceptor layer thickness in *Abca4*$^{-/-}$ mice was similar at the age of 4 month, but was reduced in animals 8 months and older. The authors stated that "these findings indicated a relationship between RPE lipofuscin accumulation and photoreceptor cell death". In our study, there appeared to be a ceiling effect of AF- and A2E levels in pigmented *Abca4*$^{-/-}$ mice, with a steep increase up to the age of 3 months, approximating a maximum with only little additional increase thereafter. Furthermore, we found in pigmented mice that high levels of lipofuscin/A2E in the retinal pigment epithelium does not adversely affect retinal structure or function over prolonged time intervals. The extent of photoreceptor layer thinning and reduction of amplitudes on electroretinography testing in pigmented *Abca4*$^{-/-}$ mice only showed minor changes similar to the normal aging effect observed in wild type controls. Thus, we cannot confirm a relation between RPE lipofuscin accumulation and photoreceptor cell death in pigmented *Abca4*$^{-/-}$ mice.

In line with the previously reported difference between albino and pigmented mice, overall A2E levels were higher in our study compared to the levels reported by Sparrow *et al*. In accordance with the higher A2E levels in pigmented mice, one might expect higher AF levels than in albino mice. However, AF measures are not directly comparable between the two studies due to the differences in assessing AF intensity (see above). Of note, higher AF levels have recently been shown in albino *BALB/c* compared to pigmented *129S4/Sv* mice (figure 9 in [2]), which might be explained by the lack of melanin as an absorber of the excitation light. Moreover, albino *BALB/c* regularly begin to exhibit autofluorescent spots early in life [2] which may also occur in other wild type mouse strains, but at a much later time point. These spots might represent photoreceptor debris or macrophages and they influence grey levels analysis performed in quantitative AF assessment. If autofluorescent spots occur more frequently in *Abca4*$^{-/-}$ than in WT controls, this

might explain the slightly higher fold difference of AF intensity between *Abca4*$^{-/-}$ and wild type mice in the study by Sparrow *et al*. compared to our study. However, this has not been investigated or reported so far.

The increased photoreceptor loss of *Abca4*$^{-/-}$ mice compared to controls observed by Sparrow *et al*. might be explained by the higher levels of all-*trans*-retinal in the albino mouse eye, and thus might be independent from lipofuscin accumulation in the retinal pigment epithelium. Although A2E levels are higher in pigmented compared to albino mice, increased photoreceptor loss was not observed in our experiments using pigmented mice. These findings rather suggest the lack of a direct causative relation between A2E accumulation and photoreceptor loss. This might also explain the paradox observed in heterozygote albino knockout (*Abca4*$^{+/-}$) mice, which show lipofuscin/A2E-measures similar to wild type controls while at the same time have photoreceptor loss similar to homozygous knockout (*Abca4*$^{-/-}$) mice. The photoreceptor loss in *Abca4*$^{-/-}$ albino mice might be due to increased all-*trans*-retinal toxicity, while the increased lipofuscin/A2E levels would have no relevant effect on retinal structure and function. Notably, pigmented heterozygote *Abca4*$^{+/-}$ mice have A2E levels in between homozygous knockout (*Abca4*$^{-/-}$) and homozygous wild type (*Abca4*$^{+/+}$) mice, without a difference in photoreceptor degeneration between the three genotypes.[8]

Photoreceptor loss may also occur secondarily to cell death within the retinal pigment epithelium. However, the latter would be visible as qualitative changes on cSLO AF images. We have not found major defects resembling e.g. human geographic atrophy in *Abca4*$^{-/-}$ mice up to an age of 18 months, but such analysis was not reported by Sparrow *et al*. If the albino mice used by Sparrow *et al*. develop RPE atrophy earlier than pigmented mice, for instance due to an increased abundance of cytotoxic oxidation products of A2E, one would rather expect declining AF intensity with age. Continuously high AF values despite declining A2E values in aged mice might be explained by the accumulation of fluorescent debris and/or macrophages in mice with faster degeneration of the outer retina. In this case, however, corresponding fundus changes should be visible on AF images, and a linear relationship between A2E and qAF measures in older *Abca4*$^{-/-}$ mice would be unlikely.

3. Further differences between the two studies

Sparrow *et al*. did not use a contact lens because they identified a lower AF signal with use of a contact lens. The reasons for this observation may include inconsistencies of lens placement, which would also explain their more variable qAF measures when using a contact lens. Certainly, there may also be manufacturing-dependent variation between the custom-made mouse contact lenses. Light absorption by the lens material (PMMA) appears unlikely to provide a full explanation, because the spectral transmittance curves of this material routinely show >90% transmittance of light above 300 nm and would not explain a 40% decrease in AF signal intensity.

An additional reason for us to record images with a contact lens was the requirement of a very exact positioning of the mouse and alignment of the camera to achieve consistent results. In our hands, this procedure took more than 30 seconds, which is the time allowed if an image with additional bleaching for 20 seconds should be recorded within the first minute. This short time window for the set up was suggested by Sparrow *et al*. in order to avoid the considerable drop in AF measures due to incident lens opacity without the protection with a contact lens.

When recording images, Sparrow *et al*. did not use the ART mode as we did. Instead, they recorded a video consisting of 9 frames and averaged those images after reviewing each one for quality. This approach is certainly more reliable to reduce noise from blink or movement artifacts as frequently encountered in humans. We suggest that using the ART mode is also a valid approach because such artifacts very seldom occur in anesthetized mice.

Sparrow *et al*. used a custom made software program to eliminate the influence of retinal vessels on the measured grey level. This is indeed a more elaborate way of obtaining valid measures of AF derived from the RPE. Assuming vessel brightness does not vary considerably, including the dark vessels in the average grey value of the analyzed area would underestimate differences between strains. Thus, our results would rather underestimate the effects *Abca4* deficiency on fundus AF intensity measures.

References:

1. Kim SR, Fishkin N, Kong J, Nakanishi K, Allikmets R, Sparrow JR. Rpe65 Leu450Met variant is associated with reduced levels of the retinal pigment epithelium lipofuscin fluorophores A2E and iso-A2E. *Proc Natl Acad Sci U S A* 2004;101:11668-11672.
2. Charbel Issa P, Singh MS, Lipinski DM, et al. Optimization of in vivo confocal autofluorescence imaging of the ocular fundus in mice and its application to models of human retinal degeneration. *Invest Ophthalmol Vis Sci* 2012;53:1066-1075.
3. Boyer NP, Higbee D, Currin MB, et al. Lipofuscin and N-retinylidene-N-retinylethanolamine (A2E) accumulate in retinal pigment epithelium in absence of light exposure: their origin is 11-cis-retinal. *The Journal of biological chemistry* 2012;287:22276-22286.
4. Sparrow JR, Blonska A, Flynn E, et al. Quantitative fundus autofluorescence in mice: correlation with HPLC quantitation of RPE lipofuscin and measurement of retina outer nuclear layer thickness. *Investigative ophthalmology & visual science* 2013;54:2812-2820.
5. Delori F, Greenberg JP, Fischer J, et al. Quantitative measurements of autofluorescence with the scanning laser ophthalmoscope. *Invest Ophthalmol Vis Sci* 2011;52:9379-9390.
6. Radu RA, Mata NL, Bagla A, Travis GH. Light exposure stimulates formation of A2E oxiranes in a mouse model of Stargardt's macular degeneration. *Proc Natl Acad Sci U S A* 2004;101:5928-5933.
7. Weng J, Mata NL, Azarian SM, Tzekov RT, Birch DG, Travis GH. Insights into the function of Rim protein in photoreceptors and etiology of Stargardt's disease from the phenotype in abcr knockout mice. *Cell* 1999;98:13-23.
8. Mata NL, Tzekov RT, Liu X, Weng J, Birch DG, Travis GH. Delayed dark-adaptation and lipofuscin accumulation in abcr+/- mice: implications for involvement of ABCR in age-related macular degeneration. *Invest Ophthalmol Vis Sci* 2001;42:1685-1690.

Clinical & Experimental Ophthalmology

Clinical and Experimental Ophthalmology 2012; 40: 39–47 doi: 10.1111/j.1442-9071.2011.02649.x

Review

Non-viral retinal gene therapy: a review

Peter Charbel Issa FEBO[1] and Robert E MacLaren DPhil FRCOphth[1,2]
[1]Nuffield Laboratory of Ophthalmology, Division of Clinical Neurosciences, University of Oxford, Oxford and [2]Oxford Eye Hospital, Oxford & Moorfields Eye Hospital, London, UK

Abstract

In the developed world, diseases of the retina are common causes of untreatable blindness. In many cases, a genetic component to the aetiology has been identified, making the development of gene-based treatments a logical long-term goal. The clinical strategy for retinal gene therapy broadly encompasses two distinct advantages over systemic drug delivery. First is that gene delivery can limit expression of a therapeutic protein to a specific target cell, which is rarely possible even with local drug delivery methods. Second, by delivering DNA that remains stable and non-degraded, gene expression and hence protein production could in theory be indefinite, obviating the need for repeated tablets or injections. Viruses have evolved distinct mechanisms, such as receptor mediated uptake and genomic integration, which efficiently encompass these two properties. For non-viral gene therapy approaches, however, nuclear localization and stable long-term transgene expression remain significant hurdles that need to be overcome. The challenge of non-viral gene therapy is therefore to harness current laboratory and molecular-based techniques to develop a man-made system that can approach the efficiency of a natural biological process. In the unique environment of the retina, this goal may not be insurmountable and would overcome the major limiting factor of adeno-associated viral vectors, which is the size of gene that can be delivered.

Key words: nanoparticle, non-viral gene therapy, retinal degeneration, retinal dystrophy, retinal gene therapy.

Introduction

Diseases of the outer retina, which includes those affecting the photoreceptors and the retinal pigment epithelium (RPE), are major causes of untreatable vision loss worldwide. There are a large number of inherited retinal degenerations[1] and to date, more than 200 retinal disease loci have been mapped and more than 160 genes have been identified (Retinal Information Network: http://www.sph.uth.tmc.edu/Retnet). Many other retinal diseases, such as age-related macular degeneration and myopia are likely to be dependent on a complex interaction of several genes and environmental risk factors, but nevertheless still have a genetic aetiology.[2,3] Recent pharmacological developments targeting vascular endothelial growth factor have been effective in treating the acute complications of age-related macular degeneration. However, there is still little evidence that a generic treatment may influence the long-term progression of monogenic or complex genetic retinal degenerations.[1] The underlying genetic basis of these diseases suggests that a gene therapy approach is logical, either to replace or reduce the expression of defective genes.

The principal feasibility of retinal gene therapy has been proven in a large number of animal models and so far in six human clinical trials, four of which used adeno-associated viral (AAV) vectors and

■ **Correspondence:** Prof. Robert E MacLaren, Nuffield Laboratory of Ophthalmology, University of Oxford, The John Radcliffe Hospital Headley Way, Oxford OX3 9DU, UK. Email: enquiries@eye.ox.ac.uk

Received 29 December 2010; accepted 21 June 2011.

Conflict/competing interest: No stated conflict of interest.

Funding sources: Research funding support for both investigators is provided by: Fight for Sight, the European Commission FP7 Marie Curie Intra-European Fellowship 237238, the Royal College of Surgeons of Edinburgh, the Medical Research Council (G0601588), the Health Foundation and the National Institute for Health Research Ophthalmology and Oxford Biomedical Research Centre.

two earlier studies administered adenoviral (Ad) vectors.[4–9] Most importantly, the human trials have not suggested any relevant safety concerns that would impede further clinical evaluation of retinal gene therapy. Hence, now that this key stage in translating gene therapy technology to the eye has been passed successfully, it is likely that there will now be a rapid increase in gene therapy treatments being tested for currently incurable retinal degenerations.

In general, viral and non-viral methods to deliver the gene of interest may be distinguished. Most information is available on viral approaches and currently registered human retinal gene therapy trials are all viral based (http://www.clinicaltrials.gov, accessed 20 June 2011). Evolutionary, a number of viruses have optimized strategies to transduce non-dividing neuronal cells, an ability that is now being used for efficient gene delivery to the retina using non-pathogenic viruses. However, there are potential limitations to viral retinal gene therapy. These include a restricted packaging ability of many viruses, possible side effects such as immune reactions against the viral capsid, or insertional mutagenesis. In the latter, ectopic chromosomal integration of viral DNA may disrupt the expression of a tumour-suppressor gene or activate an oncogene leading to the malignancy. Thus, it has been suggested that non-viral retinal gene delivery merits investigation. The aim of this review is to provide a short overview on current strategies to deliver genes of interest to the retina without viral packaging.

The retina as target for gene therapy

Currently, the primary targets for retinal gene therapy are monogenetic retinal dystrophies where the correction of one gene would suffice to avoid disease manifestation or progression. However, dystrophies with gene–gene interaction or complex diseases with a clear genetic component may in the future also benefit from advances in retinal gene therapy. For instance, correction of a genetic mutation that has an impact only on disease progression might avoid pronounced visual dysfunction without avoiding disease manifestation. Complex retinal diseases include myopia and age-related macular degeneration which are common causes for legal blindness in the far Eastern and Western worlds, respectively.

Compared with other organs which have previously been targeted, such as the liver, muscle and lung, the retina presents a far more straightforward target for gene therapy (Table 1). It is easily accessible, allowing treatment without the necessity of systemic gene delivery. The subretinal space is also a discrete anatomical compartment which in recent retinal gene therapy clinical trials has been shown to contain vector spread. The small volume of the target tissue requires only minor amounts of therapeutics, further decreasing the likelihood of systemic adverse events. Moreover, the therapeutic effect can be monitored anatomically, due to the clear media of the eye, as well as functionally, for example, by visual field testing or retinal electrophysiology.

Table 1. Summary of factors facilitating (+) and impeding (–) retinal gene therapy

+	–
Easy accessibility	Postmitotic cells
Localized drug delivery	Sensitivity to toxic effects
Small tissue volume	Large number of gene defects
Little drug escape into systemic circulation	
Good control of success (functional testing, retinal imaging)	

The two key requirements for any gene therapy approach are a safe delivery of the therapeutic gene with its associated regulatory elements into the cell nucleus and the subsequent adequate and continuous expression of the gene product. Compared with other diseases such as cystic fibrosis, retinal gene therapy still has the principal challenge that hundreds of different genes are involved and would ideally need to be targeted individually in each patient. This makes selection and recruitment for clinical trials highly complex.

Various routes for gene delivery include direct application by intravitreal injection or subretinal application. Both have a low systemic burden and low risk for systemic side effects because of the small therapeutic doses needed, the closed organ and the blood-retina barrier. Intravitreal injections are easier to administer, but risk systemic distribution through the trabecular meshwork or distal intracranial expression of the transgene via retinofugal projections of ganglion cells. The vitreous network of collagen fibrils bridged by proteoglycan filaments and the surrounding hyaluronan may also immobilize gene delivery vehicles. Also, the inner neurosensory retina and internal limiting membrane present an additional anatomic barrier to overcome for targeting the outer retina. Subretinal injection is usually the preferred route of delivery in retinal gene therapy. It is more invasive, but higher concentrations and a longer contact time of the gene construct can be achieved at the site of the target cells, which are usually the photoreceptors and/or the RPE. The pharmacological benefit of subretinal delivery is highlighted by the human clinical trial data, which has shown that the minimum dose required to achieve therapeutic effect with AAV2 in the retina is approximately 10^{10} genome particles (gp),[10] whereas a total AAV2 dose of 10^{14} gp or higher may be

required to transduce the liver.[11] A systemic application, for example, using targeting peptides, appears conceivable, but higher viral vector doses would be needed to reach a therapeutic concentration in the retina, thus resulting in a less advantageous risk profile with potentially systemic side effects.

Gain, loss and augmentation of function

Depending on the mutational effect on protein function, three different strategies to target the genetic defect may be applied. First, mutations resulting in loss of function usually show recessive or x-linked inheritance (or haploinsufficiency, where the gene product of only one functional allele is insufficient) and may be treated by gene replacement. In gene replacement, the coding sequence corresponding to the spliced exons of the functional 'wild-type' gene is delivered to the target cells.

Second, mutations resulting in a gain of function are usually associated with dominant inheritance (mutation results in a gene product with abnormal function) and could be treated by silencing of the mutant gene,[12] possibly in combination with replacement of the normal gene.[13] Either approach might be appropriate in diseases caused by dominant negative mutations, where an altered gene product antagonizes the wild-type product. For gene silencing, currently available strategies would include various methods to imitate endogenous RNA interference (RNAi) resulting in a transient suppression of transcription and/or translation of the mutated gene. Such a short-term effect may only be desirable in acute events, for example, choroidal new vessels, but not in the treatment of chronic diseases such as inherited retinal degeneration. A potentially permanent silencing effect with a single application could theoretically be achieved by AAV gene therapy using shRNAs or miRNA constructs, but delivery of RNA constructs by plasmid would not have a long-term effect unless the plasmid could somehow be modified to allow permanent and sustained transgene expression. In broad terms therefore, gene silencing is subject to the same general principles as gene replacement.

A third possible approach is to apply retinal gene therapy as a means of expressing a protein that is not itself directly involved in the disease process, but which may have additional therapeutic benefits, such as neuroprotective proteins and growth factors.[14] This would potentially be broadly applicable to a wide range of inherited retinal degenerations independent of the specific genetic cause, which would have additional benefits for cases where there is no specific molecular diagnosis. If the therapeutic protein is secreted and may diffuse to its target cells (e.g. photoreceptors), such strategy might even allow achieving therapeutic effects through protein production by non-retinal ocular tissue, which may be easier to target and which may be less sensitive than the neurosensory retina. Proof-of-concept studies in animal models have shown that DNA electrotransfer to ciliary muscle cells may be result in a local and sustained production of proteins that are secreted into the vitreous.[15]

Why non-viral retinal gene therapy?

Besides concerns regarding immunological reactions against viral vectors for gene delivery, viral gene therapy may be limited by the packaging capability of viral vectors that can safely be used for retinal gene delivery. Recombinant AAV vectors, which are currently used in clinical retinal gene therapy trials, have a packaging capacity of about 4.7 kB genomic DNA per viral particle flanked by two inverted terminal repeats. Besides the therapeutic gene sequence, this will also include the promoter sequence, poly-adenylation site and possibly additional genetic sequences to enhance effectiveness. Thus, there is a size-limit for genes delivered in a single AAV particle. Figure 1 illustrates the relationship between the DNA coding sequence of genes commonly encountered in retinal degenerations against the theoretical packaging limit of AAV. Allocca *et al*. previously challenged this 4.7 kB limitation, by showing that using the AAV5 serotype may result in efficient retinal gene transfer of expression cassettes containing the *ABCA4* or the *MYO7A* gene, with sizes of 8.9 kB and 8.1 kB, respectively.[16] More recent studies, however, have shown that the AAV packaging limit is not exceeded, but the transgene is most likely split into fragments across independent vector particles, which limits efficacy of transgene delivery.[17] Despite such progress, larger genes delivered using AAV appear to be expressed less efficiently. Moreover, a packaging limit of around 10 kB for AAV still appears to apply, even though this is higher than previously assumed.[18,19] Also, it has been shown that inclusion of non-coding elements (e.g. introns) into the DNA sequence may result in an improved gene expression *in vivo*. This would result in much larger DNA constructs than suggested by the size of genes as illustrated in Figure 1. Viruses with larger loading capacities such as lentiviruses involve a higher risk for genomic insertional mutagenesis and the presence of a cell membrane envelope is likely to contribute to immune responses. Strategies to obviate these concerns are being developed.[20] However, in parallel with improving viral delivery systems, these challenges highlight the need to develop non-viral alternatives.

Non-viral retinal gene therapy promises to be less immunogenic than viral approaches. Moreover, the

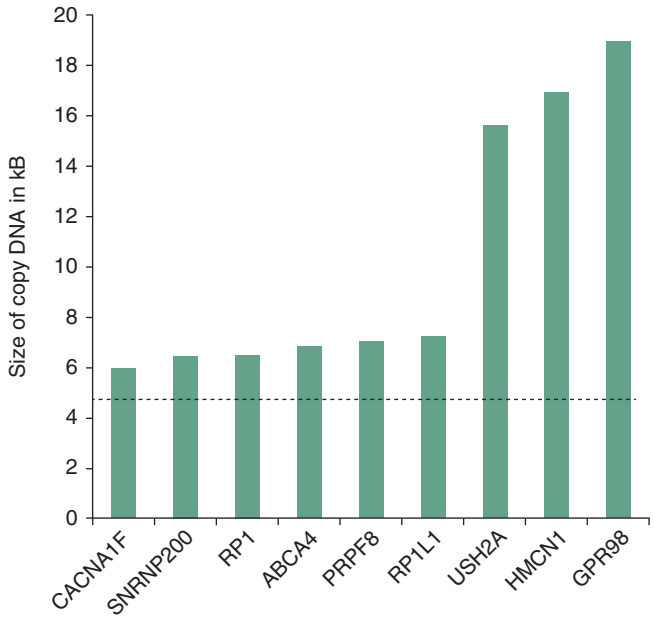

Figure 1. Examples of large genes associated with inherited retinal diseases (coding sequence from the consensus coding sequences database; http://www.ncbi.nlm.nih.gov/projects/CCDS). The dashed line marks the approximate transgene limit of 4.7 kB for adeno-associated viral vectors. Mutations in the shown genes may cause the following diseases: CACNA1 (calcium channel, voltage-dependent, L type, alpha 1F subunit): congential stationary night blindness type 2. SNRNP200 (small nuclear ribonucleoprotein 200 kDa [U5]): autosomal-dominant retinitis pigmentosa (ad RP). RP1 (retinitis pigmentosa 1): ad or autosomal recessive (ar) RP. ABCA4 (ATP-binding cassette, subfamily A, member 4): Stargardt disease, ar cone-rod dystrophy, ar RP. PRPF8 (pre-mRNA processing factor 8 homologue): ad RP. RP1L1 (retinitis pigmentosa 1-like 1): occult macular dystrophy. Ush2A: Usher syndrome, type 2A and ar RP. HMCN1 (hemicentin 1): ad macular dystrophy. GPR98 (G protein-coupled receptor 98): Usher syndrome, type 2.

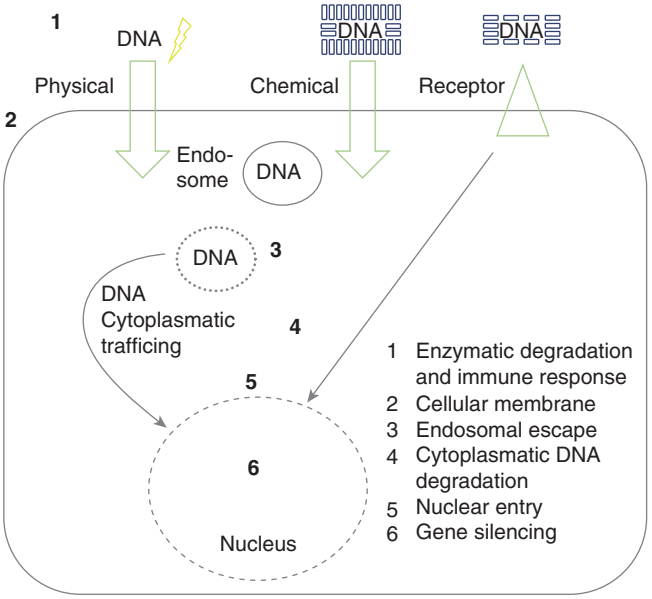

Figure 2. Schematic overview on barriers (numbered) limiting non-viral gene therapy. Methods to facilitate crossing of the cell membrane may be classified into (i) physical, such as electroporation or iontophoresis, and (ii) chemical, which includes the use of liposomes, polymers or compacted nanoparticles. For the latter, a receptor mediated cell entry mechanism has been described.

gene size appears not to be limited, possibly allowing the delivery of entire genomic DNA fragments including gene regulatory elements and intronic sequences to increase expression efficiency. Production of non-viral gene delivery vehicles may be less expensive than viral-based methods which always risk including wild-type virus in the production process and thus need more extensive purification steps. Moreover, the regulatory authorities may classify non-viral methods as drugs rather than as biologics, further cutting costs and administrative efforts.

Challenges in non-viral retinal gene therapy

As pointed out above, subretinal injection is usually performed to target photoreceptors. However, subretinal injection of naked plasmids is by no means guaranteed to result in significant gene expression. The wild-type AAV2 viral capsid has evolved together with the viral DNA to optimize delivery of the viral gene into the nucleus of the human host cell. A DNA plasmid has no vehicle to overcome the natural cellular barriers to viral infection and is itself exposed to intracellular nucleases which would result in rapid degradation of naked DNA. Several barriers (Fig. 2) need to be overcome before gene delivery results in protein expression. These challenges include escape from extracellular DNA degradation and immune response, efficient cell entry of plasmid DNA, its escape from the liposome or endosome, subsequent resistance from cytoplasmic degradative enzymes and passage through the nuclear envelope which is not possible during cell division in postmitotic retinal cells (Fig. 2). Agents or procedures used to assist and facilitate gene delivery to retinal cells must not be toxic for retinal structures. An additional fundamental problem remains even if the DNA was successfully delivered to the nucleus. Ideally, the gene would persist in the nucleus and continuously express the protein. However, DNA in postmitotic cells which is not integrated into the cell genome is usually silenced and degraded.

Therefore, DNA delivery has to be complemented with methods that aid its passage through the cell membrane and ideally also help to overcome further barriers and silencing. Such methods have been

developed *in vitro* and *in vivo*, and many have also been tried to deliver DNA to the outer retina. Generally, physical and chemical methods to move the transgene into the cell can be distinguished (Fig. 2). Physical methods include electroporation or iontophoresis that aim at permeating the cell membrane for DNA molecules by means of electrical stimuli. Chemical methods such as liposomes, polymers and compacted nanoparticles make use of forming complexes with DNA that allow – in some instances receptor-mediated – passage through/into cell membranes.

Methods of non-viral gene delivery investigated in animal models

Electroporation

To date, one of the best studied *physical* methods to aid ocular gene delivery is electroporation (electrotransfer).[21] The underlying principle is that electrical currents may alter the structure and permeability of cell membranes and thus facilitate the penetration of molecules. Matsuda and Cepko applied electroporation (with electrodes placed at either side of the head) after subretinal injection in newborn mouse and rat pups.[22] Interventions were performed at P0 and resulted in expression of the reporter gene in most cells of the neurosensory retina throughout the observational period up to 50 days with a gradual decrease by 3–4 weeks after electroporation.[23]

In adult mice, transfection by electroporation is usually achieved only in the RPE and not in the neurosensory retina. The latter could be more challenging because of the barrier imposed by the fully developed photoreceptor segments. Kachi *et al*. applied electroporation in adult mice directly after subretinal injection of a plasmid carrying a reporter gene.[24] They achieved a transient transgene expression within the RPE which was not present in the control group where electroporation was omitted. Similarly, Johnson *et al*. found that electroporation has the ability to greatly enhance transfection efficiency in the RPE of adult mice.[25] Up to 30% of RPE cells in the injected area expressed the reporter gene. Extensive optimization of modifiable parameters appeared necessary because high electroporation currents were shown to result in damage to the photoreceptors. Some degree of transfection in other intraocular tissues was attributed by the authors to their injection technique.

Iontophoresis

A second electrical approach is iontophoresis, a technique whereby charged molecules move through tissue within an electrical field. A potential promise of iontophoresis is that it might allow targeting intraocular structures without globe penetrating procedures. Transcorneal iontophoresis has been investigated in more detail, mainly to enhance drug delivery. However, transscleral iontophoresis would be necessary to effectively target the outer retina. The proof of principle for transferring DNA across the human sclera has been shown *in vitro* by Davies *et al*.[26] RNA, linear double stranded DNA (up to 12 kB tested) and plasmid DNA could be transferred through scleral fragments interposed in agarose gel lanes.[26] Two early reports demonstrated the capability of iontophoresis to deliver oligonucleotides and DNA to the intraocular posterior segment.[27,28] Souied *et al*. later applied iontophoresis to transfer plasmids through the sclera and express transgenes in the photoreceptor layer of adult normal and newborn rd1 mice.[29]

In one study, transpalpebral iontophoresis was used to enhance the penetration through the retina and target photoreceptors after intravitreal injection of labelled oligonucleotides.[30] A marked effect was reported in newborn rd1 mice when the electric current was applied before the oligonucleotide injection. This finding was explained by current-induced tissue permeation, a potential additional effect of iontophoresis. This model is also far from representative of the clinical scenario, as the newborn mouse retina is still developing and photoreceptors do not begin to form until the second postnatal week. In treating the human retina in a diseased state all photoreceptors would be fully formed, as would the surrounding anatomical barriers that exist in the adult retina.

To date, evidence for effective gene delivery to outer retinal cells by transscleral iontophoresis remains scarce. Besides the sclera, the choroid and the RPE need to be traversed. Also, in adults, the fully developed photoreceptor segments present an additional obstacle. Studies on the effect of iontophoresis after subretinal DNA delivery are lacking. Comparison with effects after extrascleral gene delivery would allow estimation of the loss of DNA across the differential anatomical barriers.

Liposomes

Liposomes are self-assembled and biodegradable vesicular structures of amphiphilic lipid-molecules such as phospholipids. Complexes of cationic liposomes and negatively charged plasmid DNA packaged into the liposomal cavity are called lipoplexes. Additional compounds such as DOPE (1,2-dioleoyl-3-phosphatidylethanolamine) can be used to facilitate DNA-release from the endosomal compartment. Kachi *et al*. used two different lipid carriers to deliver

plasmids into the subretinal space in adult mice.[24] Transfection of RPE cells was achieved; however, this was complicated by potential toxic effects on photoreceptors depending on the lipofection agent used. No effective photoreceptor transfection was reported after subretinal delivery.[24]

Polymers

Cationic polymers spontaneously form so-called polyplexes with negatively charged DNA. There are a large number of polymers used for non-viral gene therapy, such as polyethyleneimines (PEI), poly-L-lysine, chitosan, polyamidoamine starburst dendrimers, and their derivatives. PEI is one of the most commonly used vehicles for non-viral gene delivery and had been shown to facilitate transfection of post-mitotic retinal cells *in vitro*.[31] PEI is commercially available in a branched or linear form and at different molecular weights, both being factors affecting its biological properties such as transfection effectiveness and toxicity. After endosomal uptake, endosomal escape is caused by the high positive charge of PEI that results in a so-called 'proton sponge effect' with subsequent increased osmotic pressure and eventual rupture of the vesicle. PEI has also been used to transfect inner retinal cells *in vivo*;[32] however, there is a risk of toxicity when PEI polyplexes are injected into the subretinal space.

Compacted nanoparticles

Compacted nanoparticles contain a single DNA molecule which together with several positively charged peptide molecules may exhibit similar properties as native DNA-histone complexes. The DNA molecule is compacted by polyethylene glycol (PEG)-substituted 30-mer lysine peptides (CK30PEG).[33] The composition of compacted nanoparticles results in a number of favourable characteristics. Their minimal diameter is much smaller (usually <25 μm) compared with other nanoparticles which would allow compacted nanoparticles to cross nuclear pores without the need for active transport.[33] Moreover, compacted nanoparticles use an additional way to enter cells: they may directly bind to a cell surface receptor, nucleolin, which among others is involved in nucleocytoplasmatic transport and transports them into the nucleus.[34] Phenotypic rescue of the *rds*$^{+/-}$ (retinal degeneration, slow) mouse model of retinitis pigmentosa was shown after subretinal injection of compacted nanoparticles carrying the *Peripherin 2* gene which is mutatet in the rds$^{+/-}$ mouse model. An effect was reported in mice injected before (postnatal day 5) and after (postnatal day 21) terminal differentiation of photoreceptors, although therapy in the latter was less effective.[35,36] Persistent gene expression was observed during follow-up periods of up to 15 months.[37] Notably, subretinal delivery of compacted nanoparticles did not result in immune responses or toxic effects to the mouse retina.[36,38] Thus, this form of non-viral DNA delivery promises to be safe and efficient, with persistent gene expression. However, direct comparisons with viral gene delivery have not been published so far and, as recently pointed out by Kumar-Singh, some unexplained patterns of transgene expression are difficult to explain without further investigation.[39]

Optimization of non-viral gene therapy

There are various ways to improve the efficiency of gene delivery and persistence of gene expression, independent of the method used for non-viral gene therapy. Promising approaches include targeted vector integration, minicircle DNA technology or inclusion of a so-called scaffold matrix attachment region.

Persistent expression can be achieved by vector integration. Because random genomic integration may lead to insertional mutagenesis, targeted insertion has been suggested. The bacteriophage ΦC31 integrase allows plasmid DNA with a specific recognition sequence to integrate at several chromosomal hotspots with a low risk of insertional mutagenesis.[40] Chalberg *et al*. used this integrase system to overcome transient gene expression after electroporation for retinal gene delivery.[41] In their study, electroporation resulted in ~1000-fold higher transgene expression compared with subretinal plasmid injection without subsequent electroporation in 1-month-old adult rats. Additional co-injection of ΦC31 integrase resulted in a ~85-fold higher expression after 4.5 months. A similar system is the so-called Sleeping Beauty Transposon Transposase.

Alternatively, gene silencing can be minimized by reducing unmethylated and potentially immunogenic CG dinucleotides (CpGs) or omitting the entire bacterial backbone from the plasmid, resulting in so-called minicircles.[42] The bacterial backbone usually consists of an antibiotic resistance gene and a DNA sequence required for the plasmid production in bacteria and is therefore not necessary for successful gene expression in the target cell. Also, inclusion of a scaffold matrix attachment region has been suggested to overcome gene silencing in non-viral retinal gene therapy.[37] These AT-rich sequences may attach the DNA to transcriptionally active regions of the nuclear scaffold/matrix and thus ensure high transgene transcription. Scaffold matrix attach-

ment regions are thought to isolate active from inactive chromatin and may also protect DNA from methylation.

In addition to improving efficient transfection and persistence of the transgene, optimization may involve expression and control of promoters that either vary in their efficiency or that are only active in specific target cells. In experiments using electroporation the transfection efficiency of certain cell types was shown to depend upon the specific promoter. For instance, the CAG (chicken β-actin promoter with CMV enhancer) and ubiquitin C promoters appear to be more efficient than the CMV or human EF1α (elongation factor 1α) promoters in the developing rat retina.[23] Taking advantage of this, Lagali *et al*. used the cell-specific metabotropic glutamate receptor mGluR6 to exclusively transfected ON bipolar cells with channelrhodopsin-2 in the degenerated retina of the rd1 mouse.[43] Kachi *et al*. showed that non-viral gene delivery can be used to evaluate different promoters independent of influence of viral vectors.[44] Their data suggested that mammalian promoters are superior to viral promoters because the latter may be more prone to transcriptional silencing even though they may show a more pronounced initial effect.

A further improvement would be to target the outer retina by much safer intravitreal instead of subretinal injections. However, ineffective gene delivery via the intravitreal route has been explained to be due to aggregation and adherence of, for example, lipoplexes to fibrillar structures in the vitreous.[45] Adherence to vitreal structures could be prevented by attaching hydrophilic polyethylene glycol chains to the lipoplexes[45,46] or possibly additional pharmacological vitreolysis. However, additional strategies would be needed to overcome the neurosensory retina which still remains as a barrier between the vitreous and the photoreceptors and the RPE.[47]

Systemic routes for gene delivery to the retina have also been explored. One group of researchers investigated systemic intravenous administration to target the eye in non-human primates as well as in mice.[48,49] They included a monoclonal antibody against the insulin receptor or transferring receptor into the liposome to enable crossing of the blood-retina barrier. The reporter gene was under control of a bovine rod opsin promoter. The authors reported expression of the reporter gene in the retina but also other ocular tissues including lens, iris and cornea, which would not ordinarily express rhodopsin. Because of such unexplained findings, these studies need to be repeated before making firm conclusions about this method of transgene delivery.

Conclusion

Despite many potential advantages of non-viral retinal gene therapy, success has been limited to date and many studies have not been independently replicated. It remains difficult to target photoreceptor cells and to achieve high and persistent transgene expression without causing harm to the sensitive neuronal tissue by using physical or chemical transfections methods. To better estimate its effectiveness, non-viral retinal gene therapy should ideally be tested against viral vectors in future studies.

Future developments may include new non-viral biological gene delivery vehicles that have so far been unexplored for retinal gene therapy.[50] For instance, exosomes have been targeted to neurons in the brain;[51] however, their current loading capacity for oligonucleotides would need to be improved for delivery of complete gene coding sequences. The future concept of using DNA plasmid-based approaches instead of viral vectors for retinal gene therapy is very appealing, but still long way off.

Acknowledgement

We thank Dr Alun Barnard (Nuffield Laboratory of Ophthalmology, Division of Clinical Neurosciences, University of Oxford) for critical revision of the manuscript.

References

1. Berger W, Kloeckener-Gruissem B, Neidhardt J. The molecular basis of human retinal and vitreoretinal diseases. *Prog Retin Eye Res* 2010; **29**: 335–75.
2. Scholl HP, Fleckenstein M, Charbel Issa P, Keilhauer C, Holz FG, Weber BH. An update on the genetics of age-related macular degeneration. *Mol Vis* 2007; **13**: 196–205.
3. Young TL, Metlapally R, Shay AE. Complex trait genetics of refractive error. *Arch Ophthalmol* 2007; **125**: 38–48.
4. Bainbridge JW, Smith AJ, Barker SS *et al*. Effect of gene therapy on visual function in Leber's congenital amaurosis. *N Engl J Med* 2008; **358**: 2231–9.
5. Hauswirth WW, Aleman TS, Kaushal S *et al*. Treatment of leber congenital amaurosis due to RPE65 mutations by ocular subretinal injection of adeno-associated virus gene vector: short-term results of a phase I trial. *Hum Gene Ther* 2008; **19**: 979–90.
6. Campochiaro PA, Nguyen QD, Shah SM *et al*. Adenoviral vector-delivered pigment epithelium-derived factor for neovascular age-related macular degeneration: results of a phase I clinical trial. *Hum Gene Ther* 2006; **17**: 167–76.
7. MacLaren RE. An analysis of retinal gene therapy clinical trials. *Curr Opin Mol Ther* 2009; **11**: 540–6.
8. Chevez-Barrios P, Chintagumpala M, Mieler W *et al*. Response of retinoblastoma with vitreous tumor

seeding to adenovirus-mediated delivery of thymidine kinase followed by ganciclovir. *J Clin Oncol* 2005; **23**: 7927–35.
9. Maguire AM, Simonelli F, Pierce EA *et al*. Safety and efficacy of gene transfer for Leber's congenital amaurosis. *N Engl J Med* 2008; **358**: 2240–8.
10. Maguire AM, High KA, Auricchio A *et al*. Age-dependent effects of RPE65 gene therapy for Leber's congenital amaurosis: a phase 1 dose-escalation trial. *Lancet* 2009; **374**: 1597–605.
11. Manno CS, Pierce GF, Arruda VR *et al*. Successful transduction of liver in hemophilia by AAV-Factor IX and limitations imposed by the host immune response. *Nat Med* 2006; **12**: 342–7.
12. Gorbatyuk MS, Pang JJ, Thomas J Jr, Hauswirth WW, Lewin AS. Knockdown of wild-type mouse rhodopsin using an AAV vectored ribozyme as part of an RNA replacement approach. *Mol Vis* 2005; **11**: 648–56.
13. O'Reilly M, Palfi A, Chadderton N *et al*. RNA interference-mediated suppression and replacement of human rhodopsin in vivo. *Am J Hum Genet* 2007; **81**: 127–35.
14. Buch PK, MacLaren RE, Ali RR. Neuroprotective gene therapy for the treatment of inherited retinal degeneration. *Curr Gene Ther* 2007; **7**: 434–45.
15. Touchard E, Kowalczuk L, Bloquel C, Naud MC, Bigey P, Behar-Cohen F. The ciliary smooth muscle electrotransfer: basic principles and potential for sustained intraocular production of therapeutic proteins. *J Gene Med* 2010; **12**: 904–19.
16. Allocca M, Doria M, Petrillo M *et al*. Serotype-dependent packaging of large genes in adeno-associated viral vectors results in effective gene delivery in mice. *J Clin Invest* 2008; **118**: 1955–64.
17. Hirsch ML, Agbandje-McKenna M, Samulski RJ. Little vector, big gene transduction: fragmented genome reassembly of adeno-associated virus. *Mol Ther* 2010; **18**: 6–8.
18. Dong B, Nakai H, Xiao W. Characterization of genome integrity for oversized recombinant AAV vector. *Mol Ther* 2010; **18**: 87–92.
19. Wu Z, Yang H, Colosi P. Effect of genome size on AAV vector packaging. *Mol Ther* 2010; **18**: 80–6.
20. Yanez-Munoz RJ, Balaggan KS, MacNeil A *et al*. Effective gene therapy with nonintegrating lentiviral vectors. *Nat Med* 2006; **12**: 348–53.
21. Bejjani R, Andrieu C, Bloquel C, Berdugo M, Benezra D, Beharcohen F. Electrically assisted ocular gene therapy. *Surv Ophthalmol* 2007; **52**: 196–208.
22. Matsuda T, Cepko CL. Analysis of gene function in the retina. *Methods Mol Biol* 2008; **423**: 259–78.
23. Matsuda T, Cepko CL. Electroporation and RNA interference in the rodent retina in vivo and in vitro. *Proc Natl Acad Sci U S A* 2004; **101**: 16–22.
24. Kachi S, Oshima Y, Esumi N *et al*. Nonviral ocular gene transfer. *Gene Ther* 2005; **12**: 843–51.
25. Johnson CJ, Berglin L, Chrenek MA, Redmond TM, Boatright JH, Nickerson JM. Technical brief: subretinal injection and electroporation into adult mouse eyes. *Mol Vis* 2008; **14**: 2211–26.
26. Davies JB, Ciavatta VT, Boatright JH, Nickerson JM. Delivery of several forms of DNA, DNA-RNA hybrids, and dyes across human sclera by electrical fields. *Mol Vis* 2003; **9**: 569–78.
27. Voigt M, de Kozak Y, Halhal M, Courtois Y, Behar-Cohen F. Down-regulation of NOSII gene expression by iontophoresis of anti-sense oligonucleotide in endotoxin-induced uveitis. *Biochem Biophys Res Commun* 2002; **295**: 336–41.
28. Asahara T, Shinomiya K, Naito T, Shiota H. Induction of gene into the rabbit eye by iontophoresis: preliminary report. *Jpn J Ophthalmol* 2001; **45**: 31–9.
29. Souied EH, Reid SN, Piri NI, Lerner LE, Nusinowitz S, Farber DB. Non-invasive gene transfer by iontophoresis for therapy of an inherited retinal degeneration. *Exp Eye Res* 2008; **87**: 168–75.
30. Andrieu-Soler C, Doat M, Halhal M *et al*. Enhanced oligonucleotide delivery to mouse retinal cells using iontophoresis. *Mol Vis* 2006; **12**: 1098–107.
31. Horbinski C, Stachowiak MK, Higgins D, Finnegan SG. Polyethyleneimine-mediated transfection of cultured postmitotic neurons from rat sympathetic ganglia and adult human retina. *BMC Neurosci* 2001; **2**: 2.
32. Liao HW, Yau KW. In vivo gene delivery in the retina using polyethylenimine. *Biotechniques* 2007; **42**: 285–6.
33. Liu G, Li D, Pasumarthy MK *et al*. Nanoparticles of compacted DNA transfect postmitotic cells. *J Biol Chem* 2003; **278**: 32578–86.
34. Chen X, Kube DM, Cooper MJ, Davis PB. Cell surface nucleolin serves as receptor for DNA nanoparticles composed of pegylated polylysine and DNA. *Mol Ther* 2008; **16**: 333–42.
35. Cai X, Nash Z, Conley SM, Fliesler SJ, Cooper MJ, Naash MI. A partial structural and functional rescue of a retinitis pigmentosa model with compacted DNA nanoparticles. *PLoS One* 2009; **4**: e5290.
36. Cai X, Conley SM, Nash Z, Fliesler SJ, Cooper MJ, Naash MI. Gene delivery to mitotic and postmitotic photoreceptors via compacted DNA nanoparticles results in improved phenotype in a mouse model of retinitis pigmentosa. *FASEB J* 2010; **24**: 1178–91.
37. Conley SM, Naash MI. Nanoparticles for retinal gene therapy. *Prog Retin Eye Res* 2010; **29**: 376–97.
38. Ding XQ, Quiambao AB, Fitzgerald JB, Cooper MJ, Conley SM, Naash MI. Ocular delivery of compacted DNA-nanoparticles does not elicit toxicity in the mouse retina. *PLoS One* 2009; **4**: e7410.
39. Kumar-Singh R. Barriers for retinal gene therapy: Separating fact from fiction. *Vision Res* 2008; **48**: 1671–80.
40. Chalberg TW, Portlock JL, Olivares EC *et al*. Integration specificity of phage phiC31 integrase in the human genome. *J Mol Biol* 2006; **357**: 28–48.
41. Chalberg TW, Genise HL, Vollrath D, Calos MP. phiC31 integrase confers genomic integration and long-term transgene expression in rat retina. *Invest Ophthalmol Vis Sci* 2005; **46**: 2140–6.

42. Gill DR, Pringle IA, Hyde SC. Progress and prospects: the design and production of plasmid vectors. *Gene Ther* 2009; **16**: 165–71.
43. Lagali PS, Balya D, Awatramani GB *et al*. Light-activated channels targeted to ON bipolar cells restore visual function in retinal degeneration. *Nat Neurosci* 2008; **11**: 667–75.
44. Kachi S, Esumi N, Zack DJ, Campochiaro PA. Sustained expression after nonviral ocular gene transfer using mammalian promoters. *Gene Ther* 2006; **13**: 798–804.
45. Peeters L, Sanders NN, Braeckmans K *et al*. Vitreous: a barrier to nonviral ocular gene therapy. *Invest Ophthalmol Vis Sci* 2005; **46**: 3553–61.
46. Sanders NN, Peeters L, Lentacker I, Demeester J, De Smedt SC. Wanted and unwanted properties of surface PEGylated nucleic acid nanoparticles in ocular gene transfer. *J Control Release* 2007; **122**: 226–35.
47. Pitkanen L, Pelkonen J, Ruponen M, Ronkko S, Urtti A. Neural retina limits the nonviral gene transfer to retinal pigment epithelium in an in vitro bovine eye model. *AAPS J* 2004; **6**: e25.
48. Zhang Y, Schlachetzki F, Li JY, Boado RJ, Pardridge WM. Organ-specific gene expression in the rhesus monkey eye following intravenous non-viral gene transfer. *Mol Vis* 2003; **9**: 465–72.
49. Zhu C, Zhang Y, Zhang YF, Yi Li J, Boado RJ, Pardridge WM. Organ-specific expression of the lacZ gene controlled by the opsin promoter after intravenous gene administration in adult mice. *J Gene Med* 2004; **6**: 906–12.
50. Seow Y, Wood MJ. Biological gene delivery vehicles: beyond viral vectors. *Mol Ther* 2009; **17**: 767–77.
51. Alvarez-Erviti L, Seow Y, Yin H, Betts C, Lakhal S, Wood MJ. Delivery of siRNA to the mouse brain by systemic injection of targeted exosomes. *Nat Biotechnol* 2011; **29**: 341–5.